School of Chemical Engineering and Advanced Materials

Faculty of Science, Agriculture and Engineering

DEVELOPMENT OF INTENSIFIED CATALYTIC REACTORS FOR ENERGY CONVERSION

ELIJAH CHIREMBA

Thesis Submitted for the Degree of Doctor of Philosophy at

Newcastle University, Newcastle upon Tyne

22ND JANUARY 2014

AUTHOR'S DECLARATION

This thesis is submitted in fulfilment of the requirements for the degree of Doctor of Philosophy at Newcastle University, Newcastle upon Tyne, United Kingdom. All the studies described within are solely my work unless expressly stated otherwise and were undertaken in the School of Chemical Engineering and Advanced Materials under the guidance of and supervision of Professor Galip Akay from November 2009 to November 2013.

Neither the author nor Newcastle University at Newcastle upon Tyne accepts any liability for the contents of this document.

“The very essence of science and the reason it is so fascinating is that we don’t know where our ideas and experiments will lead. It is totally unpredictable”, David Suzuki

“Scientists have been warning about global warming for decades. It’s too late to stop it now, but we can lessen its severity and impact”, David Suzuki

DEDICATION

This Thesis is dedicated to my family and my late parents. To my late Father, your words still echo in my mind.

"Be kind, be honest and be faithful".

ACKNOWLEDGEMENTS

I would like to first thank my family, particularly my wife, Anna, for the untiring support and for single-handedly working day and night for the up-keep of the family through the full four years of my engagement on this full-time study. To you Anna my darling, I say you were God given to me.

Secondly, I will always be grateful to friends who stopped to ask how things were going and encouraged me to soldier on. I particularly cannot thank Amos Bwanya and family enough for the encouragement and support in too many ways than I can mention.

My Thanks also go to many colleagues in CEAM who supported me in this work, Stewart, Iain Strong, Iain Ditchburn, Jamie and Simon. My sincere thanks to Pauline for the help in SEM/EDS and Maggie for the XRD analyses respectively. But Andrea Jordan deserve special mention for all the effort and time to travel from Sheffield to take me through how to operate the Gas Chromatograph, Kui Zhang, for all the support in plasma experiments (you challenged and enriched my ideas), and to Pier Pablo and Teresa Ndlovu for your kindness and support especially in the darkest moments during the past four years. Thanks for shoulders to lean on when I needed support.

Lastly but by no means the least, I would like to thank my Supervisory Team, Prof Galip Akay and Prof S bull for guidance. This thesis would not have been possible without my first Supervisor, Prof Akay who made all this happen. The countless hours reading and reflecting on my work and encouragement, your keen interest and guidance. Prof Akay has been the ideal PhD Supervisor. I thank him from the depths of my heart for the opportunity to work with such a great mind and talent.

I would also like to thank (sponsoring organisation) without whose generous sponsorship this research would not have been possible, and Copiride partners for the enriching teleconference meetings on the project.

ABSTRACT

In this work, two intensified catalytic reactor systems applicable for energy conversion have been studied. The first is an intensified membrane reactor combining oxygen separation from air using dense oxygen selective composite perovskite type membranes with a chemical reaction at the permeate side. In this part of the work, a membrane reactor made of stainless steel was designed, constructed and a fabricated planar oxygen ceramic membrane of the $L_{0.6}S_{0.4}C_{0.2}F_{0.8}O_{3-\delta}$ (LSCF6428) type tested in it. A challenge in this work was developing a procedure to hermetically seal the ceramic membrane to the stainless steel holder. An inexpensive soft glass composition was used and with some surface treatment of the stainless steel substrate was found to bond well with both the ceramic membrane and the stainless steel casing. Oxygen permeation experiments were conducted using the membrane reactor at a temperature of 650^{o}C, under inert (helium) and reactive (CH_4 or CO) conditions. Results obtained have shown that oxygen permeation increased with a chemical reaction by 1-2 orders of magnitude compared to permeation under permeate inert conditions. At operating temperature of 650^{o}C, oxygen flux of about 0.025mLmin^{-1}cm^{-2} and 0.40mlmin^{-1}cm^{-2} under air/helium gradient and air/(He+CO) or air/(He+CH_4) gradient respectively were obtained. This result shows that from an oxygen permeation point of view, performance is superior in a combined separation and combustion mode than in a separation first to produce oxygen and combustion in a separate chamber. Further studies can explore the possibility of depositing catalytic nanoparticles on the permeate membrane surface to prevent complete oxidation and rather promote partial oxidation of methane to CO and H_2. Post operation examination of membrane showed permeate side surface changes which show some chemical stability issues of the membrane material.

The second is a DBD plasma activated reforming of methane to hydrogen or syngas. In this study, the effects of different parameters such as applied plasma power, feed gas mixture flowrate, molar composition ratio of CO_2 and CH_4 and inclusion of catalyst particles in plasma volume on the conversion of reactants and selectivity of products were experimentally investigated. Results obtained have shown the potential of plasma activated reforming of methane with carbon dioxide in one step to produce hydrogen or syngas and Higher Hydrocarbons (HCs) and oxygenates. The results from the experimental investigations in parametric effects can be used to optimise the process for the desired conversions and product selectivity. An important finding of this work was that the main products of this reforming process is not syngas as widely reported in literature, but a mixture of HCs and oxygenates, which may actually be very valuable products. Only about 10-20% of the carbon in the converted methane forms CO while the rest forms HCs, oxygenates, and, depending on conditions, carbon black. Experimental results have shown that carbon black forms in low concentration of CO_2 in the feed gas. CO_2 in higher quantities inhibits formation of carbon deposits in the plasma volume. The reported energy inefficiency (in literature) of plasma based reforming process may have been concluded from a syngas yield point of view while other products were considered as worthless by-products. An analysis of the “by-products” has shown that this might not be the case.

TABLE OF CONTENTS

CHAPTER 1 : THE PROBLEM AND MOTIVATION FOR THIS STUDY..........1

1.1 Introduction..........1
  1.1.1 Hydrogen..........2
  1.1.2 Hydrogen production technologies..........3

1.2 Motivation..........7
  1.2.1 Oxygen selective membrane reactor for POM in process intensification..........10
  1.2.2 Non-thermal plasma activated methane reforming in Process Intensification...11

1.3 Study Objectives..........11
  1.3.1 Study objectives- Intensified membrane reactor..........11
  1.3.2 Study objectives -Intensified plasma reactor for natural gas reforming..........12

1.4 Thesis layout..........12
  1.4.1 Part I: Intensified Membrane Reactor..........13
  1.4.2 Part II: Intensified Non-equilibrium plasma reactor..........13

CHAPTER 2 : OXYGEN PRODUCTION SYSTEMS..........15

2.1 Introduction..........15

2.2 Cryogenic separation method..........15

2.3 Membrane based separation systems..........16
  2.3.1 Swing Adsorption Methods..........16
  2.3.2 Polymeric membranes..........17

2.4 Molten metal method..........17

2.5 New oxygen production method – Electrochemical method..........17
  2.5.1 Pure oxygen conducting materials..........19
  2.5.2 Mixed ionic-electronic conducting materials..........19

2.6 Historical background of inorganic oxygen membranes..........23

2.7 Overview of Perovskite type materials..........25
  2.7.1 Perovskite materials tuning by doping..........28

2.8 Oxygen permeation process through a MIEC membrane..........31
  2.8.1 Modelling oxygen permeation in terms of oxygen partial pressure gradient (Wagner expression)..........32

2.9 Oxygen permeation in the bulk lattice in terms of oxygen vacancy gradient

(Fick's Law of diffusion) 37

2.10 Surface exchange reactions 39

2.11 Implications of the Wagner Equation 42

CHAPTER 3 : CATALYTIC MEMBRANE REACTOR CONCEPTS 47

3.1 Introduction 47

3.2 Membrane reactors classifications 48
  3.2.1 Extractor type Membrane Reactor (MR) 48
  3.2.2 Contactor type MR 49
  3.2.3 Distributor type MR 50

CHAPTER 4 : MEMBRANE REACTOR DESIGN, MATERIALS, METHODS AND EXPERIMENTAL SET-UP 52

4.1 Introduction 52

4.2 Membrane Reactor Description 53

4.3 Membrane Fabrication 55

4.4 Membrane module design 56

4.5 Copper gasket sealing concept 58

4.6 Experimental set-up 59

4.7 Testing procedure gasket sealing and membrane integrity 61

4.8 Cartridge heaters 62

4.9 Ignition System 63

4.10 Experiment Procedure 63

4.11 Experimental data processing 63
  4.11.1 Oxygen flux correction in permeation under inert conditions 64
  4.11.2 Oxygen flux corrections in permeation with reaction 65

4.12 Analytical Tools 68
  4.12.1 Gas Chromatography basic principles 68

4.13 Characterization techniques 72
  4.13.1 SEM and EDS – basic principles 73
  4.13.2 X-Ray Diffraction-basic principles 74

4.14 Mass Flow Meters and Controllers calibration 76

CHAPTER 5 : MEMBRANE FABRICATION AND CHARACTERISATION ... 77

5.1 Introduction 77

5.2 Membrane materials 78

CHAPTER 6 : MEMBRANE SEALING AND CHARACTERISATION 83

6.1 Introduction 83

6.2 High Temperature Sealing Options 84
  6.2.1 Brazing 85
  6.2.2 Metal O-rings 86
  6.2.3 Soft Glass 87
  6.2.4 The chemistry of glasses 90

6.3 SLG bonding to 304SS and dense LSCF6428: Experimental 95
  6.3.1 Bonding of SLG on stainless steel (304SS) 95
  6.3.2 Bonding of SLG on LSCF6428 95
  6.3.3 Bonding experiment results 95

6.4 Leakages 104

CHAPTER 7 : OXYGEN PERMEATION EXPERIMENTS AND RESULTS ... 105

7.1 Introduction 105

7.2 Permeation under inert conditions (Helium sweep gas) 106

7.3 Permeation under reactive conditions (Methane sweep gas) 107

7.4 Permeation under reactive conditions (CO sweep gas) 109

7.5 Interpretation of permeation results 110
  7.5.1 Permeate side surface reactions 111
  7.5.2 Electrical circuit equivalence of oxygen transport through the membrane...... 115
  7.5.3 Time dependent permeation experiments 117

7.6 Influence on oxygen flux of switching between inert and reactive sweep gas . 119

7.7 Effect of Carbon Monoxide or Methane concentration in sweep gas on oxygen permeation 121

7.8 Post operation analysis of membrane 125
  7.8.1 Post Operation X-Ray Diffraction Analysis 125

7.8.2 Post operation SEM analysis 127

7.9 CONCLUSIONS 133

7.10 Implication of findings 136

7.11 Limitations of study 136

CHAPTER 8 : PLASMA ACTIVATED HYDROGEN PRODUCTION FROM METHANE 137

8.1 Plasma fundamentals 137

8.2 Types of plasma 138
- 8.2.1 Thermal plasma 138
- 8.2.2 Cold /Non-thermal plasma 139
- 8.2.3 Non-thermal Plasma activated chemical reactions 141

8.3 Some current non-equilibrium plasma applications 143

8.4 DBD plasma 144
- 8.4.1 Analytical illustration of the effect of dielectric packing in DBD plasma 145

8.5 Non-thermal plasma in Process Intensification 147

CHAPTER 9 : EXPERIMENTAL 149

9.1 Investigation of hydrogen/syngas production from methane and carbon dioxide using plasma technology 149

9.2 Experimental Section 150

9.3 Products analysis and calculations 153
- 9.3.1 Volume change, conversions and selectivity calculations 153
- 9.3.2 Reactant conversion calculations from GC analysis 155

9.4 Selectivity (S_i) and yield (Y_i) and parameters 155

9.5 Calculation of Volumes Reactants and Products 157

9.6 Product ratio and Carbon balance parameters 157

CHAPTER 10 : PLASMA BASED REFORMING EXPERIMENTAL RESULTS AND DISCUSSIONS 158

10.1 Introduction 158

10.2 Decomposition of pure methane in plasma 158

10.3 Dry reforming of equi-molar CH_4/CO_2 feed (total flowrate of 25ml/min) with varying applied plasma power 160

10.4 Evaluation of the effect of CO_2 on CH_4 conversion 164

10.5 Effect of CH_4/CO_2 feed ratio on conversions and product distribution 165

10.6 Effect of feed flowrate 170

10.7 Effect of flowrate on pure methane conversion using plasma 175

10.8 Interpretation of results in terms of Input Energy Density (IED) 178
10.8.1 Pure Methane conversion 178
10.8.2 CH_4/CO_2 equi-molar mixture 180

10.9 High Hydrocarbons formed in methane reforming 181

10.10 Stability of plasma reactions over extended continuous operation 184
10.10.1 Plasma polymerisation 188

10.11 Combining non-thermal plasma and catalysis 189
10.11.1 Possible role of catalyst in hybrid plasma catalytic reactions 190
10.11.2 Experimental investigation of the effect of catalyst in non-thermal plasma dry reforming of CH_4 with CO_2 192
10.11.3 Comparisons with reports in literature 195
10.11.4 Discussions on effect of catalyst on plasma reactions 195
10.11.5 Effect of type and size of dielectric material packed in plasma zone 198

10.12 Conclusions 204

CHAPTER 11 : GENERAL CONCLUSIONS, SIGNIFICANCE AND RECOMMENDATIONS FOR FUTURE WORK 207

11.1 Introduction 207

11.2 Catalytic Membrane Reactor 207

11.3 Non-Thermal Plasma Reactor 208

LIST OF FIGURES

Figure 2-1 Schematic illustrating single and dual phase materials adapted from (Sunarso et al., 2008) 20

Figure 2-2 The ideal perovskite structure: octahedral view schematic (adapted from (Raduly-Scheuermann et al.)) 26

Figure 2-3 The ideal perovskite structure: the cubic view schematic 26

Figure 2-4 Schematic diagram of oxygen migration in membranes (adapted from (Liu et al., 2006) 30

Figure 2-5 Schematic of oxygen permeation showing the possible steps through ceramic membrane. Adapted from (Leo et al., 2009) 31

Figure 2-6 Schematic illustrating a simplified series of reactions during oxygen permeation through a MIEC perovskite membrane (adapted from (Kozhevnikov et al., 2009)) 40

Figure 2-7 Asymmetric membrane structure (adapted from (Baumann et al., 2013) 43

Figure 3-1 Schematic of an extractor type membrane reactor 49

Figure 3-2 Schematic showing contactor type reactor (adapted from (Miachon and Dalmon, 2004) 49

Figure 3-3 Schematic showing distributor type membrane reactor 50

Figure 4-1 Schematic section view of assembled reactor 54

Figure 4-2 Reactor Head Block 54

Figure 4-3 Membrane module 55

Figure 4-4 Schematic illustrating the steps in disc pressing (a) adding ceramic powder into die, (b) levelling ceramic powder using plunger,(c) ceramic powder between stainless steel die pellets,(d) pressing using hydraulic press,(e) pressed green ceramic pellet evacuation, (f) evacuated green ceramic pellet still between stainless steel die pellets, (g) resulting pressed green pellet ready for sintering, and (h) exploded ceramic disc green body. 56

Figure 4-5 Membrane module design 56

Figure 4-6 Exploded sectional view of glass seal between membrane and stainless stell housing wall. 57

Figure 4-7 Images of membrane module: (a) assembly before sealing, (b) assembly after sealing 58

Figure 4-8 Copper gasket assembly 58

Figure 4-9 Schematic of the experimental permeation cell 60

Figure 4-10 Photographic image of experimental set-up 61

Figure 4-11 Image of reactor (a) not insulated, (b) insulated to minimise heat loss during heating up the reactor. 62

Figure 4-12 Calibration chromatogram, calibration table and calibration curve (for hydrogen) example 71

Figure 4-13 Schematic showing the principles of XRD 75

Figure 5-1 Schematic illustrating the steps in disc pressing (a) adding ceramic powder into die, (b) levelling ceramic powder using plunger,(c) ceramic powder between stainless steel die pellets,(d) pressing using hydraulic press,(e) pressed green ceramic pellet evacuation, (f) evacuated green ceramic pellet still between stainless steel die pellets, (g) resulting pressed green pellet ready for sintering 79

Figure 5-2 Specac Atlas T25 Automatic Hydraulic Press used to press membrane discs. 80

Figure 5-3 The 32mm Dia, 2mm thick pressed ceramic green body and the 25mm Dia, 1mm thick disc sintered at 1150^{o}C.......... 80

Figure 5-4 Surface SEM of LSCF6428 sintered at 1150^{o}C:- Magnifications: (a) x2000, (b) x 5000 and (c) x10000 81

Figure 5-5 LSCF6428 Membrane fracture SEM:- (a) = x 100, (b) = x 5000, (c) = x 10000 81

Figure 6-1 Schematic showing glass structure (Mahapatra and Lu, 2010a) 91

Figure 6-2 Sodium oxide modifier effect on glass chain structure, breaking the silica long chains into shorter ones. 93

Figure 6-3 (a) SLG and un-pre-oxidized 304SS, (b) SLG and pre-oxidized 304SS.......... 96

Figure 6-4 SEM micrographs of SLG-304SS interface at different magnifications: (a) x 500, (b) x 500 Backscattered Electron Image (BEI) showing interface layer thickness, (c) x 2000 BEI and (d) x5000 BEI 97

Figure 6-5 SEM micrographs of SLG-LSCF6428 interface at different magnifications: (a) x 200, (b) x 2000, (c) x 5000 and (d) x10000 98

Figure 6-6 Schematic showing the role of a metal oxide layer in strong chemical bond between glass and metal substrate (a) a relatively thick metal oxide layer, and (b) a relatively thin metal oxide layer; (adapted from (Pask, 1977)) 100

Figure 6-7 Schematic showing how the absence of a metal oxide layer results in weak van der Waals forces between glass and metal substrate (adapted from (Pask, 1977)). 100

Figure 6-8 EDX spectra of sodalime glass (SLG) 101

Figure 6-9 SLG-304SS interface EDS spectra 102

Figure 6-10 Back scattered Image SLG-304SS interface image 102

Figure 6-11 SLG-LSCF6428 interface EDS spectra 103

Figure 6-12 SLG-LSCF6428 Interface SEM 103

Figure 7-1 Oxygen flux as a function of time under inert conditions 107

Figure 7-2 Results of permeation experiment with 99.99% purity CH_4. 109

Figure 7-3 Results of permeation experiment with Helium diluted CO. 110

Figure 7-4 Oxygen vacancy concentration gradient under reactive conditions at steady state conditions 114

Figure 7-5 Equivalent electrical circuit of oxygen flux through membrane 116

Figure 7-6 Schematic showing effect of CO2 adsorption on permeate membrane oxygen vacancies and blocking oxygen ion transport 119

Figure 7-7 Oxygen permeation with different sweep gas compositions 120

Figure 7-8 Effect of CO content in permeate sweep gas on oxygen permeation 122

Figure 7-9 Effect of CH_4 content in permeate sweep gas on oxygen permeation 122

Figure 7-10 XRD patterns for as-purchased membrane material powders 126

Figure 7-11 XRD patterns for membrane material after sintering at 1150^{o}C for 5 hours 126

Figure 7-12 XRD patterns for membrane material after permeation experiments 127

Figure 7-13 (a) Pre-operation surface (b) Airside surface and (c) Reaction side 128

Figure 7-14 Post-Operation Air-side EDS 129

Figure 7-15 Post-Operation Permeate side EDS 129

Figure 7-16 Pre-Operation membrane surface EDS 130

Figure 8-1 An illustration of Maxwell –Boltzmann Electron Energy Distribution function. 140

Figure 8-2 Two typical Maxwell-Boltzmann distribution functions P_A and P_B of electron energies in plasma excited by two different voltages, V_A and V_B with $V_B>V_A$, showing that an increase in applied voltage shifts the electron energy distribution function to the right (higher energy), leading to an increase in excitation and ionisation coefficients of the discharge gas in the plasma zone. 141

Figure 8-3 Main geometric configurations of DBD plasma (a) planar, (b) concentric. 145

Figure 9-1 Schematic showing plasma reactor used 149

Figure 9-2 Cross-sectional view of plasma reactor packed with dielectric balls 150

Figure 9-3 Plasma reactor set-up 152

Figure 9-4 Picture of the plasma taken in darkness 153

Figure 10-1 CH_4 conversion, H_2 selectivity, H_2 content and H_2 flowrate 159

Figure 10-2 H_2 selectivity versus applied plasma power 160

Figure 10-3 Effect of applied Plasma power on reactants conversion CH_4/CO_2 (equi-molar): flowrate of 25mL/min 161

Figure 10-4 H_2 and CO selectivities and yields 161

Figure 10-5 Distribution of Carbon in converted CH_4 164

Figure 10-6 Conversion of CH_4, CO_2 and O_2 content in effluent 167

Figure 10-7 Calculated flowrates of component effluent gases. 167

Figure 10-8 H_2 and CO selectivities and H_2/CO ratio 168

Figure 10-9 Effect of flowrate on reactants conversions 171

Figure 10-10 Syngas constituents' flowrates in effluent gases 171

Figure 10-11 H_2, CO selectivities and H_2/CO ratio 172

Figure 10-12 H_2 and CO yields 172

Figure 10-13 Schematic of plasma reactor with separation of syngas and recovery of unreacted CH_4 and CO_2 174

Figure 10-14 Relative proportions of gaseous HCs in effluent 175

Figure 10-15 Effect of flowrate on conversion of pure methane using plasma 176

Figure 10-16 Volume per unit time of CH_4 converted and H_2 produced 176

Figure 10-17 H_2 selectivity and yield 176

Figure 10-18 Schematic of plasma reactor with an upstream separation unit 177

Figure 10-19 Pure CH_4 conversion-constant applied power and varying flow rate 179

Figure 10-20 Pure CH_4 conversion – constant feed flow rate and varying applied power 179

Figure 10-21 Equi-molar CH_4/CO_2- Mixture- Constant total feed flow rate and varying applied plasma power 180

Figure 10-22 Equi-molar CH_4/CO_2 Mixture - Constant applied plasma power and varying total flow rate. 181

Figure 10-23 CO_2-CH_4 dry ice cold trap liquid products 182

Figure 10-24 Typical cold water trap products chromatogram 184

Figure 10-25 Long range conversions 185

Figure 10-26 Long range product yield performance 185

Figure 10-27 CH_4 derived carbon distribution between CO and other products e.g. HCs 186

Figure 10-28 Picture of reactor walls coated with golden brown film 188

Figure 10-29 Graphical representation of reactant conversions with different catalysts 194

Figure 10-30 Effect of SLG pellet size on conversion 201

Figure 10-31 Effect of pellet size on equi-molar, 50ml/min flowrate, varying power; on conversions 201

LIST OF TABLES

Table 5-1: Some discrepancies in oxygen flux through $SrCo_{0.8}Fe_{0.2}O_{3-\delta}$ reported in literature under supposedly similar conditions. 82

Table 6-1 SLG spectra 101

Table 6-2 SLG-304SS 102

Table 6-3 SLG-LSCF6428 103

Table 7-1 Comparison of stoichiometric ratios of membrane cations for surfaces of spent membrane (air side and permeate side) and fresh membrane............ 129

Table 10-1 Conversion of pure methane at 25mL/min flowrate and varying applied plasma power 159

Table 10-2 Dry reforming of equi-molar CH_4/CO_2 feed with varying applied plasma power............ 161

Table 10-3 Comparison of CO formed and CO_2 converted............ 163

Table 10-4 Relative concentrations of HC detected by FID 164

Table 10-5 Comparison of CH_4 conversion with and without CO_2 co-feed under same flow and applied plasma power conditions (*applied plasma power of 24W) 165

Table 10-6 Effect of CO_2 content in CH_4/CO_2 mixture on conversions 166

Table 10-7 Effect of flowrate on conversion of equi-molar CH_4/CO_2 mixture 170

Table 10-8 Effect of residence time on pure methane reforming using plasma 175

Table 10-9 Pure CH_4 conversion-constant applied power and varying flow rate 178

Table 10-10 Pure CH_4 conversion – constant feed flow rate and varying applied power 179

Table 10-11 Equi-molar CH_4/CO_2 Mixture- Constant total feed flow rate and varying applied plasma power............ 180

Table 10-12 Equi-molar CH_4/CO_2 - Mixture- Constant applied plasma power and varying total flow rate 181

Table 10-13 Conversion of CH_4 and CO_2 in non-thermal plasma with and without catalysts 193

Table 10-14 Products selectivities with and without catalysts............ 193

Table 10-15 Effect of pellet size on conversion............ 200

NOMENCLATURE

304SS	Stainless Steel Grade 304
A	Membrane area in [cm^2]
A_f	Pre-exponential constant for forward reaction
A_{fp}	Pre-exponential constant forward reaction (permeate side)
A_r	Pre-exponential constant for reverse reaction
A_{rp}	Pre-exponential constant reverse reaction (permeate side)
ASU	Air Separating Unit
ATR	Auto-thermal Reforming
B_c	Carbon balance
BCM	Billion Cubic Metres
BEI	Back-scattered Electron Image
BSCF	BaSrCoFe
BSG	Borosilicate Glass
BTO	Barium Titanate
CCS	Carbon Capture and Sequestration/Storage
CMR	Catalytic Membrane Reactor
c_{N_2}	Nitrogen concentration in bulk gas [mol%]
$c_{N_{2\_leak}}$	Concentration of leaked nitrogen [mol%]
c_{O_2}	Oxygen concentration in bulk gas [mol%]
$c_{O_{2\_leak}}$	Concentration of leaked oxygen [mol%]
$c_{O_{2\_measured}}$	Concentration of measured oxygen in stream [mol%]
$c_{O_{2\_perm}}$	Concentration of permeated oxygen in stream [mol%]
CTE	Coefficient of thermal Expansion
$c_{V_{\ddot{o}}-air}$	Oxygen vacancies concentration at air side
$c_{V_{\ddot{o}}-perm}$	Oxygen vacancies concentration at permeate side
DBD	Dielectric Barrier Discharge
DMR	Dry Reforming of Methane
$D_{V_{\ddot{o}}}$	Oxygen vacancies diffusion coefficient [mol m^{-2}]
ΔH^0	Standard Heat of Formation [Jmol^{-1}]
e	electronic charge [Coulombs]

E	Electric Field intensity [Vm^{-1}]
E_{a_fa}	Activation energy for forward reaction (airside) [$Jmol^{-1}K^{-1}$]
E_{a_fp}	Activation energy forward reaction (permeate side) [$Jmol^{-1}K^{-1}$]
E_{a_fa}	Activation energy for reverse reaction (airside) [$Jmol^{-1}K^{-1}$]
E_{a_rp}	Activation energy reverse reaction (permeate side) [$Jmol^{-1}K^{-1}$]
ECD	Electron Capture Detector
EDS	Energy Dispersion Spectroscopy
$E_{electron}$	Electron energy [eV]
E_t	Threshold electron energy [eV]
FBA	Flash Back Arrestor
FID	Flame ionization Detector
FPD	Flame Photometric Detector
F-T	Fischer Tropsch
G	Gas flow rate [$mLmin^{-1}cm^{-2}$]
GC	Gas Chromatograph
GHG	Greenhouse Gases
$\dot{h}$	electron hole
HC	Higher Hydrocarbons
HX	Heat Exchanger
ID	Inside Diameter
IED	Input Energy Density
IMR	Inert Membrane Reactor
ITM	Ion Transport Membrane
J_e	Electron Flux
$J_{O^{2-}}$	Oxygen Ion flux
J_{O_2}	Oxygen Flux [$mLmin^{-1}cm^{-2}$]
$J_{V_{\ddot{O}}}$	Flux of oxygen vacancies
k_{fa}	Forward rate constant (airside)
k_{fp}	Forward rate constant (permeate side)
k_{ra}	Reverse rate constant (airside)
k_{rp}	Reverse rate constant (permeate side)

L	Membrane thickness [mm]
LSCF6428	$La_{0.6}Sr_{0.4}Co_{0.2}Fe_{0.8}O_{3-\delta}$
m	mass of particle [g]
MFC	Mass Flow Control
MFM	Mass Flow Meter
MIEC	Mixed Ionic Electronic Conducting
MR	Membrane Reactor
MSW	Municipal Solid Waste
NBO	Non-Bridging Oxygen
OD	Outside Diameter
OTM	Oxygen Transport Membrane
O_O^x	Lattice (bulk) oxygen ion
P_1	Oxygen partial pressure (permeate side) [bar]
P_2	Oxygen partial pressure (airside) [bar]
PEG	Polyethylene glycol
PI	Process Intensification
PID	Photo Ionization Detector
PIM	Process Intensification and Miniaturisation
POM	Partial Oxidation of Methane
POX	Partial Oxidation
PRV	Pressure Relief Valve
PSA	Pressure Swing Adsorption
PTSA	Pressure and Temperature Swing Adsorption
PVSA	Pressure and Vacuum Swing Adsorption
R	Universal Gas Constant [$Jmol^{-1}K^{-1}$]
RAB	Reactive Air Brazing
R_{bdr}	Bulk diffusion resistance [Ω]
R_{sra}	Surface exchange resistance at airside [Ω]
R_{srp}	Surface exchange resistance at permeate side [Ω]
RETs	Renewable Energy Technologies
RT	Retention Time [s]

SEM	Scanning Electron Microscopy
S_j	Selectivity of species j
SLG	Soda lime glass
SMR	Steam Methane Reforming
SOFC	Solid Oxide Fuel Cell
TC	Thermocouple
T_e	Plasma Electron Temperature [K]
T_i	Plasma ion Temperature [K]
T_n	Plasma neutrals Temperature [K]
TSA	Temperature Swing Adsorption
UNFCCC	United Nations Framework Convention on Climate Change
UV	Ultra Violet
V	Applied Plasma voltage [V]
V_b	Break-down voltage [V]
$V_{\ddot{o}}$	Lattice (bulk) oxygen vacancy
VOCs	Volatile Organic Compounds
VSA	Vacuum Swing Adsorption
WGS	Water Gas
XRD	X-Ray Diffraction
Y_j	Yield of species j
YSZ	Yttria Stabilized Zirconia
z	Ion Charge number

GREEK LETTERS

∇	$\frac{\partial}{\partial x}+\frac{\partial}{\partial y}+\frac{\partial}{\partial z}$
η	Electrical potential
μ	Chemical potential
ϕ	Electrostatic potential
σ_e	Electronic conductivity
σ_i	Ionic conductivity

Publications

This work was part of a patent application whose Confirmatory Assignment is as below.

Newcastle University

IP and Legal Services
University of Newcastle Upon Tyne
Mezzanine Floor
Research Beehive
The Old Library Building
Newcastle upon Tyne
NE1 7RU

4th April 2013

Dear Elijah Chiremba,

Re: Confirmatory Assignment of the Rights and Interests in Patent Applications GCC No.2013/23374 (Saudi Arabia/GCC Countries)

You are an originator of the inventions described in GCC application No. 2013/23374 the title of which is "Integrated Intensified Biorefinery for Gas-to-Liquid Conversion" (the "Patent").

You were a full time postgraduate student of the University of Newcastle upon Tyne ("University") when you undertook the research which led to the inventions described in the Patent.

In order for the Patent to be filed in Saudi Arabia and GCC countries you are required as an inventor to sign the attached assignment (documents P216474GC) ("Assignment"). In consideration of you assigning your rights to the Patent the University will treat you as though you were a member of staff for the purpose of rewarding inventors under its Intellectual Property Policy.

In the event that the University commercializes the Patent, any income that the University receives as a result of such commercialization will be distributed to yourself and any other inventors of the inventions described in the Patent in accordance with the Policy.

Yours sincerely

Andrea Wright-Watkinson
Head of IP and Legal

The University of Newcastle upon Tyne trading as Newcastle University. VAT No. 499672470

Chapter 1 : THE PROBLEM AND MOTIVATION FOR THIS STUDY

1.1 Introduction

The global warming and climate change threat has been one of the major issues that have occupied minds of many researchers, governments and environmentalists in recent decades. Global warming is a phenomenon that is believed to be caused by the accumulation of Greenhouse Gases (GHG) in the atmosphere which has accelerated in recent years as a result of increasing (anthropogenic) human consumption of fossil fuels in energy production and other industries which produce CO_2 as a by-product (Balat, 2008, Luis et al., 2012, IEA). This has been exacerbated by growth in world population as well as the rapid economic growth of developing countries such as China, Brazil and India with the attendant consumption of growing amounts of fossil fuels such as coal, gas and petroleum (Chandran Govindaraju and Tang, 2013).

Carbon dioxide contributes a significant proportion of the overall greenhouse gases accumulating in the atmosphere which include other gases such as methane (CH_4), nitrous oxide (N_2O), sulphur hexafluoride (SF_6), hydrofluorocarbons (HFC) and perfluorinated carbons (PFC). For instance (Lupis, 1999, Kats, 1990), 82% of the USA greenhouse gas emission was CO_2. The major sources of carbon dioxide emission are combustion of coal, oil and natural gas for heating, electricity generation, transportation and industrial purposes. Many countries have introduced legislation and policies for the control and reductions in CO_2 emissions from fossil fuel combustion. This has also been partially driven by international initiatives such as the Kyoto Protocol and the United Nations Framework Convention on Climate Change (UNFCCC) Intergovernmental Panel on Climate Change {Lau, 2012 #1260.

Concerted efforts have been made to introduce and increase the contribution of renewable energy in the overall global energy mix from 19% in 2010 {Lund, 2010 #1263}, along with other strategies such as improving the energy efficiency (Kamal, 1997, Kats, 1990) in both conversion and use, to reduce carbon dioxide emissions indirectly by reducing the amount of energy wasted. However, renewable energy technologies (RETs) are not likely to make a big impact to the global energy consumption in the short to medium term due to high cost of conversion of most forms of renewable resources compared to fossil fuels (Arent et al., 2011). Fossil fuels are therefore likely to continue playing a major role in the medium to long-term in energy supply. Moreover, the demand for primary energy is likely to keep rising to keep pace with global economic growth. Most of this new demand will inevitably have to be met by consumption of even more fossil fuels. With the realisation of the inevitability of continued use of fossil fuels, research has intensified on modes of efficiently converting these fossil fuels to cleaner forms of energy or operating fossil fuels fired plants in much environmentally cleaner ways, i.e. ways that minimise emission of greenhouse gases into the atmosphere. Use of clean energy technologies with the cheap and abundant fossil fuels in ways that facilitate carbon emission control stand out as one of the most viable ways to reduce emissions. In this context, production of hydrogen, considered a future energy vector, from fossil fuels, could allow a smooth transition between fossil fuels and renewable energy systems. Natural gas, one of the most plentiful and least carbon-intensive fossil fuels with the highest H/C ratio, has been gaining widespread use as a source of hydrogen. However, energy costs in chemical processes to convert natural gas to hydrogen have become an issue of major concern because conventional methods are both capital and energy intensive, resulting in emissions of large quantities of CO_2 in the process. This has led to a search for more efficient novel ways for these conversions. This thesis explores potentially more efficient and environmentally friendly novel ways of converting natural gas to hydrogen and other products.

1.1.1 Hydrogen

Hydrogen offers advantages both in terms of reducing GHG emissions as well as being an alternative fuel which could eventually reduce the consumption rate of fossil fuels. Currently, it finds heavy use in upgrading fuels in the petroleum industry, food processing, hydrogenation processes and in the manufacture of chemical products such as ammonia and methanol. It is considered the ideal fuel for use in fuel cells. Fuel cells are seen as having potential for generating electricity much more efficiently (up to 60%) (Hotza and Diniz da Costa, 2008) than contemporary technologies such as internal combustion engines (20-30%). Fuel cells oxidize the hydrogen electrochemically producing only water as a by-product, which is environmentally clean. Hydrogen is also used in specific mixtures with carbon monoxide (commonly called syngas), to manufacture liquid sulphur-free fuels through the Fischer-Tropsch synthesis process.

Hydrogen is not an energy source, it is an energy vector. Due to its highly reactive nature, it is not a primary energy existing freely in nature, but is found in combined state with other elements in chemical compounds. It is therefore obtained by manufacturing it just like electricity. It is abundantly available in natural sources such as hydrocarbons, water and biomass which are the major feedstock for its production. Natural gas, mainly composed of methane and other hydrocarbons, is seen as one rich source of hydrogen. It is the cleanest and most hydrogen-rich of all hydrocarbon energy sources. And more significantly, natural gas resources discovered but as yet to be exploited, remain plentiful. There have been recent claims that the world is entering a “golden age of gas” (McGlade et al., 2013) with the development in shale gas technology which will enable exploitation of reportedly huge deposits of unconventional shale gas deeper in the earth’s crust. In addition, a considerable portion of the world’s reserves of natural gas are also “stranded”. This term is used for natural gas that is located remotely from consumers and conventional means of transportation using pipelines is usually not practical because of geographical, political and diplomatic limitations and the owners of such “stranded” reserves have difficulties in exploiting them (Dong et al., 2008, Wood et al., 2012). Another source of natural gas being put to waste by being released into the atmosphere with detrimental effects of exacerbating global warming is Associated Natural Gas being flared from oil mines. Gas flaring is a widely used practice for disposal of associated gas in oil production and processing facilities with insufficient infrastructure for utilisation of the gas, e.g. Russia, Nigeria and many oil producing countries in the Middle East. Global flaring has remained largely stable at about 139 billion cubic metres (BCM) annually (Elvidge et al., 2009). This is a significant amount of wasted energy source, estimated at 4.6% of the world natural gas consumption (Davoudi et al., 2013). With new novel technologies, efficient exploitation of such resources and other small scale distributed resources has the potential to play a big role and is becoming a big necessity.

1.1.2 Hydrogen production technologies

Extraction of hydrogen from the natural gas resources involves chemical processing and energy input. For the development of the much talked about hydrogen economy, there is a need to develop efficient and environmentally friendly hydrogen production processes at a cost comparable to that of fossil fuels (Mueller-Langer et al., 2007). There are several state of the art industrial processes used for hydrogen production, broadly classified as thermochemical, electrochemical or biological, based on the nature of the chemical process and/or energy input (Chaubey et al., 2013). Among these, thermochemical, specifically Steam Methane Reforming (SMR), Partial Oxidation of Methane (POX/POM), Auto-thermal Reforming (ATR) and Dry Reforming of Methane (DRM) are the most popular and responsible for the production of the bulk of the global annual hydrogen tonnage.

1.1.2.1 Steam Methane Reforming

Steam reforming of natural gas is credited for producing almost 85-95% of the world's hydrogen (Simpson and Lutz, 2007, Rehman et al., 2012, Bhat and Sadhukhan, 2009). Although it is now a mature process, SMR main disadvantage is that it is highly endothermic, normally carried out at 973-1073K and catalysed by noble metals and therefore remain energy intensive and expensive. In order to sustain this endothermic reaction, heat is supplied to the reforming reactor by burning part of the natural gas in a furnace. The syngas produced is cooled and shifted to the Water-Gas Shift reactor where the carbon monoxide component reacts with steam to produce additional hydrogen and carbon dioxide. Eqn 1.1 and Eqn 1.2 illustrate the initial steam reforming and the subsequent WGS reaction respectively to produce hydrogen and carbon dioxide. The WGS reaction requires temperature conditions ranging 573-723K and catalysts based on Fe, Cu, Mo, Fe-Pd alloys (Alves et al., 2013).

$$\mathrm{CH_4 + H_2O \leftrightarrow CO + 3H_2} \qquad \text{Eqn 1.1}$$

$$\mathrm{CO + H_2O \leftrightarrow CO_2 + H_2} \qquad \text{Eqn 1.2}$$

To obtain high purity hydrogen, the carbon monoxide and/or carbon dioxide in the product gas mixture after SMR and/or WGS reactions must be effectively separated.

1.1.2.2 Partial Oxidation reforming

POX/POM is essentially incomplete combustion of methane to form H_2 and CO. Complete combustion would yield CO_2 and H_2O (Tonkovich et al., 2011) and no hydrogen at all. Partial oxidation can be achieved by incorporation of a catalyst that promotes the partial oxidation route instead of complete oxidation. The catalyst can also lower the operating temperature. Mixed oxide solutions of NiO-MgO, Ni-Mg-Cr-La-O and Ca-Sr-Ti-Ni are reported to exhibit high activity for partial oxidation to syngas at >1073K (Alves et al., 2013, Dantas et al., 2012). This is called Catalytic Partial Oxidation (CPOX). Partial oxidation of methane can be represented by the reaction Eqn 1.3:

$$\mathrm{CH_4} + \frac{1}{2}\mathrm{O_2} \leftrightarrow 2\mathrm{H_2} + \mathrm{CO} \qquad \text{Eqn 1.3}$$

However, in practice, it is difficult to achieve 100% selectivity of hydrogen and carbon monoxide, and carbon dioxide and water are also produced in side reactions as by-products. The $\frac{\mathrm{H_2}}{\mathrm{CO}}$ ratio of 2 is ideal for methanol production by F-T process.

Although POM is possible in air, some downstream steps cannot tolerate presence of nitrogen (Balachandran et al., 1995). Partial oxidation in air results in syngas with a high concentration of nitrogen. If produced for Fischer-Tropsch processes, the reactions between CO and H_2 are always performed under pressurized conditions with CO:H_2 = 1:2 and dilutants such as nitrogen(Lu et al., 2005) are a big inconvenience from both energy and cost perspectives due to energy required to unnecessarily heat the huge amount of accompanying nitrogen, reducing efficiency and bringing about a severe engineering demand for purification of the product (Pantu et al., 2000). The nitrogen has either to be separated from the syngas or before the partial oxidation by separating oxygen from air and using the oxygen in partial oxidation reactions. Removing nitrogen from partial oxidation products is very difficult compared to separation of oxygen from air. Therefore the partial oxidation is ideally done with pure oxygen rather than air to avoid dilution of the syngas produced by relatively inert nitrogen. However, either way, the increased number of process steps decreases system efficiency. The highest cost associated with POX using pure oxygen is the oxygen separation plant. State of the art oxygen production methods such as cryogenic distillation of air is too expensive for this process and would result in high unit costs of production. A cheaper and more efficient oxygen production method is therefore required. Even better, integration of process units such as combined separation and POX in one unit will go a long way towards improving process efficiency.

1.1.2.3 Auto-thermal reforming

The third thermochemical alternative is auto-thermal reforming (ATR) where partial oxidation (exothermic reaction) and steam reforming (endothermic reaction) are carried out in the same reactor.

1.1.2.4 Dry Reforming

The fourth thermochemical route to production of hydrogen/syngas from natural gas is dry reforming of methane (DRM). Conventionally, this is a catalytic reaction at high temperatures between methane and carbon dioxide to yield syngas. The overall reaction is given by:

$$\mathrm{CH_4 + CO_2 \leftrightarrow 2CO + 2H_2 \quad \Delta H^0 = 247kJmol^{-1}} \qquad \text{Eqn 1.4}$$

DRM is seen as important in two main respects; recycling carbon dioxide produced in other processes to produce economically valuable products as well as from an environmental standpoint since it consumes two gases that contribute to the greenhouse effect (Centi and Perathoner, 2009).

This catalytic thermochemical process is still beset with several challenges among which is that it is highly endothermic. It operates at high temperatures with the risk of catalyst sintering which results in loss of specific catalyst surface area thus reducing the number of effective catalyst active sites. The other problem is susceptibility of the catalyst to coke deposition which results in catalyst de-activation. This slows down the conversion and leads to the need to re-activate the catalyst by de-coking it before it can be put to use again. The catalyst is needed mainly to reduce the high activation energy of the highly endothermic breaking of the strong H-CH_3 bonds in CH_4 and O-CO bonds in CO_2 and selectivity of required products. Although some noble metals such as Rh, Ru and Pt have shown high activity and selectivity with little carbon deposition, high cost and availability of these metals have prevented their use in commercial use for this reaction. Instead Ni and Co based catalysts have been developed based on availability and lower price (San-José-Alonso et al., 2009).

1.2 Motivation

At present, these conventional processes have largely proven ineffective in exploitation of smaller scale natural gas resources or even renewable source based biogas, because their competitiveness is premised on the strength of economies of scale. The assumption in this concept is “bigger is better”, and that it is more advantageous to use a big machine than many small ones to achieve the same output. While this may be true in some systems, the paradigm of economies of scale has become increasingly questionable in chemical processing and is sometimes regarded as a major hindrance to development of novel technologies (Alamaro, 1994). Another main drawback of the these processes is that they are all equilibrium limited and they invariably produce hydrogen rich gas mixtures containing oxides of carbon and that for pure hydrogen production, a number of additional processing units are required, significantly lowering system efficiency (Gallucci et al., 2013).

These limitations can be circumvented via innovative integrated intensified systems. This is motivating the design of flexible decentralised chemical processes and plants which are small, safer, more flexible, more efficient and less costly and are, in chemical process engineering, summarized as process intensification.

Process Intensification (PI)

Process intensification is a concept that has attracted a great deal of interest in the past few years. When the concept was first pioneered by Colin Ramshaw in the 1970s, the original intension was to make big reductions in the cost of processing systems without impairing production rate. Over time it became apparent that there were other benefits like improvement in safety, reduction in environmental impact, energy consumption and enhancement of processing yields (Ramshaw, 1999). The concept has since evolved over time resulting in a variety of definitions of what process intensification is. Stankiewicz and Moulin (Stankiewicz and Moulijn, 2003) have defined it as:

> *"Novel equipment, processing techniques and process development methods that, compared to conventional ones, offer substantial improvements in (bio)chemical manufacturing and processing."*

Jean-Claude Charpentier (Charpentier, 2007) has given a more elaborated but lengthy definition:

> *"Process intensification concerns the design of novel equipment based on scientific principles and new production methods and is obtained by using either multi-functional reactors, or new operating modes, or microengineering and microtechnology for both high throughput and formulation screening and for chemical production. Thus process intensification leads to more or less complex technologies that replace large, expensive, energy intensive equipment, or processes with ones that are smaller, less costly, more efficient plants, minimising environmental impact, increasing safety and improving remote control and automation, or that combine multiple operations into a single apparatus or into fewer devices".*

The two definitions above show that process intensification encompasses a number of themes that include multi-functionality, plant size, sustainability, increased efficiency, reduced energy use, reduced waste generation, and increased process safety. In particular, with multi-functionality, two or more processes which would have traditionally required individual units, can occur simultaneously in one unit thereby optimising the integration of processes in terms of mass and heat transfer resulting in reduced investment costs, significant energy recovery or savings, improved conversion, product selectivity and reduction in raw material consumption (Dautzenberg and Mukherjee, 2001, Liu et al., 2005).

For instance, in SRM, there is scope for combining reaction and separation of products through removal of hydrogen which shifts the equilibrium to the right, enhancing conversion. Partial oxidation that combines separation of a reactant, oxygen from air; and reaction to form nitrogen-free syngas, is another form of intensified multi-functional reactor. Such a system would obviate the need for expensively producing pure oxygen for partial oxidation using conventional methods.

Multi-functionality and miniaturization of plant or integration of several processes have become hallmarks of Process Intensification (Moulijn et al., 2008). Process Intensification has the potential to reduce the size and cost of chemical processing hardware (Yildiz et al., 2005). (Akay, 2004, Akay, 2006) has proposed the concept of Process Intensification and Miniaturization, dubbed PIM which can reduce processing volumes by factors of 10-1000, and such intensified operations can deliver low specific capital and operating costs in addition to reduced start up and shutdown times. Scaling up can be achieved through a combination of several intensified units.

Application of alternative or non-conventional forms of energy sources in chemical processing is one possible tool in the process intensification toolbox that has attracted a lot of interest among chemical engineers. Such unconventional forms of energy include sonochemistry (ultrasound), photochemistry (light), gravitational (rotating disc), microwave, plasma (thermal and non-thermal) and others (Stankiewicz and Moulijn, 2000). Of these sources of energy, the application of non-thermal plasma to activate chemical reactions is seen as very promising as it enables chemical reactions which are normally equilibrium limited in conventional systems to occur under non-equilibrium conditions, at temperatures as low as room conditions and at atmospheric pressure conditions. This can result in huge energy savings in terms of energy that would have been needed to heat the reactants and high pressure in conventional systems.

The present work studies two forms of intensified reactors for the conversion of natural gas that could overcome some of the limitations of conventional processes. They are:

1. Membrane reactor combining oxygen separation from air and chemical reaction in one unit. This intensified process obviates the need for a separate air separation unit (ASU) to generate oxygen for partial oxidation to syngas

by combining separation and reaction in a single device.

2. Using a non-conventional activation energy, non-thermal (non-equilibrium) plasma, to convert natural gas, or with carbon dioxide as a soft oxidant to produce hydrogen or syngas and other products.

These two systems are amongst several processes that can be considered as process intensification.

1.2.1 Oxygen selective membrane reactor for POM in process intensification

Oxygen permeable membrane reactors combining separation and reaction fit in well with the multi-functional theme (Stankiewicz and Moulijn, 2000). They are at least bi-functional as they integrate a reaction and separation in one unit. According to (Drioli et al., 2011), membrane operations show a higher efficiency than conventional separation and reaction unit operations. They are potentially energy efficient in that they are thermally self-sustaining as the released heat of reaction can sustain the elevated temperatures required for oxygen transport through the ceramic membrane (Armor, 1998). They are compact and have the potential for miniaturization and adaptable to small scale applications unlike cryogenic based oxygen production that is only viable for large scale production. They are safer, as the membrane prevents pre-mixing of oxygen and the fuel gas thereby providing an extra dimension of safety by avoiding explosive mixtures of the two reactants as oxygen is added controllably through the oxygen selective dense membranes (Armor, 1998). In addition, smaller size reactors reduce the heat and mass transfer resistance common in large scale plants. Scaling up can be achieved by replicating the small miniaturized units.

The other benefit is that the oxidation reaction does not produce NO_x as the membrane is impermeable to nitrogen. Unlike conventional oxygen production systems requiring large scale operations for viability on the basis of economies of scale, these systems could lend themselves to inexpensive small scale operations and make it possible to exploit smaller resources which would not be viable with conventional methods.

1.2.2 Non-thermal plasma activated methane reforming in Process Intensification

A key aspect of process intensification is the use of alternative sources of energy in combination with intensified module. Application of non-thermal plasma, which is essentially applying electric field in chemical processes, is seen as fitting into the definition of Process Intensification (Charpentier, 2007) (Reay, 2005, Stankiewicz and Moulijn, 2003). In this part of the present work, energy of electric fields is applied in chemical processes and reactions take place in non-conventional media. There are several advantages with non-thermal plasma; short reaction times thus saving energy, increased safety because reactions occur in mild conditions (room temperature and atmospheric pressure).

Catalytic dry reforming of methane is one process where non-thermal plasma could be employed. Here, two greenhouse gases, methane (main component of natural gas), and carbon dioxide can be simultaneously utilised to produce hydrogen, an ecologically clean fuel, or syngas which can be further processed via F-T processes to produce liquid products such as methanol. Non-thermal plasma is also adaptable to small scale operation and can lend itself to exploitation of small scale resources such as biogas and low grade natural gas which are already mixtures of methane and carbon dioxide.

1.3 Study Objectives

This thesis focuses on the development of intensified reactors for conversion of primarily gaseous fuels such as natural gas to other forms of energy or products such as hydrogen, syngas and liquid fuels. Two intensified reactor processes have been considered in this work. They are oxygen selective membrane reactor and non-thermal plasma activated reforming reactor.

1.3.1 Study objectives- Intensified membrane reactor

The present work aims at developing a membrane reactor for separation of oxygen from air. An essential part of this work is the design and construction of a membrane reactor, including developing a method of achieving high temperature sealing of the membrane reactor. The reactor is tested in two modes of operation (1) oxygen production and (2) reactive membrane reactor in which the separated oxygen is consumed in a chemical reaction as it is separated and the oxygen separation performance is evaluated under inert and reactive conditions.

1.3.2 Study objectives -Intensified plasma reactor for natural gas reforming

This part of the current work investigates the applicability of intensified DBD plasma technology for intensified fuel conversion. A novel DBD plasma reactor is used to study the conversion of natural gas with and without carbon dioxide to hydrogen/syngas and higher hydrocarbons. The current work will experimentally investigate how non-thermal plasma based process parameters such as plasma power (or Voltage), reagent(s) flowrate, composition, type of dielectric material pellets and catalyst inclusion can influence conversion, product selectivity and energy and material consumption. In particular, a better understanding of these and any synergy between non-thermal plasma and heterogeneous catalysis is very necessary to optimise the operation of future chemical plants based on non-thermal plasma.

1.4 Thesis layout

This thesis has been divided into two parts. The first part deals with the development of an intensified membrane reactor combining oxygen separation and a combustion reaction in one unit. It demonstrates not only the possibility of fuel conversions with reaction products free from high levels of nitrogen dilution, but also oxygen separation enhancement compared to separation without reaction. This is covered in Chapters 2-7. The second part deals with the development of an intensified non-equilibrium DBD non-thermal plasma reactor for conversion of methane to hydrogen or syngas at ambient temperature and pressure conditions.

Chapter 1 sets the stage by defining the problem which this thesis tries to contribute solutions to. It defines in terms of shortcomings of conventional systems in natural gas conversions and suggests intensified reactors as possible alternatives to the conventional systems. Two intensified catalytic reactor systems are selected for study owing to their good potentials to out-perform contemporary technologies. The selected systems are oxygen selective catalytic membrane reactor for natural gas conversion, and non-thermal plasma assisted conversion.

1.4.1 Part I: Intensified Membrane Reactor

Chapters 2 presents current oxygen production systems and their limitations, and the theory of oxygen permeable ceramic membranes upon which the membrane reactor is based.

Chapter 3 presents the concept of membrane reactors and the different roles of the membrane in the chemical processes.

Chapter 4 describes the design and construction of the membrane reactor, the instruments used for collecting experimental data and characterisation techniques.

Chapter 5 describes the fabrication and characterization of LSCF based dense membranes used to test this concept.

An important aspect of membrane reactor application for fuel conversion is the development of suitable high temperature sealing materials and sealing procedure. **Chapter 6** describes a procedure for sealing the membrane reactor using glass, including the characterization of the joints the glass make with the ceramic membrane and the stainless steel holder.

Chapter 7 presents the membrane reactor testing and compares two modes of its operation; (1) oxygen production for sequential separate use in fuel conversion and (2) combined or simultaneous oxygen separation and chemical reaction, post operation membrane characterization, the results obtained and the ensuing discussion.

1.4.2 Part II: Intensified Non-equilibrium plasma reactor

This part of the thesis is covered by Chapters 8-10. **Chapter 8** reviews plasma fundamentals, theory and concepts combined with a review of the literature of non-equilibrium plasma.

Chapter 9 describes the methodology used in the study of DBD non-thermal plasma for fuel conversion.

Chapter 10 describes the experiments conducted to investigate the effects of different operating parameters, and discusses the results and their implications.

Chapter 11 covers conclusion on the two intensified reactor systems and suggested future work.

Chapter 2 : **OXYGEN PRODUCTION SYSTEMS**

2.1 Introduction

Oxygen is ranked as one of the top five most widely used commodity chemicals in the world(Burggraaf and Cot, 1996) and its demand continues to grow, currently finding numerous applications e.g. steel making, pulp and paper, chemical, waste water treatment and petrochemical industries and in the medical field(Zhao et al., 2010). It goes without saying, therefore, that, with the new demands for clean energy technologies requiring oxygen free from nitrogen as a feed such as oxyfuel combustion, POX and oxygen blown gasification, its (oxygen) production is a growing business and new cost effective methods for its production to supplement or replace expensive, energy intensive and/or inefficient conventional ones need to be explored.

At present, cryogenic air separation, membrane based systems such as Swing Adsorption techniques and polymer membranes are the main processes used in oxygen production.

2.2 Cryogenic separation method

Cryogenic separation is more cost effective for large scale production while Swing Adsorption methods are cost effective for small-to-medium scale oxygen production. The cryogenic technique is mature and has been in use for about a century. It exploits the differences in the relative volatilities of the air constituents. Air is compressed and liquefied at very low temperatures and the constituents can be selectively separated in distillation columns. The main disadvantage is that this process involves a number of very capital and energy intensive steps. The steps include filtering the inlet air, compressing it, chilling it to -180^{o}C, and distilling the air constituents through large columns to separate them. Purities of the order of 99% are achievable using this process and all components of air, nitrogen, oxygen and trace gases are recoverable using this method (Tonziello and Vellini, 2011). The process is however so energy intensive and expensive for feasibly coupling to oxy-fuelled power plants or for partial oxidation of methane to syngas (POM). The cryogenic air separation process would reduce the overall power generation efficiencies from the current best practice of around 40%, to 30% and below (Andersson and Johnsson, 2006, Leo et al., 2009, Pehnt and Henkel, 2009) or, in the case of partial oxidation of methane, it increases the cost of production. If used in oxy-fuelled power generating units, it is estimated that up to 15% of the power plant's electrical output will be consumed in the cryogenic oxygen separation from air process (Herzog and Golomb, 2004). The current major suppliers of this technology in the world are Air Products, Air Liquide, BOC Gases, Praxair and Linde.

2.3 Membrane based separation systems

The membrane based conventional systems include swing adsorption methods and polymeric membranes.

2.3.1 Swing Adsorption Methods

The Swing Adsorption method in its various variants, Vacuum (VSA), Pressure (PSA), Temperature (TSA), Pressure and Vacuum (PVSA) and Pressure and Temperature (PTSA) are also mature and can achieve gas purities of 90-95% and recovery rates of up to 94%.

In air separation, adsorption processes are based on the ability of some materials to preferentially adsorb nitrogen. Most of these systems rely entirely on zeolites to trap nitrogen in order to produce oxygen rich air (Leo et al., 2009, Hashim et al., 2011). In zeolites, non-uniform electric fields exist in the void spaces in the material, causing preferential adsorption of molecules that are more polarisable. Nitrogen molecules are more strongly adsorbed than oxygen and therefore when air is passed through zeolitic material bed, an oxygen-rich stream exits the bed. When the bed is saturated with nitrogen, it can be removed and the adsorbent regenerated by heating the bed or reducing the pressure to reduce the equilibrium nitrogen holding capacity. Heating is referred to as TSA while pressure reduction as PSA or VSA (Smith and Klosek, 2001). The advantage of adsorption based separation compared to cryogenic is their relatively lower investment costs, lower energy consumption and easier handling (He et al., 2009), However, one major disadvantage is that it is a cyclic process consisting of adsorption step to separate oxygen from nitrogen and regeneration of adsorbent bed by de-saturating it.

2.3.2 Polymeric membranes

Polymeric membrane systems work on the basis of the difference in rates of diffusion of oxygen and nitrogen through the membrane which separates high pressure and low pressure process streams. As molecular sieves with pore sizes of the same order of magnitude as the size of air molecules, due to the smaller size of the oxygen molecule, it is more permeable than nitrogen and such membrane systems produce oxygen enriched air with 25-50% oxygen (He et al., 2009, Smith and Klosek, 2001) and still unsuitable for downstream processes in which the presence of nitrogen is undesirable. Major benefits of polymeric membranes are simplicity, low cost, easy fabrication or moulding, can be operated continuously and need to be operated to not too high temperatures and pressures.

2.4 Molten metal method

Another oxygen production technology is the chemical process that is based on the ability of some materials such as molten salt to absorb and desorb oxygen in particular pressure and temperature conditions. Pressurised air cleaned of water vapour and carbon dioxide is blown through the molten metal absorbent bed and the oxygen reacts chemically with the molten salt until the bed reaches saturation with oxygen. This is followed by subjecting the oxygen bearing molten salt to reduced pressure conditions to desorb the oxygen. Air Products and Chemicals operated a pilot plant using this technique and found it not cost effective due to corrosion problems of the salt/oxygen two phase areas of the plant (Hashim et al., 2011, Smith and Klosek, 2001).

2.5 New oxygen production method – Electrochemical method

Conventional oxygen production systems are increasingly seen as inefficient due to their high appetite for large amounts of energy per unit of product, capital intensity and the fact that they are only considered economical when operated as large scale units. The quest for lower cost option for oxygen separation has promoted increasing interest in the development of cheaper methods. In recent years there has been a paradigm shift and a rising trend towards process intensification with simple plant construction and operation, relatively low power consumption and compactness (Pekdemir et al., 2003), increasing plant efficiency, lower capital costs, waste minimization, and reduction in environmental impact and process safety (Drioli et al., 2011) (Erkoç et al., 2002).

The development of alternative compact, low-cost, energy efficient and/or additional methods of pure oxygen production to substitute or to augment the conventional methods described above (cryogenic, Swing Adsorption techniques and polymeric), to meet the ever increasing pure oxygen demand has been identified as a significant research area and has generated growing academic, economic and industrial interest. A promising new class of materials for this is dense ceramic membranes which can permit the separation of oxygen from air at elevated temperatures >600^{o}C. They are generally referred to as solid electrolytes. So promising is this technology that large global air products suppliers such as Air Products and Praxair have been actively involved in research in these new materials.

The ability of such materials to selectively separate oxygen has been known for several decades now. Unlike microporous polymer membranes, oxygen permeation in these materials is related not to membrane morphology, but to material composition (Zhao et al., 2010). In principle, all solid electrolytes have both ionic and electronic conductivity to some extent. However, it has been arbitrally agreed by material scientists that solid electrolytes in which the transference number for ions is two or more orders of magnitude higher than that for electrons are considered as “pure” ionic conductors. If, on the other hand, the transference numbers of ions and electrons are comparable, the solid electrolyte is considered “mixed” conductor (Garagounis et al., 2010). The ionic conductivity of solid electrolytes is not due to their porosity, but is based on ionic displacement through their lattice. Numerous types of these inorganic materials capable of conducting oxygen ions have been widely reported in literature. They include pyrochlores with chemical formula ($A_2B_2O_7$), brownmillerites ($A_2B_2O_5$), Ruddlesden-Popper series ($A_{n+1}B_nO_{3n+1}$), fluorite (AO_2) and perovskite (ABO_3) structured materials.

Among these, perovskite structured materials which fall in the “mixed” conductors as explained above, are by far the most widely studied and reported due to their superior oxygen conductivity properties compared to the rest. The membranes made from these are termed Mixed Ionic-Electronic Conducting (MIEC) and alternative names often used are Ion Transport Membranes (ITMs) or Oxygen Transport Membranes (OTMs) and these terms may be used interchangeably in this thesis. Fluorites have received significant attention as well due to their good ionic conductivity and poor electronic conductivity, but focus on these has been mainly in the development of solid oxide fuel cells which ideally require high ionic conductivity and high electrical resistance, for generation of electricity in which electrons flow via the external circuit (Zhang et al., 2011) instead of through the solid electrolyte. These are called oxygen inorganic pure oxygen conducting membranes.

2.5.1 Pure oxygen conducting materials

For pure oxygen ion conducting membranes, an external electrical power source and electrodes are required to drive the ionic current which results in oxygen diffusion. The external electric field provides a “pumping” force and can be used to pump oxygen to either side of the membrane regardless of the oxygen partial pressure difference. They can even drive oxygen ionic current against partial pressure gradient, hence the term “pump”. Examples of pure oxygen ion conducting materials include Yttria Stabilised Zirconia (YSZ), popular as a solid electrolyte in Solid Oxide Fuel Cell applications which are operatively the reverse of the oxygen pumps, generating electricity instead. Because of the structural complexities of connecting electrical power to electrodes in high temperature oxidizing and reducing environments, electrical field driven oxygen pumps using these materials are not an attractive option for oxygen separation.

2.5.2 Mixed ionic-electronic conducting materials

The mixed ionic–electronic conducting materials are solid ceramic membranes which contain defects in the form of oxygen ion vacancies in their crystal lattice. It is through these vacancies that they are able to conduct oxygen ions under suitably high temperature conditions. MIECs are also able to simultaneously conduct electrons in the opposite direction to preserve local electrical neutrality. Oxygen will thus be transported through the material without the need for an external electric circuit and electrodes to drive the process. Since oxygen ions are the only ionic species that are transported, these materials can exhibit absolute selectivity for oxygen transport unlike polymeric and porous ceramic membranes (Gür et al., 1992). By applying high temperature conditions and an oxygen partial pressure gradient across a membrane made from such materials, oxygen in the form of ions is driven from the high partial pressure side to the low pressure side. Perovskite structured MIEC membranes are widely seen as having the potential to outperform conventional oxygen production systems in terms of efficiency and cost. Although a reliable economic comparison of this technology with state of the art oxygen production technologies like cryogenic distillation is difficult due to lack of reliable data of capital costs of membrane technology, some authors have estimated a reduction of more than 35% (Leo et al., 2009), (Hashim et al., 2011, Kakaras et al., 2007a, Kakaras et al., 2007b) and when integrated into oxyfuel power plants for clean fuel conversion Carbon Capture and Storage technologies, they have the potential to reduce the cost of CO_2 capture by 50% compared to post-combustion Carbon Capture and Storage (CCS) (Stadler et al., 2011). In coal and biomass gasification, partial oxidation of methane and oxy-fuel combustion applications, this is a promising technology as air can be used as the oxidant without mixing of large quantities of nitrogen in the product stream. The air is supplied to one side of the membrane and only oxygen permeates the dense membrane to react with the fuel at the other side. In addition the heat produced during the exothermic reaction with the fuel potentially makes the process thermally self-sustaining.

MIEC materials can consist of either dual phase or single phase materials. *Figure 2-1* illustrates the structures of dual and single phase MIECs.

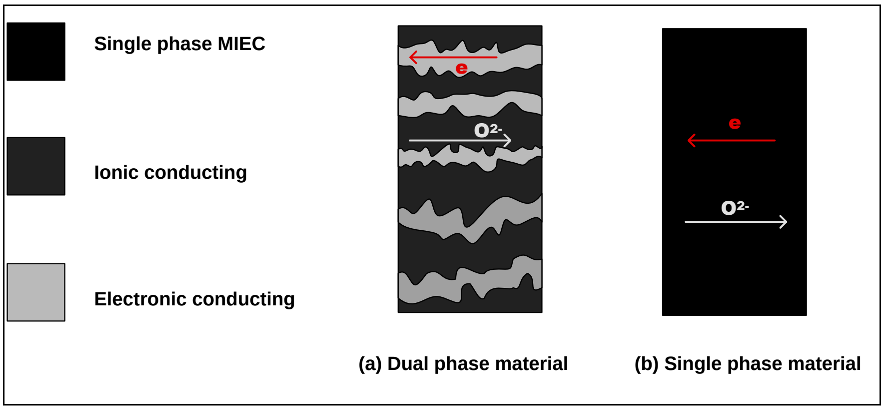

Figure 2-1 Schematic illustrating single and dual phase materials adapted from (Sunarso et al., 2008)

2.5.2.1 Dual phase materials

An alternative to single phase MIEC materials is the dual phase materials. Dual phase materials contain two phases where one has oxygen ion conducting capabilities and the other electronic conduction. Dual phase composite materials were proposed by (Mazanec et al., 1992) and further investigated by (Chen et al., 1997). These materials have attracted a lot of attention in the past few decades as an alternative to single phase materials which have generally exhibited difficulties in meeting all necessary requirements such as high permeability, stability and mechanical strength. It has been observed that generally, in single phase materials, improvement of some aspects simultaneously resulted in the degradation of other essential properties. For example, single phase materials exhibiting high oxygen permeability have been found to exhibit poor stability properties under typical operating conditions of elevated temperatures, oxygen partial pressure difference and presence of carbon dioxide in the product stream. MIEC materials based on Barium, Strontium, Cobalt and Iron (BaSrCoFe) systems are a case in point. These materials exhibit among the highest oxygen permeability so far obtained, but very poor stability in CO_2 containing environments.

Dual phase materials consist of percolation networks of two phases, with one of the phases, usually a perovskite or flourite structured phase e.g. zirconium or cerium based solid electrolytes, capable of ionic oxygen conduction, and the other phase, usually an noble metal such as Ag, Pd, Au or Pt, capable of electronic transport (Yang et al., 2005, Liu et al., 2006) to form the so called cermet (short for ceramic-metal composite). *Figure 2-1* (a) illustrates the structure of dual phase materials. To ensure continuous electron transport pathway through the membrane bulk, the noble metal phase should occupy a minimum of 30 vol% fraction in the membrane (Chen et al., 1997). This presents some problems;

1. High material costs associated with use of expensive noble metals,
2. Thermal expansion differences between the noble metal and ion conducting phases can cause membrane failure particularly during thermal cycling,
3. The noble metal phase can obstruct the transport of oxygen ions leading to a

reduced ionic conductivity,

4. The difficulties in designing preparation procedures especially regarding method of mixing and particle size of chosen material.

Dual phase materials can also consist of two perovskite phases with one phase being ion conducting, and the other phase being electronic conducting instead of using a noble metal. However, compatibility issues have been observed with this kind of dual phase materials. For example, zirconia, an oxygen conducting material, has been found to react with electronic conducting perovskite oxides to form zirconates and pyrochlores when sintered together at high temperatures resulting in new compounds with poor electronic and ionic conductivities, or block transport of both electrons and ions (Zhu et al., 2012).

2.5.2.2 Single phase materials

Single phase materials consist of just one phase with the capability of conducting both ionic and electronic species simultaneously. Single phase MIEC materials usually are perovskite structured ceramics with the general formula $A_xA'_{1-x}B_yB'_{1-y}O_{3-\delta}$ where A and A' elements belong to the group consisting of *La*, *Ba, Sr, Ca or Zr*; while B and B' are elements from the group consisting of *Co, Fe, Mn, Cr, Ti, Ni, Cu, Ga* and *Mg*. One of the advantages of single phase material is the higher utilisation of membrane area as the ionic and electronic species do not need distinct transport pathways. However, a handicap of this type is their instability in some atmospheres. For example, $Ba_xSr_{1-x}Co_yFe_{1-y}O_{3-\delta}$ perovskite have high oxygen permeability but poor CO_2 tolerance due to the presence of alkaline earth cations at the A-site (Ba^{2+} and Sr^{2+} which tend to react with CO_2 to form carbonates (Shao et al., 2000). It is well established that barium is one of the least alkaline earth CO_2 tolerant dopants while strontium is one of the most tolerant (Sammells and Mundschau, 2006) for the A-site of the perovskite structure. The formation of these carbonates has generally been found to be difficult to reverse and they also inhibit oxygen permeation (Luo et al., 2011). There is also stability issues related to the choice of B-site cations in the material. Cobalt containing perovskite membrane materials are generally seen to exhibit high oxygen permeation but also have been observed to undergo dimensional changes (expansion) in a reducing environment, causing cracks resulting in membrane failure.

From the foregoing, it is clear that both dual and single phase materials have pros and cons and the choice of materials boils down to a compromise. A material that has been found to be a good compromise is the $La_xSr_{1-x}Co_yFe_{1-y}O_{3-\delta}$ family of perovskite materials in stoichiometric ratios that try to balance oxygen flux and stability concerns.

2.6 Historical background of inorganic oxygen membranes

The roots of inorganic oxygen membranes can be traced back to the late1800s when a German physical chemist, Walter Hermann Nernst noticed that a current of 'oxygen molecules' could flow through some dense ceramics at high temperature when subjected to a partial oxygen pressure. This oxygen current resembled the electronic current in metallic conductors under an electrical field, with the oxygen partial pressure playing the role of driving force much as electrical potential difference does in the electrical circuit equivalent. According to (Yantovsky et al., 2009), Nernst collaborated with Albert Einstein culminating in the formulation of the Nernst-Einstein formula:

$$\mathrm{J_{O_2}} = \frac{\mathrm{RT}}{16\mathrm{LF}^2}\sigma_\mathrm{i}\ln\left(\frac{\mathrm{P_2}}{\mathrm{P_1}}\right) \qquad \text{Eqn 2.1}$$

where $\mathrm{J_{O_2}}$ is the oxygen flux density in moles per unit area per unit time, σ_i is the oxygen ionic conductivity of the membrane material, R is the gas constant, L is the membrane thickness, F is Faraday's constant, T is temperature in K, $\mathrm{P_1}$ and $\mathrm{P_2}$ are oxygen partial pressures at the oxygen leaner side and oxygen richer side of the membrane respectively. This is also referred to as the integrated or simplified Wagner Equation or Wagner theory in some literature, e.g.(Tonziello and Vellini, 2011, Chen et al., 1997, Sunarso et al., 2008, Wagner, 1975, Wiik et al., 2002, Bouwmeester et al., 1994, Qiu et al., 1995, van der Haar, 2001, Oyama and Stagg-Williams, 2011, Park et al., 2011, van Hassel et al., 1994), after Carl Wagner who derived the same equation when studying the effect of chemical and electrical potentials on mass transport processes involving charged species (ions) in ionic solids. This behaviour by these materials is now much more understood following extensive fundamental research efforts in the past few decades. It is now known that these materials are able to conduct oxygen due to defects (oxygen vacancies) in the crystal structures of the materials. The vacancies concentration depends on the composition of the material (Sunarso et al., 2008, Oyama and Stagg-Williams, 2011, Cook and Sammells, 1991) . At low temperatures, these vacancies remain ordered in the lattice, but at high temperatures above a certain threshold, typically around 600^{o}C, the vacancies are thermally agitated and become conduction sites and the oxygen ions acquire adequate energy to overcome the thermal energy barrier to hop to neighbouring vacancy sites in the lattice. When subjected to an oxygen partial pressure gradient, there is a net flow of oxygen ions hopping from the oxygen rich side to the oxygen lean side of the membrane (Qiu et al., 1995, Sirman and Chen, 2003). Since only one species (oxygen ions) are transported by this mechanism through such materials under the above conditions, oxygen can be separated from oxygen containing gas mixture with 100% purity, provided the membrane is gas-tight with no continuous pores or cracks, and that the two sides are hermetically sealed with no leakage from one side of the membrane to the other.

Also, from their studies (Cales and Baumard, 1982, Cales and Baumard, 1984) proposed that permeation occur through dense membranes made from such materials due to the ability of the material to conduct both electrons and oxygen ions, and they classified them as “mixed conducting”. It is now widely accepted that the oxygen flux through such materials depends on the so-called ambipolar conductivity, a function of partial ionic and electronic conductivities of the membrane, and on rates of oxygen exchange at the membrane/gas boundaries (Lu et al., 2005, Kharton et al., 2002). Either of these processes can be the rate determining factor of the oxygen flux through the membrane. When the membrane is so thick that bulk diffusion is the rate determining factor, the oxygen flux is governed by the expression:

$$J_{O_2} = \frac{RT}{16LF^2}\frac{\sigma_e\sigma_i}{\sigma_e+\sigma_i}\ln\left(\frac{P_2}{P_1}\right) \qquad \text{Eqn 2.2}$$

where σ_i is the oxygen ionic conductivity of the membrane material, σ_e is the electronic conductivity and the rest are as previously defined. The relative values of σ_e *and* σ_i are often used to determine the oxygen permeability determining factor between the two. When $\sigma_e \gg \sigma_i$, as in La, Sr, Co and Fe perovskite material, where σ_e can be three orders of magnitude greater than σ_i, the term $\frac{\sigma_e \sigma_i}{\sigma_e + \sigma_i}$ approximates the value of σ_i as $(\sigma_e + \sigma_i \approx \sigma_e)$ and the flux expression reduces to:

$$J_{O_2} = \frac{RT}{16LF^2} \sigma_i \, ln\left(\frac{P_2}{P_1}\right) \qquad \text{Eqn 2.3}$$

which is the same equation reportedly formulated by Nernst and Einstein.

2.7 Overview of Perovskite type materials

The perovskite type of inorganic oxygen membranes have been reported extensively as having high oxygen fluxes. The work of Teraoka et al (Teraoka et al., 1988, Teraoka et al., 1985) was pioneering in the current research on perovskite-type materials in oxygen separation. Following their discovery in the early 1980s that perovskite structured membranes exhibited appreciably high oxygen fluxes, there has been a lot of interest in recent years on these types of materials as potential materials for fuel cell cathode electrodes, in oxygen sensors, chemical loop reactions, oxygen generators as well as in partial oxidation of natural gas as an intermediate process towards its conversion to liquid fuels. (Sunarso et al., 2008), (Hashim et al., 2010) and (Liu et al., 2006) have presented extensive reviews on the theoretical principles behind this technology, including summaries of latest achievements that had been made at the times of their reviews.

Perovskites get their name from the mineral Perovskite (Calcium Titanium Oxide ($CaTiO_3$), first discovered by Gustav Rose in 1839 from samples gathered from the Ural Mountains, which he later called perovskite after the famous Russian mineralogist Count Lev Aleksevich von Perovski, (Bayani, 2001). The ideal perovskite structure has the chemical formula ABO_3 commonly visualised as a three dimensional network of regular corner linked BO_6 octahedra. This is illustrated in *Figure 2-2*.

Alternatively, the ideal perovskite structure can also be viewed as a cubic close packing with the A-cations located at the corners of a cube. O-ions occupy the centres of the faces of the cube, and the smaller B-cation sits at the centre of the cube (Gellings and Bouwmeester, 1996). *Figure 2-3* shows a schematic of this view.

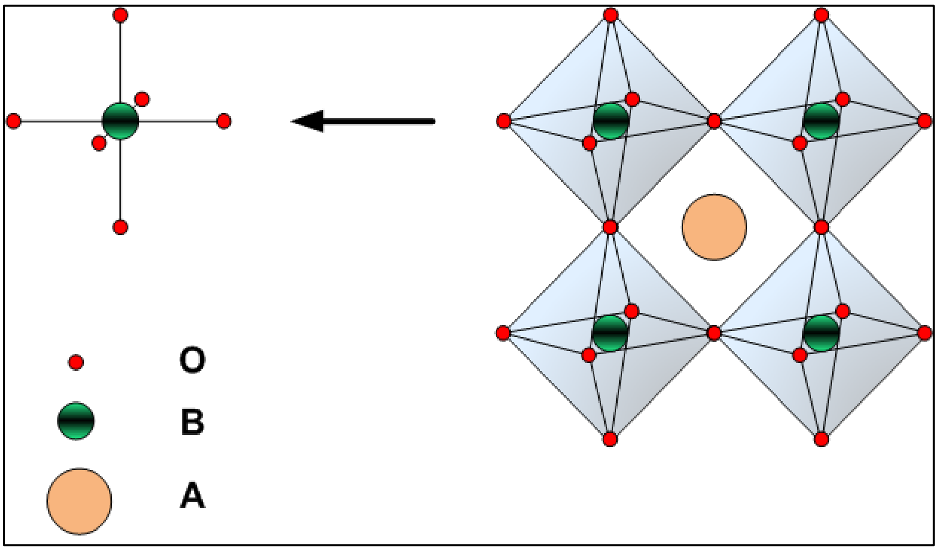

Figure 2-2 The ideal perovskite structure: octahedral view schematic (adapted from (Raduly-Scheuermann et al.))

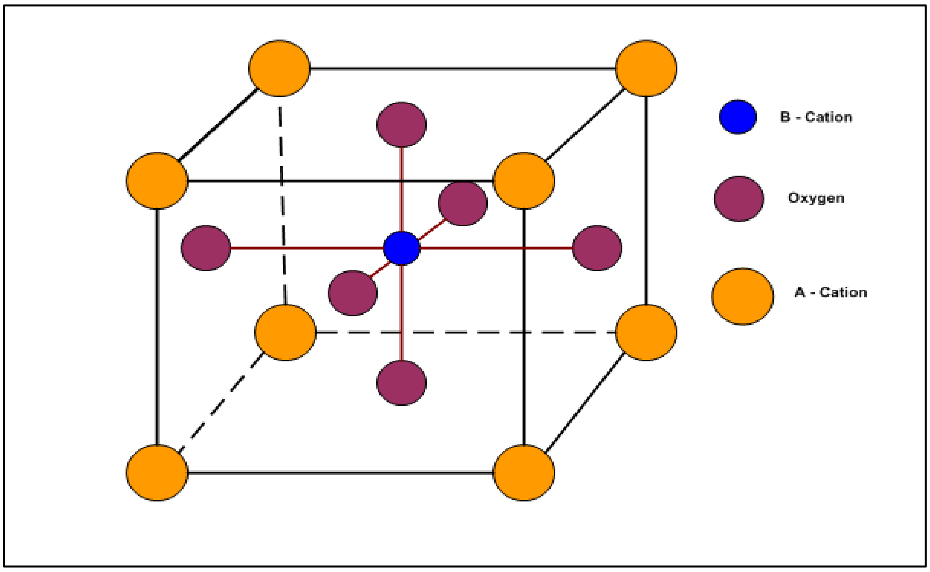

Figure 2-3 The ideal perovskite structure: the cubic view schematic

The A-site ion may be occupied by either alkali, alkaline earth ion. The B-site may be occupied by a transition metal. O is the oxygen anion. The A-site cation is generally larger than the B-site cation. In the ideal structure, the atoms are touching one another and the B-O distance is equal to $a/2$ while A-O distance is $a/\sqrt{2}$ and a is the cubic unit cell parameter (Pena and Fierro, 2001). The ionic radii of the atoms involved in the formation of the perovskite structure are important parameters and the geometric factor defined by Goldschmidt that has become known as the Goldschmidt tolerance factor is:

$$t_f \quad = \quad \frac{r_A + r_O}{\sqrt{2}(r_B + r_{O)}} \qquad \text{Eqn 2.4}$$

where r_A, r_B and r_O are the radii of the A-site metal ion, B-site metal ion and oxygen ion respectively. The Goldschmidt factor is often used to describe the deviation from the ideal perovskite structure and is a measure of the ‘‘cubicness’’ (Raduly-Scheuermann et al.) of structure. Stable perovskite-type structures are usually obtained in the range $0.75 \leq t_f \leq 1.0$. For an ideal cubic perovskite structure, $t_f = 1.0$ (Burggraaf and Cot, 1996, Liu et al., 2006, Tsai et al., 1998), and:

$$r_A + r_O = \sqrt{2}(r_B + r_O) \qquad \text{Eqn 2.5}$$

With the above range for the tolerance factor, the perovskite structure is thus quite tolerant with respect to deviations from the ‘ideal’ ionic radii of A and B. The relative size differences between the A and B cations can lead to the tilting of the BO_6 octahedra resulting in the structure adopting other crystal structures such as orthorhombic and rhombohedra shapes (Leo et al., 2009). Tolerance factors between 0.75 and 0.9 promote buckling of the corner shaped octahedron giving rise to orthorhombic structures.

It has been claimed by various researchers that the perovskite structure is also retained even if some parts of A or B site cations are substituted by other elements of similar size. This feature enables a wide range of “recipes” with perovskite-type compounds made out of varying compositions in both constituent elements and their stoichiometric proportions, giving different properties which can be exploited for different applications. Among these properties are gas separation (mainly oxygen and proton (hydrogen)), magnetic, optical and electrical properties (Pena and Fierro, 2001). The current work is on gas separation properties of perovskite-type compounds.

In the general ABO_3 structure, the A and B cations have a total charge of +6 (with typically A^{2+} and B^{4+}), balancing the 3 oxide anions of charge 2^- each (Thursfield and Metcalfe, 2004). However, compositions such as A^{1+} $B^{5+}O_3$ and $A^{3+}B^{3+}O_3$ are also possible. Typically, the A-site is generally occupied by large alkali metals such as Ba, La or Sr, and B-site by smaller transition metals such as Ce, Ga, Co, or Fe. With these alternatives, although the structure may be more or less the same, the properties can be very different. As an example, the $BaCoO_3$ and $SrCoO_3$ perovskites exhibit oxygen conduction and can, with their derivatives, find use in oxygen separation applications while $BaCeO_3$ and $SrCeO_3$ are proton conductors (Liu et al., 2006)**,** and can find use in hydrogen separation applications.

2.7.1 Perovskite materials tuning by doping

Theoretically, an ideal perovskite with structure ABO_3, without any defects/vacancies, does not exhibit ionic conductivity. It is only when there are defects/vacancies present in the lattice that it becomes an ionic conductor. Doping by introducing heterovalent cations at both A and B sites is one way of introducing defects into the lattice to form oxygen ion conducting solid electrolytes (Thursfield and Metcalfe, 2004).

Perovskite type solid state oxygen conductors are generally solid solutions of oxides of divalent cations in oxides of trivalent metals at the A-site of the perovskite structure. The conductivity is based on the oxygen vacancies created in the lattice of the trivalent metal oxide when doped with the oxide of the divalent cation. In basic perovskite–type ABO_3 compounds, the A-site trivalent cations are partially substituted by divalent cations while the B-site is occupied by cations with variable oxidation states such as transition metals, a combination, or one of two possible things take place. The first is the formation of defects or oxygen vacancies and the second is a change in the valence state of B cations (charge compensation) in order to maintain charge neutrality (Tsai et al., 1998, Lee et al., 2003). For example, in LSCF oxides, upon substitution of strontium for lanthanum, the difference in ionic charge between Sr^{2+} and La^{3+} must be compensated and this can be done it two ways, creation of oxygen vacancies or oxidation of other species in the structure such as $Co^{3+}$to Co^{4+} (Yin and Lin, 2007). It is the existence of oxygen vacancies in the lattice that facilitates oxygen diffusion at high temperatures. At low temperatures, these vacancies remain ordered in the lattice, but at high temperatures, typically above 600°C, they are thermally agitated and become available for oxygen transport, and provide a path for the migration of oxygen anions from one side of the membrane to the other (Gellings and Bouwmeester, 1996, Bouwmeester, 2003). A counter-balancing flow of electronic charge carriers must take place in order to ensure electrical neutrality. If the doping strategy results in a purely ion conducting material as in fluorites, the electronic charge carriers need to be provided by means of an external electrical source. Such materials, when operated in the reverse direction, are ideal for Solid Oxide Fuel Cell (SOFC) applications where the flow of electrons through the external circuitry is the desired electricity generated to do some work. However, if the doped solid electrolyte results in a mixed ionic and electronic conducting material (MIEC), an external circuit is not necessary as the charge-compensating electronic flow is provided intrinsically from the MIEC material (Gellings and Bouwmeester, 1996). In this case oxygen transport is possible without an eternal electrical circuitry.

Oxygen lattice diffusion takes place by the movement of these vacancies through the bulk by a process called vacancy hopping. Vacancy hopping mechanism is when an ion on a normal site in the lattice jumps into an adjacent unoccupied (vacant) site, and the vacancy moves into the site left by the ion (Liu et al., 2006). The two necessary conditions for ionic conduction to be possible by vacancy hopping are (Riess, 2008, Baumann et al., 2013):

1. The temperature is high enough to be able to excite the ion and allow it to overcome the energy potential barrier that separates the two sites.

2. That not far from the site where the ion is located there is an empty site (vacancy) to which the ion can hop.

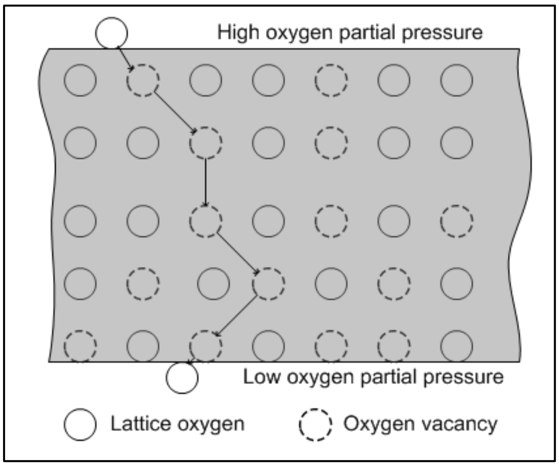

Figure 2-4 Schematic diagram of oxygen migration in membranes (adapted from (Liu et al., 2006)

Figure 2-4 illustrates the transport of oxygen ions through a dense MIEC membrane by vacancy hopping.

Essentially, the hopping of an ion to a vacancy is the same as a movement of the vacancy in the opposite direction. In oxygen MIECs at high temperatures, under the influence of thermal agitation, these vacancies/oxygen ions move randomly within the lattice. If an unbalanced force such as a vacancy concentration gradient or electrical potential is applied these agitated vacancies are influenced to drift in some direction depending on the nature of the force. For an oxygen vacancy gradient, they flow from high concentration region to a low concentration region (Lin et al., 1994).

One of the materials that have been under intense study in the past few years is the $(LaSr)(CoFe)O_{3-\delta}$ family conceptually obtainable from partially doping $LaCoO_3$ by Sr at La sites and Fe at Co sites. These materials can be expressed in the general chemical formula $La_{1-x}Sr_xCo_{1-y}Fe_yO_{3-\delta}$.

$La_{1-x}Sr_xCo_{1-y}Fe_yO_{3-\delta}$ has been found to have a good promise as a potential oxygen separation material on a commercial basis and a considerable amount of literature has been published by researchers (Burggraaf and Cot, 1996, Tai et al., 1995). In general, they have been found to have high ionic conductivities in air, at temperatures 700-1000^{o}C, that can be one or two orders of magnitude larger than that of known zirconia-based solid electrolytes.

2.8 Oxygen permeation process through a MIEC membrane

A typical configuration of a mixed ionic-electronic conducting membrane is shown in *Figure 2-5.*

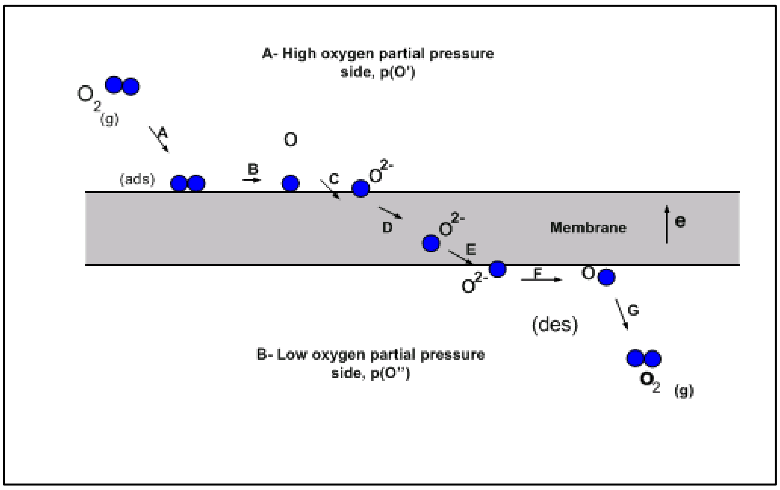

Figure 2-5 Schematic of oxygen permeation showing the possible steps through ceramic membrane. Adapted from (Leo et al., 2009)

Oxygen from the air feed stream is incident onto the membrane at surface on the air feed side, the high oxygen partial pressure side of the membrane. In order to diffuse through the membrane, oxygen must first be incorporated into the crystal lattice structure. A series of reactions that include dissociation, adsorption, and electron transfer take place to form oxide ions as illustrated in *Figure 2-5*. The species transformations may be broken down into the following possible steps (Bredesen and Sogge, 1996, Manning et al., 1996):

Mass transfer of oxygen molecules in air feed stream onto the membrane surface.

$\mathrm{O}_{2_{(g)}} \rightarrow \mathrm{O}_{2_{ads}}$ Oxygen molecules adsorbed onto the membrane surface

$\mathrm{O}_{2_{ads}} \rightarrow 2\mathrm{O}_{ads}$ Adsorbed oxygen molecules dissociate into atoms

$\mathrm{O}_{ads} + \dot{e} \rightarrow \mathrm{O}^{-}_{ads}$ Electron transfer to dissociated adsorbed oxygen

$\mathrm{O}^{-}_{ads} + \dot{e} \rightarrow \mathrm{O}^{2-}_{ads}$ Further electron transfer to adsorbed oxygen ionized species.

The O^{2-} in the lattice, which is sometimes represented as O^{X}_{O} then diffuses into the

MIEC membrane bulk by vacancy hopping as illustrated in *Figure 2-4*, towards the lower oxygen partial pressure side of the membrane (Sammells and Mundschau, 2006, Gellings and Bouwmeester, 1996)**.** At the permeate side, oxygen ions emerge and are desorbed in a series of reactions in reverse order of the reaction at the air feed side surface (*Figure 2-5*). The oxygen ions emerge, lose electrons to the lattice and combine as atoms to form molecules (Gellings and Bouwmeester, 1996). The freed electrons can ionize more oxygen at the airside membrane surface and the cycle continues as long as the required conditions remain. In a membrane reactor combining separation and reaction, the oxygen can be immediately consumed in a combustion reaction at the permeate side of the membrane. The key parameters that determine oxygen transport capabilities of the membrane are the surface chemical kinetics on air feed side and/or permeate side, and the oxide ion diffusivity in the membrane bulk.

The following sections present transport equations of oxygen ions through the membrane bulk in terms of oxygen partial pressure differences at the membrane surfaces and in terms of oxygen vacancy concentrations in the membrane bulk.

2.8.1 Modelling oxygen permeation in terms of oxygen partial pressure gradient (Wagner expression)

In this section, it is shown that the Wagner equation is a simplified case of the Nernst-Planck equation (Eqn 2.6) which describes flux of charged species in a solid solution at steady state conditions under an electrochemical gradient:

$$\mathrm{J_j} = -\frac{\sigma_\mathrm{j}}{(\mathrm{z_j F})^2}\nabla \eta_\mathrm{j} \qquad \text{Eqn 2.6}$$

where σ_j is the electrical conductivity of species j and z_j is its charge (including the polarity), F is the Faraday constant and, and $\nabla\eta_j$ is the electrochemical potential gradient of the charged species j .

In general, when a specific ion is mobile, both the chemical potential gradient and electrical potential affect the current density. The total driving force for mass transport of charged particles is the electrochemical potential which is the sum of the chemical potential and the electrical potential as given by:

$$\eta = \mu + zF\phi \qquad \text{Eqn 2.7}$$

where μ is the chemical potential and ϕ is the electrical (or electrostatic) potential.

Therefore the electrochemical potential gradient is given by:

$$\nabla\eta_j = \nabla\mu_j + z_jF\nabla\phi \qquad \text{Eqn 2.8}$$

Where:

$$\nabla = \frac{\partial}{\partial x} + \frac{\partial}{\partial y} + \frac{\partial}{\partial z} \qquad \text{Eqn 2.9}$$

For oxygen, z = -2, hence Eqn 2.6 becomes

$$J_{O^{2-}} = -\frac{\sigma_{o^{2-}}}{4F^2}\nabla\eta_{o^{2-}} \qquad \text{Eqn 2.10}$$

Combining with Eqn 2.8, Eqn 2.10 becomes:

$$J_{O^{2-}} = -\frac{\sigma_{o^{2-}}}{4F^2}\{\nabla\mu_{o^{2-}} - 4F^2\nabla\phi\} \qquad \text{Eqn 2.11}$$

Similarly for electron current density, with z_i = -1:

$$J_e = -\frac{2\sigma_e}{F^2}\left\{\nabla\mu_e - \frac{1}{2}F^2\nabla\phi\right\} \qquad \text{Eqn 2.12}$$

Since the net current density J_t flowing in the membrane in steady state conditions is zero, the following condition hold:

$$\mathrm{J_t = J_{O^{2-}} + J_e = 0} \qquad \text{Eqn 2.13}$$

That is:

$$\mathrm{J_t} \quad = -\frac{\sigma_{o^{2-}}}{4F^2}\{\nabla\mu_{o^{2-}} - 4F^2\nabla\phi\} - \frac{\sigma_e}{2F^2}\{\nabla\mu_e - 2F^2\nabla\phi\}$$

$$= -\frac{\sigma_{o^{2-}}}{4F^2}\nabla\mu_{o^{2-}} + \sigma_{o^{2-}}\nabla\phi - \frac{\sigma_e}{2F^2}\nabla\mu_e + \sigma_e\nabla\phi$$

$$= -\frac{\sigma_{o^{2-}}}{4F^2}\nabla\mu_{o^{2-}} - \frac{\sigma_e}{2F^2}\nabla\mu_e + \nabla\phi(\sigma_{o^{2-}} + \sigma_e) \qquad \text{Eqn 2.14}$$

Since $J_t = 0$, Eqn 2.14 can be re-written as

$$\nabla\phi(\sigma_{o^{2-}} + \sigma_e) = \frac{\sigma_{o^{2-}}}{4F^2}\nabla\mu_{o^{2-}} + \frac{\sigma_e}{2F^2}\nabla\mu_e \qquad \text{Eqn 2.15}$$

This gives

$$\nabla\phi = \frac{\sigma_{o^{2-}}}{4F^2(\sigma_{o^{2-}} + \sigma_e)}(\sigma_{o^{2-}}\nabla\mu_{o^{2-}} + 2\sigma_e\nabla\mu_e) \qquad \text{Eqn 2.16}$$

Substituting Eqn 2.16 in Eqn 2.11;

$$\mathrm{J_{O^{2-}}} = \frac{\sigma_{o^{2-}}}{4F^2}\left(\nabla\mu_{o^{2-}} - \frac{1}{\sigma_{o^{2-}} + \sigma_e}\{\sigma_{o^{2-}}\nabla\mu_{o^{2-}} + 2\sigma_e\nabla\mu_e\}\right) \qquad \text{Eqn 2.17}$$

$$\mathrm{J_{O^{2-}}} = \frac{1}{4F^2}\frac{\sigma_{o^{2-}}}{\sigma_{o^{2-}} + \sigma_e}\{\sigma_{o^{2-}}\nabla\mu_{o^{2-}} + \sigma_e\nabla\mu_{o^{2-}} - \sigma_{o^{2-}}\nabla\mu_{o^{2-}} - 2\sigma_e\nabla\mu_e\} \qquad \text{Eqn 2.18}$$

$$\mathrm{J_{O^{2-}}} = \frac{1}{4F^2}\frac{\sigma_{o^{2-}}}{\sigma_{o^{2-}} + \sigma_e}\{\sigma_e\nabla\mu_{o^{2-}} - 2\sigma_e\nabla\mu_e\} \qquad \text{Eqn 2.19}$$

$$J_{O^{2-}} = \frac{1}{4F^2}\frac{(\sigma_{O^{2-}})(\sigma_e)}{\sigma_{O^{2-}} + \sigma_e}\{\nabla\mu_{O^{2-}} - 2\nabla\mu_e\}$$ Eqn 2.20

In equilibrium conditions between gas phase oxygen, oxygen ions and electrons in the membrane system can be represented by:

$$\frac{1}{2}O_2 + 2e \leftrightarrow O^{2-}$$ Eqn 2.21

The chemical potentials of the three species can be related from Eqn 2.21

$$\frac{1}{2}\mu_{O_2} + 2\mu_e = \mu_{O^{2-}}$$ Eqn 2.22

$$\therefore \frac{1}{2}\mu_{O^2} = \mu_{O^{2-}} - 2\mu_e$$ Eqn 2.23

Substituting Eqn 2.23 in Eqn 2.20

$$J_{O^{2-}} = \frac{1}{4F^2}\frac{(\sigma_{O^{2-}})(\sigma_e)}{\sigma_{O^{2-}} + \sigma_e}\nabla\left[\frac{1}{2}\mu_{O_2}\right]$$ Eqn 2.24

$$J_{O^{2-}} = \frac{1}{8F^2}\frac{(\sigma_{O^{2-}})(\sigma_e)}{\sigma_{O^{2-}} + \sigma_e}\nabla\mu_{O_2}$$ Eqn 2.25

Substituting for the oxygen chemical potential in terms of partial pressure P_{O_2}, Universal Gas R and absolute temperature T and recognising that in a thin mixed conducting membrane, the transverse variations of charged species concentrations are negligible and the concentrations gradients only exists in the membrane thickness x (one dimensional approximation), and that the chemical potential gradient across the membrane of thickness Δx at temperature T can be written as:

$$\nabla \mu_{O_2} \quad = \quad RT \frac{\Delta \ln C_{O^{2-}}}{\Delta x} \qquad \text{Eqn 2.26}$$

where $c_{O^{2-}}$ is the concentration of oxygen ions. At membrane surfaces, $c_{O^{2-}}$ is proportional to gaseous phase oxygen partial pressure, hence

$$\nabla \mu_{O_2} \quad = \quad RT \frac{\Delta \ln(P_{O_2})}{\Delta x} \qquad \text{Eqn 2.27}$$

Substituting Eqn 2.27 into Eqn 2.25,

$$J_{O^{2-}} \quad = \quad \frac{RT}{8F^2} \frac{(\sigma_{o^{2-}})(\sigma_e)}{\sigma_{o^{2-}} + \sigma_e} \frac{\Delta \ln P_{O_2}}{\Delta x} \qquad \text{Eqn 2.28}$$

Eqn 2.28 represents the flux of O^{2-} ions. Since two O^{2-}re-associate to form one molecule of oxygen (O_2), the flux of molecular oxygen in moles $cm^{-2}s^{-1}$ can therefore be written as :

$$J_{O_2} \quad = \quad \frac{RT}{16F^2} \frac{(\sigma_{o^{2-}})(\sigma_e)}{\sigma_{o^{2-}} + \sigma_e} \frac{\Delta \ln P_{O_2}}{\Delta x} \qquad \text{Eqn 2.29}$$

$$J_{O_2} \quad = \quad \frac{RT}{16F^2} \frac{(\sigma_{o^{2-}})(\sigma_e)}{\sigma_{o^{2-}} + \sigma_e} \frac{\Delta \ln P_{O_2}}{\Delta x} \qquad \text{Eqn 2.30}$$

Integrating across the membrane of thickness L from a membrane surface at oxygen partial pressure of P_{perm} to the other surface at an oxygen partial pressure of P_{air} we obtain:

$$J_{O_2} \quad = \quad \frac{RT}{16F^2} \frac{(\sigma_{o^{2-}})(\sigma_e)}{\sigma_{o^{2-}} + \sigma_e} \int_{P_{perm}}^{P_{air}} \frac{d \ln P_{O_2}}{L}$$

$$= \frac{RT}{16LF^2}\frac{(\sigma_{O^{2-}})(\sigma_e)}{\sigma_{O^{2-}} + \sigma_e}\ln\left\{\frac{P_{air}}{P_{perm}}\right\} \qquad \text{Eqn 2.31}$$

This is the Wagner equation. The only material parameter in the Wagner equation is the ambipolar conductivity $\frac{(\sigma_{O^{2-}})(\sigma_e)}{\sigma_{O^{2-}}+\sigma_e}$. When $\sigma_{O^{2-}} \ll \sigma_e$, this approximates to approximates $\sigma_{O^{2-}}$.

It is important to note that the partial pressures refer to the local values directly adjacent to either side of the membrane in gaseous phase which may differ from the bulk volume oxygen partial pressures further away from the membrane surface. Similarly temperature refers to the local value at the membrane surface.

2.9 Oxygen permeation in the bulk lattice in terms of oxygen vacancy gradient (Fick's Law of diffusion)

Within the membrane bulk, oxygen ion flux $J_{O^{2-}}$ is proportional to the oxygen ion concentration gradient, $\frac{\partial C_{o^{2-}}}{\partial x}$ and the flux of oxygen ions may be re-written as:

$$J_{O^{2-}} \propto \frac{RT}{8F^2}\frac{(\sigma_{O^{2-}})(\sigma_e)}{\sigma_{O^{2-}} + \sigma_e}\frac{\partial c_{O^{2-}}}{\partial x} \qquad \text{Eqn 2.32}$$

And at a given temperature T

$$J_{O^{2-}} \propto \frac{\partial C_{o^{2-}}}{\partial x} \qquad \text{Eqn 2.33}$$

Oxygen transport involves the hopping of the oxygen ion from an occupied site in the lattice to an adjacent unoccupied (vacant) site, while the vacancy moves into the site left by the ion. Since an oxygen vacancy is the same as the absence of oxygen ion at the site, oxygen ion concentration gradient is equal and opposite the oxygen vacancy concentration gradient as in Eqn 2.34:

$$\frac{\partial C_{o^{2-}}}{\partial x} = -\frac{\partial C_{V\ddot{o}}}{\partial x}$$ Eqn 2.34

where $C_{V\ddot{O}}$ is the concentration of vacancies. Eqn 2.33 can be re-written as

$$J_{O^{2-}} \propto -\frac{\partial C_{V\ddot{O}}}{\partial x}$$ Eqn 2.35

Assuming a linear variation of vacancy concentration across the membrane of thickness L, with $C_{V\ddot{o}\_air}$ and $C_{V\ddot{o}\_perm}$ being the oxygen vacancy concentrations at the air side membrane surface and permeate membrane surface respectively, the oxygen ion flux within the membrane bulk is given by:

$$J_{O^{2-}} = D_{V\ddot{o}} \left\{ \frac{C_{V\ddot{o}\_perm} - C_{V\ddot{o}\_air}}{L} \right\}$$ Eqn 2.36

where $D_{V\ddot{o}}$ is the oxygen vacancy diffusion coefficient which depends on material and temperature.

Since two oxygen ions are required to form one oxygen molecule, the molecular oxygen flux through the membrane is represented by the expression:

$$J_{O_2} = \frac{1}{2} D_{V\ddot{o}} \left\{ \frac{C_{V\ddot{o}\_perm} - C_{V\ddot{o}\_air}}{L} \right\}$$ Eqn 2.37

$D_{V\ddot{o}}$ is a function of oxygen ion conductivity of the membrane material but varies with temperature-for a given material composition. As defined above $C_{V\ddot{o}\_perm}$ and $C_{V\ddot{o}\_air}$ are the oxygen vacancies concentrations on the membrane surfaces at permeate and air sides and exposed to permeate side oxygen partial pressure P_{perm} and airside oxygen partial pressure P_{air} respectively. In equilibrium, the oxygen vacancies concentrations decrease with increasing oxygen partial pressure in the gas phase. $\mathrm{C}_{\mathrm{V}_{\ddot{\mathrm{O}}}\_\mathrm{perm}}$ is therefore larger than $\mathrm{C}_{\mathrm{V}_{\ddot{\mathrm{O}}}\_\mathrm{air}}$ since $\mathrm{P}_{\mathrm{perm}}$ is smaller than $\mathrm{P}_{\mathrm{air}}$.

Eqn 2.37 shows that according to this model, the Fick's diffusion mechanism; oxygen flux within the membrane bulk depends on the oxygen vacancy gradient between the airside and permeate side surfaces of the membrane.

2.10 Surface exchange reactions

As explained earlier, other than bulk diffusion, there are two other flux determining steps. They are the oxygen exchanges at the gas-solid interface of the air side and the permeate side. The exchange process between the gas phase oxygen molecules and solid membrane surfaces includes a series of reaction steps. Surface reactions at air side proceed by adsorption, disassociation, charge transfer (ionization), oxygen ion incorporation into surface layer lattice at the membrane (Besecker et al., 2006, Kusaba et al., 2006). Although these reactions occur on both sides of the membrane if both sides have oxygen on them, the membrane side with the higher oxygen partial pressure determine the net flow of the oxygen ions, i.e. from the side with the higher oxygen partial pressure to the lower. This is the reason why partial pressure difference affects the oxygen transport. On arrival at the oxygen leaner side of the membrane, the net surface reactions proceed in the reverse order with the oxygen ions releasing their electrons to form atoms which recombine to form oxygen molecules. Again this also happens on both sides of the membrane but the net effect, i.e. net desorption is determined by the side with the lower oxygen partial pressure.

The net reactions at both sides as well as oxygen ion diffusion in the membrane bulk are illustrated in *Figure 2-6*. Diffusion occurs when an oxygen ion in the lattice hops into a vacancy. Without a driving force, this hopping is statistically distributed. However, when an oxygen partial pressure driving force is applied, the effective hopping is in the direction from the high oxygen partial pressure side to the low oxygen partial pressure side as previously illustrated *Figure 2-4*. At the high partial pressure side, the remaining vacancies are re-occupied by oxygen ions generated by dissociation and ionization of molecular oxygen in the gas phase. At the low oxygen partial pressure side, oxygen is released into the gas phase.

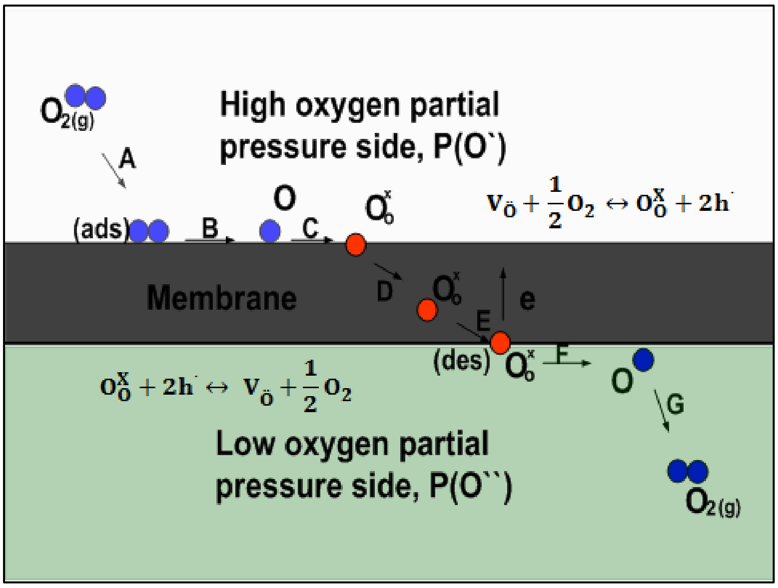

Figure 2-6 Schematic illustrating a simplified series of reactions during oxygen permeation through a MIEC perovskite membrane (adapted from (Kozhevnikov et al., 2009))

Steps A, B and C, which constitute air side surface exchange, can be summarised by equation:

$$V_{\ddot{O}} + \frac{1}{2}O_2 \quad \overset{k_{fa} > k_{ra}}{\longleftrightarrow} \quad O_{\ddot{O}}^X + 2\dot{h} \qquad \text{Eqn 2.38}$$

where $V_{\ddot{O}}$ is oxygen vacancy on the membrane surface $O_{\ddot{O}}^X$ is lattice oxygen and $\dot{h}$ is an electron hole, a theoretical concept representing the absence of an electron where it should be; and k_{fa} and k_{ra} are the forward and reverse rate constants respectively. Eqn 2.38 shows molecular oxygen interacting with oxygen vacancy $(V_{\ddot{O}})$ to form two electron holes $(2\dot{h})$ and lattice oxygen $(O_{\ddot{O}}^X)$ at the feed side. This is a reversible reaction with a forward rate constant k_{fa} greater than the reverse rate constant k_{ra}:

$$k_{fa} \quad > \quad k_{ra} \qquad \text{Eqn 2.39}$$

The rate constants are strong functions of temperature and usually described by Arrhenius type equations as follows.

$$k_{fa} = A_{fa} e^{\frac{-E_{a\_fa}}{RT}}, \quad k_{ra} = A_{ra} e^{\frac{-E_{a\_ra}}{RT}} \qquad \text{Eqn 2.40}$$

where A_{fa} and A_{ra} are pre-exponential constants for the forward and reverse reactions respectively, and E_{a_fa} and E_{a_ra} are activation energy for forward and reverse reactions respectively at the air side.

Airside forward surface exchange reactions generally consist of mass transport of gas phase oxygen to the membrane surface, adsorption on membrane surface, dissociation to atoms, electron transfer to form O^{2-} ions, and incorporation of oxygen O^{2-} ions into membrane surface lattice oxygen vacancies while reverse reactions define oxygen ion desorption and loss of electron, re-association to form molecules. The forward reaction is a function of temperature, oxygen partial pressure as well as oxygen vacancy concentration at that side. As $k_{fa} > k_{ra}$ the net effect is in the forward direction and the incorporated ions diffuse by vacancy hopping mechanism through the membrane bulk to the permeate side.

Steps E, F and G, which constitute desorption of oxygen at the permeate side, are summarised by equation:

$$O_O^x + 2\dot{h} \xleftrightarrow{k_{fp} > k_{rp}} \frac{1}{2}O_2 + V_{\ddot{O}} \qquad \text{Eqn 2.41}$$

Eqn 2.41 shows lattice oxygen (O_O^x) at the permeate membrane surface reacting with a pair of electron holes ($2\dot{h}$) to form atoms that re-combine to molecules that are desorbed from the membrane surface to leave oxygen vacancies ($V_{\ddot{O}}$). This is a reversible reaction with a forward rate constant k_{fp} and a reverse rate constant k_{rp} with:

$$k_{fp} > k_{rp} \qquad \text{Eqn 2.42}$$

for net desorption of oxygen from membrane lattice to molecular oxygen on permeate side. The rate constants are also expressed using Arrhenius equations and given by:

$$k_{fp} = A_{fp} e^{\frac{-E_{a\_fp}}{RT}}, \quad k_{rp} = A_{rp} e^{\frac{-E_{a\_rp}}{RT}} \qquad \text{Eqn 2.43}$$

where A_{fp} and A_{rp} are pre-exponential constants for the forward and reverse reactions respectively, and E_{a_fp} and E_{a_rp} are activation energy for forward and reverse reactions respectively at the permeate side.

Permeate side forward surface exchange reactions generally consist of desorption of oxygen ions, loss of electrons to the lattice, re-association to form molecules and gas phase mass transfer from the membrane surface (in inert conditions), while reverse reactions consist of oxygen adsorption, electron gain to form ions, and incorporation of ions into the lattice. As $k_{fp} > k_{rp}$ the net effect is the forward reaction.

2.11 Implications of the Wagner Equation

The Wagner equation applies when the flux determining factor is the diffusion of oxygen through the bulk material. Under these conditions, the Wagner equation predicts that the oxygen permeation flux should be linearly proportional to the term $\ln\left(\frac{P_2}{P_1}\right)$, linearly proportional to temperature measured on the absolute temperature scale (Kelvin), inversely proportional to the membrane thickness and directly proportional to the oxygen ionic conductivity of the membrane material. The ionic conductivity of the membrane is a property of the material from which the membrane is made and largely depends on the membrane material composition. It is also widely accepted that regarding temperature, there is a threshold below which there is no permeation that can take place. For most materials identified so far, this threshold temperature is around 600°C (873K). The threshold temperature represents the minimum thermal activation energy required to drive the permeation process. Above this threshold, oxygen flux increases with increase in temperature as higher temperatures facilitate both oxygen diffusion as well as surface exchange reactions.

The Wagner expression shows that oxygen transport within the membrane bulk depends on the membrane thickness in an inverse relationship. This implies that flux can be optimised by decreasing the membrane thickness. Practically this is limited by the membrane mechanical strength effects of thickness reduction. To overcome this problem, several fabrication methods have been proposed the most popular of which is asymmetric membrane in which a thin dense layer is supported by a thicker porous layer.

The function of the porous layer is to provide mechanical strength for the thin dense membrane while its porosity provide pathways for gas phase diffusion of the permeate oxygen to or from the thin dense membrane. A continuous connection of pores in the porous layer is necessary to allow diffusion of gases to or from the active dense layer. The size of the pores is important in allowing rapid diffusion of gas such that the gaseous phase diffusion is not the limiting factor. *Figure 2-7* shows a cross section a showing the microstructure of a typical asymmetric membrane.

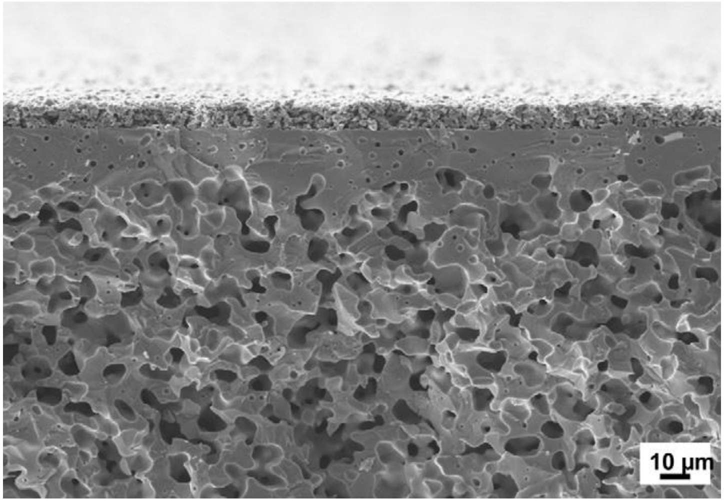

Figure 2-7 Asymmetric membrane structure (adapted from (Baumann et al., 2013)

There are two approaches that have been under consideration from researchers in fabricating thin dense membranes supported on porous supports. One is where the membrane is prepared on a support of same chemical composition as it. The other is where the membrane and support are made from materials of different compositions (Araki et al., 2008, van der Haar and Verweij, 2000). The latter is attractive from an economic viewpoint. Since perovskite materials are extremely expensive, it is desirable to fabricate the support layer from cheaper and readily available materials such as Al_2O_3 and only use the more expensive active membrane material for the thin dense layer. Unfortunately such an approach presents its own challenges to the stability of the membrane. These challenges include possible discordance in thermal expansion, densification and final shrinkage kinetics (Middleton et al., 2004) of the different materials during heat treatment and cooling. This discordance can cause the membrane to delaminate, crack or deform and result in failure of the structure. For example, experiments carried out by (van der Haar, 2001) using pulsed laser deposition (PLD) method to deposit $La_{0.5}Sr_{0.5}CoO_{3-\delta}$ membrane of the order of 1µm thickness on porous α-Al_2O_3 substrate were unsuccessful due to thermal properties mismatch of the two materials. In addition to thermal expansion mismatch problems when using different materials for the support and dense layers, there is the possibility of a solid state reaction between the dense layer material and the porous layer material at the interface to form a new phase which may inhibit the permeation of oxygen. (Chen et al., 1996) have reported the solid state reaction of Al_2O_3 porous layer and $La_{0.3}Sr_{0.7}CoO_3$ to form the phase $CoAl_2O_4$ at the interface of the two layers if sintering temperature exceed 800^{o}C and concluded that alumina is not a suitable material to support because of its chemical interaction with $La_{0.3}Sr_{0.7}CoO_3$.

Several research other groups, e.g. (Kovalevsky et al., 2006) have reported difficulties in fabricating supported membranes using different materials for the dense and porous support layers. However, (Middleton et al., 2004) have claimed success using this approach to fabricate an LSCF thin dense gas tight layer on a porous MgO substrate using the co-tape casting method to prepare the asymmetric membrane. In contrast, (Chen et al., 2007) using BSCF5528 and BSCF5582 for the two layers with the former as the dense layer, claim they were successfully able to fabricate a supported membrane.

Other methods that have been used require fabrication of the porous support followed by deposition of the thin dense layer. They include the sol-gel coating (Kueper et al., 1992), chemical and electrical vapour deposition (EVD) (Minoru and Atsuchi, 1997), spray pyrolysis (Meng et al., 2002), dip coating of particulate slurries, sputtering (Setogchi et al., 1990) and pulsed laser deposition(van der Haar, 2001) on pre-sintered porous support. Atomic scale deposition techniques such as vapour phase or solution often face difficulties in stoichiometric control and filtration into the porous layer while particle deposition techniques such as electrophoretic deposition and screen printing have difficulties in achieving required densities and required thicknesses (Xia and Liu, 2001, Will et al., 2000). Many of these thin film deposition techniques are complex and expensive.

Turning back to the Wagner expression and focussing particularly on the logarithmic term; this can be varied in a number of ways to maximise the term, such as applying high pressure air at the oxygen rich side to correspondingly increase the oxygen partial pressure, and minimizing the oxygen partial pressure at the oxygen lean (permeate) side. Using high pressure has practical limits, not least the limited mechanical strength of the membrane, given that it is also desirable to have as thin a membrane as possible to optimise flux. In addition, mathematically it is clear that the impact of increasing air side pressure ten-fold will only increase the $\ln\frac{P_2}{P_1}$ by a factor of 2.3. So increasing air side pressure from 1 Atm to 11 Atm with other operating conditions remaining constant only just about more than double the flux. Increasing pressure is therefore not a very effective intensification strategy.

The value of the logarithmic term can also be manipulated by sweeping away the oxygen from the permeate side as soon as the permeate oxygen emerges from the membrane. This can be done using an inert sweep gas such as helium. Generally, oxygen flux has been observed to increase with permeate sweep gas flow rate, but with a continuously decreasing slope, showing a limitation of this strategy (Zhang et al., 2007). This strategy has been proposed for oxy-fuel combustion in electricity generation in which carbon dioxide, which is considered inert, is used as sweep gas to carry the permeate oxygen to the combustion zone to burn the fuel. The attraction of this method is that the products of combustion are mainly more carbon dioxide and water. The water can be condensed while some of the carbon dioxide can be captured and stored while the remainder is recycled as sweep gas.

Using an oxygen consuming reaction at the permeate side is another way of increasing the $\frac{P_2}{P_1}$ ratio and thus the logarithmic term. The reaction reduces the partial pressure at the permeate side by removing the permeate oxygen almost as soon as it desorbs from the membrane surface to leave a very small oxygen partial pressure and amplifying the ratio $\frac{P_2}{P_1}$. A fast combustion reaction can reduce oxygen partial pressure to very small levels such as 10^{-20} to 10^{-22}Pa (Julbe et al., 2005, Kawahara et al., 2011). As a result such a reaction increases the flux. From this modelling, a reactive configuration promise to be a viable intensification strategy. However it is only suitable where the combustion reaction is the required process.

Chapter 3 : CATALYTIC MEMBRANE REACTOR CONCEPTS

3.1 Introduction

A membrane is a material that selectively separates at least one of the components of a mixture to which it is exposed. During the process, one or more components permeate through the membrane to the exclusion of others. The components that permeate the membrane are called *permeates* while the residual components at the feed side are called the *retentates.* Membrane processes have been applied since the 1970s in many applications in gas separation for recovery, enrichment, purification and removal of specific components.

A membrane reactor is a multi-functional device that can simultaneously process a membrane based separation with a chemical reaction in the same physical unit (Reddy et al., 2013), in which at least one of the reactants or products is supplied or removed partly or wholly through a membrane (Stoukides, 2000, Koros et al., 1996), thus playing the role of both separator and reactor. In membrane reactors, generally, membranes can perform a wide variety of functions. These functions can be categorised according to the essential role of the membrane. They can be employed to introduce/separate/purify reactant(s) and/or products, to provide a surface for reactions, to provide a structure for reaction medium or to retain a specific catalyst (Sirkar et al., 1999). One special category is catalytic membrane reactors. Catalytic membrane reactors are structured reactors combining a membrane that controls mass transfers and a catalyst providing chemical activity, in a single unit with the main components being the membrane and the catalyst. These two, membrane and catalyst, have three possible arrangements:

1. The catalyst is applied in conventional form, e.g. in a packed-bed and the membrane has a sole function of separation.

2. The catalyst is dispersed on the membrane surface.

3. The membrane is inherently catalytic

For case (1), the term Inert Membrane Reactor (IMR) is usually used, while for cases (2) and (3) the term Catalytic Membrane Reactor (CMR) applies and the membrane is used for separation and enabling the reaction and no fixed bed is needed (Julbe and Guizard, 2001) and (Emig and Liauw, 2002).

3.2 Membrane reactors classifications

There are different classifications of membrane reactors, e.g. based on membranic material (inorganic and polymeric), and porosity (micro, meso, macro and dense) (Lu et al., 2007). In addition, they can be classified according to reactor design configurations and role of membrane in the process, into extractor type, distributor type and interfacial contactor type (Miachon and Dalmon, 2004, Reddy et al., 2013).

3.2.1 Extractor type Membrane Reactor (MR)

An MR that works on the extractor configuration selectively removes, in-situ, a product from the reaction products mixture (Sirkar et al., 1999), and if the reaction is thermodynamic equilibrium restricted/limited, this removal can shift the reaction equilibrium to enhance the conversion (Julbe et al., 2005, Westermann and Melin, 2009), and according to Le Chatelier's principle. This is a potential area for application of intensified reactors which allows Steam Methane Reforming (SMR) and Water Gas Shift (WGS) reactions to occur simultaneously in a single device while a hydrogen selective membrane simultaneously extracts hydrogen from the reaction zone, thereby shifting the chemical equilibrium and increasing hydrogen productivity (Zaman and Chakma, 1994), (Julbe and Guizard, 2001), (Lu et al., 2007). This can also allow the reforming reaction to occur at less severe temperatures and pressure without any methane conversion loss (Iulianelli et al., 2010, Alves et al., 2013, Lu et al., 2007). *Figure 3-1* shows a schematic of an extractor type MR with component C selectively separated from the reaction zone. The removal of C via the separation function has the following effects on the reaction (Sirkar et al., 1999):

1. The equilibrium condition of the reversible reaction $\mathrm{A + B \leftrightarrow C + D}$ is shifted to the right leading to higher equilibrium conversion of A and B to C and D.

2. If there are undesirable side reactions such as $\mathrm{B + C \leftrightarrow E}$ taking place in the reactor, the separation of C from the reaction mixture reduces loss of reactant

B and increases the selectivity of C.

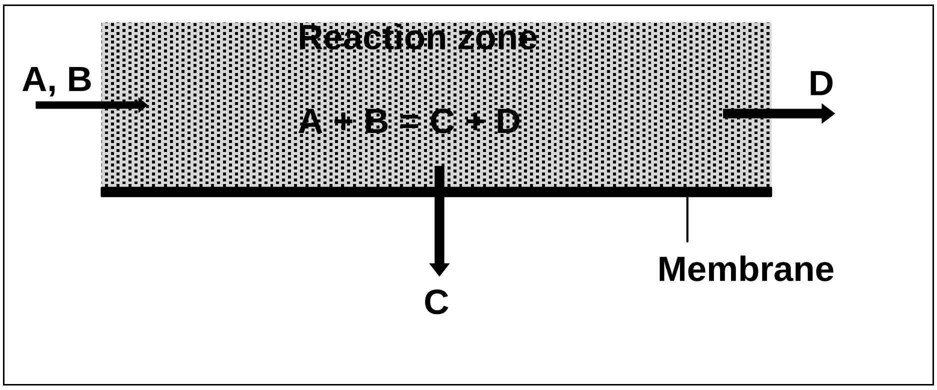

Figure 3-1 Schematic of an extractor type membrane reactor

3.2.2 Contactor type MR

In the contactor mode, the membrane facilitates contact between reactants and catalyst, in other words, it provides a surface for reactions to take place on or the membrane is also a catalyst support (Sirkar et al., 1999). This type of membrane reactor applies mainly to porous membranes.

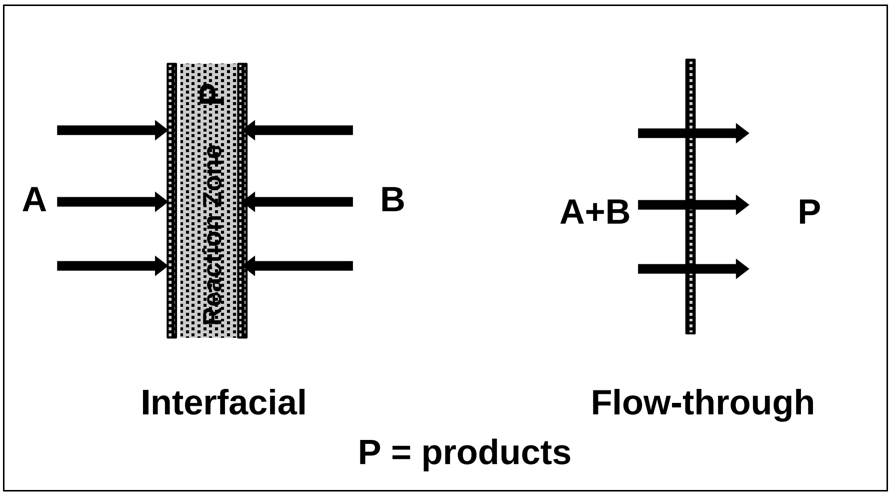

Figure 3-2 Schematic showing contactor type reactor (adapted from (Miachon and Dalmon, 2004)

The contactor type MR can be used in two possible modes; the interfacial contactor mode or the flow-through mode. In the interfacial configuration, the reactants are separately introduced from each side of the membrane and meet in the catalyst zone. For the flow-through mode, the reactants mixture is forced through the catalytic membrane pores.

3.2.3 Distributor type MR

In the distributor type configuration, the membrane facilitates controlled addition of one of the reactants in the reaction zone. In this way, the concentration of the distributed reactant is kept at a controllable value and may help limiting secondary reactions. A potential application of this type is the subject of this study, using high oxygen-permselective inorganic dense membranes in membrane reactors combining separation and reaction in one unit. The membrane not only prevents nitrogen dilution in reaction products, but also facilitates controlled addition of oxygen. It also prevents pre-mixing reactant with oxygen into possibly an explosive mixture, as well as improving selectivity in the conversion process (Mallada et al., 2000). In the schematic shown in Figure 3-3, air is represented by A and B (oxygen and nitrogen). The membrane selectively separates A (oxygen) from air into the reaction zone where it can react with reactant C to form products D and E.

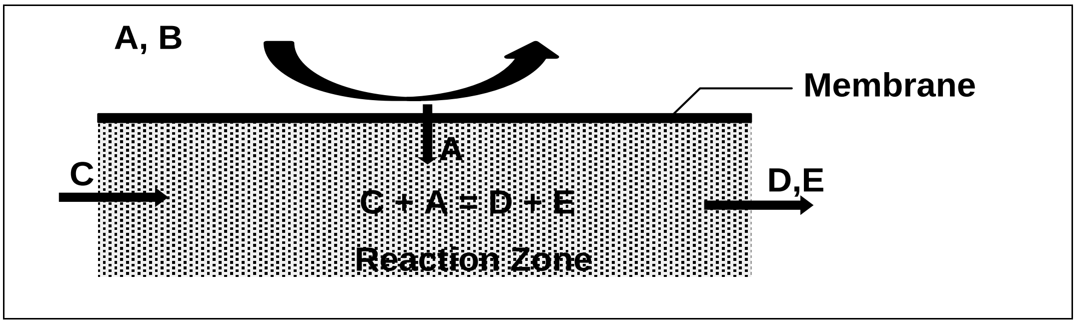

Figure 3-3 Schematic showing distributor type membrane reactor

Thus the oxygen membrane can be used to distribute oxygen to the reaction chamber in a controlled manner using the distinct properties of MIECs, of selectively conducting an ionic oxygen flux (excluding nitrogen) when one side is exposed to air and a chemical reaction uses the oxygen at the other. When such a membrane is used with air on one side and methane on the other, with a suitable catalyst, partial oxidation to syngas can be achieved without nitrogen contamination. This obviates the need for a separate pure oxygen production plant (Balachandran et al., 1997). The oxygen separation from air with a chemical reaction enhances the separation process by the removal of the permeate oxygen, thereby increasing the chemical potential driving force which drives the separation process. In the present work a mixed ionic electronic conducting perovskite oxide LSCF6428 has been applied as a dense membrane for oxygen supply in a reactor for CO or CH_4 combustion. This is an initial step towards using such reactors for catalytic partial oxidation of methane to syngas by depositing appropriate catalyst on the membrane permeate surface.

In this MR type, the membrane may be inert, inherently catalytic (catalytic membrane) or a catalyst may be deposited on it to influence the reaction path (Julbe and Guizard, 2001, Coronas et al., 1994, Dalmon et al., 2007). In addition, owing to the nature of oxygen transport through the membrane, the process can provide different types of oxygen species at the membrane permeate side surface, e.g. O^{2-}, O^{-} and O_2 where the catalyst and reactants are located (Yang et al., 2005).The permeate oxygen at the permeate membrane surface can react with a reactive sweep gas following a Mars-van Krevelen mechanism if either a catalyst is coated or the membrane itself is inherently catalytic.

Partial oxidation of methane (POX) using MIECs based membrane reactors that combine air separation and POX in a single unit is an example of distributor type membrane reactor. In this case the MIEC membrane acts as an oxygen separator and distributor as oxygen is selectively added to the permeate stream through ion transport and not via a convective flow or molecular sieving as in conventional or porous reactors. Crucially, coating of appropriate catalytic nanoparticles on the membrane surface can influence the oxidation reaction in a desired way, such as partial oxidation of methane to syngas instead of complete oxidation to carbon dioxide and water.

The membrane reactor this study has adopted is on the distributor configuration of a Catalytic Membrane Reactor (CMR) where a dense inorganic Mixed Ionic-Electronic Conducting (MIEC) membrane separates the air side from the reaction side of the membrane reactor. The MIEC's oxygen permselectivity allows only oxygen species to across it to the reaction side to react with a fuel gas such as methane.

Chapter 4 : MEMBRANE REACTOR DESIGN, MATERIALS, METHODS AND EXPERIMENTAL SET-UP

4.1 Introduction

Until now, experiments in oxygen separation from air using ceramic membranes have been conducted with laboratory materials not suitable for real life industrial application. Reactor vessels in majority of cases were made from quartz tubes and precious and inert metals such as gold and silver used as sealing materials. Such experiments were understandably mainly for fundamental research to understand more on oxygen permeation processes and in search of higher performance membrane compositions to meet high membrane stability and high flux requirements to meet industrial scale throughputs. Little, if any, effort has been expended applying these membranes in membrane reactors constructed out of engineering materials typically suitable for industrial application such as stainless steel for the vessel and cheaper sealing materials such as glass. The current work seeks to study the application of these oxygen membranes with these more appropriate engineering materials. This chapter describes in detail the membrane reactor designed and constructed for this purpose.

In this work, perovskite type material of the Lanthanum-Strontium-Cobalt–Iron (LSCF) family, in particular the $La_{0.6}Sr_{0.4}Co_{0.2}Fe_{0.8}O_{3-\delta}$ type, has been selected as the prototype material for this demonstrative study due to its high oxygen permeability and good chemical stability (Li et al., 1999, Jin et al., 2001, Zeng et al., 2007). Using notation that is often used in the literature, $La_{0.6}Sr_{0.4}Co_{0.2}Fe_{0.8}O_{3-\delta}$ will hereinafter be denoted as LSCF6428. In this abbreviated notation, the first letters of the element symbol of each metal cation are written down followed by a list of numbers corresponding to the first significant figure of the stoichiometry of the respective metal cation. In this instance, L, S, C and F respectively stand for La, Sr, Co and Fe while the numbers 6, 4, 2 and 8 stand for 0.6, 0.4, 0.2 and 0.8 respectively, the stoichiometry of these cations in the material. Any other perovskite material that may be mentioned in this thesis may also be denoted using this notation. It is important to mention that Barium-Strontium-Cobalt-Iron (BSCF) type of perovskite materials have so far exhibited amongst the highest oxygen permeabilities (Shao et al., 2000) (Wang et al., 2002), but due to their poor chemical stability in CO_2 containing atmospheres due to ease carbonate formation, they have not been for use in the present work. Strontium does form a carbonate as well, but is known to have a high tolerance of CO_2. In this respect, it is a good compromise as it is seen as responsible for oxygen vacancy creation in the material. The oxygen vacancies play a very important role in oxygen permeation.

4.2 Membrane Reactor Description

The membrane reactor designed and constructed consists of a stainless steel cylindrical shell (101) in the schematic in *Figure 4-1*. The top cover consists of a disc shaped lid (102) and head block (103), which has a protruding section at the centre on which a membrane holding module (104) is installed. Through the Top Cover and Head Block, holes for gas pipe fittings (105), thermocouple (106) and Watlow cartridge heaters (107) were drilled as illustrated Figure 4-2. The Top Cover and Head Block are fixed to the shell by means of 12 (108) studs with a thermoculite gasket (109) between the cylindrical shell (101) and one (103), and another thermoculite gasket (110) between (102 and 103).

At the bottom of the shell is a stainless steel base (111) which functions as its bottom lid. This bottom lid is sealed to the cylindrical shell by means of a thermoculite gasket (112) and screws (113). Through the base is drilled several holes for the permeate side gas pipe fittings (114), igniter system (115) and thermocouple (116).

The membrane module is sealed to (103) by four screws (bolts) (117) and copper gaskets (118) and a stainless steel spacer (119).

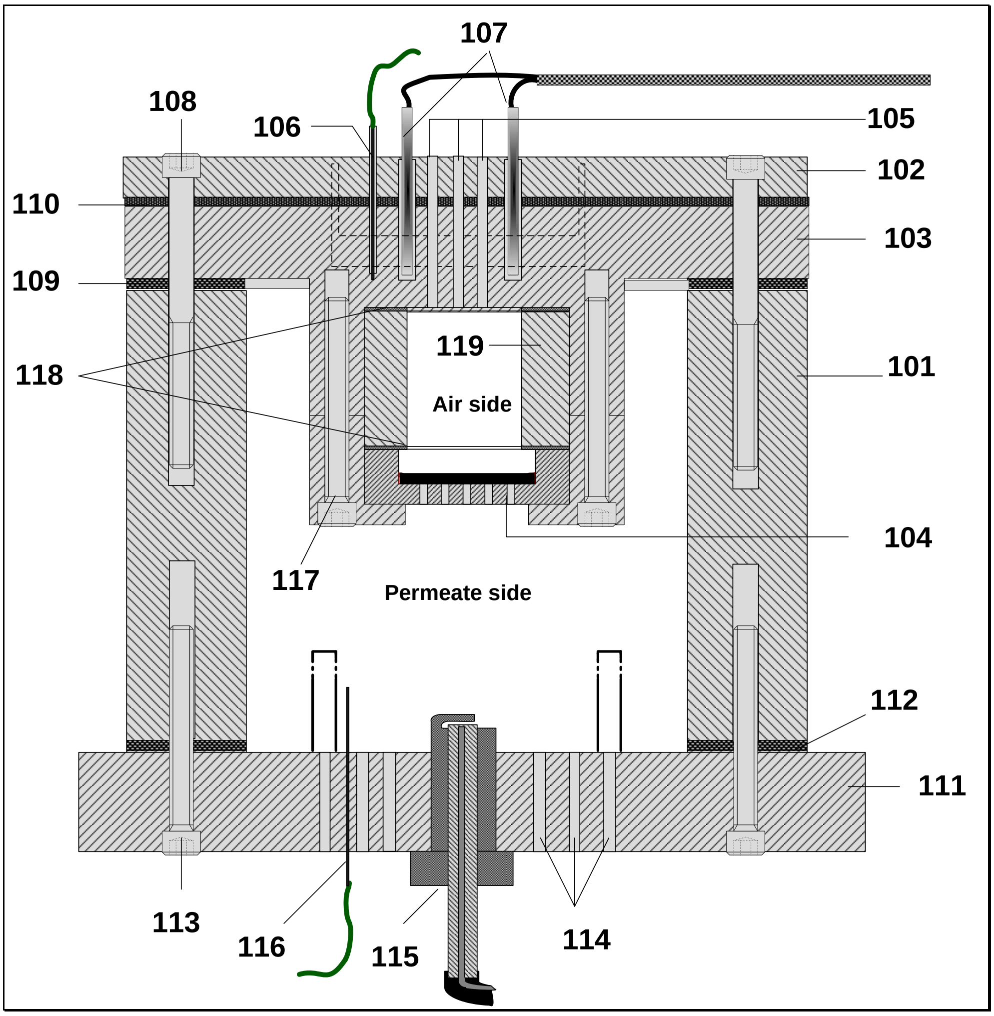

Figure 4-1 Schematic section view of assembled reactor

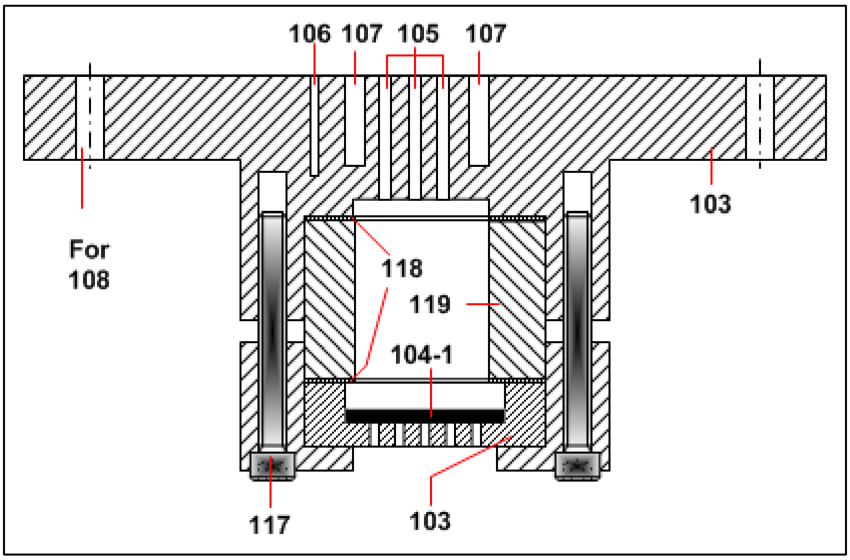

Figure 4-2 Reactor Head Block

The membrane module designed is as illustrated in *Figure 4-3*.

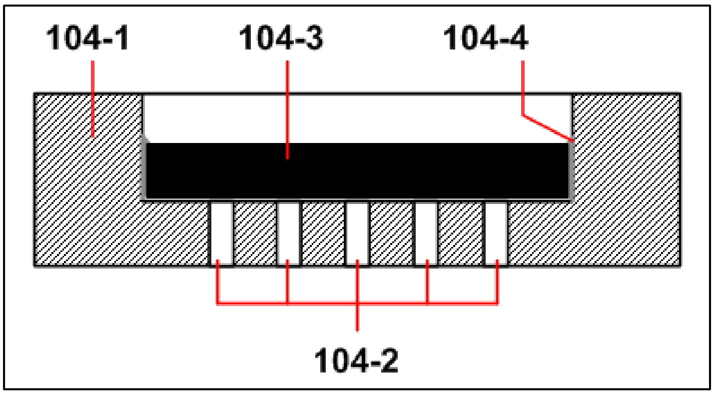

Figure 4-3 Membrane module

The membrane holder (104-1) in which the membrane (104-3) was sealed with glass, was fabricated from a stainless steel tablet of 35.9mm diameter and 12mm thickness which was machined into a cup of internal diameter (25.2mm) just slightly more than the diameter of the membrane disc (25.00mm), with several 2mm diameter holes (104-2) at the base. The purpose of the holes is to allow permeate oxygen emerging from the membrane to flow into the permeate chamber, or alternatively to allow the sweep gas to reach the permeate side membrane surface. The membrane holder was then heat treated in a furnace at 800^{o}C to facilitate glass metal bonding during sealing. The heat treatment forms a thin layer of metal oxide film to facilitate bonding with the glass sealant. A thin layer of soft glass paste made from soft glass ground into fine powder and polyethylene glycol (PEG) was applied onto the inner walls of the membrane holder and the membrane (104-3) gently placed into the membrane holder cavity, taking care not to rub off the thin glass-PEG paste. With the membrane disc placed in position, the assembly was heated in a furnace to the melting point of the glass to make it flow into the gap between the edge of the membrane disc and the membrane holder wall. When the temperature is lowered the molten glass solidifies and creates a continuous layer of glass (104-4) between the membrane and the stainless steel cavity walls.

4.3 Membrane Fabrication

The as purchased LSCF6428 powders (Reagent grade Sigma Aldrich) were compressed into discs of 32mm diameter and 3.5mm in thickness in a stainless steel die under a hydraulic load of 8t on an area of 8cm^2 by unilateral press (Model Atlas 25T series, Specac Limited, UK). After 7 minutes, the pressure was released and the disc evacuated from the die. The pressing process is summarised in the schematic shown in *Figure 4-4*. The discs were sintered at 1150^0C for 2 hours with a heating rate of 2^oC/min in a Lenton Furnace. The furnace does not have a forced cooling facility, hence the sintered discs were allowed to slowly cool by natural loss of heat from the furnace (about 36 hours). The sintered membrane has an outer diameter of 25.0mm.

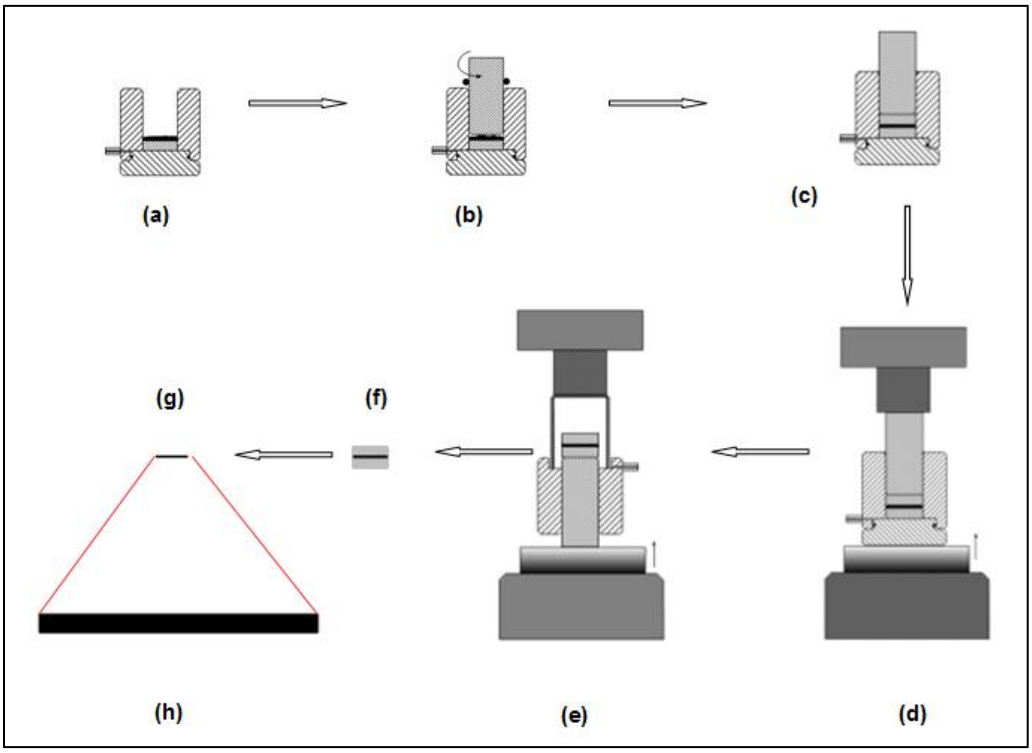

Figure 4-4 Schematic illustrating the steps in disc pressing (a) adding ceramic powder into die, (b) levelling ceramic powder using plunger,(c) ceramic powder between stainless steel die pellets,(d) pressing using hydraulic press,(e) pressed green ceramic pellet evacuation, (f) evacuated green ceramic pellet still between stainless steel die pellets, (g) resulting pressed green pellet ready for sintering, and (h) exploded ceramic disc green body.

4.4 Membrane module design

The membrane module design adopted is illustrated in *Figure 4-5.*

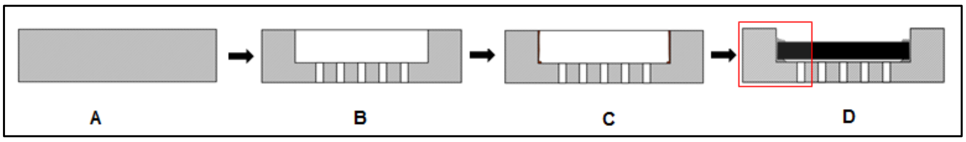

Figure 4-5 Membrane module design

The membrane holder in which the membrane was sealed with glass was fabricated from a stainless steel tablet of 35.9mm diameter and 12mm thickness *Figure 4-5*(A) which was machined into a cup (*Figure 4-5)* B of internal diameter (25.2mm) just slightly more than the diameter of the membrane disc (25.00mm), with several 2mm diameter holes at the base. The purpose of the holes is to allow permeate oxygen emerging from the membrane to flow into the permeate chamber or to allow the permeate side sweep gas to flow to the membrane surface. The membrane holder was then heat treated in a furnace at 800^{o}C to pre-oxidize the sealing surface and facilitate glass-metal bonding during sealing. A thin layer of soft glass paste made from soft glass ground into fine powder, and PEG was applied onto the inner walls of the membrane holder as illustrated in *Figure 4-5*(C) and the membrane gently placed into the membrane holder cavity, taking care not to rub off the thin glass-PEG paste (*Figure 4-5*D). The assembly was placed in the oven and heated from room temperature to 300^{o}C at 1^{o}C ramp rate to dry the paste for 30 minutes before changing the oven heating programme to heat at 4^{o}C per minute to 1050^{o}C and dwell for 20 minutes to melt the glass and allow it to flow into the gap between the membrane disc edge and the membrane holder wall. The assembly was allowed to cool slowly with the glass melt solidifying in the gap as well as bonding with the metal on one side and ceramic membrane on the other to form a gas-tight seal. Figure 4-6 is an exploded schematic of the glass seal between the metal (stainless steel) membrane holder and the ceramic disc. A detailed study of the bonding between the glass seal with stainless steel and dense LSCF6428 membrane is covered elsewhere in this thesis.

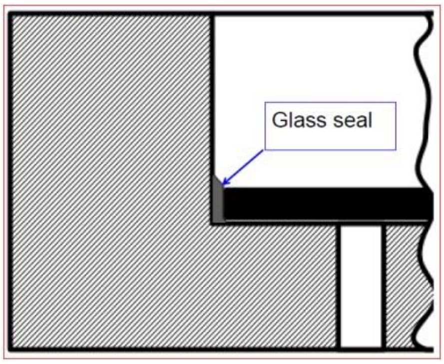

Figure 4-6 Exploded sectional view of glass seal between membrane and stainless stell housing wall.

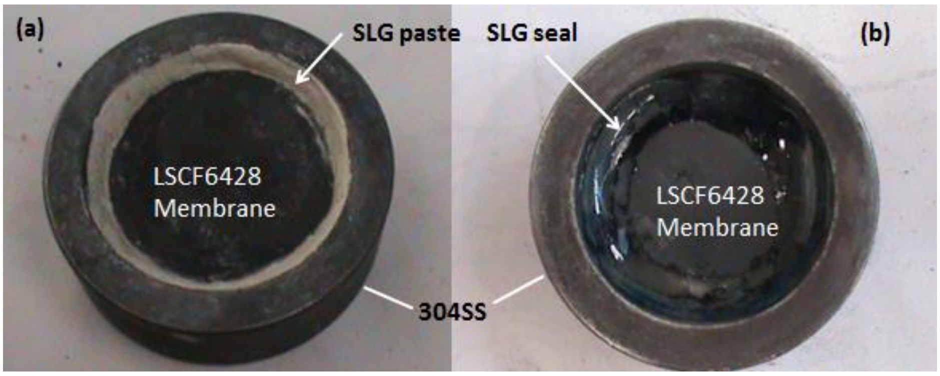

Figure 4-7 Images of membrane module: (a) assembly before sealing, (b) assembly after sealing

4.5 Copper gasket sealing concept

Figure 4-8 illustrates the concept of gaskets used to achieve a good gas-tight seal between the airside and permeate side chambers. Figure 4-8 (a) shows a photograph of a cylindrical stainless steel spacer and the copper gaskets as they will sit in the reactor assembly. Figure 4-8 (b) shows the cross-sectional view of the assembly, including the membrane module and fastening studs.

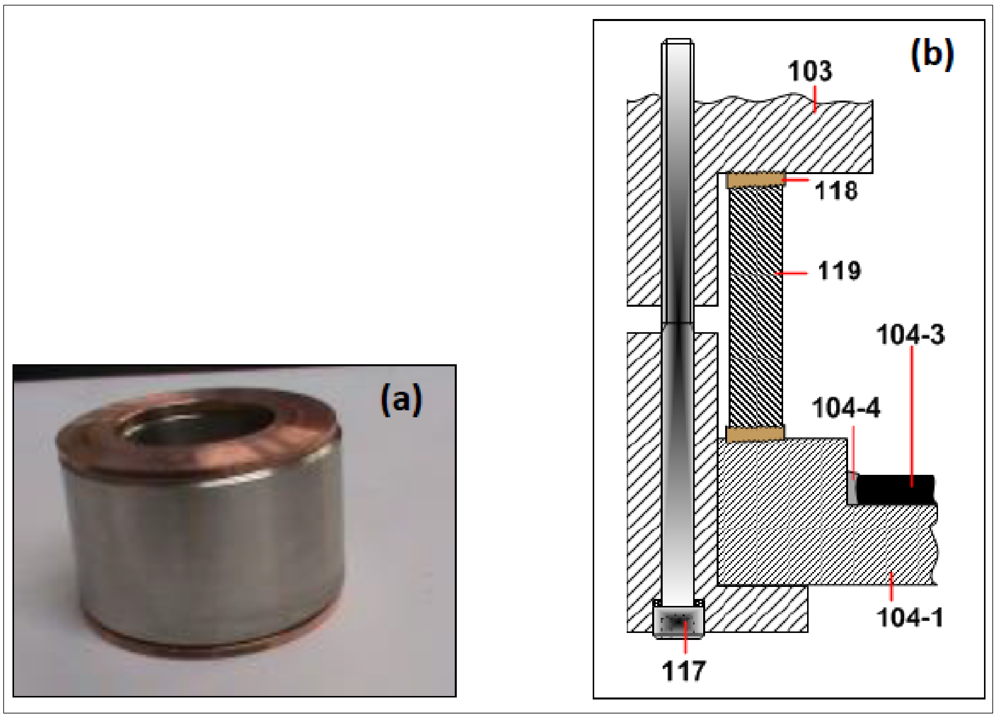

Figure 4-8 Copper gasket assembly

Copper was selected as a material for the gasket for its higher CTE, softness and malleability under high compression. This sealing concept relies on plastic deformation under mechanical compressive stress exerted by tightening studs *Figure 4-8* (117) as well as thermally induced stress due to copper’s higher coefficient of thermal expansion compared to the mating material, 304SS. Since the gasket is made from low stiffness material, it readily deforms in response to stresses generated at the interfaces with sealing surfaces. Its softness and malleability enables it to smear into small imperfections in the mating surfaces thereby enhancing the seal performance. The loading for the mechanical compression force to achieve the seal was provided by tightening the studs *Figure 4-8*(117) and the spacer stainless steel cylinder *Figure 4-8*(119) provided the mating surfaces. In addition, copper was also selected for its high thermal conduction properties. Heat produced by the Watlow cartridge heaters in the Head Block Figure 4-8(103) need to be efficiently conducted to the membrane module to provide the thermal activation to the membrane which can only operate at elevated temperatures.

4.6 Experimental set-up

The experimental setup for the oxygen permeation has been designed and constructed as shown in the schematic overview in *Figure 4-9*. It is a multipurpose rig that can be used for permeation tests in different configurations, oxygen production as well as oxygen separation combined with chemical reaction. It can also be used for hydrogen separation from hydrogen containing gas mixture by substituting a hydrogen membrane for the oxygen in the current set up.

As used in the current work for selective oxygen separation from air and inert/reactive permeate conditions, the set up consists of:

An air feed side with the associated pressurised air cylinder (Cyl-1), Mass Flow Meter (MFM-1).

The permeate side with feed gases supplies for cylinders CO (Cyl-2), CH_4 (Cyl-3), syngas (Cyl-4), He (Cyl-5) and associated Mass Flow Controllers (MFC-1, MFC-2, MFC-3 and MFC-4). The flammable gas bottles, methane and syngas, are equipped with 2-stage pressure regulators for safety. Flashback arrestors (FBA-1, FBA-2 and FBA-3 were also installed on the fuel gas lines for safe operation with flammable gases. For additional safety, the set-up was equipped with pressure relief valves

(PRV-1 and PRV-2) connected to both airside and permeate side chambers, which could be activated in the event of pressure in the respective chambers of the reactor exceeding pre-defined safe limits.

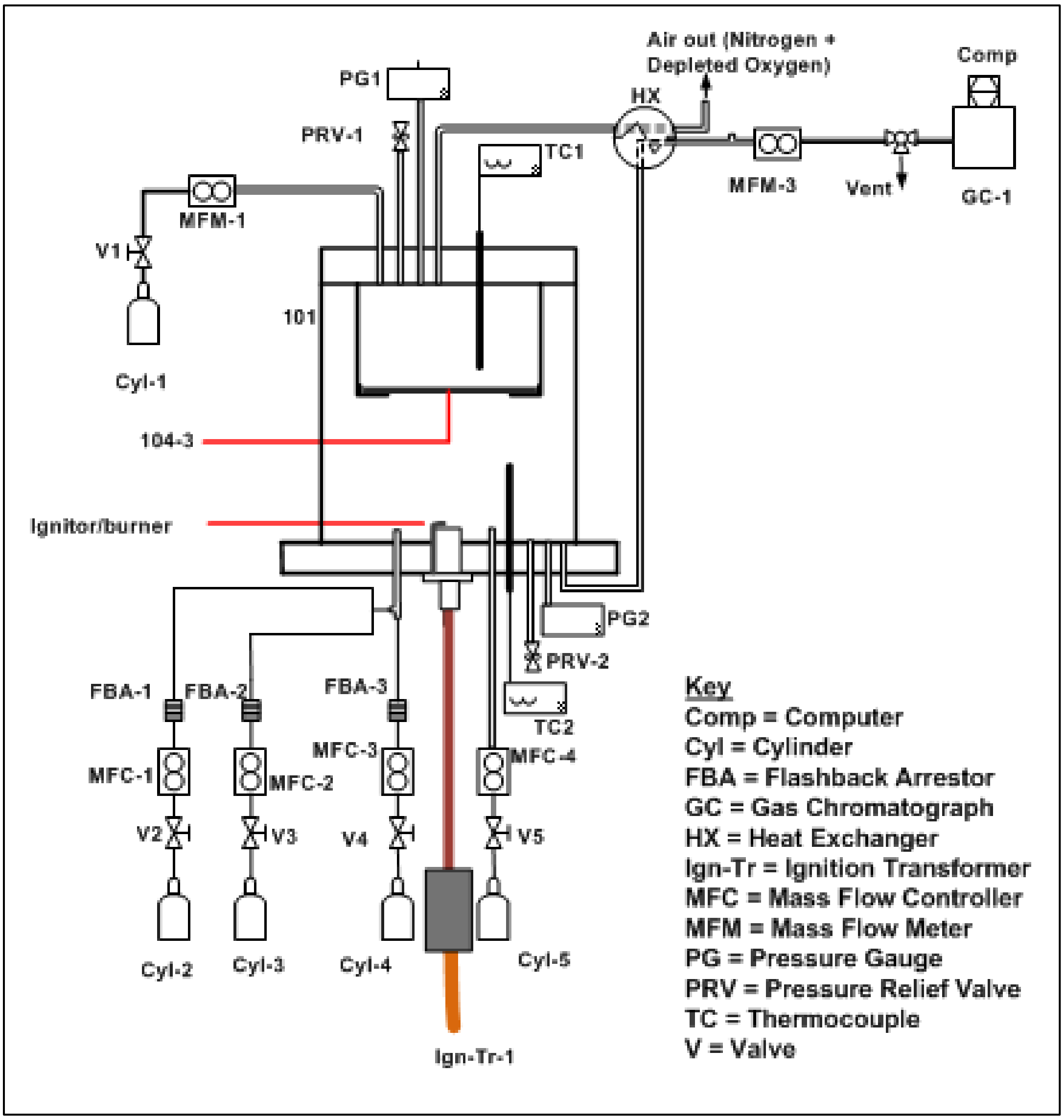

Figure 4-9 Schematic of the experimental permeation cell

The heating system consists of cartridge heaters *Figure 4-1* (107) to elevate the membrane temperature to the required levels required for oxygen permeation.

The hot effluent gas from the permeate side passed through a Heat Exchanger HX to cool them down before reaching upstream heat sensitive units such as the Mass Flow Meter (MFM-3).

The control and analytical systems consisted of thermocouples TC-1 and TC-2 to measure and monitor temperature of the membrane and permeate areas; a Bronkhorst Mass Flow Meter (MFM-3) and an on-line Gas Chromatography (GC-1) to analyse the permeate side gases. *Figure 4-10* shows the photographic image of the experimental set-up.

Figure 4-10 Photographic image of experimental set-up

4.7 Testing procedure gasket sealing and membrane integrity

The membrane module was fixed inside the reactor as shown previously in *Figure 4-1*. Screws (117) provide and maintain the compressive force required to seal at the copper gaskets (118). Gasket seal integrity was tested at room temperature using a blank stainless steel tablet of same dimensions as the real membrane holder. The airside was pressurised up to 5 bar and the pressure in the permeate side was monitored Bronkhorst Pressure Transducer PG2. Gasket seal integrity at room temperature was confirmed by absence of pressure build up in the permeate chamber as the air side was pressurised. A build-up of pressure measured by PG2 when the airside chamber was pressurised would be an indication the gasket seals were leaking. Use of a dummy membrane holder was done to test any leakage through the copper gaskets without the possible leakage through the membrane. With the hermetic seal of the copper gaskets confirmed the same was done with a membrane module with a membrane sealed by glass in it, to test for the seal integrity at room temperature. With seals integrity confirmed at room temperature, the equipment was tested for integrity at elevated temperature. This was done with the reactor heated to 650^{o}C and the air feed side pressurised up to 2bar above ambient pressure and the permeate side at ambient pressure.

4.8 Cartridge heaters

Provision for heating the membrane was by means of four Watlow 220V (290Watts), 6 inch (152.4mm) concentric heaters fitted in the Head Block (103) as shown previously in *Figure 4-1* and *Figure 4-2*. The heaters were controlled by heating controller and a K-type thermocouple which was also fitted in a port (106) on the head block. Initial tests on the experimental set-up showed the difficulty in heating the membrane reactor to the required targeted operating temperature of 650^{o}C. This was due to heat losses to the surroundings from the reactor walls. To circumvent this problem, the reactor was insulated with ceramic fibre blanket wrapped around it and held in position by means of an aluminium foil tape as shown in *Figure 4-11*.

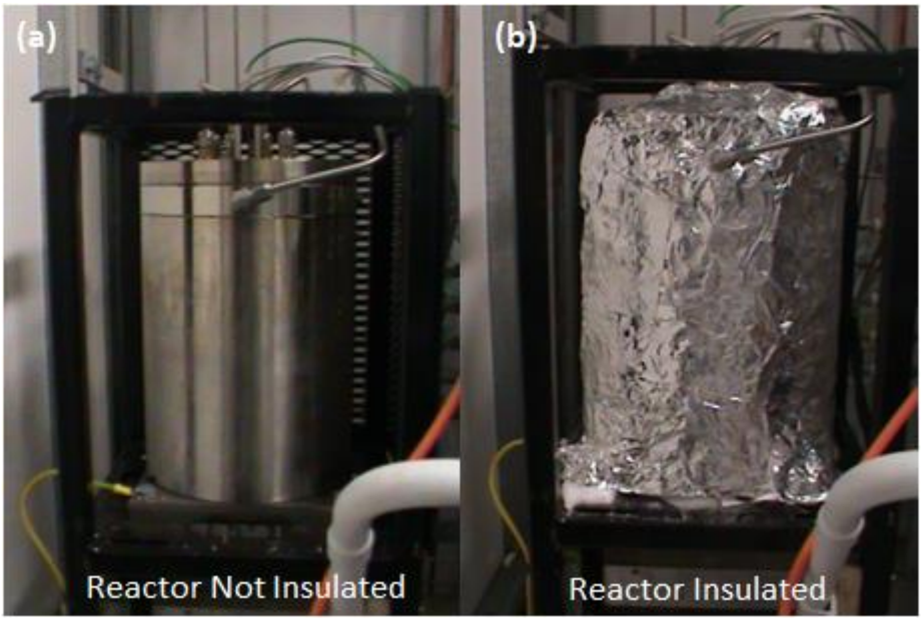

Figure 4-11 Image of reactor (a) not insulated, (b) insulated to minimise heat loss during heating up the reactor.

4.9 Ignition System

The igniter system was provided for other optional applications this novel piece of equipment might be used for where there might be need for an ignition system. The ignition system consists of a long range automobile spark plug fixed at the bottom of the permeate chamber as shown in *Figure 4-1* (115). The spark plug is energised to generate a continuous stream of spark across the gap by a high AC voltage generated from the mains supply using a variable transformer and an ignition transformer connected in series. The ignition transformer was supplied by Duomo UK plc. The igniter was capable of generating a continuous stream of sparks when a sufficient AC voltage is applied via the variable transformer and Duomo ignition transformer. The igniter system was a provision to enable ignition to initiate gas phase combustion reaction should that be required in the course of this study.

4.10 Experiment Procedure

Air was fed into the airside chamber at a controlled flowrate and measured by MFM-1. At the permeate side inert sweep gas Helium (for the oxygen permeation under inert conditions) was fed at a controlled flowrate, from a gas bottle supplied by BOC through a Bronkhorst Mass Flow Controller (MFC-5). Both the air side and permeate side were maintained at ambient pressure.

The same procedure was used in the permeation test under chemical reaction conditions in the permeate side but with the permeate side fed with a fuel gas, e.g. methane, diluted with helium.

The outlet stream flow rate was measured using a Bronkhorst Cori-flow (MFM-3). The composition of the outlet stream was measured using an Agilent 6890N Gas Chromatograph (GC-1 in *Figure 4-9*) with a Thermal Conductivity Detector (TCD) and Helium as carrier gas. The GC is equipped with two columns, a Supelco 60/80 Molseive 5A column 6ft x 1/8 in; and an 80/100 Haysep Q column 8ft x 1/8 in.

4.11 Experimental data processing

Determination of oxygen permeation values in this work depended on the flowrate and composition of the permeate side sweep gas. For a simple case where an inert gas, pure helium is used as sweep gas, the oxygen permeation flux in mL/cm^2/min can be calculated from the total effluent flow rate G (mL/min), the oxygen concentration c_{O_2} (%) as measured by the GC, and the effective area of the membrane A (cm^2) using the following formula:

$$J_{O_2} = \frac{c_{O_2} \times G}{100 \times A} \qquad \text{Eqn 4.1}$$

where c_{O_2} is the oxygen concentration in the bulk gas in the permeate space and is not necessarily that of the permeate membrane surface. This assumes that there is no leakage of air into the permeate chamber. In practice, it is difficult to achieve perfect sealing. Corrections of computed oxygen flux are therefore necessary. This can be done for both experiments under inert and reactive conditions.

4.11.1 Oxygen flux correction in permeation under inert conditions

The effluent was composed mainly of N_2 and O_2. The presence of N_2 revealed that the membrane reactor assembly was not perfectly sealed and had gas leakage which allowed some air into the permeate chamber. The GC measured N_2 in the permeate effluent was assumed to be the nitrogen component of the leaked air. It was reasonable to assume that oxygen in the permeate resulting from air leakage was in the same concentration ratio with nitrogen as it is in the synthetic air used during the experiment O_2 (21%) and N_2 (79%), $\left(\frac{21}{79}\right)$. The leaked oxygen was calculated using the value of detected nitrogen and the known composition of synthetic air or atmospheric air. The leaked oxygen concentration could be estimated by $(\frac{21}{79} \times c_{N_2})$. Some researchers, e.g. (Schiestel et al., 2005) assumed leakage by Knudsen diffusion in which case the leaked oxygen and nitrogen are related by:

$$\frac{J_{O_2}^{leak}}{J_{N_2}^{leak}} = \sqrt{\frac{28}{32} \times \frac{0.21}{0.79}} = 0.249 \qquad \text{Eqn 4.2}$$

This means that the diffusion of each component is inversely proportional to the square root of its molecular mass and directly proportional to its concentration. Knudsen diffusion assumes only leakage through pores and cracks of sizes of the order of the size of O_2 and N_2 molecules. In current work, it was recognised that there were several possible sources of leakage such as the gaskets systems in which Knudsen diffusion might not apply. It has been therefore assumed, for current work, O_2 and N_2 leak into the permeate side at rates only proportional to their concentrations in air. The computation for electrochemical permeated oxygen can therefore be corrected in the following way.

The concentration of leaked oxygen is given by:

$$c_{O_{2-\mathrm{leak}}} = \frac{0.21}{0.79} c_{N_{2-\mathrm{leak}}} \qquad \text{Eqn 4.3}$$

where $c_{N_{2-\mathrm{leak}}}$ is concentration of leaked N_2 and is directly measured by the in-line GC. The concentration of leaked oxygen can be obtained and taken out of the total O_2 concentration measured by the GC, to give:

$$c_{O_{2\_\mathrm{perm}}} = c_{O_{2\_\mathrm{measured}}} - c_{O_{2-\mathrm{leak}}} \qquad \text{Eqn 4.4}$$

where $c_{O_{2\_\mathrm{perm}}}$ is the concentration of permeated oxygen, $c_{O_{2_\mathrm{measured}}}$the measured oxygen concentration and $c_{O_{2-\mathrm{leak}}}$is leaked oxygen as in Eqn 4.3.

The corrected oxygen flux equation under inert conditions becomes:

$$J_{O_2} = \frac{G \times c_{O_{2-\mathrm{perm}}}}{A} \qquad \text{Eqn 4.5}$$

4.11.2 Oxygen flux corrections in permeation with reaction

In permeation with reaction experiments, similar corrections in computing electrochemically permeated oxygen is required. Calculations for CH_4 and CO oxidation are presented in the following subsections.

4.11.2.1 CH_4 oxidation

In the experiment with methane or helium diluted methane as permeate side sweep gas, the detected effluent gases were composed of carbon dioxide, nitrogen, unreacted methane and small traces of oxygen. Helium was not detected since the GC used in the experiment used helium as the mobile phase. This composition of the effluent gases indicates that:

The converted methane was fully oxidized to carbon dioxide and water as there were no traces of hydrogen detected.

The small traces oxygen far below the amount of computed leaked oxygen indicate that some of the leaked oxygen may have also reacted homogeneously with methane to form carbon dioxide and water.

The oxygen involved in the permeate side can be estimated from the following considerations:-

The simplest oxidation mechanisms that can be assumed are the stoichiometric reaction of deep oxidation of methane given by:

$$\mathrm{CH_4 + 2O_2 \rightarrow CO_2 + 2H_2O} \qquad \text{Eqn 4.6}$$

assuming gaseous phase reaction, or,

$$\mathrm{CH_4 + 4O_o^x \rightarrow CO_2 + 2H_2O + 8e} \qquad \text{Eqn 4.7}$$

assuming heterogeneous reaction between methane and lattice oxygen.

It assumes that the only products of methane oxidation are CO_2 and H_2O. LSCF family of perovskites has been reported to have inherent catalytic activity that is selective for CO_2 (Tan et al., 2007). In the current work, experiments have shown that only complete oxidation products, CO_2 and H_2O are formed as no H_2 or CO were detected by the GC. From these equations the amount of oxygen used can be derived directly from the measured CO_2 concentration. The underlying assumption made is that the CO_2 is only coming from methane oxidation and not from anywhere else. This assumption is reasonable since the amount of any CO_2 leaked from air side or from the atmosphere is negligible, given that the concentration of CO_2 in air is 0.03%. The oxygen consumed in deep oxidation of methane is therefore obtained by simply doubling the measured CO_2 concentration in the effluent. From this, the leakage oxygen can be subtracted to obtain the electrochemically permeated oxygen through the membrane.

The formula for this computation is:

$$\mathrm{c_{O_{2-perm}}} = 2\mathrm{c_{CO_{2-measured}}} - \frac{21}{79}\mathrm{c_{N_{2-leaked}}} + \mathrm{c_{O_{2-measured}}} \qquad \text{Eqn 4.8}$$

where $c_{O_{2-perm}}$ is the equivalent concentration of permeated oxygen, $c_{CO_{2-measured}}$ is the concentration of CO_2 measured by the GC, $c_{O_{2-measured}}$ is the concentration of measured unreacted O_2, and $\frac{21}{79}c_{N_{2-leaked}}$ as previously defined, is the leaked oxygen calculated from concentration of N_2 measured by the GC. The oxygen flux through the membrane, in mLmin^{-1}cm^{-2} is computed using the formula:

$$\mathrm{J_{O_2}} = \frac{\mathrm{G} \times \mathrm{c_{O_{2-perm}}}}{\mathrm{A}} \qquad \text{Eqn 4.9}$$

where $\mathrm{J_{O_2}}$ is the oxygen flux in mLmin^{-1}cm^{-2} G is the effluent gas flowrate in mLmin^{-1} and A is the membrane area in cm^2.

4.11.2.2 CO oxidation

For the experiment using helium diluted CO as sweep gas, the permeate side reaction is assumed to be:

$$\mathrm{CO} + \frac{1}{2}\mathrm{O_2} \rightarrow \mathrm{CO_2} \qquad \text{Eqn 4.10}$$

Similarly to methane above, it was assumed the CO_2 measured by the GC in the effluent gases was solely from oxidation of CO to CO_2. In this experiment, the effluent gases detected were CO_2, unreacted CO, N_2 and traces of O_2. The oxygen consumed in the reaction was derived from the equation above by halving the measured CO_2 concentration and the electrochemically permeated oxygen was computed from the formula:

$$c_{O_2-\text{perm}} = \frac{1}{2} c_{CO_2-\text{measured}} - \frac{21}{79} c_{N_2-\text{leaked}} + c_{O_2-\text{measured}} \qquad \text{Eqn 4.11}$$

The oxygen flux through the membrane, in $mLmin^{-1}cm^{-2}$ was computed using the formula:

$$J_{O_2} = \frac{G \times c_{O_2-\text{perm}}}{A} \qquad \text{Eqn 4.12}$$

where J_{O_2} is the oxygen flux in $mLmin^{-1}cm^{-2}$ G is the effluent gas flowrate in $mLmin^{-1}$ and A is the membrane area in cm^2.

4.12 Analytical Tools

The analytical tools used in the current work included mainly Gas Chromatography (GC), Scanning Electron Microscopy (SEM) and Energy Dispersion Spectroscopy (EDS). The basic working principles of these analytical tools are discussed in the next few sections.

4.12.1 Gas Chromatography basic principles

Gas chromatography is a method for identifying and measuring the chemical composition of gas mixtures. The sample of the mixture being analysed is mixed with a carrier gas (mobile phase) which transports it through column(s) where the separation actually takes place. The columns are capillary tubes with an active layer (stationary phase), coated on the inner walls of the column. The stationary phase absorbs the sample components (analytes), and releases them later at the other end of the column. The differences in the chemical and physical properties of analytes and their interactions with the stationary phase are the basis of the separation process. In most cases, every analyte has a different absorption and release rates on the stationary phase and therefore will elute at column exit at different times. As the analytes elute at the other end of the column one by one, they pass through a detector. The amount of time a component is retained in the column before elution is termed Retention Time (RT). The retention time is used for identifying components in the sample according to the prior GC calibration. It is however possible to have more than one analyte with the same retention time. Retention times on their own are therefore not an absolute method of identifying analytes. In many cases, a further analysis is required such as mass spectrometry. In the current work, analyte identification was based only on retention times as there was a high degree of confidence with RT only owing to the limited possible reaction products during the experiments.

4.12.1.1 Detectors

There are several types of detectors that can be used in Chromatography in general. These include Thermal Conductivity Detector (TCD), Flame Ionization Detector (FID), Electronic Capture Detector (ECD), Photo-Ionization Detector (PID), Flame Photometric Detector (FPD) which all use different phenomena, but for gas chromatography, the main types of detectors are the TCD and the FID.

TCD is a detector that is usually used in detecting permanent gases such as nitrogen, oxygen, hydrogen, carbon dioxide, carbon monoxide and methane. GCs with TCD detectors normally use helium as the carrier gas, as did the GC used in the current work, because helium has the highest thermal conductivities of all gases with the exception of hydrogen. TCDs work on the basis of different thermal conductivities of different gases. The gas flow through the detector is helium most of the time except when a component of the sample being analysed is eluting. When an analyte is eluting, the thermal conductivity of the gas in the detector cell now a mixture of helium carrier gas and the analyte, changes due to the presence of the less heat conducting analyte. This change results in a change in heat flow from the heated sensor, a thermistor. Since the sensor is being heated at a constant rate, owing to slower heat transfer, its temperature rises. The change in temperature of the sensor/thermistor results in a change in resistance. The change in resistance upsets the balance of a Wheatstone Bridge which the sensor is part of. This generates a voltage signal which is fed into the computer and results in a peak on the Voltage – Time plot of a chromatogram. The signal strength depends on the gas component as well as its concentration.

FID is mainly used for detecting hydrocarbons. As each hydrocarbon elutes from the column into the FID detector, it is mixed with hydrogen and air. Carbon atoms in the hydrocarbon are ionized during oxidation of hydrogen mixed with air and these ions in the cell hit a plate connected to a very sensitive voltmeter. The voltage is amplified and fed into a computer. The number of carbon ions generated is proportional to the number of carbon atoms in the hydrocarbon’s molecule. Larger hydrocarbon components or higher concentrations have more carbon atoms and therefore give a larger response. For example, butane has twice the number of carbon atoms as ethane, so it will, within limits, produce a response twice that of ethane, assuming same concentration.

In this part of the study only permanent gases are involved or expected to be used and a GC with TCD is used. The Agilent 6890N GC equipped with two columns, a Supelco 60/80 Molseive 5A (6ft x ⅛ in) and a Supelco 80/100 Haysep Q (8ft x ⅛ in). Helium was used as carrier gas.

4.12.1.2 GC Calibration – general

Before the GC is used for measuring gas samples, it has to be calibrated. During calibration, a calibration sample or standard is used. This is a sample containing a known mixture of species (both identity and concentration), which includes the species to be identified in the unknown sample. The standard may be purchased from chemical suppliers. The calibration standard is injected into the columns to produce a chromatogram on a time scale showing peak and retention time for each component in the standard. From this run, a calibration table, which specifies conversions of peak areas into concentrations, can be constructed. With the peak areas obtained the response factor for each component can be established by relating the area under the peak and the known concentration of the component. The calibration table also contains retention time (RT) of each component.

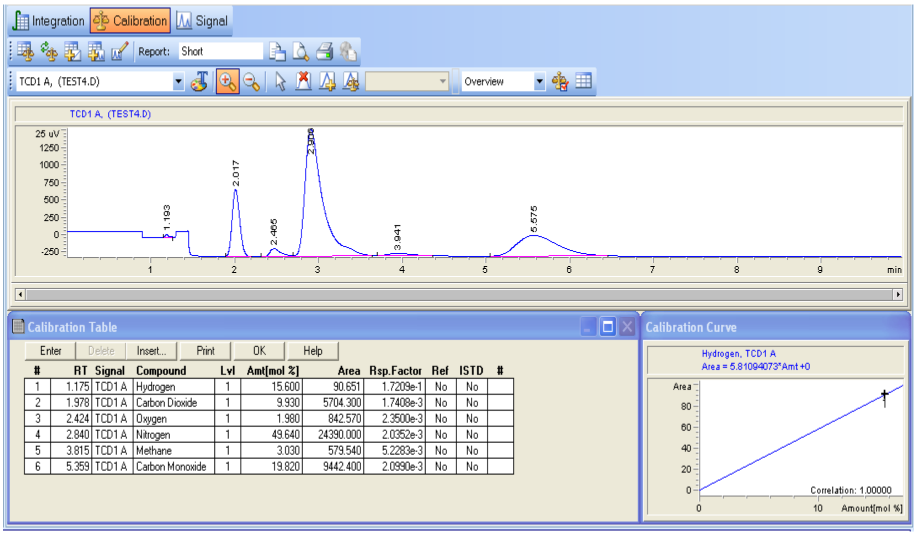

#	RT	Signal	Compound	Lvl	Amt[mol %]	Area	Rsp.Factor	Ref	ISTD	#
1	1.175	TCD1 A	Hydrogen	1	15.600	90.651	1.7209e-1	No	No	
2	1.978	TCD1 A	Carbon Dioxide	1	9.930	5704.300	1.7408e-3	No	No	
3	2.424	TCD1 A	Oxygen	1	1.980	842.570	2.3500e-3	No	No	
4	2.840	TCD1 A	Nitrogen	1	49.640	24390.000	2.0352e-3	No	No	
5	3.815	TCD1 A	Methane	1	3.030	579.540	5.2283e-3	No	No	
6	5.359	TCD1 A	Carbon Monoxide	1	19.820	9442.400	2.0990e-3	No	No	

Figure 4-12 Calibration chromatogram, calibration table and calibration curve (for hydrogen) example

The retention times of peaks are used for comparison with retention times of peaks from a sample run to identify components in the sample. Where a match occurs, the peak is assumed to represent the same compound as in the calibration table. This assumption is only valid if the sample is run under exactly the same Method or GC settings as was the calibration sample. In theory, it is also possible to have different compounds with the same Retention Time, so from this perspective 100% confidence cannot be claimed. From area under the respective peak of each component, the concentration of the component in the sample can be obtained. The GC however will not be able to identify a component not calibrated from the standard although it may show a peak for it. For example, if carbon monoxide was not in the calibration standard and therefore not calibrated, and it is one of the compounds in the unknown sample, it will produce a peak but the GC will not be able to identify it as carbon monoxide.

4.12.1.3 Calibrating the Agilent GC 6890N

The special calibration standard gas bottle supplied by STGas Ltd was used. The bottle contained the following gases and their certified concentrations: hydrogen (15.60 %), carbon dioxide (9.93 %), oxygen (1.98 %), carbon monoxide (19.82 %), methane (3.03 %) and nitrogen (49.64%). A standard containing the above compounds was chosen because these are the compounds expected to be encountered either as reactants or products of reactions during the experiment.

The calibration standard bottle was connected securely to the injection port of the GC and the standard gas allowed to flow through and vented out by bubbling it through de-ionized water to flash out any air in the pipes for about 10 minutes. This was to ensure only the standard gas sample without contamination by air trapped in the pipes was analysed for calibration purposes. The GC was run to construct a calibration curve. Several such runs were made until consecutive runs gave very close concentrations and adopted as the true calibration curve and table. When a component of the calibration standard pass through the TCD detector, a signal is generated whose peak is plotted against time to produce a chromatograph. For each analyte peak two pieces of information are obtained, the RT and the peak area (the numerical integral of the peak above the baseline). As the concentration of the analyte is known from the certificate provided by the supplier of the standard gas, the peak area can be related to the concentration to compute the response factor which is a ratio of peak area to the concentration.

The basic principle is that once the GC has been calibrated using a given GC Method with a given set of GC devices settings, if the same settings are used in experiments to measure given samples, the compounds in the samples should show the same retention times as the same compounds in the calibration standards, thus enabling identifying the presence or absence of the compound in a given sample. The concentration of the compound can be computed from the peak area and response factor and this is all done automatically by the Chemstation software controlling the GC.

The Agilent GC 6890N used in the study was controlled using Chemstation software on a laptop computer. In the Chemstation the GC Method can be stored and loaded into the GC when required. The Methods in the Chemstation can easily be edited to change parameters whenever required.

4.13 Characterization techniques

The analytical tools used in the current work to characterise microstructural and phase changes in materials include Scanning Electron Microscopy (SEM) in combination with Energy Dispersive Spectroscopy (EDS); and X-Ray Diffraction (XRD)

4.13.1 SEM and EDS – basic principles

SEM is a method capable for high resolution and high magnification mapping and imaging of material surfaces using high energy electrons. An incident beam of electrons is raster-scanned, in the same way as an electron beam scans the screen of a Cathode Ray Tube (CRT) in vacuum tube television monitors, across the specimen surface. The resultant secondary or backscattered electrons emitted from the sample are collected by a detector and processed to form an image of the surface. SEM is particularly useful for characterising material microstructure such as existence or not of porosity or cracks, grain sizes estimations, etc.

Energy Dispersive Spectroscopy (EDS) is a powerful tool for qualitative and quantitative compositional analysis for identifying elements in different parts of specimen. It is an analytical technique that uses the X-rays emitted from the sample during bombardment by an electron beam to characterise the elemental composition of the analysed volume. Using SEM in combination with an EDS makes it possible to observe the morphology of the surface and cross section of the samples as well as the elemental composition of the different phases in the sample. When the high energy electron beam bombards the area of interest on the specimen, the incident electrons interact with the atoms in the specimen and secondary electrons are emitted. The emitted electrons can be from inner electronic shells of the atoms. This leaves the atom in an excited state and, to attain a more stable state, electrons from the outermost shell drop down to occupy the electron holes left behind by the emitted secondary electrons. Since electrons in the outer shell are at a higher energy state, when the electron drops down to an inner shell at a lower energy state, the atom must lose some energy equivalent to the difference in energy levels of the two electron shells involved, and this happens through emission of an X-ray photon. The X-rays photon emitted is characteristic of the element involved in the interaction, in terms of energy and wavelength. These X-ray photons are detected by the Energy Dispersive detector. The energy and wavelength of these characteristic X-rays allow the elements making up the sample at the area of interest to be identified while the intensities of their peaks allow the concentrations of the elements to be quantified. EDS is capable of examining microscopic area as small as 1μm and minimum detection limits can be as small as o.1%. The output of an EDS is a spectrum plotting intensity (counts) versus Energy (eV). Quantitative data is also produced showing atomic count percent of elements identified.

In some of the investigations, SEM required the sample to be conductive to avoid charging effects. This is achieved by coating the sample with gold using a sputter coater. EDS does not require coating the specimen and is considered as a non-destructive analytical technique.

The SEM investigations in the current work were carried out using an FEI XL30 ESEM-FEG (environmental scanning electron microscope-field emission gun).

4.13.2 X-Ray Diffraction-basic principles

XRD is a basic tool for characterising phases present in a given specimen. The technique is used to determine the crystalline structure of the specimen based on the interpretation of diffractograms resulting from the interference of X-rays scattered on atomic planes in the material under study. The source of the X-rays is a beam of high energy electrons generated by a heated tungsten filament and accelerated towards a metal target, normally copper or molybdenum. A high energy electron can eject an electron from an inner shell of the atom of this metal target. When an outer shell electron of this atom drops to the inner shell to fill the vacancy left by the ejected electron, this is accompanied by the emission of an X-ray photon with characteristic energy of the target metal, normally copper/molybdenum.

When this photon strikes the surface of a crystal, the angle of the scattered x-ray beam can be used to calculate the spacing between two layers of atoms in the specimen using Bragg's Law:

$$2d\sin\theta = n\lambda \qquad \text{Eqn 4.13}$$

where d is the lattice spacing in nm, θ (rad) is the angle between the incident ray and the scattering plane, λ is the wavelength of the X-ray (m) and n is an integer. An illustration of mathematical derivation of Bragg's Law is as follows:

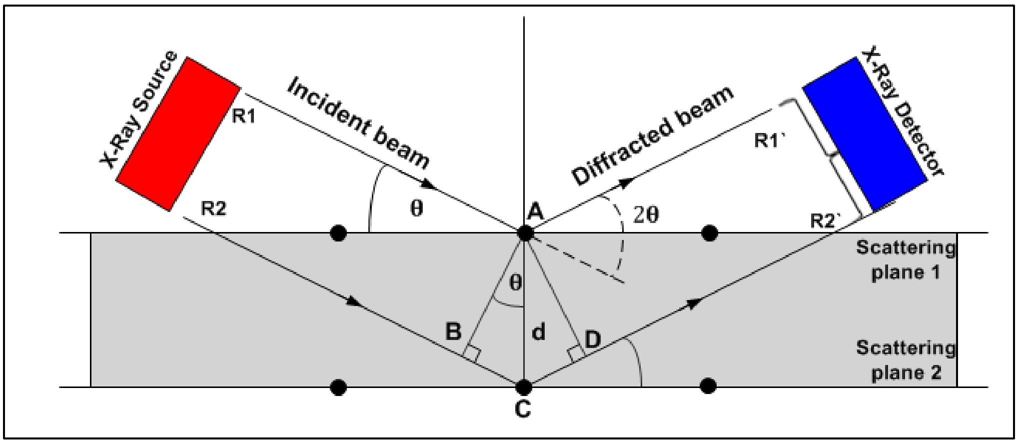

Figure 4-13 Schematic showing the principles of XRD

Consider as in *Figure 4-13* two incident rays R1 and R2 each making an angle θ with atomic (or scattering planes 1 and 2) planes. The scattered (diffracted) rays R1` and R2` will have a maximum intensity if the two rays are in phase with each other (coherent/constructive interference). For them to be in phase, the difference in path lengths (BC+CD) travelled by the two rays must be an integral number of wavengths (nλ). In other words, from *Figure 4-13*:

$$\mathrm{BC} + \mathrm{CD} = \mathrm{n}\lambda \qquad \text{Eqn 4.14}$$

But:

$$\mathrm{BC} = \mathrm{CD} = \mathrm{d}\sin\theta \qquad \text{Eqn 4.15}$$

$$\therefore \mathrm{d}\sin\theta + \mathrm{d}\sin\theta = \mathrm{n}\lambda \qquad \text{Eqn 4.16}$$

$$2\mathrm{d}\sin\theta = \mathrm{n}\lambda \qquad \text{Eqn 4.17}$$

This is Bragg’s Law.

From *Figure 4-13*, it can be seen that the diffracted ray has a deviation of 2θ from the incident. If an X-Ray Diffraction detector scans the intensity of the diffracted radiation at values of θ that satisfy Bragg’s Law, the detector picks high intensity of the diffracted radiation. The result of an XRD measurement is diffractograms showing phases (peak positions) in terms of 2θ, the deviation of the diffracted ray from the incident ray, and phase concentrations (peak heights). Qualitative analysis is possible by comparing the XRD patterns of the specimen under study to a library of known patterns (a search and match method).

The peaks of the diffraction pattern are directly related to the lattice spacing which is characteristic of the particular crystal phase. This interpretation of the diffractograms can provide some structural information of the material such as crystalline phase identification. This is possible because each crystalline solid has a unique X-ray diffraction pattern (fingerprint).

4.14 Mass Flow Meters and Controllers calibration

The schematic in *Figure 4-9* shows the layout design of the experimental rig. The flammable gas bottles, methane and syngas, are equipped with 2-stage pressure regulators and connected to the membrane reactor permeate chamber via stainless steel pipes through Bronkhorst Mass Flow Controllers (MFCs). Compressed air and inert gas, Helium /CO_2 are connected to the to the air compartment and permeate chambers respectively via Mass Flow Meter (MFM1) and Mass Flow Controller (MFC4) respectively. All the mass flow meters and controllers are controlled using software on a computer. Flashback arrestors protected the fuel gases methane and syngas mixture.

Synthetic air (O_2 + N_2) fed to the air side chamber was supplied from a BOC cylinder through stainless steel tubes via a MFM to measure the flow rate. At the permeate side, high purity gases (inert sweep gas Helium, fuel gases (methane, carbon monoxide) were supplied from cylinders via stainless steel tubes as well but via Mass Flow Controller (MFC) to control and measure the flow rates. The MFMs and MFCs were calibrated using an Agilent bubble flow meter. Both sides of the membrane were maintained at ambient pressure which was monitored by Bronkhorst electronic pressure sensors Models P-502C-21KR-RAD-22V. The reactor membrane module was heated using Watlow cartridge heaters and controlled by a controllable temperature controller around the membrane, whose temperature was measured by a concentric 6 inch K-Type thermocouple.

Chapter 5 : **MEMBRANE FABRICATION AND CHARACTERISATION**

5.1 Introduction

The ultimate goal of this research is production of syngas (a mixture of hydrogen and carbon monoxide) from partial oxidation of methane using oxygen selective membranes. The work experimentally evaluates oxygen permeation under inert conditions versus oxygen permeation under reactive conditions. The first mode of operation is oxygen production where the oxygen is separated from air and collected as gaseous phases oxygen swept from the permeate side using an inert gas such as helium. In this mode of operation, the oxygen can be used later in other processes. The second mode of operation is where the membrane reactor combines oxygen separation from air and a chemical reaction in one unit. In this mode of operation, permeate oxygen is used to react with a fuel gas at the permeate side the membrane. In its simplest form, a fuel gas such as CO, CH_4 (or diluted with an inert gas such as helium), is used as sweep gas without regard to the end products of reaction as the intention is to investigate the effect of an oxygen consuming reaction. However, ultimately, what is desired as further work is the development of a catalyst to selectively influence the reaction pathway at the permeate side to produce a desired product mix such as syngas, a mixture of hydrogen and carbon monoxide which can be used in downstream processes such as FT to produce methanol. However the scope of the membrane reactor investigations does not include catalyst development. Its scope is design and construction of a bench scale membrane reactor using common industrial materials such as stainless steel, sealing the ceramic membrane in a metal housing and testing the reactor at elevated temperatures. It is in the membrane reactor materials and membrane sealing areas that this investigation has some novelty. Prior work by other researchers consisted of quartz based reactors in which gold or silver wires or pastes were used for sealing membrane to quartz tubes. For example (Teraoka et al., 1985) used silver rings to weld the membrane to a mullite tube and (Kruidhof et al., 1993) used pyrex glass on a quartz tube. While these served its purpose in fundamental research on oxygen membranes, it is far from practical application on many grounds such as the use of expensive precious materials in sealing. This will render syngas produced this way very expensive. In the present work glass is used as a sealant between a ceramic membrane and a metallic housing. Glass is much cheaper than noble metals such as silver and gold.

In the present work, the reactor designed and constructed was used in oxygen separation from air under permeate side inert and reactive conditions. Under reactive conditions, helium was used as a sweep gas. Although helium is not likely to be the sweep gas for choice in industrial scale oxygen separation using this novel technology, helium was chosen for ease of measurement of oxygen permeation through the membrane. An alternative was CO_2 with its high C-O bond energy, but due to the fact that CO_2 is oxygen containing species, its effect on oxygen permeation through the membrane is not clearly known and might influence the permeation process. In literature, laboratory experiments using Quartz based reactors have been carried out at temperatures as high as 800-1000^{o}C (1073-1273K) using tubular furnaces to elevate and attain these temperatures. In the present work the reactor was heated using Watlow cartridge heaters inserted into the stainless steel component on which the membrane module is installed. In addition, due to other design limitations of this reactor, the permeation experiments could only be carried out at a maximum of 650^{o}C (923K), the lower end of the temperature range in which the membranes operate. It is well known that temperature has a favourable effect on oxygen permeation owing to the acceleration of oxygen ions diffusion in the membrane bulk and surface exchange reaction rates. With regard to oxygen diffusion through the membrane bulk, this is illustrated by the Wagner Equation:

$$\mathrm{J_{O_2}} = \frac{\mathrm{RT}}{4^2\mathrm{F}^2\mathrm{L}}\left(\frac{\sigma_\mathrm{i}\sigma_\mathrm{e}}{\sigma_\mathrm{i}+\sigma_\mathrm{e}}\right)\ln\left(\frac{\mathrm{P_2}}{\mathrm{P_1}}\right) \qquad \text{Eqn 5.1}$$

where $\mathrm{J_{O_2}}$ is the oxygen flux in NmLcm^{-2}min^{-1}, R is the gas constant, F is Faraday's constant, L is the membrane thickness (cm), σ_i is the oxygen ionic conductivity of the membrane material, σ_e is the electronic conductivity of the material, $\mathrm{P_2}$ and $\mathrm{P_1}$ are respectively the oxygen partial pressures at the air side and permeate side respectively, and T is the membrane temperature in K.

5.2 Membrane materials

The membrane materials chosen for this study is the perovskite type

The LSCF6428 powders used in the experiments were supplied by Praxair (PI-KEM, Tamworth, UK) and their specifications were as follows; (particle sizes d_{10} = 0.6µm, d_{50} = 0.9µm and d_{95} = 3.9µm). The LSCF6428 powders were used without any further treatment for fabrication of disc shaped membranes. For each disc, 2.0g of the powder were measured and pressed using Specac Atlas T25 Automatic Hydraulic Press and a die of 32mm diameter. The disc pressing process is illustrated in *Figure 5-1* and images of the Specac Atlas T25 Automatic Hydraulic Press are shown in *Figure 5-2*.

The pressed discs were heat treated in a box furnace from room temperature to 1150^{o}C at a ramp rate of 1^{o}C and dwelled at that temperature for 5 hours before being let to cool back to room temperature slowly. The discs shrunk from 32mm diameter and 2mm thickness to 25mm diameter and 1mm thickness (*Figure 5-3*).

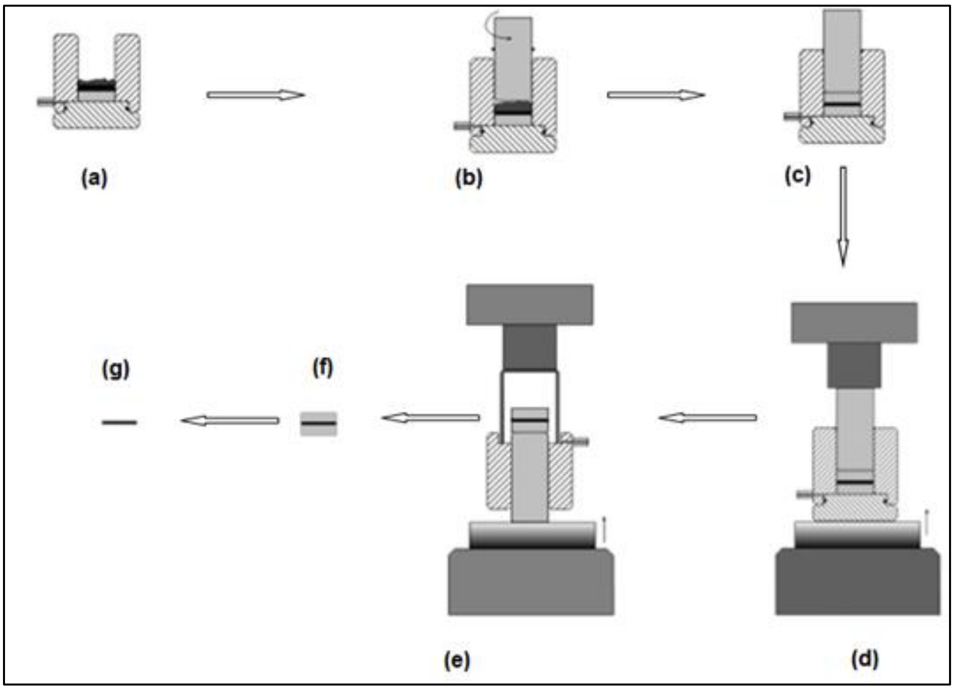

Figure 5-1 Schematic illustrating the steps in disc pressing (a) adding ceramic powder into die, (b) levelling ceramic powder using plunger,(c) ceramic powder between stainless steel die pellets,(d) pressing using hydraulic press,(e) pressed green ceramic pellet evacuation, (f) evacuated green ceramic pellet still between stainless steel die pellets, (g) resulting pressed green pellet ready for sintering

Figure 5-2 Specac Atlas T25 Automatic Hydraulic Press used to press membrane discs.

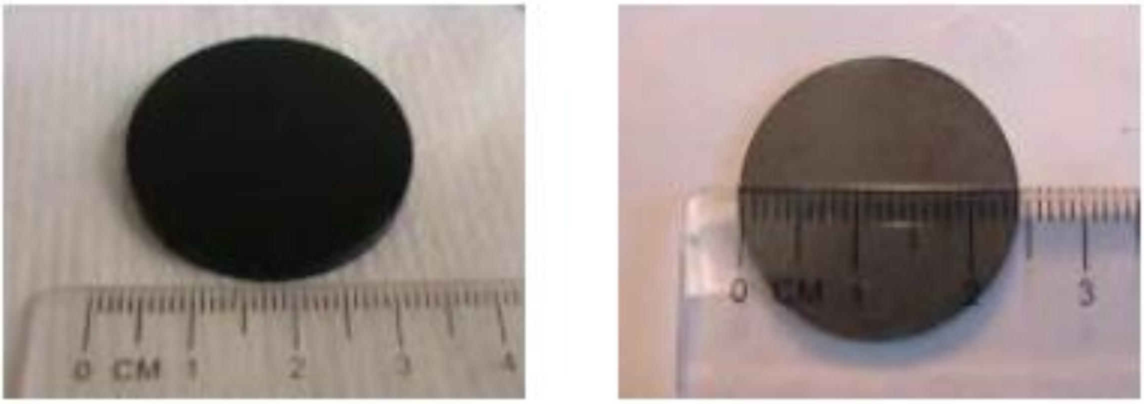

Figure 5-3 The 32mm Dia, 2mm thick pressed ceramic green body and the 25mm Dia, 1mm thick disc sintered at 1150^{o}C.

The surface and fracture morphology of one such pressed and sintered disc was examined by SEM to determine whether it was dense enough and free from continuous pores. The SEMs were carried out using a FEI XL30 ESEM-FEG (environmental scanning electron microscope- field emission gun, made by Rontec and software by Quantax), using a low vacuum mode at 20kV.

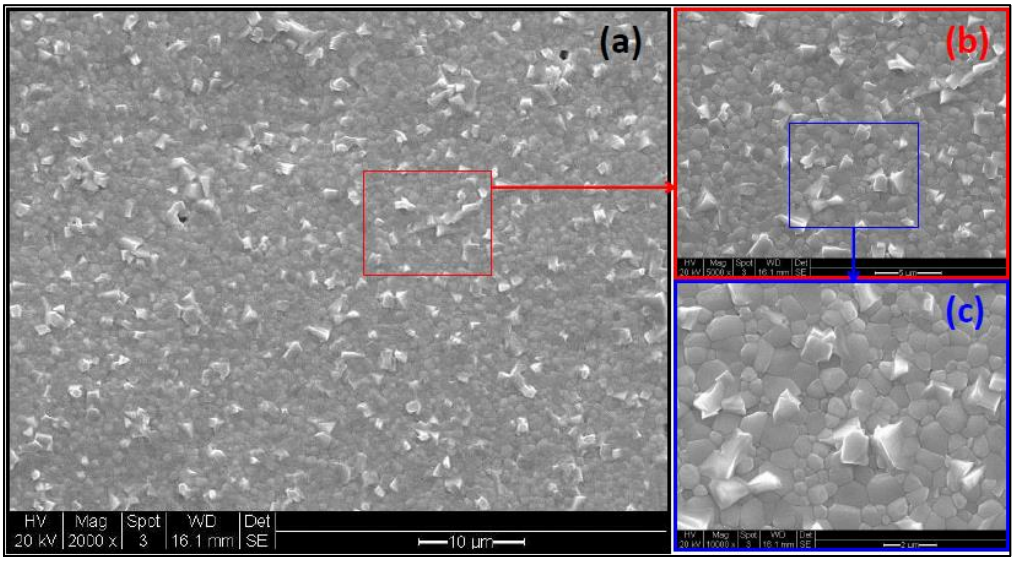

Figure 5-4 Surface SEM of LSCF6428 sintered at 1150^{o}C:- Magnifications: (a) x2000, (b) x 5000 and (c) x10000

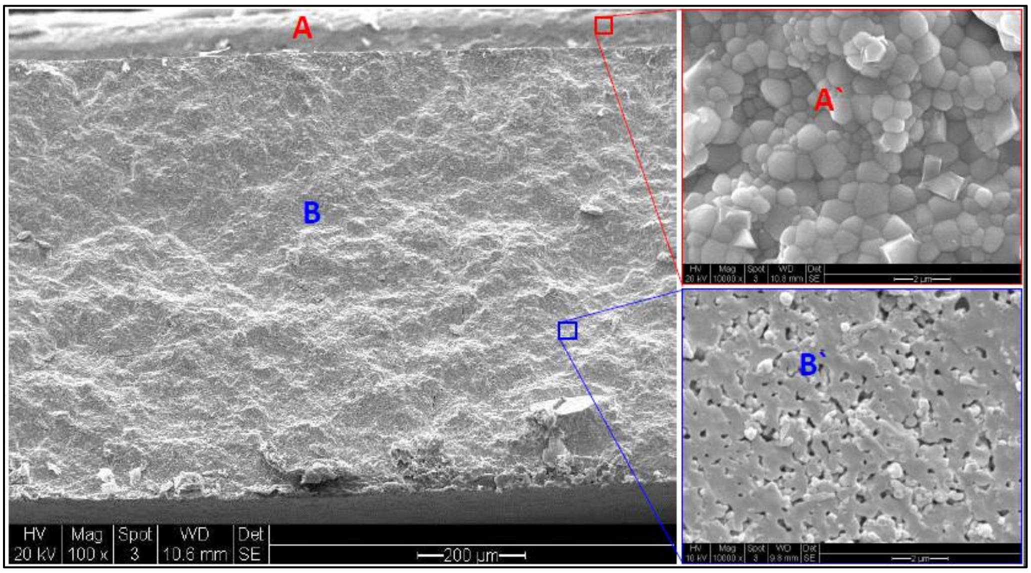

Figure 5-5 LSCF6428 Membrane fracture SEM:- (a) = x 100, (b) = x 5000, (c) = x 10000

Figure 5-4 shows representative micrographs of sintered LSCF6428 (at 1150^{o}C for 5 hours) surface at various magnifications, (a) x 2000, (b) x 5000 and (c) x 10000. The micrographs show that, save for a few isolated pores the membrane surface is generally dense and gas tight. It is here assumed the isolated pores are not continuous through the membrane thickness.

Figure 5-5 shows representative micrographs of a cross-sectional fracture surface of the same membrane. It is observed from micrograph (a) that the membrane has two visually different structures, a seemingly more dense skin at the edges of the membrane thickness and seemingly less dense structure for the bulk of the membrane thickness. Micrographs (b) and (c) represent the microstructures of the skin layer and the bulk thickness respectively at high magnifications. These two micrographs confirm that the skin has a much denser microstructure than the bulk membrane thickness. While the skin micrograph show no evident pores, that of the bulk thickness micrograph exhibits isolated pores. This result shows that the membrane was closer to 100% densification on the skin layer but much less so in the bulk thickness. However, since was no evident connected porosity even in the less densified bulk thickness, these membranes sintered at 1150^{o}C for 5 hours could be considered gas tight for oxygen permeation experiment purposes.

However, the isolated pores can have some effect on oxygen flux as the volume occupied by the pores in the membrane bulk is not available for oxygen ion conduction. This might also explain the discrepancies in oxygen flux reported in literature in which supposedly membranes made from same compositions, about same thickness and tested under supposedly similar conditions had different oxygen fluxes. *Table 5-1* illustrates the different oxygen fluxes through 1mm thick $SrCo_{0.8}Fe_{0.2}O_{3-\delta}$ membrane at 850^{o}C reported in literature.

Table 5-1: Some discrepancies in oxygen flux through $SrCo_{0.8}Fe_{0.2}O_{3-\delta}$ reported in literature under supposedly similar conditions.

Material	Oxygen flux mol.cm^{-2}.s^{-1}	Temperature (^{o}C)	Thickness (mm)	Reference
$SrCo_{0.8}Fe_{0.2}O_{3-\delta}$	2.3x10^{-6}	~850	~1	(Teraoka et al., 1985)
$SrCo_{0.8}Fe_{0.2}O_{3-\delta}$	1.8x10^{-7}	~850	~1	(Kruidhof et al., 1993)
$SrCo_{0.8}Fe_{0.2}O_{3-\delta}$	6.3x10^{-7}	~850	~1	(Qiu et al., 1995)

Several possible reasons for these discrepancies have been advanced by other researchers, e.g. different precursor powders synthesis methods (Tan et al., 2003), sintering temperature during membrane fabrication resulting grain size differences which have effect on oxygen permeability (Zhang et al., 1999), and different gas flow rates used by different researchers (Wiik et al., 2002) (Stephens et al., 2000).

In most of these reports, the researchers have not indicated the degree to which the membrane was densified.

Chapter 6 : MEMBRANE SEALING AND CHARACTERISATION

6.1 Introduction

One of the important challenges in development of the high temperature intensified catalytic membrane reactor relates to the development of suitable sealant materials and sealing procedure to hermetically separate the two chambers separated by the membrane, and to maintain the gas tightness of the system at operating temperatures typically between 600-1000^{o}C. In addition, the sealing material must be able to withstand the harsh chemical environments; a reducing or low oxygen partial pressure environment on one side, and a high oxygen partial pressure on the other. Hermeticity across the membrane is paramount to prevent leaks from the airside to the permeate side of the membrane, which would reduce the driving force (the oxygen partial pressure difference), or diluting the reaction products with nitrogen, which the use of the membrane intend to prevent. However, it is difficult to archive perfect seals. Acceptable leakage is when leaks contribute less than 2% of total oxygen transported through the membrane, that is, a of 50:1 ratio of solid state transport to gas leak transport(Stephens et al., 2000). Similar or even tighter hermeticity requirements are required in planar Solid Oxide Fuel Cell (SOFC) applications for separating the fuel gas, (e.g. H_2, CH_4) from the oxidant (air or O_2) (Ghosh et al., 2008, Meinhardt et al., 2008). In SOFC applications, leaks can result in reduced fuel cell system performance, lower power generation efficiency and poor fuel utilization.

A huge and still growing body of literature exists on sealants for SOFC applications. (Reis and Brow, 2006) presented conditions for ideal high temperature sealing in solid oxide fuel cell stacks. The ideas and concepts in this body of literature can be extended to high temperature membrane reactor applications due to the similarities in SOFC and oxygen membrane operations.

(Reis and Brow, 2006) listed the following as mechanical, chemical and thermal properties suitable for high temperature applications:

1. Good bonding to materials of interest

2. Thermal stability at elevated operational temperature conditions

3. Chemical stability under oxidizing and reducing environments
4. Thermal expansion reasonably close to that of other materials involved
5. Sealant must have some compliance or softness to allow for some mismatch between components to be joined

In industrial applications, the seal will also experience numerous thermal cycles during shutdowns and start-ups and must be able to retain its hermeticity, mechanical ruggedness and chemical stability throughout the lifetime of the device, typically in the order of hundreds of thousands of hours (Weil et al., 2005). Another big problem is the thermal expansion coefficient which must match that of the metallic framework and the ceramic membrane to avoid cracks during thermal cycling.

Commonly used rubber O-rings in most sealing engineering applications is not suitable for these applications owing to the heat resistance limit of rubber of $<400^oC$. Only inorganic materials with high melting points can be used (Qi et al., 2001). The lack of suitable joining techniques of metal-ceramic for high temperature applications such as SOFC and membrane reactors has been one of the major hindrances to industrial application.

6.2 High Temperature Sealing Options

There are numerous obstacles to successful metal-ceramic joining. Generally, the bonding between two dissimilar materials is dictated by the phase boundary between them. The interfacial properties are a function of their structure and chemistry (Wagner et al., 1995). For example, ceramics are generally inert in nature. The goal is achieving bonding between the two or the use of a suitable filler material between the two that can bond well with both, provided the filler material meets the operational requirements of the device. Surface modification of one or the other to form a new phase compatible with the materials to be bonded may be necessary. Another obstacle is difference in CTE. When joining any two dissimilar materials, high internal stresses may result from temperature changes when cooling from joining temperature due to CTE mismatches.

Ceramic-metal interfaces have structural discontinuities due to dissimilar electronic structures. Ceramics in general have covalent or ionic bonding while metals have metallic bonding. This difference in chemical structures inhibits the formation of strong bonds at the interface (Suganuma et al., 1988). Required to join the two is an intermediate material that is able to bond strongly with both the ceramic membrane and the metallic substrate at the respective interfaces (Kothiyal et al., 2008). There are two promising techniques and materials that have generated a lot of interest among researchers. They are brazing and soft glass.

6.2.1 Brazing

Brazing is a method that can be used for joining ceramic to metals. Basically, it requires a brazing alloy that contains some reactive elements which can alter the ceramic faying surface to improve its wettability by the molten braze and adherence on solidifying. Brazing is the joining of two parts by an intermediate/filler metallic material, usually an alloy of lower melting point, which melts and wets the surfaces being joined, reacts and solidifies on cooling. The filler material is heated above its liquidus temperature and will flow and fill the gap between the two joining pieces. Typical alloys include Ti-Au-Cu or Ni-Ag-Cu (Velterop, 1992). Because melted metal does not easily wet the surface of ceramics due to incompatibility of surface tension, it is difficult to obtain a gas-tight seal using this technique. (Singh et al., 2008) has listed the key parameters for successful implementation of this technique as:

1. Wettability of molten braze on the metal coated ceramic substrate
2. Adhesion of molten braze on metal coating upon solidification
3. Resistance of braze to chemical attack from reactor processes
4. Resistance to thermal stress induced by temperature changes and difference in the CTE of the braze filler and the metal oxide membrane.

Among the brazing techniques that can be used for ceramic to metal joining techniques is use of solder/brazing alloy for establishing bonding between metallized ceramic and the metal it is to be joined to. This technique has been used to join alumina to Koval/Stainless Steel using the well-established but more expensive so called Moly-Manganese (Mo-Mn) process developed in German during World War II (Twentyman, 1975) which requires vacuum metallization of the ceramic component at the faying surface first.

Another form of brazing is active brazing without the intermediate and expensive metallization process but still needs vacuum or inert conditions (Kothiyal et al., 2008). In this method, titanium is used as an active component in the brazing material made of CU, Au, Ag and Ni and their alloys through the formation of TiO or Ti_2O_3 which has been known to facilitate wetting of the alumina by the molten braze.

A recently developed brazing technique is the Reactive Air Brazing (RAB) technique designed to be done in ambient air in contrast to moly-manganese process (Kuhn et al., 2009), which is an emerging technology to braze ceramic-to-ceramic and ceramic-to-metal joints. Here the brazing material consists of noble metals such as silver and other metals for in situ oxidation e.g. copper. At the brazing temperature the copper oxidizes in the melted braze and facilitates the wetting of the ceramic by the melted braze. However, the mechanisms of wetting can vary depending on substrate composition (Bobzin et al., 2010).

Solidus temperatures higher than 930^{o}C are possible with this type brazing permitting high temperature applications such as high temperature membranes or solid oxide fuel cells. The noble metals provide good ductility, strength, high corrosion and oxidation resistance. The disadvantage of this RAB is use of noble metals which are expensive.

6.2.2 Metal O-rings

Another possible technique is the use of relatively inert metals such as silver and gold in a configuration similar to the well-known rubber O-rings. In this technique, the metal O-ring is placed in the joining gap between the ceramic membrane and the metallic support framework. The gas-tight seal is achieved by exerting a compressive force on the metal ring. The difficult with this approach is that due to the brittleness of the ceramic membrane the exerting force may cause the membrane to crack and fail (Qi et al., 2001). In addition, in practical industrial application the metal rings may be prohibitively expensive.

6.2.3 Soft Glass

The third alternative is the use of glass as a seal. Glasses are versatile material and are one of the oldest as well as newest materials to find a variety of uses in everyday life. Their applications range from the ordinary drinking glass (old) to the extraordinary optical fibre cables (new) in the communication industry. It has also found application as a joining material with other materials. That glass, under suitable conditions, will bond well to a wide variety of metals and alloys has been recognised for quite some time (Donald et al., 2008). The main limitation of this, however, is that these are low temperature applications. Glass/metal joining, for example, dates back to the invention of the electric light bulb in the early 1800s. This type of joint was improved between 1950 and 1970 and is now largely employed in the electronic industry as well as the manufacture of medical equipment. The concept of sealing material consisting of a glass matrix has been used in the sealing of high temperature halogen lamps**,** in radio tubes, encapsulation of various electrical, electronic and opto-electronic devices**.** In recent years, glasses, in wider compositions, have been designed to have unique properties for many scientific and engineering applications which are yet to find commercial application. Other advantages of glass are its viscosity, flowability and melting characteristics that can be controlled over a wide range of temperatures. Their adherence to ceramics is usually quite good. These properties make glasses potentially suitable for applications that require ceramic-ceramic joining. A more recent application still under development is use of glass or glass-ceramics in sealing Solid Oxide Fuel Cells (SOFC) to keep the fuel and air supplies hermertically separated owing to their resistance to oxidation, stability at elevated temperatures, electrical insulation, corrosion resistance mechanical strength and hermeticity properties (Gross et al., 2006). Leakage between the air and the fuel side of the cell will drastically reduce the efficiency of the fuel cell. Similarly, in the present work, leakage between the chambers separated by the membrane will allow air to leak from the air side to the permeate side, negating the whole purpose using the membrane. As fuel cell development is mainly centred on Yttria Stabilized Zirconia (YSZ) as the electrolyte, the seal is commonly between YSZ and SOFC components such as metallic interconnects made from other material such as stainless steel. The main requirements for SOFC seals include (Eicher et al., 1999, Caron et al., 2008, Weil et al., 2004):

1. Hermetic seals with less than 10^{-7}mbar s^{-1} per centimetre leakage
2. Long term chemical stability under simultaneous reducing and oxidizing environments
3. CTE well adapted to the components being joined
4. Long term resistance to degradation from thermal cycling
5. Low cost
6. Electrically resistivity of greater than 2 kilo-ohm
7. Sufficient fluidity at operating temperature to fill gaps.

While there are a lot of similarities between sealants for SOFC and those for high temperature membrane reactors for oxygen separation, there are a few differences. While SOFC sealing is usually between YSZ and metal interconnects, in the current work, the seal is required between a dense LSCF6428 perovskite disc and stainless steel. In SOFC application, the solid dense YSZ electrolyte only conducts oxygen ions when in operation and requires that the sealing material has high electrical resistivity to prevent it short circuiting the cell and impair the performance of the Fuel Cell. The whole idea of a fuel cell is to generate current flow through an external load, rather than through the solid electrolyte. In the current work the LSCF6428 membrane is a mixed ionic and electronic conducting material and conducts both oxygen ions and electrons under operational conditions. As the membrane is already intrinsically, electronic conducting, electronic conductivity of the sealant is not a limitation. There are few, if any, reports on the performance of glass based sealants on MIEC perovskite membranes on metal substrates, making this concept novel in this respect.

From a considerable amount of literature survey conducted under the current work, it has been generally observed that the majority of developers of sealants for SOFC applications are not keen to disclose their exact sealant material compositions. There are also hundreds of US Patents registered since 1984 (Wei, 2008). The compositions of most patented inorganic glasses cited in US and Japan are silicate glasses. Other systems reported widely in literature are borates, borosilicates (Qi et al., 2001) and phosphates (Larsen and James, 1998).

Several attributes make glasses attractive as potential materials for high temperature sealants. They have been listed by (Weil, 2006) and (Meinhardt et al., 2008) as:

1. They are generally inexpensive.
2. They tend to exhibit good stability under both reducing and oxidizing environments.
3. They exhibit good wetting behaviour on sealing surfaces (ceramics and stainless steel.
4. It is possible to engineer their coefficient of thermal expansion (CTE) to match or nearly match those of materials being joined.

However these authors have not offered any explanation under which glass can bond to stainless steel.

For a seal to remain hermetic, it must exhibit strong bonding at the interface with the materials being joined. In addition, the coefficients of thermal expansion of the sealant and adjoining materials must match to avoid stresses, especially tensile stresses, being exerted on the sealant which might result in loss of hermeticity due to cracks. However, matching coefficients of thermal expansions, though possible through varying chemical composition of the glass, is no easy task. An alternative is design of a compliant or self-healing glass sealant proposed by (Singh, 2007).

Seal self-healing phenomenon enables the sealant to help alleviate loss of hermeticity due thermal expansion mismatch of materials being joined. The rationale behind this is that at operating temperature, a sealing glass with appropriate properties can become viscous and can flow into cracks created during thermal transients due to differences in thermal expansions of materials joined (Singh, 2007). When the seal is subjected to thermal cycling during routine operation, it can develop micro-cracks due to even a modest thermal expansion coefficient mismatch with adjoining components (Meinhardt et al., 2008). A compliant seal is able to heal such cracks when the temperature is raised again to operating level where it becomes soft and its viscosity becomes sufficiently low that it flows and able to close the micro-cracks (Liu et al., 2010). The viscosity and softening point of glasses can be tailored by varying the glass compositions, (Wei, 2008).

6.2.4 The chemistry of glasses

It is desirable to have some understanding of the chemistry of glasses and how their physical and chemical properties, in respect of their use as sealants in the present work, may be influenced by their chemical composition. This section provides an overview of glasses and the roles of the various constituents in glass formation and in defining their physical, thermo-chemical and thermo-mechanical properties.

6.2.4.1 Formation of glass

Glass is an amorphous solid material characterised by atomic spatial disorder in which the molecules or atoms do not exhibit three dimensional periodicity and long range order as obtaining in crystalline solids. Solid glass is essentially a non-crystalline solid obtained when hot liquid glass is cooled too rapidly for the atoms in it to arrange themselves in an orderly manner (crystallize). The difference between solid glasses and liquids is that in liquids, atoms can move past one another, whereas in solid glass, atoms do not have adequate thermal energy to travel about the material. The boundary between liquid glass and solid glass is the glass transition temperature, T_g. In its random amorphous state, below T_g, glass is thermodynamically metastable and it would prefer to rearrange its random structure to a more thermodynamically (lower free energy) stable crystalline structure (Chou et al., 2011) if the atoms had enough mobility to do so. In theory, even at room temperature and over geological timescales, glass eventually crystallizes to form glass-ceramic (Richerson, 1992, Axinte, 2011). The crystallization rate at such temperatures is so slow for most commercial glasses that for practical purposes, it is zero (Freiser, 1975). Crystallization can be speeded up by raising the temperature to a level at which atomic mobility is increased to enable them to reorganise themselves into a thermodynamically more stable crystal structure. Above T_g, it becomes soft and viscous, and under other suitable conditions that drive crystallization kinetics, e.g. presence of nucleating agents (Zhu et al., 2007), it can rapidly crystallize into various crystalline phases that depend on a combination of factors such as the original glass composition.

6.2.4.2 Glass compositions

A glass matrix is a multi-component oxide system generally containing four types of constituents which all contribute to give a particular glass its properties (Mahapatra and Lu, 2010a):

1. One or several network forming oxides,
2. One or several network modifying oxides,
3. One or more intermediate oxides, and
4. One or more additives.

Glass has two types of oxygen in it, bridging and non-bridging oxygen. A schematic of glass structure showing network formers, modifiers and intermediate oxides is shown in *Figure 6-1*.

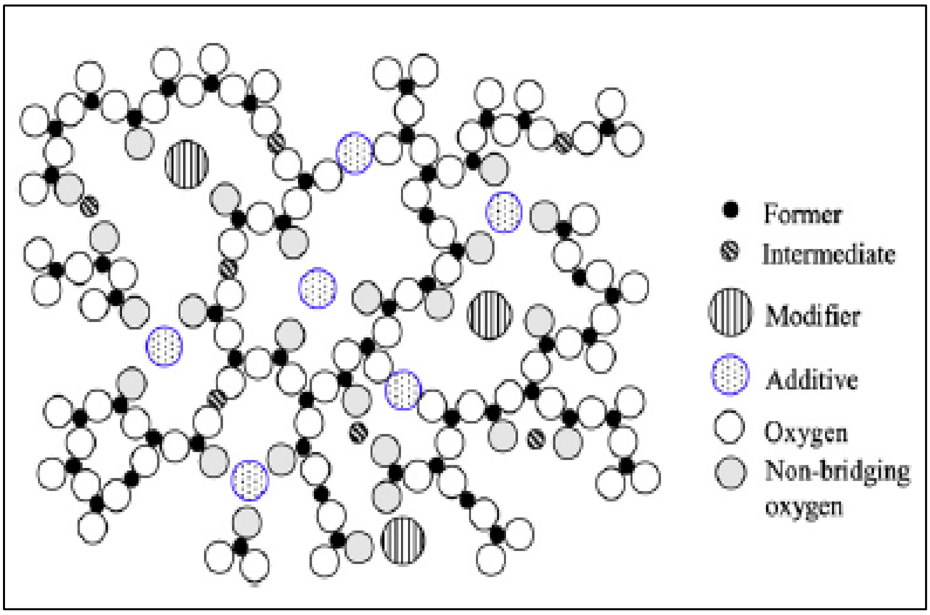

Figure 6-1 Schematic showing glass structure (Mahapatra and Lu, 2010a)

The key aspects regarding glass structure are network connectivity and homogeneity and they directly affect the thermal properties of the glass. Connectivity in a glass structure is described by the number and arrangement of bridging and non-bridging oxygen atoms which link the structural units to their neighbours. If a glass has high connectivity, it is likely to have a high glass transition temperature and high resistance to devitrification and conversely, a glass with low connectivity is likely to have a lower glass transition temperature and to readily devitrify. Increasing non-bridging oxygen content decreases glass connectivity. Glass homogeneity is directly related to the distribution of different structural units; formers, modifiers, intermediates and additives (Lu and Mahapatra, 2008).

6.2.4.2.1 Network formers

Network formers include SiO_2, B_2O_3 and P_2O_5 among others. Silicon dioxide (SO_2, or silica, as it is also called, is the glass former that has been mostly used in commercial glass applications as well as the development of glass seals for SOFC, owing to its higher chemical resistance and minimum interaction with other cell components.

Silica is held together by covalent bonds, even in its molten state as a liquid. Covalent bonds are highly directional. The chemical formula of silica, (SO_2), gives a rather simplistic view and shows only atoms associated with each silicon atom. Actually, each silicon atom forms covalent bonds with four oxygen atoms and orients those atoms at roughly the corners of a tetrahedron. Each oxygen atom in the silica forms covalent bonds with two silicon atoms and orients them at roughly two corners of a tetrahedron as well. Thus silica possesses a polymeric character consisting of an intricate network of silicon and oxygen in which each oxygen atom acts as a bridge between two adjacent silicon atoms (Si-O-Si bridges). Alternatively its structural framework can be viewed as being built of SiO_4 tetrahedra joined together by common oxygen atom situated at the corners of the tetrahedral. This interlinking structure gives silica its network former properties. These inter-linkages in the silica network can be modified by addition of network modifiers.

6.2.4.2.2 Network modifiers

Network modifying oxides are not capable of building glass networks (Mahapatra and Lu, 2010b). Common network modifiers are alkali oxides such as Na_2O, Li_2O and K_2O) and alkaline earth oxides such as BaO, SrO, MgO and CaO, (Mahapatra and Lu, 2010a) and rare earth metal oxides or mixtures thereof. If a network modifier is introduced into a glass, e.g. Na_2O into SiO_2, some of the bridging oxygen atoms are converted into non-bridging atoms. The network modifiers occupy random positions in between the polyhedra and provide additional oxygen ions to modify the network structure, (Mahapatra and Lu, 2010a). The replacement of a covalent bond between Si and O by an oxygen ion and Na^+ cation is the structural change that shortens the effective average chain length resulting in changes in properties of the glass. The effect of Na_2O in disrupting silica chains is illustrated below.

$$\text{-Si-O-Si-} + Na_2O = \text{Si-O}^-Na^+ + Na^{+}\,{}^{-}\text{O-Si-}$$

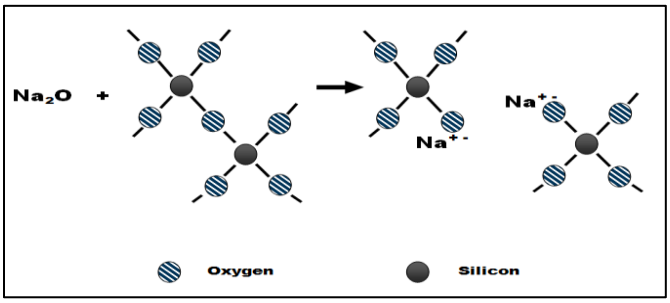

Figure 6-2 Sodium oxide modifier effect on glass chain structure, breaking the silica long chains into shorter ones.

Unlike in pure silica where the number of oxygens is twice the number of silicons, when Na_2O is fused with SiO_2, the number of oxygens is more than twice the number of silicons and some of the oxygens are bonded to only one silicon to form a non-bridging oxygen (NBO). With each NBO there is an associated negative charge which is counterbalanced by a positively charged sodium cation as illustrated in *Figure 6-2*. The introduction of Na_2O has the effect of altering the properties of the glass.

The atoms in pure silica are bound together by very strong covalent bonds that its melting point is high, about 1700^oC. However, when fused with a network modifier such as Na_2O, the melting point of the resulting glass is markedly reduced. The reason for the lower melting point of the soda (Na_2O) – silica (SiO_2) glass is because sodium ions disrupt the network structure, breaking long silica chains into shorter ones. This changes some of its physical properties, e.g. lowering the temperature of its liquidus as well as its viscosity. Modifiers also affect other physical properties such as viscosity, thermal expansion, density, refractive index, chemical durability. Also due to small ionic radius, Na^+ has higher ionic mobility. In addition, due to high solubility of Na_2O, soda glass tends to dissolve in water. Mixing of CaO with silica (to form lime-silica), instead of Na_2O has the same effect but the resultant glass is much more durable but less soluble, because calcium oxide, although ionic just like sodium oxide, is not as readily soluble in water as sodium.

6.2.4.2.3 Intermediate oxides

There are some chemical compounds that are intermediate between glass formers and modifiers and in glass chemistry they are known as intermediate oxides. On their own don't form glasses, but they may participate in the glass network. Depending on glass composition, an intermediate oxide behaves like a glass former if it participates in a glass network. Alumina (Al_2O_3) is a commonly used and an important intermediate oxide in glass based seal development. In silicate glasses, aluminium atoms from Al_2O_3 substitute for silicon in silica polyhedra chains to become part of the chain and stabilize the network. It also has the effect of improving flux, increases chemical durability and retards crystallization of glass.

6.2.4.2.4 Additives

Additives are compounds that can be added to tailor some properties of glasses. Rare earths metal oxides such as La_2O_3 and transition metal oxides such as TiO_2, ZnO and NiO are some of the materials that can be used as additives in glasses (Mahapatra and Lu, 2010b). When added in amounts of ≤ 10 mol%, in glasses, they function as nucleating agents which can tailor glass properties by influencing devitrification. ZnO, NiO, TiO_2, Cr_2O_3 and ZrO_2 are common nucleating agents that have been used in developing sealants for SOFC, (Mahapatra and Lu, 2010a).

The ability of glasses to chemically accommodate metal oxide as intermediate or additive oxides in their structures is important in understanding how glass can bond to metal substrates with oxide layers on them as will be seen in later sections. The following section describes experimental work in use of an inexpensive glass composition, sodalime glass (SLG) to seal dense LSCF6428 membrane to 304 Stainless Steel (304SS) holder.

6.3 SLG bonding to 304SS and dense LSCF6428: Experimental

Sodalime glass (SLG) bonding characteristics to stainless steel and LSCF6428 were investigated. Broadly, the sealing experiments involve preparation of metal and ceramic parts, grinding of SLG to fine powder and making a paste with it in Polyethylene glycol (PEG), applying SLG paste onto surfaces, loading into a furnace and applying a furnace heating schedule to melt the glass and cool.

6.3.1 Bonding of SLG on stainless steel (304SS)

Two 304 stainless steel (304SS) coupons (discs) of 25mm diameter and 2mm thickness were machined and subsequently degreased to remove any oil films on the surface by immersing them in boiling NaOH solution for an hour. This was followed by thorough washing and rinsing in de-ionised water and drying overnight in an oven set at 60^{o}C. One of the coupons was further heat treated in a Lenton box furnace in air at 800^{o}C for one hour. This step was to facilitate surface modification by formation of a thin oxide layer on the coupon surface.

After cooling, on each coupon a 1mm layer of milled SLG powder paste in PEG was applied on the surface. The coupons were placed in an oven and heated slowly from room temperature to 500^{o}C at a heating rate of 2^{o}C/min and dwelled at 500^{o}C for 90 minutes to burn out all the organic material and leave behind SLG. The temperature was increased to 1030^{o}C at a heating rate of 5^{o}C and dwelled for 30 minutes to allow the SLG to melt and wet the coupon surface. The coupons were allowed to cool to room temperature.

6.3.2 Bonding of SLG on LSCF6428

A layer of SLG paste in PEG was similarly applied on a 25mm diameter, 1mm thick dense LSCF6428 membrane and heat treated in air to 500^{o}C before temperature was increased to 1030^{o}C. In fact this step was carried out simultaneously and in same furnace with 304SS coupons.

6.3.3 Bonding experiment results

It was observed that the SLG melt readily delaminated from the 304SS coupon whose surface had not been modified by (pre-oxidation) *Figure 6-3* (a) while for the pre-oxidized the SLG melt was very strongly bonded *Figure 6-3*(b). The SLG bonded pre-oxidized 304SS and SLG bonded dense LSCF6428 were further studied using SEM. During preparation for SEM examination, the pre-oxidised 304SS-SLG couple was subjected to grinding and polishing, but the glass layer did not detach from the 304SS disc as can be seen in *Figure 6-3* (b), indicating strong bonding. In the case of LSCF6428, SLG also bonded very strongly. The ability of SLG to bond much more strongly to pre-oxidised 304SS compared non pre-oxidised 304SS confirms that the existence of an oxide layer on the metal surface plays a big role in bonding glass to metal.

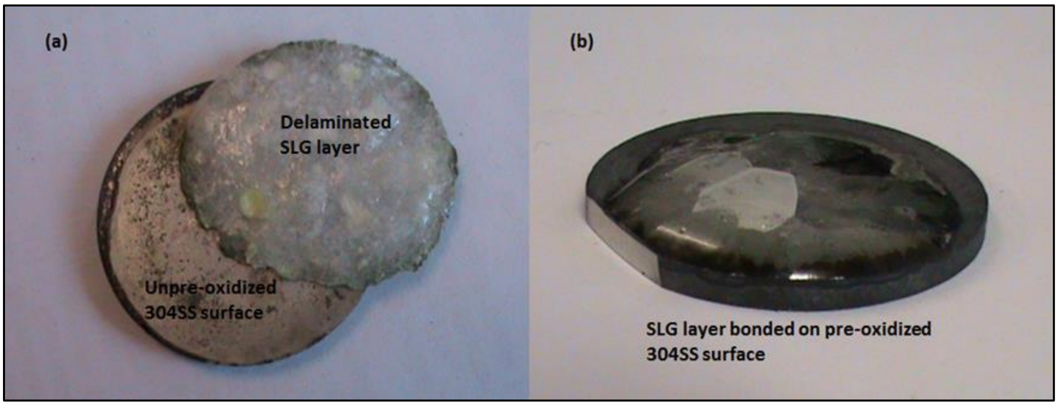

Figure 6-3 (a) SLG and un-pre-oxidized 304SS, (b) SLG and pre-oxidized 304SS

6.3.3.1 SEM Characterization of 304SS-SLG and SLG-LSCF6428 interfaces

SEM examinations were carried out on the pre-oxidized 304SS-SLG interface layer as well as the LSCF6428-SLG interface layer in order to elucidate the nature of the bonding and to record the concentration profiles across the interfaces. The results of the SEM examinations are shown in the SEM micrographs in *Figure 6-4* and *Figure 6-5* .

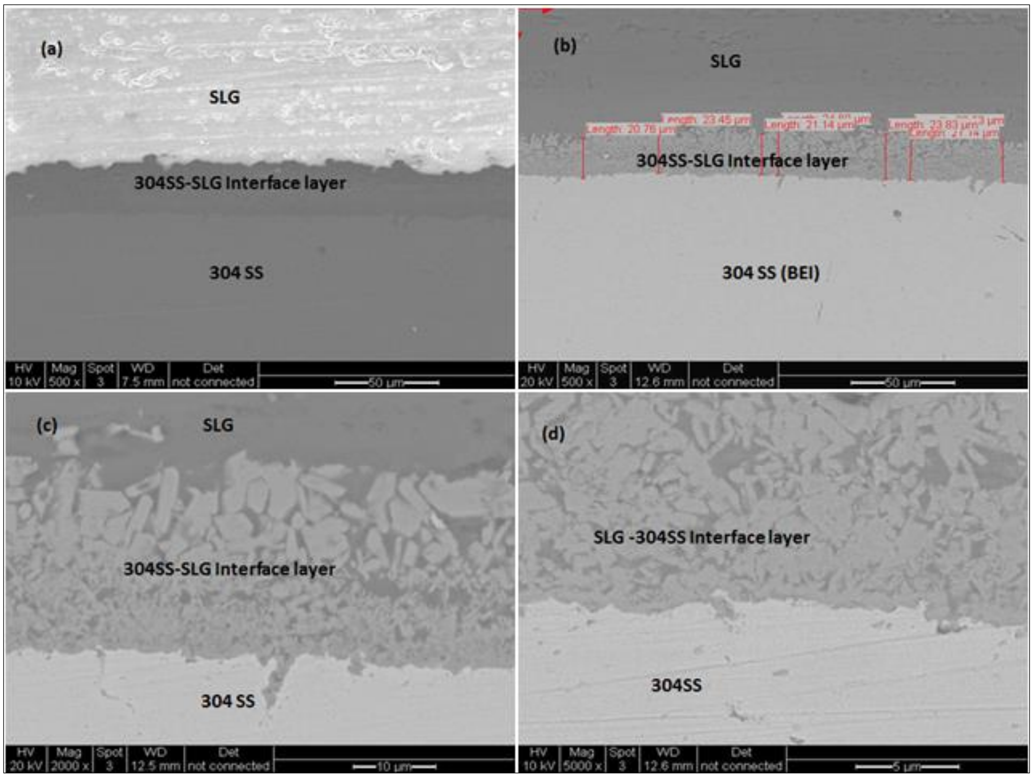

Figure 6-4 SEM micrographs of SLG-304SS interface at different magnifications: (a) x 500, (b) x 500 Backscattered Electron Image (BEI) showing interface layer thickness, (c) x 2000 BEI and (d) x5000 BEI

The SEM images show good adhesion of SLG to both membrane material (LSCF6428) and stainless steel (304SS) with no noticeable crack or delamination. Examinations on the interfaces at higher magnifications also show no noticeable continuous porosity that could result in leakage. These results show very good adhesion between SLG and LSCF6428 surface on the one hand, and SLG and 304SS surface on the other. The micrographs show that the 304SS-SLG joint has an average of 20µm thickness, while that of SLG-LSCF6428 had a thickness of about 2µm. The 20µm thickness of SLG-304SS interdiffusion may be an indication that the stainless steel might have been over pre-oxidized. Previous studies by (Yext et al., 1983) reported that an optimum of 2-10µm is required to achieve a high quality junction between glass and metal. The thickness of this interdiffusion layer is governed by the depth of the oxide layer formed on the stainless. This depth can be controlled by soaking time and or temperature during heat treatment in air.

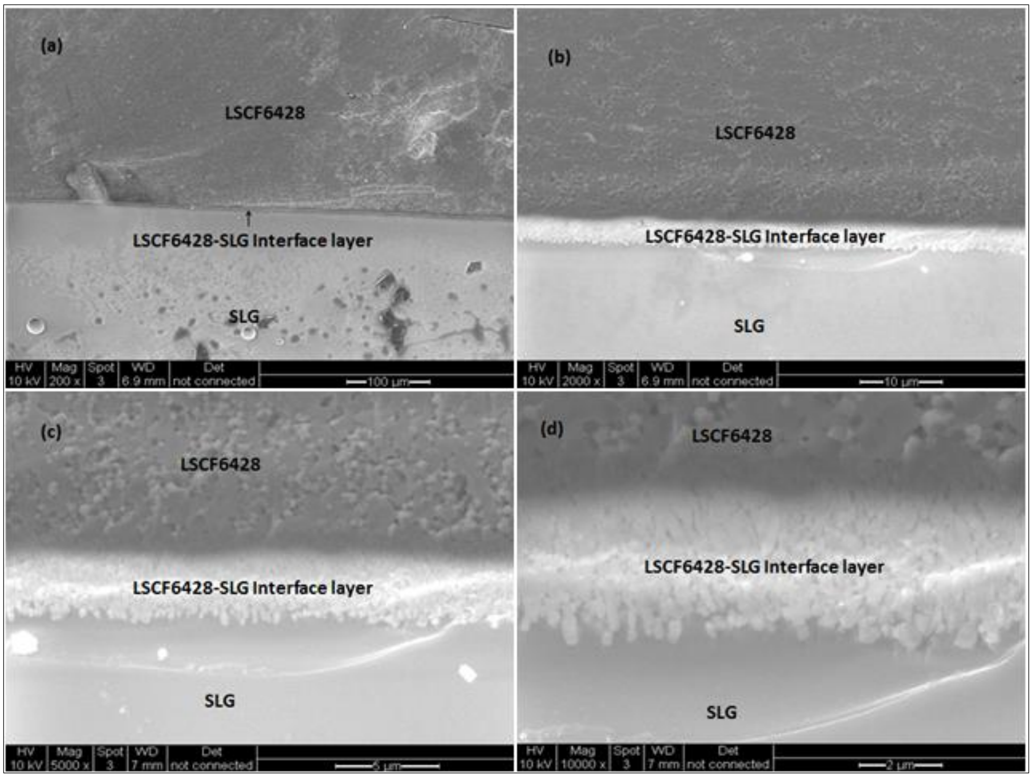

Figure 6-5 SEM micrographs of SLG-LSCF6428 interface at different magnifications: (a) x 200, (b) x 2000, (c) x 5000 and (d) x10000

These results have demonstrated that surface pre-oxidation of 304SS to form an oxide layer is effective to achieve interface adhesion between stainless steel and the sodalime glass.

These metal-glass bonding experiment results can be explained in terms of the different electronic structures in metal, metal oxide layer, glass and ceramics. Ceramics and glasses in general have covalent or ionic bonding while metals have metallic bonding. This metallurgical difference inhibits the formation of strong bonds at the metal-glass interface. For pre-oxidised 304SS, strong metal-glass bonding is possible because of the existence of a thermodynamically stable transition layer in the interfacial zone that is compatible with both the ionic-covalent bonded glass sealant and the metallic bonded substrate present in the interfacial zone (Tomsia and Pask). As explained by (Hong and Holland, 1989b, Hong and Holland, 1989a, Calata et al., 2001, Donald, 1993), the reaction of the metal oxide and glass at the interface provides a continuous structural transition from metallic bonded substrate to the essentially ionic-covalent bonded glass. The effect of the oxide layer is that it avails a phase that is soluble in both metal and glass, a transition zone in which the metallic bond in the metal bulk is gradually substituted by the ionic-covalent bonding in the glass.

In **Section** 6.2.4.2.4 it is mentioned that in manufacture of glasses some metal oxides can be deliberately added as additives to the main glass components, network formers and modifiers, to achieve some required properties in the glass. This shows that glass can chemically accommodate some metal oxides in their structures resulting in the ability to chemically bond with metal substrates with metal oxide layer on them. During the sealing procedure, the molten glass readily wet and diffuses into the metal oxide layer to form a strong chemical bond.

Without the oxide layer, the equilibrium between metal and glass is difficult to achieve because of different electronic structures and the glass sealant would be in direct contact with the metal and possibly resulting only in the much weaker van der Waals type of bonds. This explains why in the case of unpre-oxidised 304SS, the sodalime glass delaminated from the 304SS disc as shown in image in *Figure 6-3* (a). The bonding was the weaker van der Waals forces. *Figure 6-6* and *Figure 6-7* illustrate the role of the oxide layer in metal-glass bonding and how the absence of the oxide layer results only in van der Waals forces which are not strong hence the delamination (Pask, 1977). Alternatively, the bonding mechanism can be explained in terms of two distinguishable systems, non-reactive system and reactive system. A non-reactive system is where no new phase is formed at the interface such as the unpre-oxidised 304SS, and therefore only weak van der Waals forces, while a reactive system results in a new phase involving strong chemical bonds such as the use of pre-oxidised 304SS (Treheux et al., 1994).

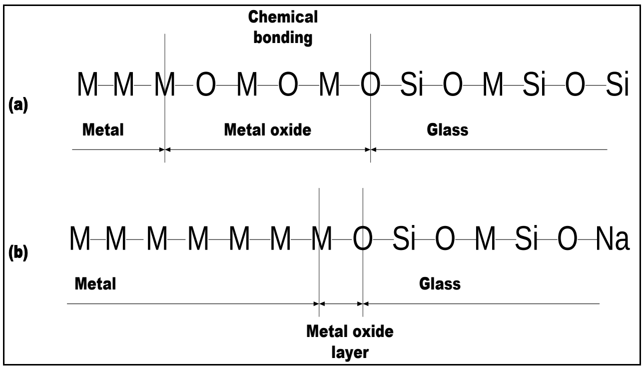

Figure 6-6 Schematic showing the role of a metal oxide layer in strong chemical bond between glass and metal substrate (a) a relatively thick metal oxide layer, and (b) a relatively thin metal oxide layer; (adapted from (Pask, 1977))

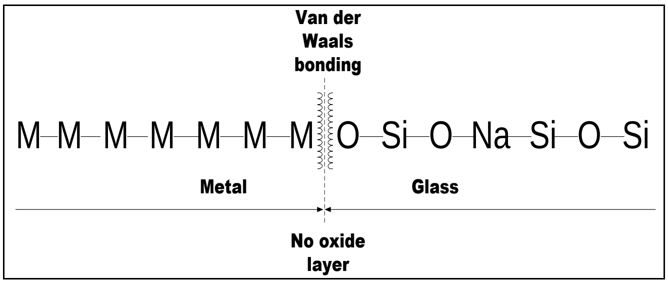

Figure 6-7 Schematic showing how the absence of a metal oxide layer results in weak van der Waals forces between glass and metal substrate (adapted from (Pask, 1977)).

6.3.3.2 EDS Characterization of SLG-304SS and SLG-LSCF6428 interfaces

Further examination of the SLG-304SS interface by EDS showed that the chemical composition of the layer contained chemical elements from both the sodalime glass and 304SS while that of the SLG-LSCF6428 showed chemical elements of SLG and LSCF6428. EDS analysis of 3 randomly selected points on the interface layers between LSCF6428-SLG and between 304SS-SLG show detection of a good mix of elements in LSCF6428 and SLG for the former and of 304SS and SLG for the latter in proportions that suggest there was inter-diffusion between the couples. The slight variation in atomic ratios indicates the non-homogeneous nature of the interface, but these results to a large extend indicate that the two materials SLG and 304SS on one hand, and SLG and LSCF6428 on the other, “dissolved” into each other.

The results of the EDS and SEM analyses of the interface layers are as shown in tables and figures as follow:

Table 6-1 and *Figure 6-8* show the results of EDS of sodalime glass on its own. In particular *Table 6-1* shows SLG elementary composition from 3 random points on SLG on its own. The composition of SLG from the EDS analysis is Na (7.72%), O (61.07%), Ca (1.65%), Si (25.36%), Al (2.31%), K (0.99%), Mg (1.06%) and Ba (0.50%).

Table 6-1 SLG spectra

EDX spectra of sodalime glass (SLG)								
Element	Na	O	Ca	Si	Al	K	Mg	Ba
Point 1*	8.5%	58.5%	1.7%	26.2%	2.3%	1.09%	1.3%	0.6%
Point 2	7.6%	62.2%	1.7%	25.6%	2.4%	0.99%	1.1%	0.5%
Point 3	7.1%	62.5%	1.6%	24.4%	2.2%	0.89%	0.9%	0.4%
Average	7.7%	61.1%	1.7%	25.4%	2.3%	1.0%	1.06%	0.5%

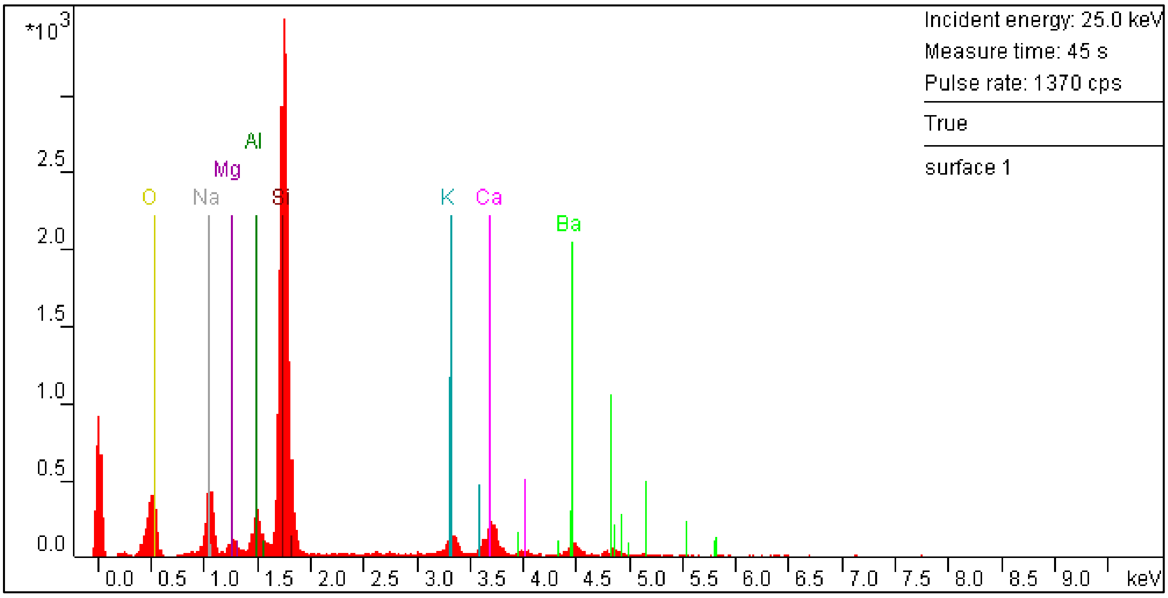

Figure 6-8 EDX spectra of sodalime glass (SLG)

Table 6-2, Figure 6-9 and *Figure 6-10* show the EDS (*Table 6-2* and *Figure 6-9*), and SEM (*Figure 6-10*) of the sodalime glass-stainless steel (SLG-304SS) interface. The EDS spectra shows elemental diffusion of SLG constituents and 304SS constituents across the interface, showing sodalime glass and the stainless steel dissolved into each other and formed strong bond between the two materials.

Table 6-2 SLG-304SS

Glass-Metal Interface EDX										
Element	Fe	Cr	Ni	Si	Na	Al	K	Ca	O	Mg
Spot GM1	20.1%	11.6%	3.2%	10.9%	10.3%	1.1%	0.5%	0.6%	41.7%	0.0%
Spot GM2	31.4%	5.3%	1.4%	9.6%	10.7%	1.1%	0.4%	0.7%	39.5%	1.3%
Spot GM3	20.7%	7.1%	4.4%	10.1%	8.9%	1.0%	0.4%	0.5%	45.5%	1.5%

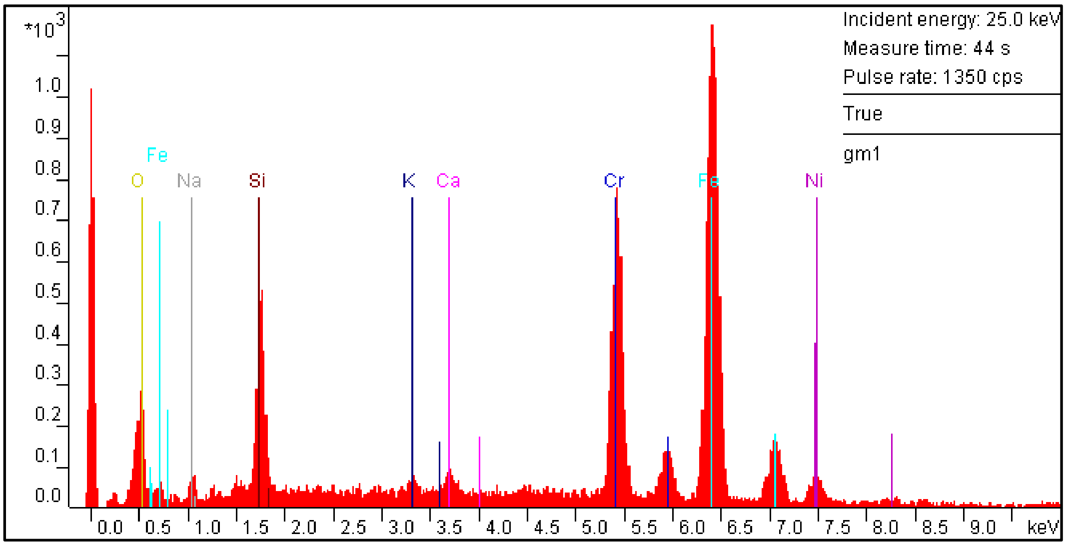

Figure 6-9 SLG-304SS interface EDS spectra

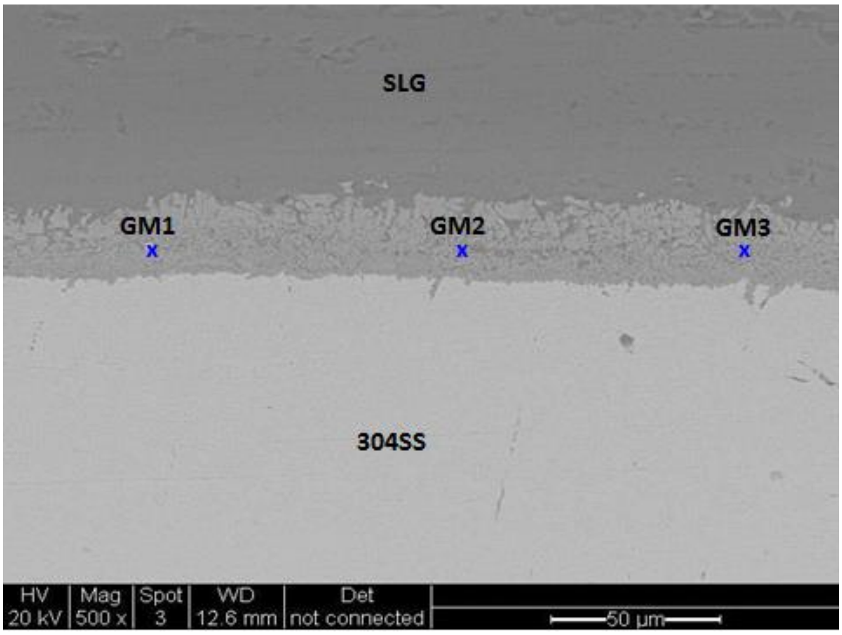

Figure 6-10 Back scattered Image SLG-304SS interface image

Table 6-3, *Figure 6-11* and *Figure 6-12* show the EDS analyses results (*Table 6-3* and *Figure 6-11*), and SEM (*Figure 6-12*) of the sodalime glass- ceramic (SLG-

LSCF6428). The EDS spectra shows elemental diffusion of SLG constituents and LSCF6428 constituents across the interface showing the sodalime glass and the ceramic dissolved into each other and formed strong bond between the two materials.

Table 6-3 SLG-LSCF6428

GLASS-CERAMIC INTERFACE										
Element	**Na**	**O**	**La**	**Fe**	**Co**	**Sr**	**Ca**	**Al**	**K**	**Mg**
Point GCER1	7.2%	67.9%	6.4%	0.5%	2.2%	1.7%	10.2%	1.7%	0.0%	0.0%
Point GCER2	6.3%	70.8%	5.6%	0.4%	1.9%	1.4%	10.1%	1.5%	0.3%	0.0%
Point GCER3	8.5%	61.2%	7.4%	0.6%	2.4%	1.9%	11.7%	1.6%	0.6%	1.7%

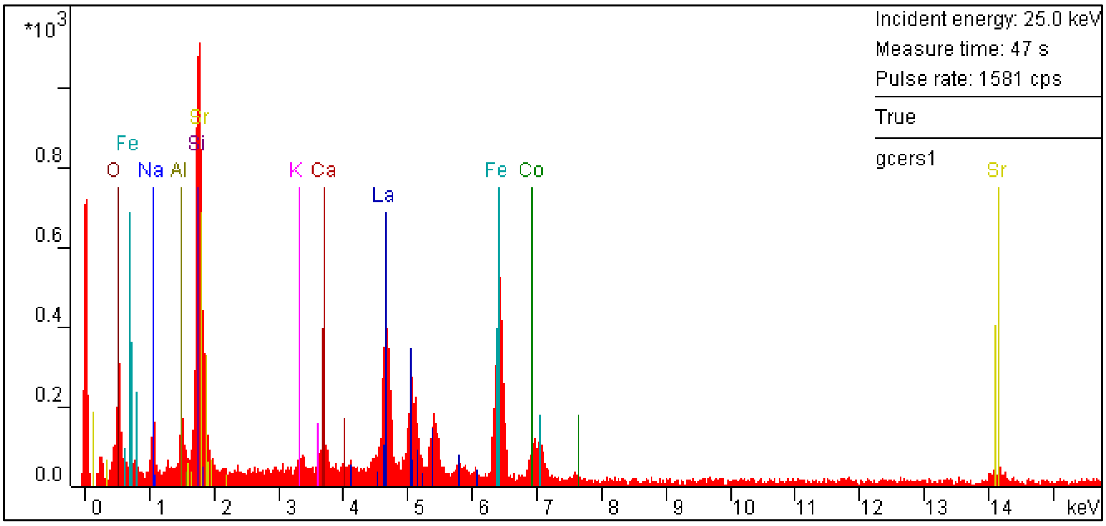

Figure 6-11 SLG-LSCF6428 interface EDS spectra

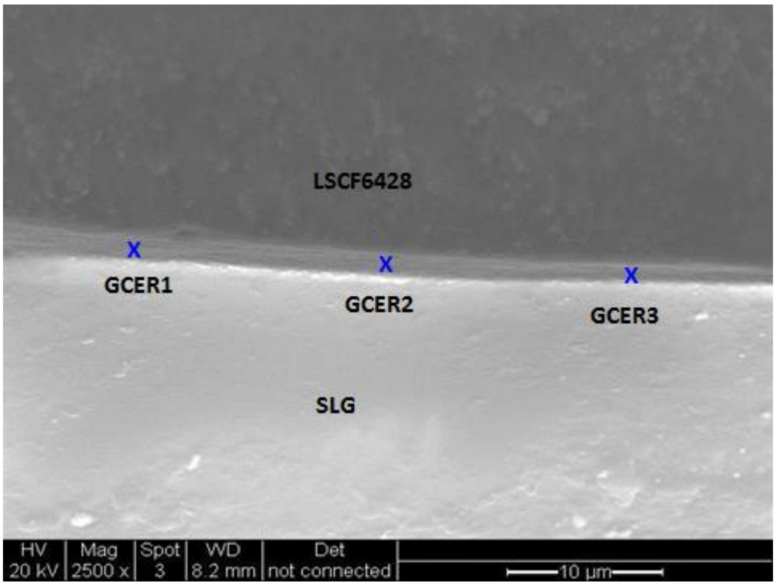

Figure 6-12 SLG-LSCF6428 Interface SEM

6.4 Leakages

In SLG-304SS bond, a strong adhesion can be expected as long as an oxide layer remains on the interface. For a good bond, the thickness of the oxide layer has to be optimal. The metal oxide is dissolved into the glass up to its saturation point at which point the system is in equilibrium. If the oxide layer is too thin the adherence may be weak. If, on the other hand, the oxide layer is too thick, the adherence of the glass to the metal will also become weak and leakage may occur along the interface between the oxide and metal (Hull and Burger, 1934, Freiser, 1975). (Kothiyal et al., 2008) have proposed that the optimum thickness of the oxide layer for achieving a high quality junction is 2-10µm. In the present work, the SLG-304SS interface layer is 20**µ**m which might explain the level of air leakage into the permeate side during permeation experiments.

In addition, permeation experiments conducted with the membrane reactor designed in the present work was initially intended to be carried out at around 800^{o}C, but owing to Health and Safety issues and other limitations of the equipment, a maximum operating temperature 650^{o}C was allowed. This temperature was probably too low for the glass seal to self-heal, hence a considerable amount of leakage was observed in permeation experiments discussed in the next chapter. Although SEM analysis discussed earlier show good bonding after sealing and cooling, when in operation, the thermal expansion mismatch problem may have come into effect and because the operating temperature was well below the glass soft point at which the glass become viscous and flow to repair cracks, self-healing did not come into effect and therefore the leakage observed. Significant leakage greater than oxygen flux was observed through the membrane module.

Chapter 7 : **OXYGEN PERMEATION EXPERIMENTS AND RESULTS**

7.1 Introduction

Oxygen permeation rates using planar LSCF6428 membranes were measured using the apparatus shown in *Figure 4-9*. The inlet gas flows were controlled by Bronkhorst Mass Flow controllers. Air was fed into the air side chamber of membrane reactor at 30mL/min. The permeate side sweep gas or gas mixture was fed into the permeate side at a flow rate of 30mL/min. The permeation experiments were conducted at ambient pressure for both air side chamber and permeate side chamber and reactor heating controller system was set to heat the reactor to a 650^{o}C. The heat was supplied by four Watlow Cartridge heaters inserted into the block on which the membrane module was fixed. The hot effluent gases were cooled by a water cooled heat exchanger and fed into an online Agilent GC6890N and analysed by a thermal conductivity detector (TCD).

The membrane reactor design details have been provided elsewhere in this thesis (Chapter 4). The key objective of this experiment was to test for oxygen permeation through these membranes under different conditions:

1. Inert conditions with helium as inert gas
2. Reactive conditions with helium diluted methane as sweep gas
3. Reactive conditions with helium diluted carbon monoxide as sweep gas.
4. The effect of CH_4/He or CO/He on oxygen flux.
5. The time dependence of oxygen flux under constant conditions.

The effluent gases from the reactor were analysed using an Agilent 6890N equipped with a TCD detector and calibrated for H_2, CO_2, O_2, N_2, CH_4 and CO. A molecular sieve column with helium as carrier was used for quantitation of O_2, N_2, CH_4 and CO, while a Haysep column with helium as mobile carrier was used to detect and quantitate H_2 and CO_2.

The oxygen content in the permeate side was calculated from concentrations of all oxygen containing species in the permeate side. However, the GC was not configured to detect and measure the concentration of water. In fact any water produced in the reactions was condensed in the heat exchanger. The following assumptions were made in calculating the oxygen consumed in the reaction.

7.2 Permeation under inert conditions (Helium sweep gas)

When pure helium is used as sweep gas, there is no reaction in the permeate side as helium is an inert gas. Any permeated oxygen is swept away as molecular oxygen which is detected and quantitated by the in-line GC. The oxygen flux is computed, and corrected for leakage as explained in Chapter 4, using Eqn 7.1 after correction for leakage.

$$J_{O_2} = \frac{G \times c_{O_2-\mathrm{permeated}}}{A} \qquad \text{Eqn 7.1}$$

where J_{O_2} is the oxygen flux in $\mathrm{mLmin^{-1}cm^{-2}}$ G is the effluent gas flowrate in $\mathrm{mLmin^{-1}}$ and A is the membrane area in $\mathrm{cm^2}$.

Despite the apparent excellent gas-tight sealing observed under room temperature conditions as described earlier, at high temperatures (650^{o}C), a substantial amount of nitrogen, up to 3% concentration in the effluent, was detected by the GC. This suggests there was significant leakage of air into the permeate chamber under such high temperature conditions necessitating the need to correct for this. This leakage is likely to be due to thermal expansion mismatches between the glass, stainless steel and membrane. This also might mean the 650^{o}C operational temperature used was too low for the self-healing property of the glass sealant to kick in. Higher operational temperatures of 800-900^{o}C might be required.

The results obtained with pure helium as sweep gas are shown in *Figure 7-1*

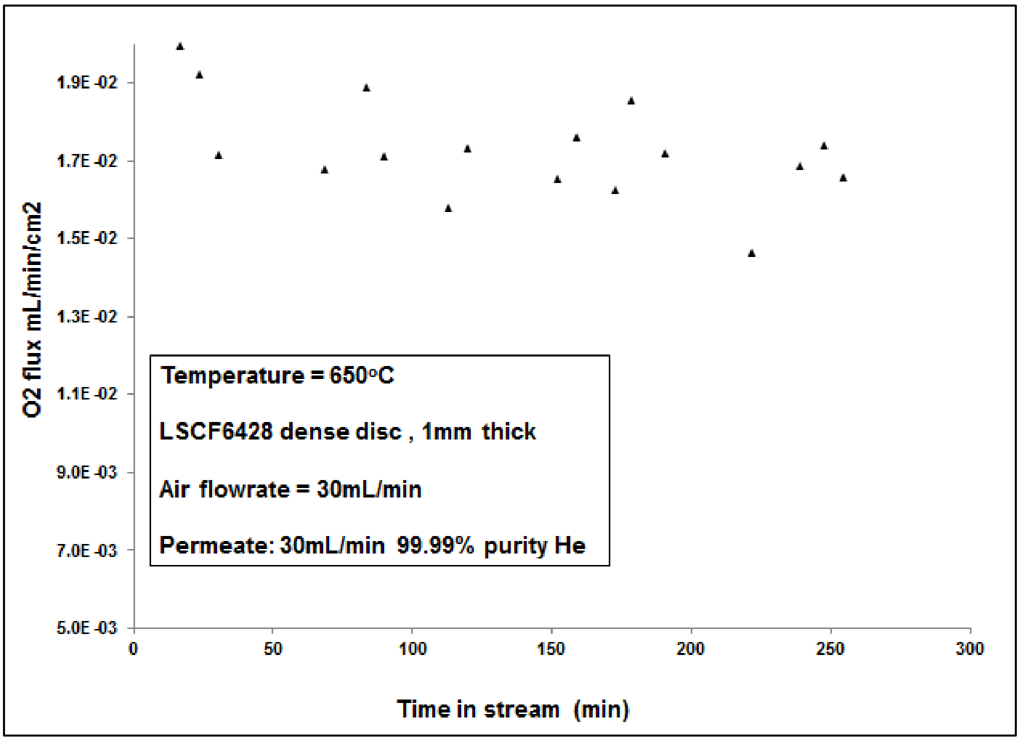

Figure 7-1 Oxygen flux as a function of time under inert conditions

The oxygen flux obtained was about 0.02mLmin^{-1}cm^{-2} as can be seen from *Figure 7-1.*

7.3 Permeation under reactive conditions (Methane sweep gas)

In this experiment 99.99% purity methane supplied by Standard Gas Ltd (UK) was used as permeate side sweep gas, and the detected effluent gases were found to be composed of carbon dioxide (CO_2), nitrogen (N_2), unreacted methane (CH_4) and small traces of oxygen (O_2). This composition of the effluent gases indicates that:

1. The converted methane was fully oxidized to carbon dioxide and water as there were no traces of hydrogen and carbon monoxide detected.
2. The small traces oxygen far below the amount of computed leaked oxygen indicate that some of the leaked oxygen may have also reacted with methane to form carbon dioxide and water.
3. LSCF6428 at 650°C does not show inherently catalytic properties for partial oxidation of methane to hydrogen and carbon dioxide.

The oxygen involved in the permeate side was estimated from the following considerations:

The simplest oxidation mechanism that was assumed is the stoichiometric reaction of deep oxidation of methane given by:

$$CH_4 + 2O_2 \rightarrow CO_2 + 2H_2O \qquad \text{Eqn 7.2}$$

It assumes that the only products of methane oxidation are CO_2 and H_2O which was a reasonable assumption since no H_2 or CO were detected by the GC. From this equation the amount of oxygen consumed is estimated directly from the measured CO_2 concentration without the need to measure water content. The underlying assumption made is that the CO_2 is only coming from methane oxidation and not from anywhere else. This assumption is reasonable since the amount of any CO_2 leaked from air side or from the atmosphere is negligibly very small, given that the concentration of CO_2 in air is 0.03%. The oxygen consumed in deep oxidation of methane is therefore obtained from the reaction stoichiometry in Eqn 7.2 by simply doubling the measured CO_2 concentration in the effluent. From this, the leakage oxygen calculated using nitrogen concentration, was subtracted to obtain the electrochemically permeated oxygen through the membrane.

The formula for this computation is as discussed in Chapter 4 was

$$c_{O_2-\text{perm}} = 2c_{CO_2-\text{measured}} - c_{O_2-\text{leaked}} + c_{O_2-\text{measured}} \qquad \text{Eqn 7.3}$$

where $c_{O_2-\text{perm}}$ is the equivalent concentration of permeated oxygen, $c_{CO_2-\text{measured}}$ is the concentration of CO_2 measured by the GC, $c_{O_2-\text{measured}}$ is the concentration of measured unreacted O_2, and $c_{O_2-\text{leaked}}$ is leaked oxygen estimated using measured leaked nitrogen. The oxygen flux through the membrane, in $\text{mLmin}^{-1}\text{cm}^{-2}$ was computed using the formula:

$$J_{O_2} = \frac{G \times c_{O_2-\text{perm}}}{A} \qquad \text{Eqn 7.4}$$

where $J_{O_2}$is the oxygen flux in $\text{mLmin}^{-1}\text{cm}^{-2}$ G is the effluent gas flowrate in mLmin^{-1}

and A is the membrane area in cm^2.

The results for oxygen permeation under reactive conditions of helium diluted methane 30mL/min as sweep gas at the permeate side are summarised in *Figure 7-2*

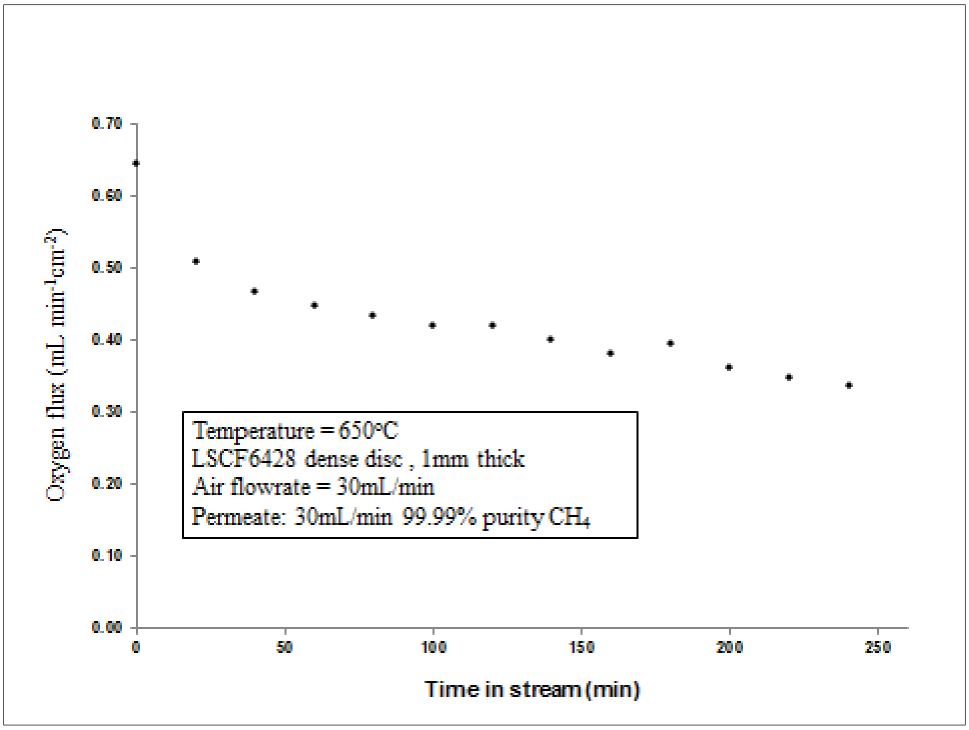

Figure 7-2 Results of permeation experiment with 99.99% purity CH_4.

7.4 Permeation under reactive conditions (CO sweep gas)

For the experiment using helium diluted CO as sweep gas, the permeate side reaction is assumed to be:

$$CO + \frac{1}{2} O_2 \rightarrow CO_2 \qquad \text{Eqn 7.5}$$

It was assumed the CO_2 measured by the GC in the effluent gases was solely from oxidation of CO to CO_2. In this experiment, the effluent gases detected were CO_2, unreacted CO, N_2 and traces of O_2. The oxygen consumed in the reaction was derived from the equation above by halving the measured CO_2 concentration and the electrochemically permeated oxygen was computed as discussed in Chapter 4, from Eqn 7.6.

$$c_{O_2-\mathrm{perm}} = \frac{1}{2} c_{CO_2-\mathrm{measured}} - c_{O_2-\mathrm{leaked}} + c_{O_2-\mathrm{measured}} \qquad \text{Eqn 7.6}$$

The oxygen flux was computed using

$$J_{O_2} = \frac{G \times c_{O_2-\mathrm{peram}}}{A} \qquad \text{Eqn 7.7}$$

where $c_{O_2-\mathrm{perm}}$ is calculated from Eqn 7.6 and other variables are as previously defined.

The results of oxygen permeation under reactive conditions with helium diluted carbon monoxide as sweep gas are as shown in *Figure 7-3*.

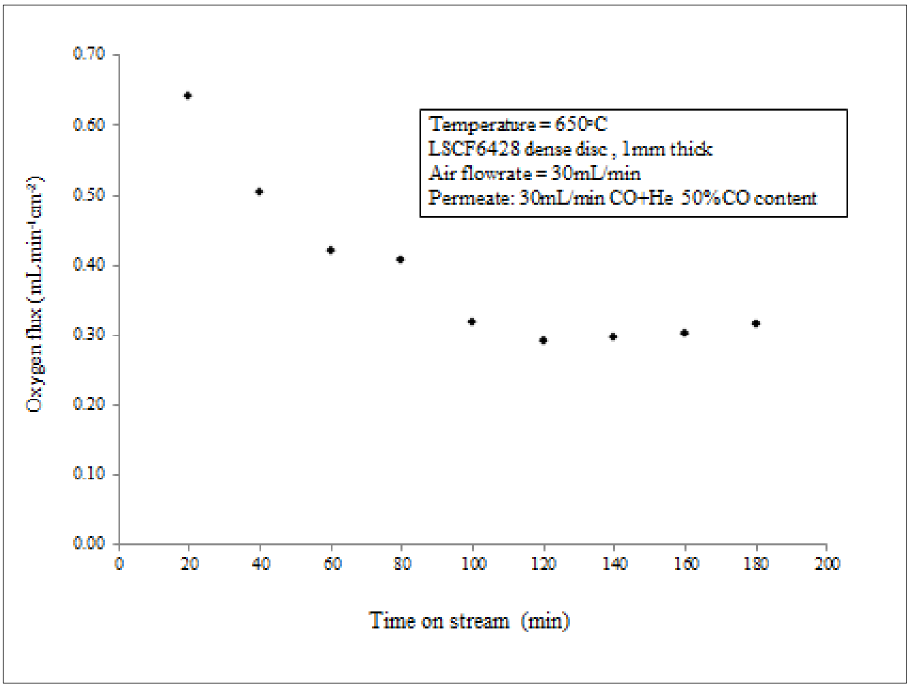

Figure 7-3 Results of permeation experiment with Helium diluted CO.

7.5 Interpretation of permeation results

In general it is well accepted that oxygen transport through ceramic membranes is governed by three main processes; oxygen surface exchanges on the air side, oxygen bulk diffusion and oxygen surface reactions on the permeate side. Any one of the three factors can be the rate limiting factor although generally the bulk diffusion is considered from most literature reports to be rate limiting for membranes $\sim 1\mathrm{mm}$ and above thick, and/or at higher temperatures, while at lower temperatures or thin membranes, surface exchange reactions are considered to be rate limiting (Kirchen et al., 2013). In light of the results explained, the next sections will try and elucidate the results in terms of surface reactions at either side of the membrane with and without reaction, as well as the effect of reactions on bulk diffusion.

7.5.1 Permeate side surface reactions

Oxygen surface reactions on the permeate side depend on the reactivity of the sweep gas at the permeate side.

7.5.1.1 Inert conditions

If an inert sweep gas is used, on emerging at the membrane permeate surface, the permeated oxygen ions recombine after losing their electrons, to form molecules which are desorbed from the membrane and swept away by the inert gas passed through the permeate side. The recombination sub-processes have a “resistance” associated with them. The surface reactions in such a case can be summarised by a reversible reaction as in :

$$\mathrm{O_o^x} + 2\dot{\mathrm{h}} \xleftrightarrow{k_{fp} > k_{rp}} \frac{1}{2}\mathrm{O_2} + \mathrm{V_{\ddot{O}}} \qquad \text{Eqn 7.8}$$

7.5.1.2 Reactive conditions

If a reactive sweep gas mixture is passed through the permeate side, the membrane surface lattice oxygen oxidizes the fuel molecules.

For CH_4, assuming the simple case of complete oxidation of CH_4 to CO_2 and H_2O, the overall reaction can be represented by the equation:

$$\mathrm{CH_4} + 4\mathrm{O_o^x} + 8\dot{\mathrm{h}} \rightarrow \mathrm{CO_2} + 2\mathrm{H_2O} + \text{Heat energy} \qquad \text{Eqn 7.9}$$

For CO, this reaction can be represented by the equation:

$$\mathrm{CO} + \mathrm{O_o^x} + 2\dot{\mathrm{h}} \rightarrow \mathrm{CO_2} + \text{Heat enrgy} \qquad \text{Eqn 7.10}$$

Clearly from reactions depicted in Eqn 7.9 and Eqn 7.10 permeation with reaction is accompanied by generation of heat from the exothermic reaction while that under inert conditions does not. In addition, they are a lot faster than the reversible recombination processes under inert conditions. There are three main consequences of the oxidation reaction between the fuel molecules and lattice oxygen. They are oxygen partial pressure reduction in the membrane surface vicinity, enhancement of lattice vacancy concentration gradient in the membrane and membrane temperature.

7.5.1.2.1 Oxygen partial pressure

The consumption of oxygen due to reactive sweep gas results in decreased oxygen partial pressure in the vicinity of the membrane surface. Some authors (Julbe et al., 2005, Kawahara et al., 2011) have suggested oxygen partial pressures of the order of 10^{-20} to 10^{-22}Pa under reaction conditions. Hashim et al (Hashim et al., 2011) have suggested permeate side oxygen partial pressure with an oxygen consuming reaction, of the order of 10^{-12}-10^{-16}Pa. If air at ambient pressure is passed at air side, the oxygen partial pressure at the airside membrane surface is 0.21 atm. This oxygen partial pressure difference translates to a huge oxygen partial pressure gradient across the membrane thickness. Inserting these values into the $\ln\left(\frac{P_2}{P_1}\right)$ term in the Wagner equation gives a value of the order of 19 – 21 for partial pressure values suggested by (Julbe et al., 2005, Kawahara et al., 2011) and a value of the order of 11-15 for oxygen partial pressure suggested by (Hashim et al., 2011).

Reports in literature (Rui et al., 2009, Li et al., 2000, Wang et al., 2011) show that when an inert sweep gas is used, oxygen partial pressure in the range 10^{-3}Pa are achieved. Insertion of this value into the logarithmic term, $\ln\left(\frac{P_2}{P_1}\right)$, of the Wagner expression, it gives a value of 1 – 2 with the air side oxygen partial pressure assumed 0.21Pa. Compared to a value of 19-21 or 11-15 under reactive conditions, this might explain the enhanced oxygen flux under reactive conditions compared to inert conditions. In addition, this analysis does not take into account the effect of oxygen partial pressure gradient on the oxygen ion conductivity through the bulk which it may be significantly influence.

Recently, in a study in which CO_2 was used as the inert sweep gas and CO_2 diluted CH_4 for the reactive conditions, using an in situ sampling technique, Kirchen et al (Kirchen et al., 2013) reported that when only CO_2 was used as sweep gas, significantly higher oxygen concentrations are seen at the membrane surface than in the gas outlet stream. (Hong et al., 2012) and (Gozálvez-Zafrilla et al., 2011) have used numerical methods using fluid flow concepts and reported similar outcomes.

The implication of these findings is that the true oxygen partial pressure at the permeate side membrane surface is much higher than is suggested by measured oxygen concentration in the bulk gas and outlet stream. In terms of the Wagner expression, this gives a smaller value of $\ln\left(\frac{P_2}{P_1}\right)$ because what matters is not the oxygen partial pressure in the bulk volume, but in the membrane surface vicinity. Kirchen at al (Kirchen et al., 2013) also reported that when CO_2 diluted CH_4 was introduced as sweep gas, the oxygen partial pressure at the permeate membrane surface was reduced. This confirmed the effect of the CH_4 in removing oxygen from the membrane surface by reaction.

7.5.1.2.2 Lattice vacancy concentration gradient

It is also proposed that the effect of reactive conditions on the permeate side is that reactive gas molecules are oxidized by lattice oxygen at the membrane surface creating a high concentration of oxygen vacancies at the membrane solid/gas boundary layer. Considering in steady state conditions a membrane thickness of L as illustrated in Figure 7-4 oxygen ion flux can be expressed as:

$$\mathrm{J}_{\mathrm{V}_{\ddot{\mathrm{O}}}} \quad = \quad \mathrm{D}_{\mathrm{V}_{\ddot{\mathrm{O}}}}\left(\frac{\mathrm{C}_{\mathrm{V}_{\ddot{\mathrm{O}}_{\mathrm{perm}}}} - \mathrm{C}_{\mathrm{V}_{\ddot{\mathrm{O}}_{\mathrm{air}}}}}{\mathrm{L}}\right) \qquad \text{Eqn 7.11}$$

where $\mathrm{J}_{\mathrm{V}_{\ddot{\mathrm{O}}}}$ is the flux of oxygen vacancies, while $\mathrm{C}_{\mathrm{V}_{\ddot{\mathrm{O}}_{\mathrm{perm}}}}$ and $\mathrm{C}_{\mathrm{V}_{\ddot{\mathrm{O}}_{\mathrm{air}}}}$ are oxygen vacancy concentrations on the membrane permeate and airside surface respectively.

Due to a higher oxygen partial pressure at the air side and a much lower oxygen partial pressure at the permeate side, the oxygen vacancy concentration at permeate surface layer is much higher than that at the airside surface layer. This is because the vacancies tend to be filled with oxygen via the reaction:

$$\frac{1}{2}O_2 \quad + \quad V_{\ddot{O}} \quad \leftrightarrow \quad O_O^x + 2\dot{h} \qquad \text{Eqn 7.12}$$

This reaction takes place more to the right in an oxygen-richer environment (higher oxygen partial pressure), than in an oxygen-leaner environment (lower oxygen partial pressure). At stead state conditions, the oxygen vacancy concentration can be assumed linear through the membrane thickness.

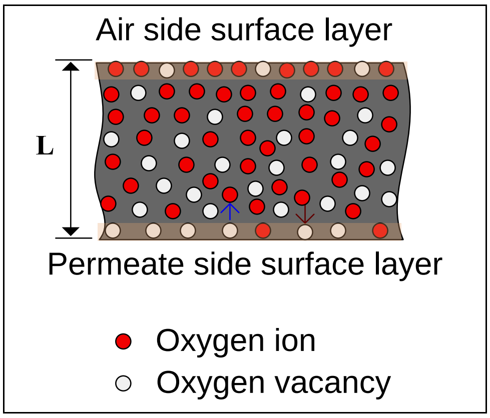

Figure 7-4 Oxygen vacancy concentration gradient under reactive conditions at steady state conditions

The obliteration of lattice oxygen by a reaction at the permeate surface layer creates a high oxygen vacancy concentration in the membrane surface layer resulting in a high vacancy concentration gradient in the membrane lattice in the vicinity of the surface layer. The huge difference in oxygen vacancy concentration at the two surfaces creates a steeper vacancy concentration gradient than if there was no reaction, which causes a higher flux of vacancies from region of high concentration to region of low concentration by Fickian diffusion mechanism according to Eqn 7.11. This flow of oxygen vacancies is equivalent to the flow of oxygen ions in the opposite direction. In other words, the consumption of lattice oxygen in oxidation of reactive sweep gas has a “pulling” effect on lattice oxygen in the bulk and ultimately oxygen from air at the air side. This way, oxidation reactions contribute to enhancement of bulk diffusion. In non-reactive operation, desorption of molecular oxygen is not as fast as removal of lattice oxygen by a combustion reaction. In fact desorption of molecular oxygen into the permeate side, depending on the rate of removal of the oxygen by the inert sweep gas, results in a relatively high oxygen partial pressure. As a result, the oxygen vacancy gradient across the membrane thickness is not as steep as in reactive operation. The “pulling” effect is therefore not as strong and hence the much lower flux.

7.5.1.2.3 Membrane temperature increase

Surface exchange reactions at the airside and bulk diffusion are temperature driven processes. At higher temperature, oxygen permeation is accelerated due to increasing diffusion coefficient ($\mathrm{D}_{\mathrm{V}_{\ddot{\mathrm{O}}}}$ which is temperature dependent). High temperatures also accelerate surface exchange reactions. Oxidation reactions with lattice oxygen at the permeate side during reactive operation are exothermic. Heat generated by this combustion reaction increases the membrane temperature which enhances oxygen ion diffusion coefficient of the membrane. The heat generated is also transferred by conduction to the air side surface of the membrane. The increase in airside membrane surface increases the air temperature near the surface and enhances the oxygen surface exchange reactions. This rise in temperature therefore has favourable effects to oxygen permeation at two fronts; enhanced air side surface reaction rates as well as bulk diffusion coefficient. In contrast, there is no such exothermic reaction to increase surface exchange reactions and bulk diffusion in the case of permeation under inert (non-reactive) conditions. However, in the current work, it was not possible to directly measure the membrane temperature to verify this.

7.5.2 Electrical circuit equivalence of oxygen transport through the membrane

One way is to view the oxygen transfer mechanism from the airside to the permeate side as being controlled by total resistance made up of surface exchange kinetics resistance at airside and permeate side, and the bulk diffusion resistance. It can be represented by an equivalent electrical circuit with series resistances; surface exchange resistance at air side($\mathrm{R}_{\mathrm{sra}}$), the bulk diffusion resistance ($\mathrm{R}_{\mathrm{bdr}}$) and the surface exchange resistance at permeate side ($\mathrm{R}_{\mathrm{srp}}$).

The oxygen flux is the ratio of the driving force and the total resistance. From this model, if any of the three resistances is the rate determining factor, it dominates the total resistance and oxygen permeation is mainly affected by that resistance.

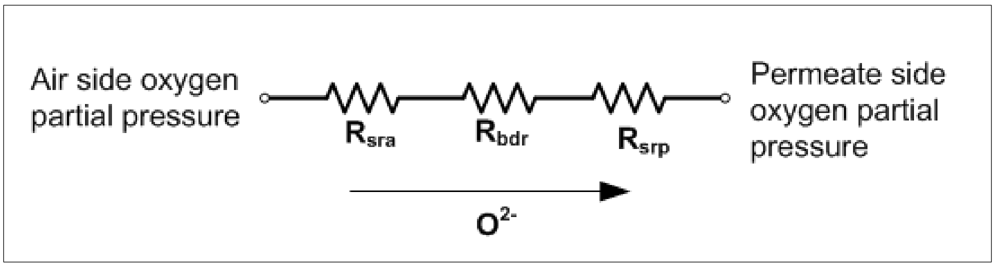

Figure 7-5 Equivalent electrical circuit of oxygen flux through membrane

The resistance of the surface reaction on each side is affected by the variation of the rate constant and oxygen partial pressure.

In the context of the experimental results obtained in the current work, the effect of introducing a chemical reaction at the permeate side is to change these resistances. In the case of an inert sweep gas, oxygen ions arriving at the permeate side surface have to lose electrons and recombine to form molecules which diffuse into the gas phase in the permeate chamber. This step represent the permeate side resistance under inert conditions. In the presence of a reactive gas such as CO, the lattice oxygen at the membrane permeate side surface reacts with the CO to form CO_2 which diffuse into the gas phase as well. This reaction represents the surface exchange reactions under reactive conditions. There are clearly significant differences in the surface exchange resistances under the two scenarios. The reactive surface exchanges are the faster between the two and therefore constitute a lower resistance (R_{srp}). In addition, the fast reaction with lattice oxygen has the effect of increasing the oxygen vacancies concentration gradient across the membrane bulk. This constitutes an amplification of the driving force for oxygen ion diffusion, or put differently, has the same effect as reducing the bulk diffusion resistance (R_{bdr}). Also, unlike inert conditions, reactive conditions are exothermic resulting in increase in membrane temperature which further promotes reduction of bulk diffusion (R_{bdr}). The heat generated during exothermic reaction can also be conducted to the airside surface, reducing airside surface resistance (R_{sra}). This model has therefore shown that an exothermic reaction at the permeate side reduces all the three resistive components in oxygen transport through the membrane. Hence the oxygen flux with a reaction increase as a result of the joint effect of partial pressure gradient and temperature rise with consequent increased oxygen diffusion through the bulk and surface reactions.

7.5.3 Time dependent permeation experiments

The time monitored oxygen permeation experiments have shown a gradual decline in measured oxygen flux as shown in *Figure 7-2* and *Figure 7-3*.

This result can be explained in terms of oxygen storage properties of oxygen conducting perovskite materials and carbon dioxide poisoning.

7.5.3.1 Oxygen storage explanation

For *Figure 7-2* and *Figure 7-3* at the beginning of each experiment, the membrane material has a certain amount of oxygen stored in it which is occupying oxygen sites in the lattice as both sides of the membrane are exposed to similar oxygen partial pressure, i.e. ambient oxygen partial pressure of 0.21Pa. Before oxygen partial pressure gradient is applied at high temperatures, the lattice oxygen can be assumed evenly distributed throughout the membrane thickness. When a reactive sweep gas is introduced to the permeate side and is oxidized by lattice oxygen at the membrane surface, this has a “pulling” on the lattice oxygen in the membrane bulk driven by the oxygen concentration gradient. Ultimately, the “pulling” effect is extended to the oxygen ions supplied by surface exchange reactions at the airside. If the airside surface exchange reactions cannot supply enough lattice oxygen to match the rate at which oxygen is consumed at the permeate side, there is a gradual depletion of stored oxygen until exchange reactions at the air are in equilibrium with oxygen consumption at the reaction side. The gradual decline in measured flux with time that has been observed in these experiments reflects the gradual decline in the initially stored oxygen. This decline will continue until the oxygen consumption at the permeate side and the oxygen ions supply from air at the airside are in equilibrium.

A literature search has shown that (Tsai et al., 1997) with LSCF2882 membranes and (Zeng et al., 1998) with LSCF2864 membranes made similar observations. (Zeng et al., 1998) have proposed that this phenomenon is likely due to release of oxygen from the membrane from an initially oxygen-rich equilibrium state to another steady-state with constant activity profile of the membrane. For (Zeng et al., 1998), they observed this decrease for 5 hours after which the activity profile levelled-off while (Tsai et al., 1997) observed a decrease for 50 hours. In the current work, experiments were conducted for much shorter periods. It is justifiable to state that in the current work, if the experiment was run for long enough, the flux was going to level off at steady state equilibrium.

7.5.3.2 Carbon dioxide poisoning explanation

(Czuprat et al., 2010) investigated the impact of CO_2 on oxygen permeation in some perovskite type membranes and concluded that CO_2 has a poisoning effect on oxygen flux on BCFZ system, a perovskite material based on Ba, Co, Fe and Zr. (Arnold et al., 2007) observed that CO_2 has poisoning effect on flux and also changes the microstructure of BSCF membranes. They were able to show that using pure CO_2 as sweep gas could cause an immediate stop to oxygen permeation, but also observed that oxygen permeability in the membrane could be easily restored by sweeping with pure helium.

(Tan et al., 2012a, Tan et al., 2012b) also observed significant poisoning effect of CO_2 on oxygen permeation through LSCF6482 based membranes and attributed this to chemical adsorption of CO_2 where the oxygen vacancy sites at the permeate side membrane surface are occupied by the oxygen atoms of CO_2.The adsorbed CO_2 had the effect of blocking transport of oxygen from the air side to the permeate side. This is illustrated in *Figure 7-6.* They also proposed a reaction between the adsorbed CO_2 and alkali earth cations to form carbonates which affected oxygen permeation as well.

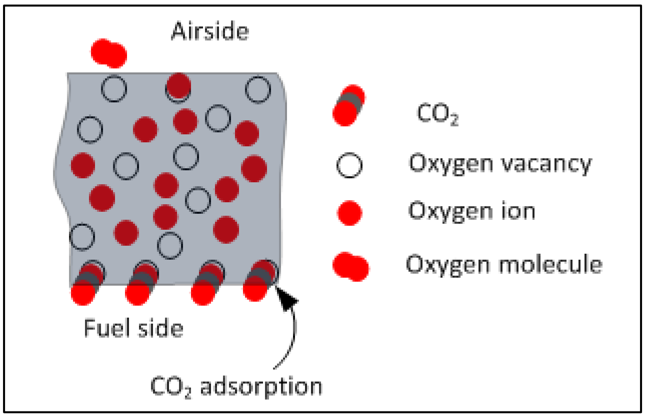

Figure 7-6 Schematic showing effect of CO2 adsorption on permeate membrane oxygen vacancies and blocking oxygen ion transport

The difference between the current work and the previous reports cited above lies in the concentrations of CO_2 to which the membrane is exposed. In (Tan et al., 2012a) and (Tan et al., 2012b), CO_2 was used as the sweep gas and therefore its partial pressure was high with a molar concentration close to 100% with no combustible component, whereas in the present work, the sweep gas used was helium diluted methane and/or helium diluted carbon monoxide. The carbon dioxide concentration was limited to that formed by oxidation reactions with permeate oxygen and was low, less than 10% concentration. Be that as it may, in the current work, CO_2 poisoning could have contributed to the flux reduction in the same way observed by (Tan et al., 2012b).

7.6 Influence on oxygen flux of switching between inert and reactive sweep gas

The influence of different sweep gas mixtures on the oxygen permeation of LSCF6428 in a four-step long experiment under similar flow conditions was investigated. In the first step the sweep gas consisted of pure helium before switching to a mixture of helium and methane, then to pure helium again and finally mixture of helium and carbon monoxide. The total sweep gas flowrate was kept constant at 30ml/min to eliminate the effect of flowrate in comparing the results. Synthetic air at ambient pressure with a flowrate of 30ml/min was used as airside feed gas.

In the first 100 minutes, pure helium was passed in the permeate chamber at a flow rate of 30ml/min and air in the air side chamber at the same rate. GC samples of the effluent gas from the permeate side were measured at intervals of about 10 minutes to measure oxygen flux. After 100 minutes the sweep gas was switched to 30ml/min of a 50% helium and CH_4 and allowed to run for 30 minutes to stabilise before GC samples were taken through the on-line GC. The He-CH_4 mixture was passed for about 60 minutes with GC samples being run about 10 minutes intervals for oxygen flux measurements. This was followed by a switch in the sweep gas to 30ml/min pure helium again and GC measurements taken. Lastly, the sweep gas was switched to 30ml/min of a 50% Helium diluted CO mixture and periodic samples of effluent analysed using the in-line GC. The oxygen flux for each sweep gas was computed as previously described using the general formula:

$$J_{O_2} = \frac{G \times c_{O_2}}{A} \qquad \text{Eqn 7.13}$$

Figure 7-7 shows the permeation results of the experiment described above.

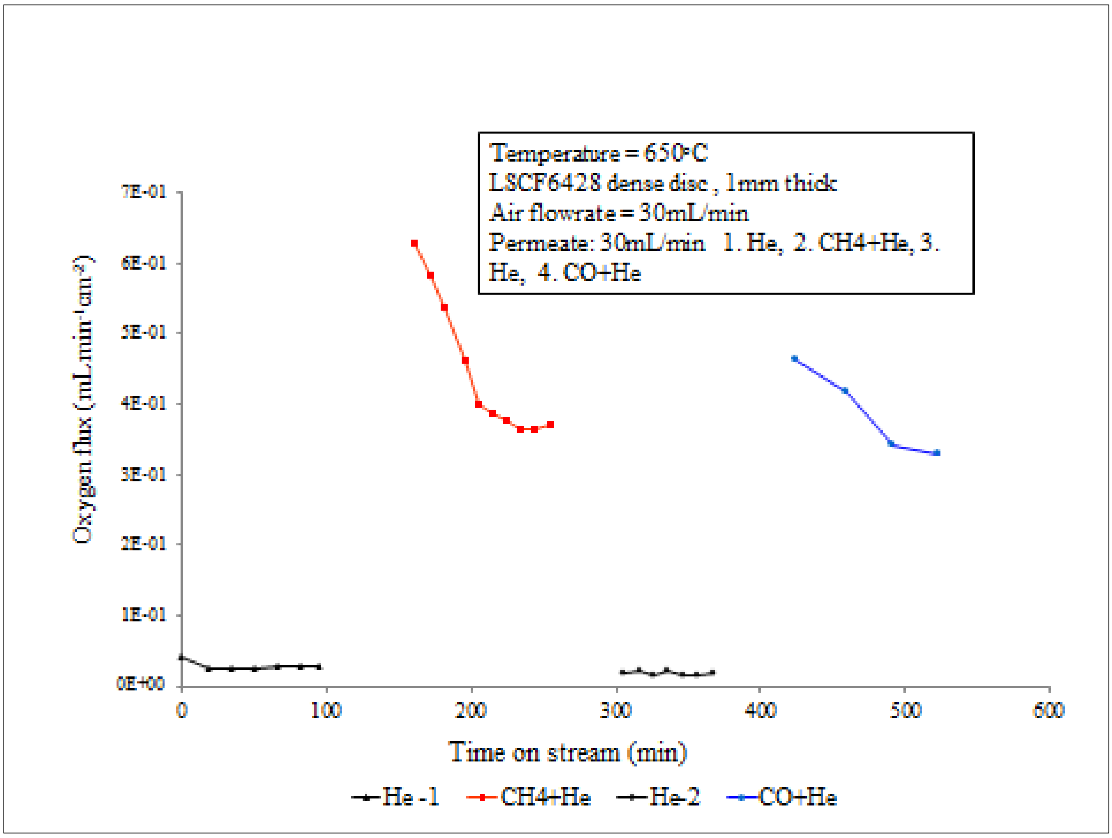

Figure 7-7 Oxygen permeation with different sweep gas compositions

When pure helium was first used, oxygen flux of about 0.02mLmin^{-1}cm^{-2} was obtained for the whole duration of this step. After switching to sweep gas consisting of helium and methane, there was a sharp increase in measured oxygen flux to 0.63mLmin^{-1}cm^{-2} followed by a rapid decrease with time to 0.40 mLmin^{-1}cm^{-2} after about 45minutes when the flux began to drop more steadily to 0.35mLmin^{-1}cm^{-2} after a further 50 minutes. At this point the sweep gas was switched back to 30mL/min pure helium. Oxygen permeation measurements for this step (third) during the experiment show the flux fell back to about 0.025mLmin^{-1}cm^{-2} and remained at these levels for the rest of the period pure helium was passed as sweep gas. In the fourth and final step of the experiment, the sweep gas was switched from pure helium to 30ml/min 50% He diluted CO. Oxygen permeation measurements show that oxygen flux initially shot up again to 0.46 ml/min/cm^2 before it started to decline again gradually to 0.33mLmin^{-1}cm^{-2} after running for about 100 minutes.

The higher oxygen fluxes with (He+CH_4) and (He+CO) as sweep gas than with pure helium alone illustrates the effect of chemical reaction at the permeate side while the flux drop with time in the step 2 (He+CH_4) and step 4 (He+CO) can be explained by the depletion of stored oxygen in the membrane lattice with time.

7.7 Effect of Carbon Monoxide or Methane concentration in sweep gas on oxygen permeation

Experiments were conducted to investigate the effect of the content of the reactive component of the sweep gas, i.e. CO or CH_4 in the sweep gas, on oxygen flux through the LSCF6428 membrane. For each mixture of helium and CO or CH_4, the membrane was first “conditioned” to fresh membrane conditions by exposing the membrane to ambient air at 650^{o}C for 1 hour before flux measurement of each sweep gas mixture. This was done to ensure similar initial oxygen content in the membrane lattice each time and therefore minimise errors due to dissimilar initial lattice oxygen content. The results of the experiments are shown in Figure 7-8 and Figure 7-9.

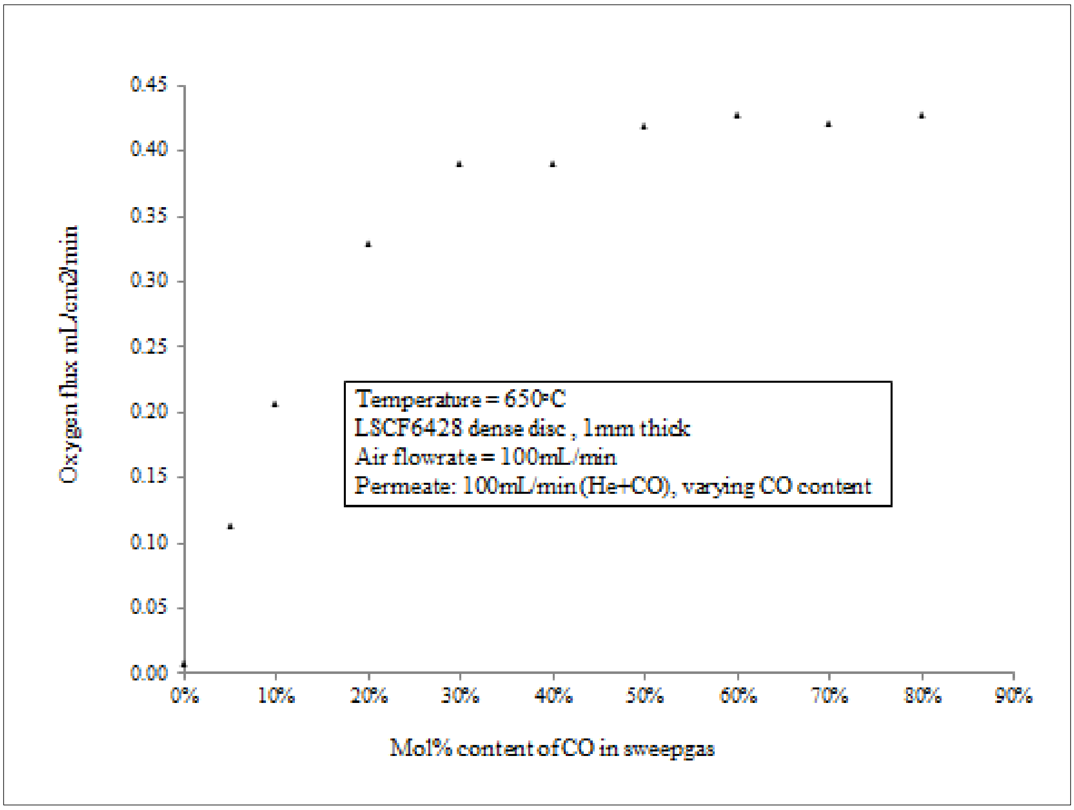

Figure 7-8 Effect of CO content in permeate sweep gas on oxygen permeation

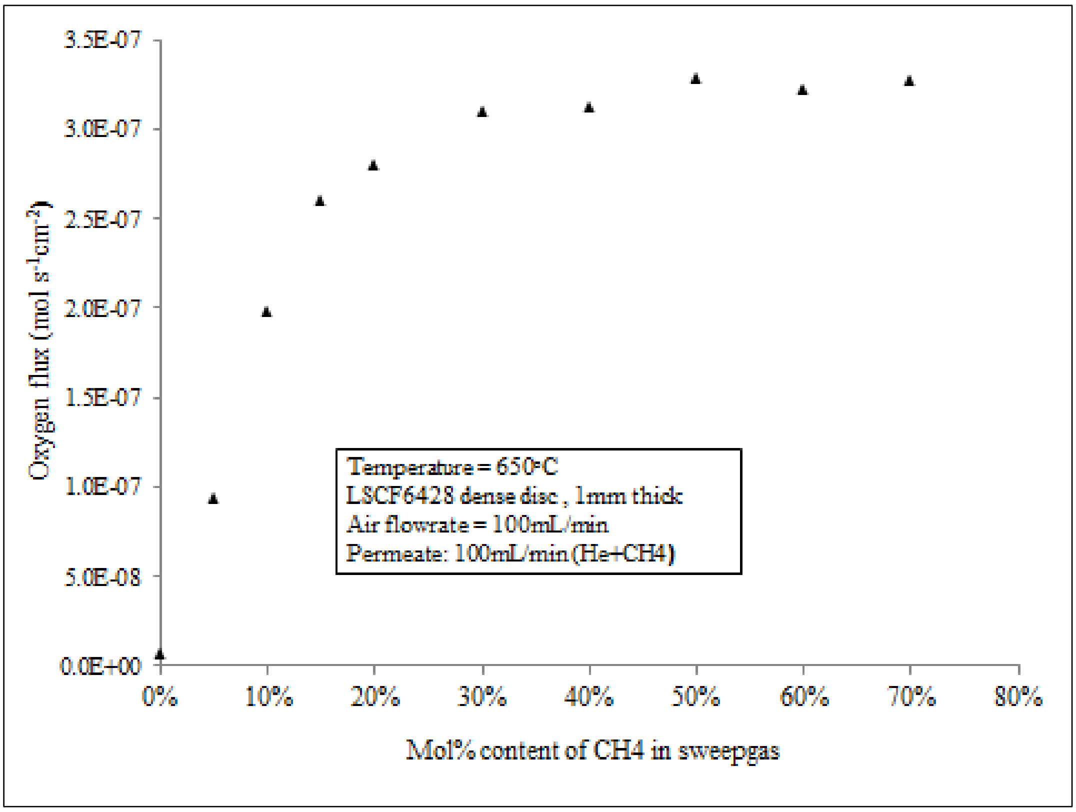

Figure 7-9 Effect of CH_4 content in permeate sweep gas on oxygen permeation

The results show a linear increase in oxygen flux with increasing reactive component (CO or CH_4) content at low concentrations end of the profiles. For (He+CO) mixture, the oxygen permeation flux increased linearly from as low as $0.01 mL min^{-1} cm^{-2}$ (5.7×10^{-9} mol $cm^{-2} s^{-1}$) for pure helium to $0.39 mL min^{-1} cm^{-2}$ (2.9×10^{-7} mol $cm^{-2} s^{-1}$) for a 30% CO in a (He+CO) mixture. Above 30% CO concentration, the flux began to plateau and further increase in CO concentration had no effect on oxygen flux. A similar phenomenon was observed for (He+CH_4) sweep gas mixture with a linear increase in flux from $0.01 mL min^{-1} cm^{-2}$ (7.1×10^{-9} mol $cm^{-2} s^{-1}$) for pure helium to $0.35 mL min^{-1} cm^{-2}$ (2.6×10^{-7} mol $cm^{-2} s^{-1}$) for 20% CH_4 concentration. Above 20% CH_4 concentration, oxygen flux began to plateau and levelled off at just above $0.4 mL min^{-1} cm^{-2}$ (3.0×10^{-7} mol $cm^{-2} s^{-1}$).

Clearly, the results *Figure 7-8* and *Figure 7-9* show that with increasing reactive component concentration in the sweep gas, oxygen flux plateaus faster with methane than with CO. This might be explained by the stoichiometry of the reaction. The proposed combustion reaction taking place with lattice oxygen on permeate side of the membrane, the reactions can be represented by Eqn 7.14 and Eqn 7.15.

$$\mathrm{CO_{(g)}} + \mathrm{O^{X}_{O(s)}} \rightarrow \mathrm{CO_{2\,(g)}} + 2e \qquad \text{Eqn 7.14}$$

$$\mathrm{CH_{4\,(g)}} + 4\mathrm{O^{X}_{O\,(s)}} \rightarrow \mathrm{CO_{2(g)}} + 2\mathrm{H_2}O_{(g)} + 8\mathrm{e} \qquad \text{Eqn 7.15}$$

These reactions show that each CO molecule requires one lattice oxygen ion for oxidation while each CH_4 requires four lattice oxygen ions for complete oxidation. This basic observation, however, does not take into account the reaction kinetics and pathways taken by these reactions. Clearly the combustion of CH_4 is likely to involve several steps.

The linear relationship between oxygen flux and the concentration of CO or CH_4 at low concentrations can be explained by the fact that not all CO or CH_4 molecules in the sweep gas make it to the gas/solid interface at the permeate membrane surface. Some, if not most, remain in the bulk gaseous stream and may react homogeneously with any gaseous phase oxygen contained in the permeate side bulk volume that, for example, may have leaked into the permeate side via the imperfect gasket seals. At very low concentrations, the probability of reactive molecules reaching the membrane surface is greatly reduced resulting in fewer reactive molecules reaching the membrane surface. As CO or CH_4 concentration is increased, the number of reactive molecules reaching the membrane surface per given time also increases, contributing to the heterogeneous reaction with lattice oxygen and hence increasing oxygen flux. Put differently, at low CO or CH_4 partial pressure in the sweep gas, gas phase CO or CH_4 transport to the membrane is the limiting factor. As CO or CH_4 partial pressure is increased, their transport to membrane surface ceases to be the rate limiting factor.

This result demonstrates that insufficient concentration of reactive component in the sweep gas diminishes the advantage of a separation with reaction because there aren’t enough reactive gas molecules reaching the membrane surface thus limiting the flux. As the reactive component concentration increases, a point is reached when the flux is limited not by the supply of reactive molecules reaching the membrane surface, but by the supply of oxygen from the airside. The increase in flux with CO/CH_4 concentration indicates that the main flux limiting factor under the conditions the experiments were conducted was surface reactions, and specifically surface reactions at the permeate side. When the CO/CH_4 concentration is too low, there is competition between CO/CH_4 oxidation and O_2 evolution.

The observed linearity of oxygen flux with concentration of CO in the sweep gas at low concentrations seems to be in agreement to ten Elshof et al (ten Elshof et al., 1996) model. In their model they suggested Langmuir-Hinshelwood (LH) type mechanism in which they assumed CO adsorbs on a surface oxygen vacancy before it reacts with a neighbouring lattice oxygen ion as illustrated by Eqn 7.16 and Eqn 7.17.

$$\mathrm{CO} + \mathrm{V}_{\ddot{\mathrm{O}}} \rightarrow [\mathrm{V}_{\ddot{\mathrm{O}}} \cdot\cdot \mathrm{CO}]_s \qquad \text{Eqn 7.16}$$

$$[\mathrm{V}_{\ddot{\mathrm{O}}} \cdot\cdot \mathrm{CO}]_s \rightarrow \mathrm{CO}_2 + 2\mathrm{V}_{\ddot{\mathrm{O}}} + 2\mathrm{e} \qquad \text{Eqn 7.17}$$

They assumed a first order kinetic expression to give an oxygen flux expression given by given by Eqn 7.18 .

$$J_{O_2} = \frac{1}{2} k_O^0 [V_{\ddot{O}}] P_{co}^s \qquad \text{Eqn 7.18}$$

where P_{CO}^s is the partial pressure of CO at the membrane surface. From this they concluded that the flux is linearly proportional to the CO partial pressure, but independent of the membrane thickness.

7.8 Post operation analysis of membrane

After permeation experiments under different conditions, the reactor was dismantled and samples of the spent membrane recovered for characterization in comparison with a fresh membrane in order to study the effect the experiments had on the membrane microstructure. The findings of these characterizations are described in the following sections.

7.8.1 Post Operation X-Ray Diffraction Analysis

In this exercise, the following nomenclature has been adopted to identify the different specimen used in characterization:

LSCF6428 AP = As Purchased LSCF6428 ceramic powders

LSCF6428 SINT = LSCF6428 powders from pressed and sintered disc

LSCF6428 PP = LSCF6428 powders from post permeation membrane

XRD patterns of the LSCF6428 AP, pressed and sintered LSCF6428 SINT and post permeation LSCF6428 PP were analysed using X-Ray Diffraction Techniques to investigate any phase changes in the membrane material during these process. XRD analysis was performed using a PANalytical X'Pert Pro diffractometer using Cu K-∝1 (λ=1.5406 Å) and phase identification by means of the X'Pert software programme High Score Plus, the ICDD Powder Diffraction File 2 database (1999) and the Chemical Open Crystallography database. The diffractograms are as per *Figure 7-10, Figure 7-11* and *Figure 7-12*. No apparent phase changes or formation of new phases can be seen from the patterns. However peaks for LSCF6428 SINT at values of 2-Theta = 46.8° and 58.2° appear to have higher intensity than the other two. The higher intensity for LSCF6428 SINT compared to LSCF6428 AP might be due to enhanced crystallisation during the sintering step while the same compared to that of spent membrane (LSCF6428 PP) might be due to some phase changes at membrane surface due to reactions.

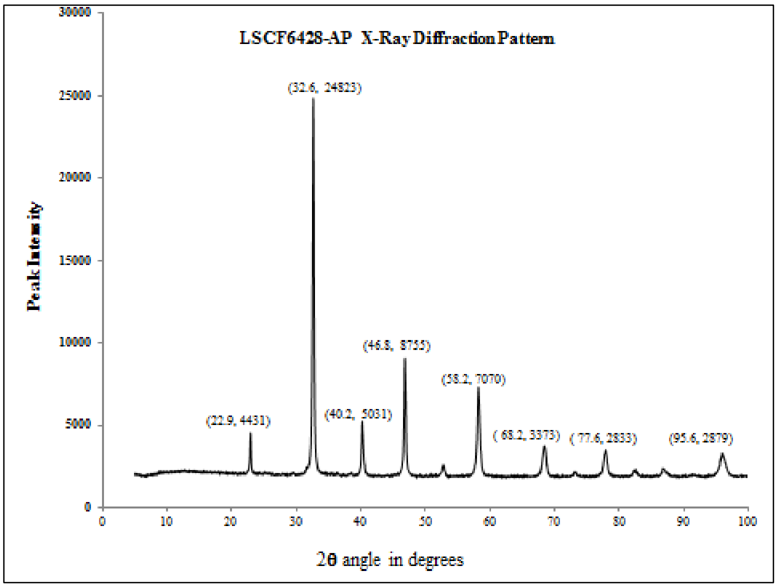

Figure 7-10 XRD patterns for as-purchased membrane material powders

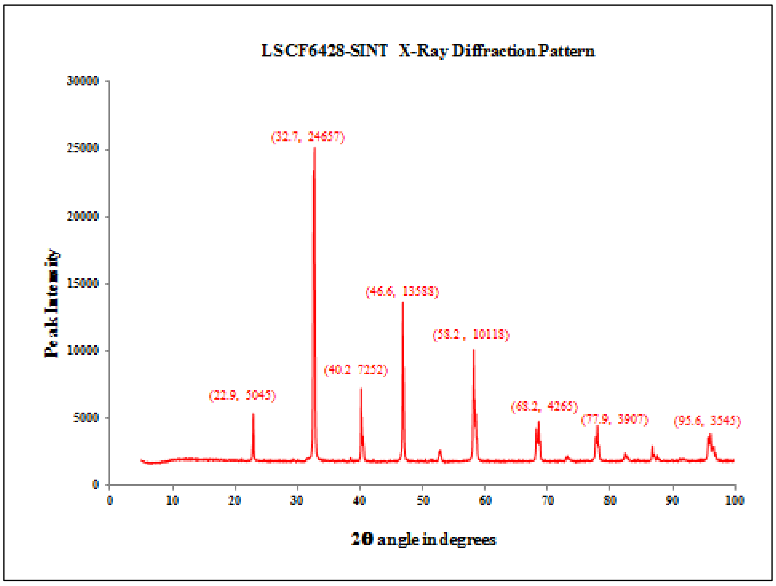

Figure 7-11 XRD patterns for membrane material after sintering at 1150°C for 5 hours

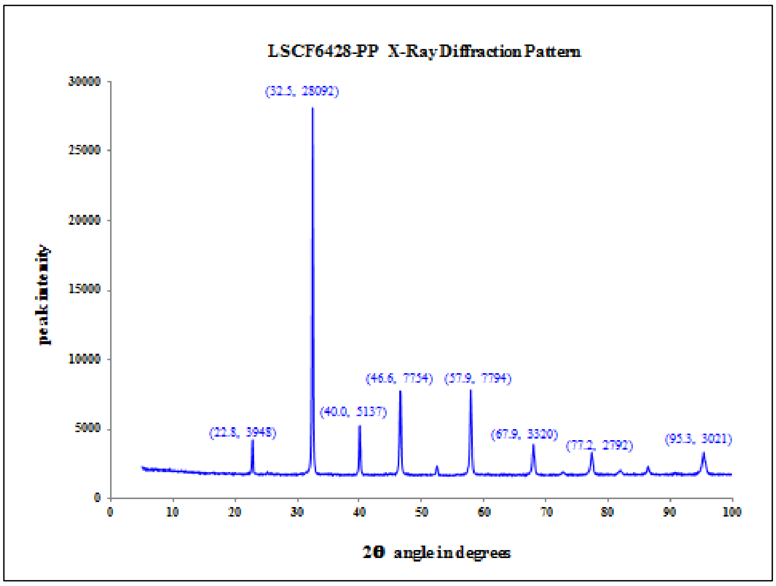

Figure 7-12 XRD patterns for membrane material after permeation experiments

7.8.2 Post operation SEM analysis

To investigate the effect of permeation experiments had on the membrane, SEM and EDS analysis were carried out on the surfaces of a fresh sintered membrane (pre-operation), spent membrane air side surface (post operation air side surface), and spent membrane permeate side (post operation permeate side surface). In *Figure 7-13* micrographs images of the (a) pre-operation surface, (b) post operation airside surface and (c) post operation permeate surface are presented. The SEM images illustrate the morphological changes that occurred to the spent membrane owing to its use in oxygen separation and chemical reaction with CO/CH_4. The fresh membrane image clearly shows the grain boundaries in the sintered ceramic. The airside SEM of a spent membrane still shows some grain boundaries, but to a lesser extent. It is apparent that there has been some surface modification during the use. The reaction side SEM hardly depict any grain boundaries at all. These results indicate some microstructural changes on both surfaces but more prominently on the permeate side.

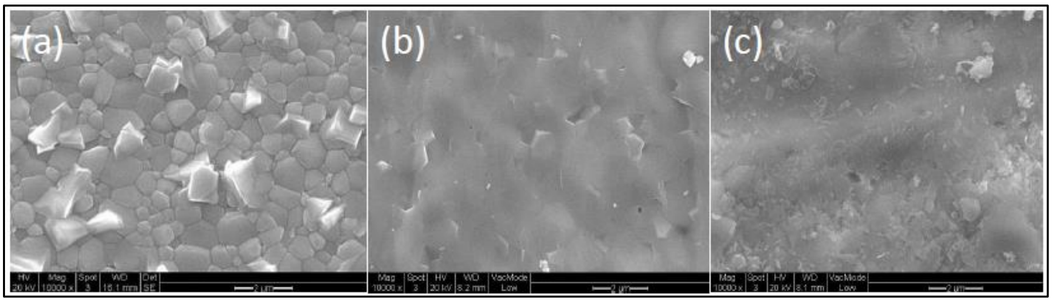

Figure 7-13 (a) Pre-operation surface (b) Airside surface and (c) Reaction side

The airside SEM still shows some crystallinity and grain boundaries while the reaction side SEM shows the original crystallinity has disappeared. The absence of visible grain boundaries on the permeate side image may be attributed to a layer of non-crystalline substance, possibly $SrCO_3$ formed from reaction of CO_2 with Sr. Comparisons of these observations can be made with reports by (Czuprat et al., 2010) who have also have proposed that CO_2 tends to corrode the membrane surface of a $BaCo_{0.4}Fe_{0.4}Zr_{0.2}O_{3-\delta}$ (BCFZ) based membrane due to formation of carbonates which they attributed to the reduced oxygen flux in the membrane and Ba enrichment due to $BaCO_3$ formation. In current studies, the membrane material does not have Ba, but Sr which is also prone to formation of $SrCO_3$ under exposure to CO_2.

Recently, (Lee et al., 2006), came to similar conclusions in a separate study. They carried out an XRD pattern of on $La_{1-x}Sr_xGa_{1-y}Fe_yO_{3-\delta}$ (LSGF) membrane after an oxidation of methane experiment with a CH_4 +He/air environment at 950°C. The results of their XRD examination showed that while the air side of the membrane retained its perovskite structure, non-perovskite decomposed phases were observed at the surface exposed to methane. Further analysis of the non-perovskite phases showed the presence of $La_2O_2(CO)$, $SrCO_3$ and some others they could not identify. They suggested that carbonates might have been formed by the reaction of the metallic ions with deposited carbon dioxide.

Table 7-1 shows the stoichiometry of these surfaces from EDS analysis. The results indicate huge stoichiometric changes on the permeate side surface while there are hardly any changes in membrane surface stoichiometry on the air side compared to that of a fresh membrane. The corresponding representative spectral EDS graphs for the post operation airside, post operation permeate side and pre-operation surfaces are shown in *Figure 7-14*, *Figure 7-15* and *Figure 7-16*.

Table 7-1 Comparison of stoichiometric ratios of membrane cations for surfaces of spent membrane (air side and permeate side) and fresh membrane.

Ratio Membrane surface	$\frac{\mathbf{La}}{\mathbf{La+Sr}}$	$\frac{\mathbf{Sr}}{\mathbf{La+Sr}}$	$\frac{\mathbf{Co}}{\mathbf{Co+Fe}}$	$\frac{\mathbf{Fe}}{\mathbf{Co+Fe}}$	$\frac{\mathbf{Co}}{\mathbf{Sr}}$	$\frac{\mathbf{Fe}}{\mathbf{Sr}}$	$\frac{\mathbf{Co}}{\mathbf{La}}$	$\frac{\mathbf{Fe}}{\mathbf{La}}$	$\frac{\mathbf{La}}{\mathbf{Sr}}$	$\frac{\mathbf{Co}}{\mathbf{Fe}}$
Air-side (spent membrane)	0.58	0.42	0.16	0.84	0.36	1.88	0.27	1.39	1.36	0.19
Reaction-side (spent membrane)	0.27	0.73	0.24	0.76	0.15	0.50	0.42	1.37	0.37	0.31
Fresh membrane	0.59	0.41	0.17	0.83	0.36	1.88	0.27	1.39	1.36	0.19

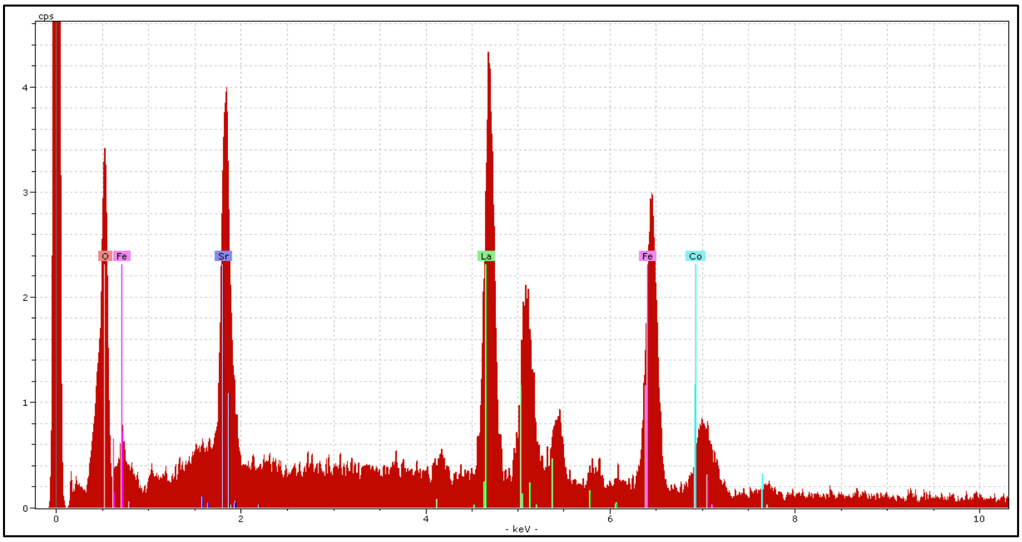

Figure 7-14 Post-Operation Air-side EDS

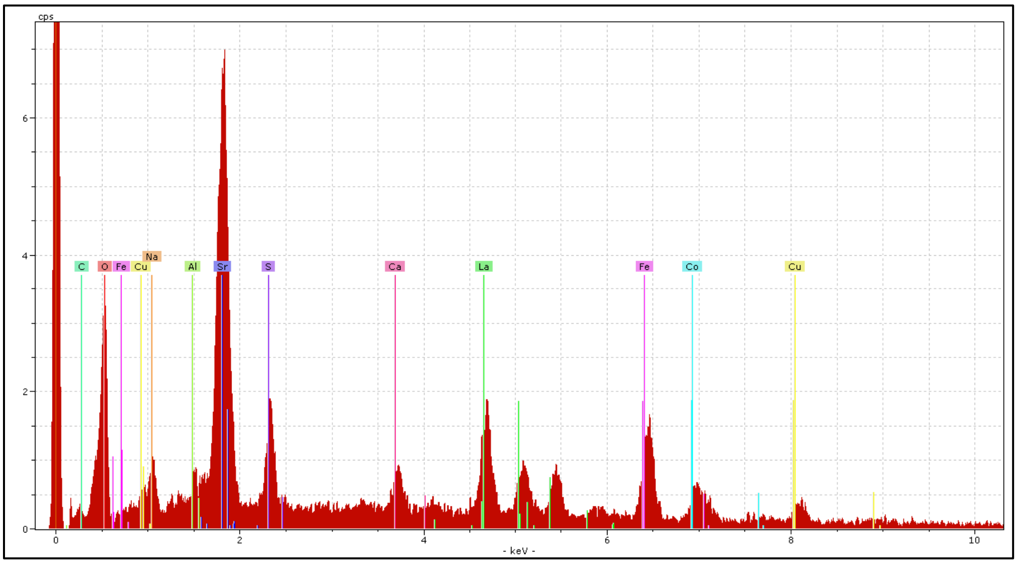

Figure 7-15 Post-Operation Permeate side EDS

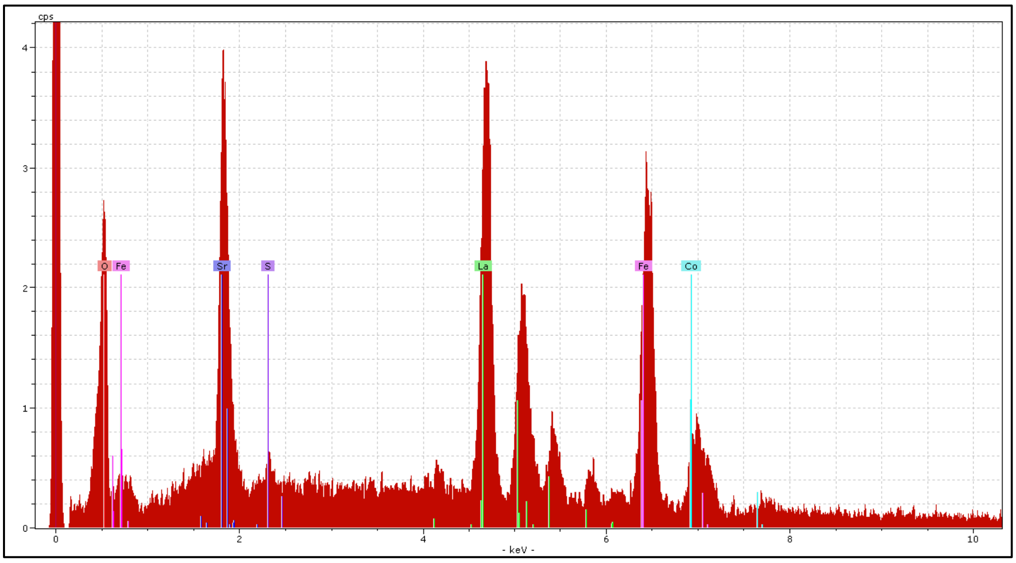

Figure 7-16 Pre-Operation membrane surface EDS

To explain these results, it has to be considered that in LSCF ceramic membranes, La and Sr occupy the A-site of the perovskite structure while Co and Fe occupy the B-site. The original as purchased powders were specified by the supplier as $La_{0.6}Sr_{0.4}Co_{0.2}Fe_{0.8}O_{3-\delta}$. From *Table 7-1*, it is clear that there has been significant compositional changes at the permeate side of the membrane surface as a result of permeation under reactive conditions. However, there are no significant differences of the parameters for the airside of spend membrane compared to those for the fresh membrane.

7.8.2.1 La/Sr ratio

The $\frac{\mathrm{La}}{\mathrm{Sr}}$ ratio of fresh membrane and the air side of the spent membrane were both equal to 1.36 while that of the reaction side was 0.37, implying an enrichment of Sr relative to La at this surface. Alternatively, it can be seen that at the reaction side the $\frac{\mathrm{Sr}}{\mathrm{La+Sr}}$ ratio has increased from 0.41 in fresh membrane to 0.73 after reaction, also showing a Sr enrichment at the permeate side relative to La.

7.8.2.2 Fe/La ratio

A look at the Fe/La ratio shows almost no change in ratio of the two cations in the fresh membrane, airside of used membrane and reaction side of used membrane with ratio values of 1.40, 1.38 and 1.39 respectively. This might mean if there is any transport of these ions during the use of the membrane in permeation experiments, they must have moved at equal velocities and in same direction.

7.8.2.3 Co/Sr ratio

With ratios of 0.36, 0.36 and 0.15 for fresh, airside and reaction side respectively for these two cations, there is clear Sr enrichment relative to Co. This might be due to the formation of $SrCO_3$ which is more thermodynamically favourable than formation of carbonates of Co. The strontium carbonate film on the membrane surface could account for the higher count of Sr atoms than Co atoms by EDX. Formation of Co and Fe carbonates is more difficult (Czuprat et al., 2010) and it is reported that La_2O_3 is more likely form $La_2O_2CO_3$ than lanthanum carbonate (Conway et al., 1992).

7.8.2.4 Fe/Sr ratio

$\frac{\mathrm{Fe}}{\mathrm{Sr}}$ ratios at the fresh membrane surface, airside of used membrane and reaction side of used membrane were 1.88, 1.88 and 0.55 As it was for $\frac{\mathrm{Co}}{\mathrm{Sr}}$ the count for Sr atoms relative to Fe seem to increase at reaction side. The air side $\frac{\mathrm{Fe}}{\mathrm{Sr}}$ ratio is as that of a fresh membrane surface.

7.8.2.5 Co/La ratio

Co/La ratios at the fresh membrane surface, air side and reaction side of spent membrane are respectively 0.27, 0.27 and 0.42. The results suggest an almost unchanging ratio for fresh membrane and air side while the reaction side in used membrane had a higher count of Co to La than in other two. It is not clear why this has happened.

The analysis above, looked at in conjunction with the presence of carbon detected by EDS analysis, might point to formation of $SrCO_3$ at the reaction side of the used membrane. $SrCO_3$ is believed to be more thermodynamically favourable than formation of carbonates of rest of the cations. The $SrCO_3$ results from reaction with CO_2 formed from CO or CH_4 oxidation. Formation of Co and Fe carbonates is more difficult (Czuprat et al., 2010) and it is reported that La_2O_3 is more likely form $La_2O_2CO_3$ than lanthanum carbonate (Conway et al., 1992). The strontium carbonate film on the membrane surface might account for the higher count of Sr atoms. The is in agreement with some literature reports (Czuprat et al., 2010, Sunarso et al., 2008, ten Elshof et al., 1995a). Ten Elshof et al (ten Elshof et al., 1995a), conducted SEM analysis after oxygen permeation experiments on LSCT6482 membranes with exposure to CO and observed an increase in specific surface area, an enhancement of surface roughness and an enrichment of strontium. After a permeation study with air/CH_4, they observed a 60-80 nm thick highly porous $SrCO_3$ layer on the membrane surface exposed to CH_4 at 1100K for 3 days. Also, (Yan et al., 2008) have reported that a small amount of CO_2 introduced in Solid Oxide Fuel Cell, the BSCF cathode was degraded with time due to formation of carbonates resulting from the reaction of alkaline earth elements with CO_2.

EDX spectra of surface of the air side of used membrane, surface of permeate (reaction) of used membrane and surface of a fresh membrane are shown in *Figure 7-14, Figure 7-15*and *Figure 7-16* respectively. Clearly, the relative intesity of Sr in the permeate side EDX spectra relative to other elements is higher than the same in the fresh and airside EDX spectra. This again confirms the Sr enrichment on the permeate side.

Other elements detected by EDX at the reaction side include Cu, Na, C, S, Ca and Al. Na, Ca, Al could have been derived from the sodalime glass composition which contained these elements. While the origin of sulphur is not immediately clear, the Cu could have been derived from the copper paste applied to the membrane module as an anti-seize. However, a small Sulphur peak was also detected in fresh membrane which had not come into contact with the anti-seize paste. This might indicate that the S could be due to contamination during handling after fabrication. The detected C at the permeate side strengthens the carbonate formation proposal.

7.8.2.6 Kinetic de-mixing

A phenomenon well documented in literature regarding perovskite membranes in operation is kinetic demixing,(Jung and Edwards, 2012, Wang et al., 2011, Wang et al., 2009, Lein et al., 2006, Belova et al., 2004). Kinetic demixing in mixed ionic-electronic conducting membranes occurs over a long time exposure of the membranes under an oxygen chemical potential gradient at elevated temperatures. It has been established that when an oxygen ion conducting membrane is exposed to an oxygen chemical potential gradient, cations diffuse to the high oxygen chemical potential side due to the thermodynamic driving force. The mobilities of different cations due to this driving force in the material are different. As a result, according to this concept, the faster cations are enriched on the high oxygen chemical potential side (the airside) while the slower cations are enriched on the lower oxygen chemical potential side (Wang et al., 2009, Martin, 2003).

The results shown in *Table 7-1* seem to rule out the kinetic demixing phenomenon on the observed compositional changes at the reaction side of the used membrane. Firstly the apparent enrichment of Sr on the reaction side relative to La and other cations does not appear to be matched by an enrichment of the other cations at the air side of the same used membrane. Secondly, kinetic demixing is believed to depend on membrane thickness and is very slow that it would take a membrane hundreds to thousands of years in operation to have effect. For example, it is estimated that 1mm thickness of YSZ membrane would take 15 000 years, but 1.5 years only for a 10μm thick film of YSZ membrane (Martin, 2003). In the present work, a membrane of about 1 mm thickness was used, and although of a different material than YSZ, the total duration which the membrane was subjected to an oxygen chemical potential gradient was under 100 hours, a timescale far too short for any meaningful kinetic de-mixing to have occurred, according to this concept. For this reason, it is argued by this author that the relative Sr enrichment at the reaction side of the membrane was due to another phenomenon. Since the permeation experiments were done in inert as well as reactive conditions for the same membrane, a possibility is chemical reactions between the membrane surface material and the gases in the reaction side as proposed and reported by (ten Elshof et al., 1995b), to form new phases such as $SrCO_3$.

7.9 CONCLUSIONS

It has been demonstrated in the current work that combustion in the permeate side increases oxygen permeation flux. This is due to the effect of the combustion reaction has in drastically reducing the permeate side oxygen partial pressure, increase in oxygen vacancy gradient in the membrane bulk and the membrane temperature rise from the combustion reaction. In contrast, non-reactive operation has much less effect on oxygen partial pressure and relies on externally supplied heat to maintain high temperatures. This result has shown that bringing multiple functions together in one device can lead to better performance than the separate functions executed sequentially.

The results have shown that oxygen permeation of LSCF6428 mixed ion electronic conducting membranes is greater under reactive conditions than under inert conditions by up to 20 times. The proposed explanation for this is as follows:

The oxidation reactions take place at the permeate membrane surface where the fuel molecules are oxidised by surface lattice oxygen. Since the reactions are exothermic, there is a temperature rise in the membrane. The heat is conducted to the air side surface of the membrane where it enhances the temperature activated oxygen surface reactions and increase the supply of oxygen ions available for conduction to the permeate side. The increase in bulk membrane temperature also increases oxygen transport through membrane bulk since this transport is a thermally activated process, as the oxygen ions require adequate energy to overcome the energy barrier to hop to the next nearby oxygen vacancy. Therefore oxygen membrane reactors combining oxygen separation and a reaction offer major advantages over conventional processes due to the interaction of reaction, mass transfer and energy transfer.

From the point of view of the Wagner equation, oxidation reactions at the permeate side drastically reduces the oxygen partial pressure resulting in the amplification of the term $\ln\left(\frac{P_2}{P_1}\right)$ in the equation:

$$J_{O_2} \quad = \quad \frac{RT}{16LF^2}\sigma_i \ln\left(\frac{P_2}{P_1}\right) \qquad \text{Eqn 7.19}$$

where P_1 and P_2 are the oxygen partial pressure at the solid-gas boundaries at the permeate and air side membrane surfaces respectively. From the point of view of Fick’s Law as it applies to bulk diffusion as given by the equation

$$J_{O_2} = \frac{1}{2} D_{V_{\ddot{O}}} \left(\frac{C_{V_{\ddot{O}}\_perm} - C_{V_{\ddot{O}}\_air}}{L} \right) \qquad \text{Eqn 7.20}$$

where $D_{V_{\ddot{O}}}$ is the vacancy or oxygen ion diffusion coefficient, $C_{V_{\ddot{O}}\_air}$ is the oxygen vacancy concentration on the air side membrane surface, $C_{V_{\ddot{O}}\_perm}$ is the oxygen vacancy concentration on the permeate side membrane surface and L is the membrane thickness.

The consumption of lattice oxygen at the permeate membrane surface results in a steep oxygen vacancy gradient in the membrane bulk, which, in addition to membrane temperature rise, also amplifies the permeation driving force.

In contrast with inert sweep gas, there is no exothermic reaction at the membrane surface and hence no temperature rise to enhance oxygen surface exchange reactions and bulk diffusion. Heat to sustain the permeation has to be supplied from an external source, imposing an additional cost. There is also no enhancement of oxygen vacancies gradient in the membrane bulk as is the case with reactive sweep gas. With an inert sweep gas, oxygen partial pressure at the permeate side membrane surface, the removal (vanishing rate) of permeate oxygen only depend on the inert sweep gas flow rate.

The oxygen permeation has also been modelled in terms of an equivalent electrical circuit with the electrical potential represented by oxygen partial pressure, electrical current by oxygen ions, electrical resistance by the combination of oxygen exchange reactions at the airside and permeate side as well as oxygen ion diffusion resistance through the dense membrane bulk. The effect of chemical reactions in increasing oxygen flux using this qualitative model is explained in terms of lowering the permeate side exchange resistance due to the fast combustion reactions, the lowering of bulk diffusion resistance due to membrane temperature from the exothermic combustion reaction, the lowering of oxygen exchange reactions from increased airside membrane surface temperature; and the driving force owing to increased oxygen partial pressure differential from consumption of permeate oxygen.

7.10 Implication of findings

An important implication of these results is that this technology is more suited for combined separation and reaction than gas phase pure oxygen production as oxygen fluxes can be up to 20 times higher with an oxygen consuming reaction at the permeate side. As the reaction takes place at the solid/gas boundary of the membrane, the most suitable form of fuel is gaseous fuels which are able to diffuse to membrane surface to be oxidized. Promising applications for this includes oxyfuel combustion of gaseous hydrocarbons and partial oxidation reactions. In contrast, solid phase fuels combustion as in gasification would require that gas phase oxygen evolve from the membrane permeate side and diffuse to the solid fuel. As has been seen from this study, oxidation at the solid/gas interface using lattice oxygen provides the essential driving force for high oxygen permeation fluxes.

By selecting suitable reaction conditions at the permeate side, e.g. depositing a suitable catalyst on the membrane surface, it may be possible to influence reaction products of lattice oxygen with a hydrocarbon such as methane. This process is particularly attractive for conversion of natural gas into syngas, a key intermediate in the chemical processing industry. It may also be possible to enhance surface exchange reactions at the air side by depositing a catalyst that enhances the exchange reactions and improve oxygen flux further. These two aspects were outside the scope of this study and is a good research area that can be looked at in future with a system that can operate at much higher temperatures thus increasing oxygen flux.

7.11 Limitations of study

A major limitation in the experiments was the working temperatures permitted for Health and Safety reasons. The maximum operating temperature was 650^{o}C, which is the lower end of the membrane activation temperature range for oxygen transport through these materials. Higher temperatures of 900-1000^{o}C could yield much higher flux, not only due to higher oxygen conduction activation, but also oxygen exchange reactions which are also temperature dependent. In addition such higher temperatures would improve the sealing performance of the soft glass as at these temperatures; it can be viscous, allowing it to heal any cracks that may have formed due to thermal expansion mismatches between the glass, stainless steel and LSCF6428 materials.

Chapter 8 : PLASMA ACTIVATED HYDROGEN PRODUCTION FROM METHANE

8.1 Plasma fundamentals

The existence of plasma was first predicted by Michael Faraday in 1820 but it was Irving Langmuir and co-workers who first studied it in 1929 during the development of vacuum tubes for large currents. They coined the term “plasma” to describe the glowing inner region they observed in the discharge tube.

Plasma has often been referred to as the “fourth state of matter”, with the other three being solids, liquids and gases. From conventional wisdom, the basic distinction between solids, liquids and gases lies in the difference between the strength of inter-particle bonds. These binding forces are strong in solids, weak in liquids and almost non-existent in gases. For any given substance to exist in any of the three fundamental states (solid, liquid or gas), it is dependent on the random kinetic energy of the particles compared to the inter-particle bonding forces. According to (Fridman, 2008), as the temperature increases, particles gain more kinetic energy and are able to break the inter-particle bonds, transforming the substance in the sequence solid → liquid → gas → plasma. Plasma is obtained when an amount of energy higher than ionization is added to neutral particles and result in the creation of free ions and electrons. This energy can be heat but it is usually in the electromagnetic form, e.g. electric field, microwave and radio frequency. For thermally activated plasma for instance, at sufficiently high temperatures, the atoms in a gas can start decomposing into charged particles (ions and electrons) to form plasma. The charged particles can be influenced by an electric field. If the ionisation energy is withdrawn, the plasma is extinguished. Plasma can be characterized by the degree of ionization. In high temperature plasma, the ionization is full and is called completely ionized plasma. If a small fraction of the gas is ionized it is called weakly ionized plasma. The density ratio of heavy charged species to that of neutral particles in conventional plasma-chemical systems is in the range 10^{-7} -10^{-4} (Eliasson and Kogelschatz, 1991).

Plasma essentially is an electrified, but quasi-neutral media (net charge is zero) (Vandenbroucke et al., 2011), consisting of a large number of different species such as positive and negative ions, free radicals, molecules, atoms and electrons. Since the masses of ions, radicals and neutral particles are much higher than the electrons in the plasma, the electrons are normally regarded as light particles while ions, radicals, and neutrals are called heavy particles.

Gas discharge is the most common approach to produce plasma. A gas discharge is created when an electric field of sufficient strength is applied to a volume of gas to generate electron–ion pairs by electron impact ionization of neutral gas molecules. Generation of plasma would normally require the presence of an initiating number of free electrons, either present from ambient conditions or purposely introduced. The growth in the densities of electron-ion is accompanied by an increase in the densities of excited states such as ions, electrons.

8.2 Types of plasma

Plasma can be divided into two types, high temperature (fusion) plasma and the low temperature plasma also called gas discharges. High temperature plasma is also referred to as thermal or equilibrium plasma while the low temperature type is called cold, non-thermal or non-equilibrium plasma, based on the relationship between the gas (heavy particles) temperature and electron (light particles) temperature. Thermal plasma is considered equilibrium plasma as the gas molecules and electrons are roughly at the same temperature whilst cold plasma is non-equilibrium because electrons are at very high temperatures (kinetic energy) while gas molecules are at much lower temperatures (ambient temperature).

8.2.1 Thermal plasma

In thermal plasma, also called thermodynamic equilibrium plasma or high temperature plasma, the temperature of the heavy particles (ions and neutral species) is close to the thermal kinetic energy of the electrons (light particles) and are therefore more or less in thermal equilibrium.

$$T_e \approx T_i \approx T_n = 10^4 - 10^5\ K$$

where T_e, T_i and T_n are electron temperature, ion temperature and neutrals temperature respectively. Common thermal plasma includes plasma torches and microwave devices which produce high fluxes of heat.

8.2.2 Cold /Non-thermal plasma

Cold plasma is plasma in which the temperature of the light particles (electrons), T_e is much higher (very hot electrons) than the temperature of the heavy particles (cold), ions and neutrals.

$$T_e \gg T_i \approx T_n \cong 300K$$

T_e is in the region 10^4-10^5 (1-10eV). (1eV = 11 600K (Bárdos and Baránková, 2010, Fridman, 2008)). The heavy particles and light particles are therefore in a state of thermal non-equilibrium. This existence of various types of plasma particles with various degrees of freedom allows cold plasma to remain away from thermodynamic equilibrium.

Cold plasma is commonly formed by adding some electrical energy which is channelled through the electron component of the plasma, thereby producing energetic electrons rather than heating the entire gas stream. A strong enough electric field applied between two electrodes accelerates charged particles in the space between the electrodes while the neutral species (e.g. molecules) are not affected by the electric field. From physics basics, acceleration a of a charged particle of mass m in an electric field E is given by Eqn 8.1.

$$a = \frac{zeE}{m} \qquad \text{Eqn 8.1}$$

where z is the charge number of the particle and e is the electronic charge. The negatively charged electron and a singly charged positive ion have the same charge of 1.6×10^{-19}C, but different masses. The mass of an electron 9.11×10^{-31}kg is approximately $10^3 - 10^4$ times lower than the mass of ions $(\text{mass number} \times (\text{proton or neutron mass } 1.67 \times^{-27}$ kg). Therefore the mass of an ion m_i is much greater than that of an electron m_e, $(m_i \gg m_e)$. The lighter mobile electrons are accelerated much more than ions (Bárdos and Baránková, 2010). Hence, due to their tiny mass, electrons are able to reach much higher kinetic energy $(\frac{1}{2}mv^2)$ than any heavy charged particle (ion) in the same electric field. This means the electron temperature is much higher than that of heavy particles, typically 10^4 - 10^5K (1-10eV) (Carman and Mildren, 2000) and 2-3 orders of magnitude higher than that of heavy particles. In low pressure plasma where collision frequency is low, and average electron energy remains high.

When delivering plasma power into a gas to form a gas discharge, only a fraction of the energetic electrons have enough energy to excite gas moles (ionization, dissociation, vibrational and rotational excitation). Electronic energy distribution in plasma is widely believed to approximate Maxwell-Boltzmann distribution function (Yang, 2003).

This is illustrated by *Figure 8-1* below showing a typical Maxwell-Boltzmann Distribution curve plotting fraction of electrons versus electron energy. For given electron energy E_t, the shaded area represents the total fraction satisfying:

$$E_{electron} \geq E_t$$

If E_t is the threshold electron energy to chemically excite a given gaseous species, the area shaded represents the fraction of the plasma energetic electron population capable of exciting that species. The remainder of the area, to the left of E_t represent the fraction of the plasma electron population with energy below the threshold required to excite reactant molecules. This represents ineffective energy that is lost. An increase in the applied activating field, e.g. voltage, shifts the function to the right as shown in *Figure 8-2*, to increase the proportion of electrons with enough energy to stimulate conversion reactions.

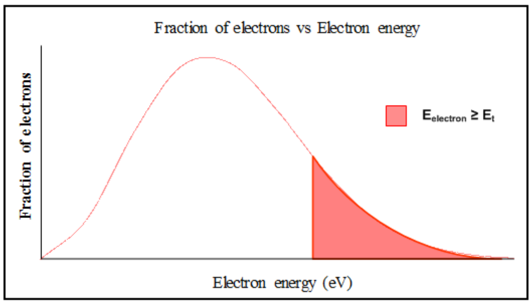

Figure 8-1 An illustration of Maxwell –Boltzmann Electron Energy Distribution function.

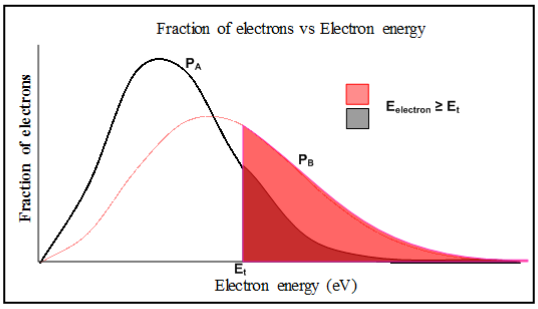

Figure 8-2 Two typical Maxwell-Boltzmann distribution functions P_A *and* P_B *of electron energies in plasma excited by two different voltages,* V_A *and* V_B *with* $V_B > V_A$*, showing that an increase in applied voltage shifts the electron energy distribution function to the right (higher energy), leading to an increase in excitation and ionisation coefficients of the discharge gas in the plasma zone.*

8.2.3 Non-thermal Plasma activated chemical reactions

Plasma in environment protection (pollution control) and chemical processing are currently the subject of intense development. Non-thermal plasma overcomes the disadvantage of high temperatures of thermochemical processes, hence their potential for low operating and capital costs. In early days, cold plasma was operated in a vacuum. However, applying vacuum made the process expensive and has given rise to cold atmospheric pressure plasma which has the potential to reduce equipment and processing costs through elimination of the need for vacuum reaction.

The high energy electrons $(1 - 10\text{eV})$ in cold plasma play an important role in initiating plasma chemistry reactions in cold plasma. They can excite most chemical species including those that are difficult or cannot be excited in conventional chemistry. For example, as is well known, it is difficult, using traditional thermocatalytic methods, to couple methane into C_2 hydrocarbons (ethane, ethene and acetylene), and higher hydrocarbons, due to high dissociation energy of the methane $\mathrm{C-H}$ bond, yet this is possible at ambient temperature and pressure conditions with non-thermal plasma (Lü and Li, 2010). There are also reports of non-thermal activated synthesis of ammonia from N_2 and H_2 (Mingdong et al., 2000), two gaseous elements with very high bond energies and requiring high temperatures and high pressures in the presence of catalysts with traditional chemistry. This illustrates that non-thermal plasma can easily overcome this energy barrier under ambient temperature conditions. The energetic electrons collide with molecules in the bulk gas to which they transfer their energy resulting in different forms of excitation thus triggering some chemical reactions between the excited species. The gas molecules are decomposed via mechanisms such as electron impact dissociation, ionization, recombinations, secondary ionization, ion-molecule reactions, radical-molecule reactions and neutral species reactions (Birmingham and Moore, 1990). A factor that influences the ability of energetic electrons to excite neutral species during collisions is the gas pressure in the plasma discharge zone (Eliasson and Kogelschatz, 1991). At any given temperature, gas pressure defines the density of the gas particles and consequently also the probability of mutual collisions among particles (collision frequency). Under high pressure conditions, inter-particle collisions occur more frequently and applying plasma under such conditions imply that the energetic electrons collide with heavier particles more frequently resulting in a shorter electron mean free path between collisions with heavy particles. This means electrons have shorter distances over which they are accelerated before the next collision and this limits the maximum velocity they can attain and consequently the maximum kinetic energy the electrons can attain. A stronger electric field would be necessary under higher pressure. The electric field strength is given by the $\frac{V}{d}$, where V is the applied voltage and d is the distance between the two electrodes. The electric field strength can be optimised by either varying V or d or both.

The energetic electrons, on collision with heavy neutrals, can trigger chemical reactions through the various interactions of the excited species (radicals, ions, vibrationally excited molecules). These excited species are highly reactive and their interactions result in the formation of new products.

Cold plasmas therefore have a unique property of being capable of generating chemically active species at low temperatures. Since the ions, radicals, vibrationally excited species and neutrals remain relatively cold; this characteristic provides the potential of using cold plasma in low temperature chemistry applications and treatment of heat sensitive materials such as polymers and biological tissues. These features can be extended to conversion of gaseous hydrocarbons such as natural gas using cold plasma chemistry. Thermodynamically, methane activation requires high temperature of up to 1373K (Kado et al., 2003). Therefore non-thermal plasma in methane activation for conversion to other products could contribute to energy savings as it eliminates or minimises the need to expend energy in heat as is necessary in thermochemical processes. Moreover, the reactor can be constructed from inexpensive materials such as glass or polymers instead of high specification high temperature resistant materials. The simplicity and possibility to miniaturize cold plasma devices potentially permit significant process intensification of traditional chemical processes, increasing efficiency and stimulating chemical reactions impossible in conventional chemistry (Fridman, 2008). Possible applications of non-thermal plasma are many, including the treatment of surfaces, gases, environmental protection from industrially emissions of Volatile Organic Compounds (VOCs) and wastewater treatment (Moreau et al., 2008).

8.3 Some current non-equilibrium plasma applications

In the past few decades, non-equilibrium plasma has attracted a lot of interest in plasma-assisted catalytic VOCs abatement (Vandenbroucke et al., 2011, Quoc An et al., 2011, Van Durme et al., 2008), wastewater treatment (Manoj Kumar Reddy et al., 2013), electronics, surface modification of polymers (Liu et al., 2004), disinfection by destruction of micro-organisms (Radacsi et al.) and ozone generation (Yehia, 2012). Ozone is a strong oxidant that can kill odours.

VOCs are a large group of pollutants emitted from various industrial chemical processes. Their volatility causes them to rapidly evaporate into the atmosphere and, depending on their chemical structure; they can cause various effects such as creation of photochemical smog, secondary aerosols and eventually intensification of global warming effects. They can also be an odour nuisance as well as cause carcinogenic effects (Vandenbroucke et al., 2011). VOCs that have been studied for their abatement using non-thermal plasma include benzene, xylene, toluene, formaldehyde, formic acid, trichloroethylene, dichloromethane (Van Durme et al., 2008). Reactive species in non-thermal plasma such as OH radicals, O_3 molecules and O atoms can react with odorous and toxic gases and vapours to convert them into non-odorous and non-toxic molecules (Preis et al., 2013).

In wastewater treatment, non-thermal discharge can play several roles. The discharge can physically destroy biological cells while the UV emitted can induce photochemistry that can destroy some micro-organisms. In the gas-liquid environment the active species formed by plasma in the gas phase can diffuse into the liquid and subsequently form hydroxyl radicals in the liquid. These can react with water to form H_2O_2, a strong oxidant that kills micro-organisms in the liquid (Fridman, 2008).

There are various forms of non-equilibrium plasma. They include corona discharge (Malik and Jiang, 1999), glow discharge, gliding arc (Rueangjitt et al., 2007), microwave (Zhang et al., 2002), radio frequency (Tsai and Hsieh, 2004), dielectric barrier discharge (DBD) (Kraus et al., 2002, Liu et al., 2001, Song et al., 2004). Reviews of these forms non-equilibrium plasmas have also been presented by (Eliasson and Kogelschatz, 1991, Moreau et al., 2008). Of these forms of non-equilibrium plasma, DBD or silent discharge is among those with the highest potential.

8.4 DBD plasma

DBD can generate non-thermal plasma in very simple and flexible ways in terms of configuration, operating medium and parameters. It has potentially a large number of industrial applications because it can operate at strongly non-equilibrium conditions at ambient pressure and reasonably high power levels using sinusoidal power supply without sophisticated pulsed power supply equipment (Fridman et al., 2005, Kogelschatz et al., 1997). DBD plasma characteristics can be easily manipulated by adjusting operating parameters such as applied voltage, frequency, pressure and operating media such as type, size and shape of dielectric pellets in the plasma zone. These features make DBD attractive for a variety of applications. It already has a long history originating from its use in ozone generation and its fundamental physical properties are now well understood (Kogelschatz, 2003).

Dielectric Barrier Discharge (DBD) plasma discharges are based on the use of, as the name implies, a dielectric barrier in the discharge gap. A key feature of DBD is that a dielectric layer covers at least one of the electrodes. The barrier has two main functions. The first is to limit the amount of transported charge and energy in a single micro-discharge. This enables it to be easily extinguished by reducing the applied voltage below the breakdown voltage. Secondly, it allows discharge filaments to form in close proximity but distribute the micro-discharges over the electrode surface

(Liu et al., 2004) thus creating a volume discharge. Sinusoidal voltages of a few kV and frequencies of between 5-500 kHz are used to generate DBD plasma. A DBD reactor can also be packed with dielectric pellets and plasma is created in the void spaces between the pellets (Birmingham and Moore, 1990). The pellets refract the electric field, making it non-uniform and stronger than the externally applied field by a factor of 10 to 250 (Holzer et al., 2005) depending on shape, porosity and dielectric properties of the pellets. Ferroelectric materials called ferroelectric ceramics with high permittivity of greater than 1000 are commonly used as packed material in DBD plasma. The key property of ferroelectric materials is that they have a significant dipole moment even in the absence of an external electric field. An external AC voltage leads to over-polarisation of the ferroelectric material and result in strong electric fields on the surface which can exceed 10^6V/cm and stimulates the discharge on the ferroelectric surfaces. Ceramics based on $BaTiO_3$ are most commonly employed for the discharges (Fridman, 2008).

DBD can be implemented using two main geometrical structures; planar with two electrodes parallel to each other, and concentric where one electrode is located inside the other as shown in *Figure 8-3*. In both cases, either one or both electrodes are covered by a thin dielectric layer for discharge stabilization and to prevent sparks. The concentric structure is the more widely used due to its simplicity and it will be used in the current work. The design and fabrication of this configuration of DBD plasma reactor is simple and is easily and scalable by using multiple units for large scale applications.

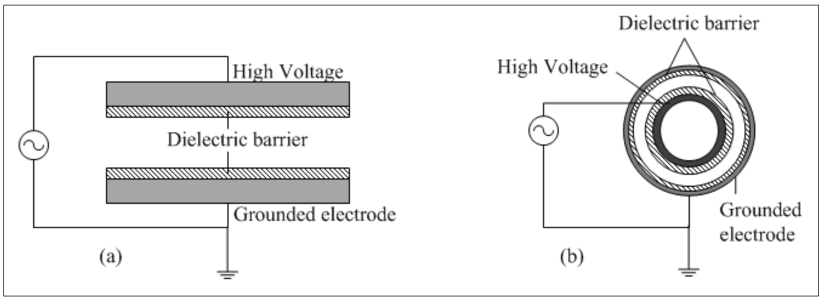

Figure 8-3 Main geometric configurations of DBD plasma (a) planar, (b) concentric

8.4.1 Analytical illustration of the effect of dielectric packing in DBD plasma

Owing to the capacitive coupling, time varying voltage is required to drive the DBD plasma and it can be shown mathematically that by treating the reactor as a concentric capacitor and consideration of discharge physics that the material dielectric constant of the material between the electrodes has an effect on charge that can be stored in the capacitor and hence the electric field and performance of the plasma device. The concentric plasma reactor configuration is considered in this illustration. It can be viewed as a cylindrical electric capacitor consisting of a solid cylindrical conductor, of radius a surrounded by a coaxial cylindrical shell of inner radius b. The length of both cylinders is L and is assumed much greater than the separation of the two cylinders, (i.e. $L \gg (b-a)$), to minimize edge effects in this analytical illustration. The capacitance of this configuration is given by:

$$\mathrm{C} \quad = \quad \frac{2\pi\epsilon_0\epsilon_r \mathrm{L}}{\ln\left(\frac{\mathrm{b}}{\mathrm{a}}\right)} \qquad \text{Eqn 8.2}$$

where C = Capacitance in Faradays, ϵ_r = relative permittivity of the dielectric material between the electrodes, $\epsilon_0 (= 8.9 \times 10^{-12} Fm^{-1})$ is the permittivity of free space, L = the length of the electrode, b = inside radius of outer electrode/shell, a = outside radius of inner electrode. In a capacitor, charge stored is related to voltage applied and capacitance by Eqn 8.3 and Eqn 8.4.

$$\mathrm{Q} \quad = \quad \mathrm{CV} \qquad \text{Eqn 8.3}$$

$$\therefore \ \mathrm{Q} \quad = \quad \frac{2\pi\epsilon_0\epsilon_r \mathrm{L} \cdot \mathrm{V}}{\ln\left(\frac{\mathrm{b}}{\mathrm{a}}\right)} \qquad \text{Eqn 8.4}$$

where Q = electric charge stored in capacitor, V = input Voltage.

According to the equation Eqn 8.4, the charge stored is proportional to relative permittivity of the dielectric material between the electrodes. This is because if the permittivity is higher, the polarisation of the dielectric will be much stronger. This charge accumulates on the surface of the packed pellets and is responsible for the high electric fields in the discharge volume especially at contact points between the pellets. The enhanced electric field result in lower breakdown voltage with materials with high relative permittivity than with materials with low relative permittivity.

8.5 Non-thermal plasma in Process Intensification

Non-thermal plasma is also seen as fitting into the definition of Process Intensification (Charpentier, 2007) (Reay, 2005, Stankiewicz and Moulijn, 2003), especially in the field of hydrogen production. Intensified non-thermal plasma activated dry reforming of methane with carbon dioxide is an attractive alternative to the energy intensive and expensive conventional steam reforming or thermocatalytic dry reforming of methane with carbon dioxide. Non-thermal plasma dry reforming is implemented at low gas temperatures (ambient) using high energy electrons (10^4-10^5K) to stimulate chemical reactions. This process provides huge energy savings by eliminating the need to heat reactors. In addition the reactors can be small, compact and can be made from less expensive materials due to low temperature operations. Scaling up can be achieved by employing multiple such compact microreactors, lending itself to small scale operations not possible with conventional processes. It is in these respects that these reactors meet process intensification criteria.

The main goal of process intensification is to make substantial improvements to the efficiencies of chemical processes and plants by developing innovative methods and technologies. Non-thermal atmospheric pressure plasma uniquely generates reactive species almost independently of temperature to initiate chemical reactions much lower than conventional thermochemical reactions.

Because of its non-equilibrium nature, non-thermal plasma allows thermodynamic barriers to be overcome, enabling thermodynamically unfavourable reactions to occur at low temperatures and pressures (Tu and Whitehead, 2012). Non-thermal plasma reforming is implemented at low gas temperatures (ambient) using high energy electrons (10^4-10^5K) to stimulate chemical reactions. This process can provide huge energy savings by eliminating the need to heat reactors. In addition the reactors can be small (miniaturized), compact and can be made from less expensive materials due to low temperature operations. Scaling up can be achieved by employing multiple such compact reactors, lending itself to small scale operations not possible with conventional processes. Potential uses include conversion of biogas resources and unconventional natural gas streams such as oil-associated gas.

A concern that has often been raised in literature regarding plasma activated reforming is the low energy efficiency. In an actual system, there are various forms of energy loss. First is the Electron Distribution function discussed in Section 8.2.2 Clearly not all electrons in the plasma have enough energy to induce chemical reactions. The proportion of electrons with inadequate energy to induce chemical reactions represents a form of energy not put to use and therefore lost. In addition, the input electrical energy is distributed not only to electrons, but also ions present in the plasma resulting in energy loss referred to as “joule heating”. A further loss is in the form of ion-electron re-combinations as well as radical recombination to original input gas. For example, in methane conversion, CH_3 and H might recombine to form original CH_4 instead of C_2H_6 and H_2 (Nozaki and Okazaki, 2013).There is therefore some lost energy associated with such re-combinations.

Chapter 9 : EXPERIMENTAL

9.1 Investigation of hydrogen/syngas production from methane and carbon dioxide using plasma technology

An alternative novel method for the production of hydrogen/syngas from methane using plasma technology was conducted. The plasma reactor used in these investigations is illustrated schematically by *Figure 9-1* which is essentially a coaxial reactor (annular) with a central rod inside the inner tube.

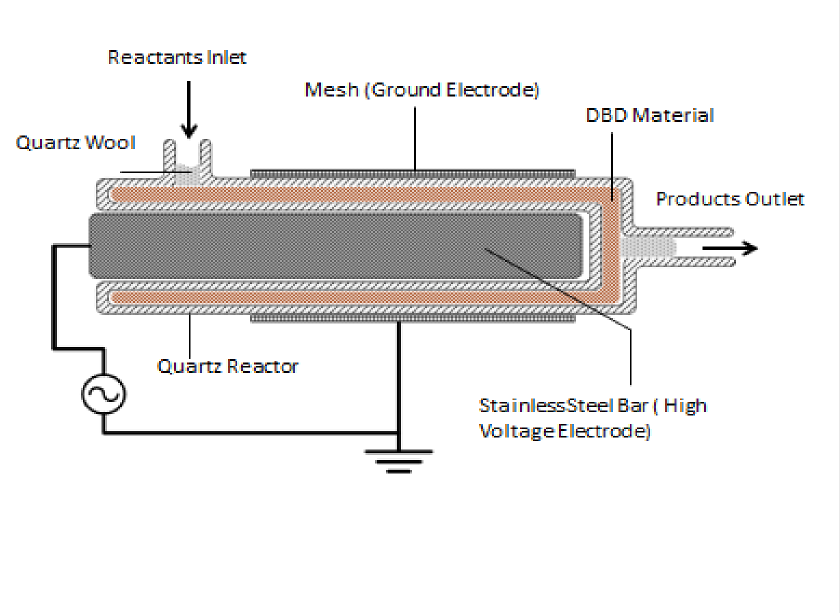

Figure 9-1 Schematic showing plasma reactor used

The plasma reactor consists of two quartz tubes of 1.5mm wall thickness, one inside the other. The outer tube had an inside diameter (ID) of 32mm and was of length 300mm. The inner tube had an outside diameter (OD) of 17mm thus leaving a 7.5mm gap between them. In general, a DBD reactor consists of one or more insulating layers between the electrodes in addition to the discharge gap. The insulating layers in the configuration used are the non-conducting walls of the concentric quartz tubes. This discharge gap is packed with different dielectric materials ($BaTiO_3$, sodalime glass or borosilicate balls). A comparison of the effect of these materials on plasma conversions of CH_4 or CH_4/CO_2 mixture was evaluated in the present work. Effect of catalyst on plasma reactions was also evaluated by dispersing supported catalyst particles (on silica/alumina) within the plasma zone, amongst the packed balls/pellets. *Figure 9-2* shows a cross sectional view of the reactor packed with balls/pellets in the annular discharge gap. A stainless steel rod inserted inside the inside tube served as the high voltage (HV) electrode while a wire gauze wrapped around the outside tube served as the ground electrode. The effective electrode length was 17.3cm, giving a plasma volume of 100mL.

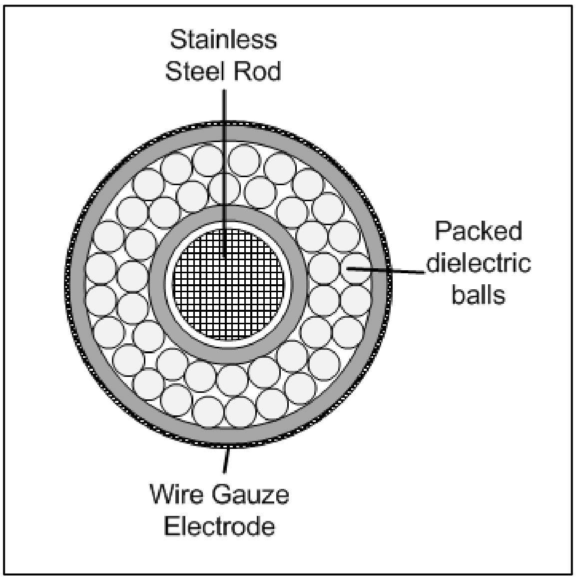

Figure 9-2 Cross-sectional view of plasma reactor packed with dielectric balls

Regarding the effect of dielectric material placed in the discharge gap:

1. Gas (no dielectric balls/pellets packed) – no plasma was generated with this size of gap even with voltage increased to the maximum possible from the power supply unit.

2. $BaTiO_3$ (BTO) balls – Plasma was easily generated even at low applied voltages.

3. Sodalime glass balls (SLG) – plasma generated, but ignition required a much higher onset voltage to ignite.

4. Borosilicate glass balls (BSG) – plasma not generated even at maximum possible voltage from the power supply unit, just as with gas in (1).

These results can be explained in terms of dielectric properties of the material packed in the discharge gap, with permittivity ε in the following order; BTO > SLG > BSG > Gas (air/methane or methane and carbon dioxide mixture).

9.2 Experimental Section

The experiments were conducted using the set-up illustrated in the schematic in

Figure 9-3. For all conditions studied, the feed gas mixture was first introduced into the reactor with the plasma turned off for about 30 min in order to purge air out of the reactor, replacing it with the gas mixture under investigation, and to stabilise the flow. The outlet gas composition was analysed with the Varian 450 GC several times to ensure the measured composition was invariant with time. The plasma was then ignited and again allowed to run for another 30 minutes to allow the system to stabilise and reach steady state conditions before the effluent composition was measured again. For each studied condition the composition was measured twice and the result averaged. During the experiments, reactor temperature was measured using an infrared thermometer. The measured temperature when plasma was on was found to be about 120^{o}C. The tubing connecting the reactor outlet to the GC was about two metres and this allowed the gas to cool down to close to room temperature. The gases were introduced into the reactor through digital mass flow meters (Bronkhorst EL-Flow) to control both the flowrate as well as mixture proportions. During plasma reactions, volume changes might occur when new products are formed. To monitor these volume changes during experiments, a small amount of nitrogen was added using a mass flow controller to the effluent before being fed into the analytical Varian 450 GC (Ref Gas). Volume changes were computed by comparing the nitrogen molar content in the effluent with the reactants introduced into the reactor with plasma power off, and with the reactants introduced at same flowrate and proportions but this time with plasma power on. Changes in the nitrogen molar content indicate volume change. The formulae for volume change calculations are presented in Section 9.3.1

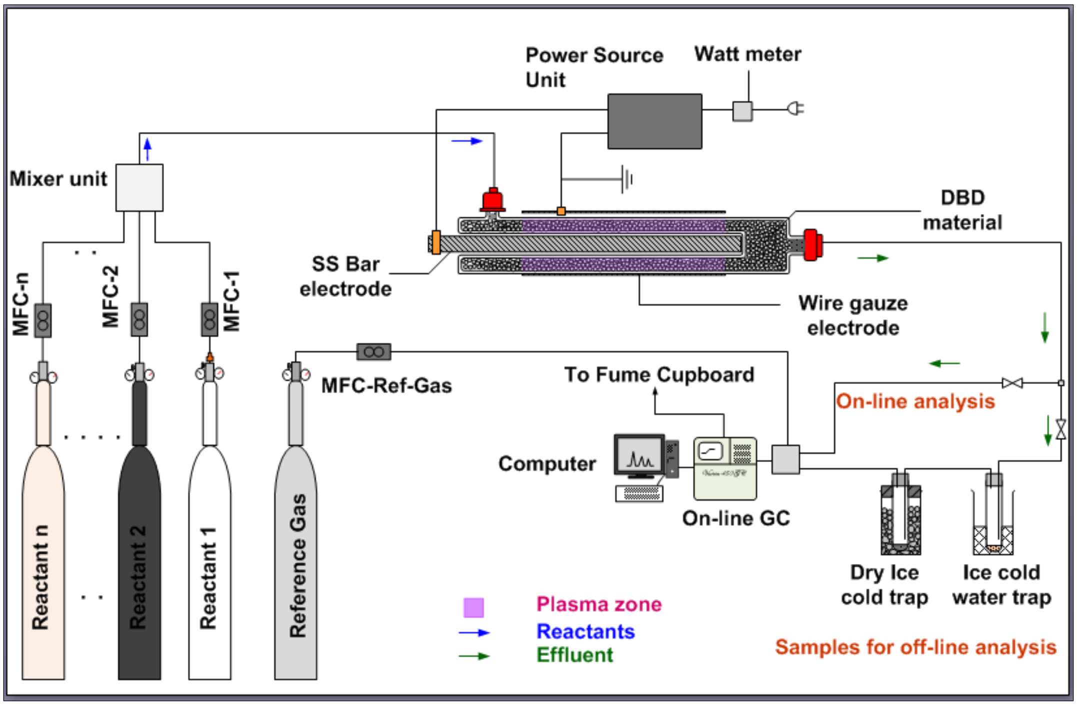

Figure 9-3 Plasma reactor set-up

The three-way Varian 450 GC used was equipped with three columns, one terminated with a TCD detector and calibrated using certified gas standards for identifying O_2, H_2, N_2, CO_2, CO and CH_4, the second column (CP-Sil5 CB) was terminated with an FID detector for detection of hydrocarbons and was calibrated to identify only a limited number of hydrocarbons such as ethane, ethene, propene, propane, butane, butene, pentene, pentane etc. The third column (CP-Wax52 CB) was terminated with an FID detector and was calibrated to identify a limited number of oxygenates such as methanol, ethanol, butanol etc.

The plasma was activated by a sinusoidal high voltage generator of up to 10kV and a fixed frequency of 20 kHz, and the electrical power supplied was measured using a digital Wattmeter. The Wattmeter, which was plugged at the wall socket, measured power consumed by the set-up which included ohmic losses in the power source unit circuitry. The applied plasma power could be varied by varying the sinusoidal voltage amplitude through a variable transformer which was part of power source unit. The actual plasma power applied was estimated by subtracting the ohmic power losses in the power source unit estimated at about 10W. *Figure 9-4* shows a photograph of the plasma reactor taken under dark conditions showing that DBD plasma is also rich in UV photons.

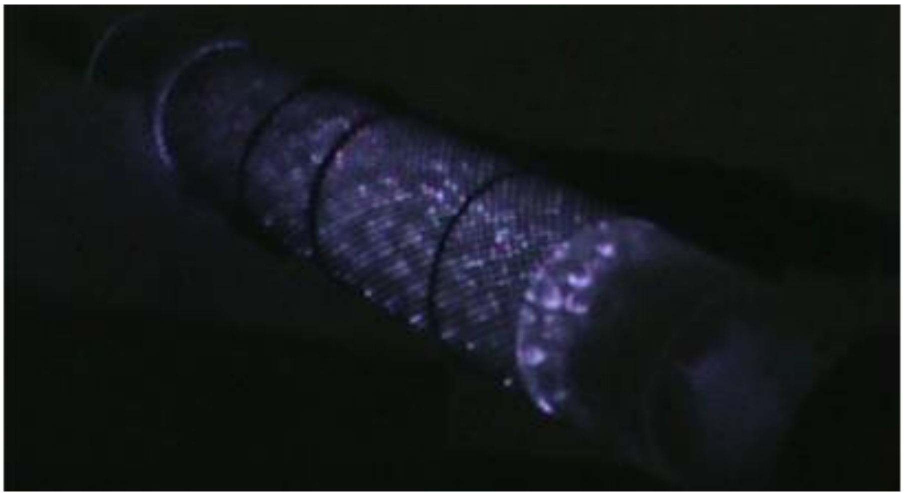

Figure 9-4 Picture of the plasma taken in darkness

A provision was made in the experimental set up to pass the effluent gases through two cold traps made from glass thimbles, connected in series for collecting liquid products. The first (nearer the reactor) was an ice cold water cold trap to condense any products with boiling points above 0^oC such as water and oxygenates that may be formed. The second was a dry ice cooled cold trap to condense any products whose boiling points were between -78^oC and 0^oC. The liquefied products captured could then be analysed off-line using the GC. In these experiments, the reactants used were pure CH_4 or CH_4/CO_2 as co-reactants while the reference gas used was N_2. The cold traps were used to capture liquefiable products of plasma reaction.

9.3 Products analysis and calculations

The following sections define the various parameters that will be used in studying the performance of the plasma based reforming of reactants.

9.3.1 Volume change, conversions and selectivity calculations

Plasma reactions may result in volume changes due to conversion of the reactants into new products. Following are the equations that relate mole concentration of gases in the product stream to their relative volume (or flow rate), using nitrogen, which does not participate in the plasma reactions and is added into the effluent stream at a known constant flowrate, as standard.

Before plasma power is applied, nitrogen mole concentration is related to nitrogen volumetric flowrate and total flowrate by:

$$N_{2\_b}\% = \frac{V_{b\_N_2} \times 100}{V_{b\_Total}} \qquad \text{Eqn 9.1}$$

After plasma power is applied, nitrogen mole concentration is related to nitrogen volumetric flowrate and total flowrate by:

$$N_{2\_a}\% = \frac{V_{a\_N_2} \times 100}{V_{a\_Total}} \qquad \text{Eqn 9.2}$$

where subscripts *b* and a stand for before/without and after/with plasma.

$$V_{b\_total} = V_{b\_N_2} + V_{b\_CH_4} + V_{b\_CO_2} \qquad \text{Eqn 9.3}$$

$$V_{a\_total} = V_{a\_N_2} + V_{a\_CH_4} + V_{a\_CO_2} \qquad \text{Eqn 9.4}$$

Hence

$$V_{b\_Total} = \frac{V_{b\_N_2}}{N_{2\_b}\%} \times 100 \qquad \text{Eqn 9.5}$$

$$V_{a\_Total} = \frac{V_{a\_N_2}}{N_{2\_a}\%} \times 100 \qquad \text{Eqn 9.6}$$

$V_{b\_N_2} = V_{a\_N_2}$ since nitrogen, the reference gas does not pass through the reactor and it is fed into the GC at a constant flow rate.

Now from Eqn 9.5and Eqn 9.6,

$$\frac{V_{a\_Total}}{V_{b\_Total}} = \frac{N_{2\_b}\%}{N_{2\_a}\%} \qquad \text{Eqn 9.7}$$

$$\therefore\ V_{a\_Total} = \frac{N_{2\_b}\%}{N_{2\_a}\%} \times V_{b\_Total}$$ Eqn 9.8

9.3.2 Reactant conversion calculations from GC analysis

For a calibrated gas on the GC, there is also a relationship between the molar concentration of a gas component and the chromatograph peak area of that component. The molar concentration is directly proportional to the area of its chromatograph peak. This relationship enables the changes in reactant concentration due to conversion, and therefore the conversions themselves, to be easily computed from the changes in reactant peak area due to plasma reactions. Calculations of reactants conversions were therefore based on peak areas according to the following expressions:

$$\mathrm{CH_4 conversion\ \%} = \frac{\mathrm{CH_4\ peak\ area\ without\ plasma} - \mathrm{CH_4 peak\ area\ with\ plasma}}{\mathrm{CH_4 peak\ area\ without\ plasma}} \times 100$$ Eqn 9.9

$$\mathrm{CO_2 conversion\ \%} = \frac{\mathrm{CO_2\ peak\ area\ without\ plasma} - \mathrm{CO_2 peak\ area\ with\ plasma}}{\mathrm{CH_4 peak\ area\ without\ plasma}} \times 100$$ Eqn 9.10

9.4 Selectivity (S_i) and yield (Y_i) and parameters

Product selectivity S_i is a measure of how much product species i is produced compared to all the other products. As an example, the selectivity of hydrogen from a reaction involving hydrogen containing reagents can be defined as:

$$S_{H_2}(\%) = \frac{\mathrm{moles\ of\ H_2\ produced}}{\mathrm{total\ moles\ of\ H_2\ in\ products}} \times 100$$ Eqn 9.11

For hydrogen produced from converted methane, the selectivity is given by:

$$S_{H_2}(\%) = \frac{\mathrm{moles\ of\ H_2\ produced}}{2 \times \mathrm{moles\ of\ CH_4\ converted}} \times 100$$ Eqn 9.12

The 2 in the denominator signifies that there are twice as much equivalent moles of

H_2 in all the products from converted methane compared to the moles of converted methane. For products CO and any hydrocarbon $\mathrm{C_mH_n}$ from dry reforming reaction of methane with carbon dioxide, the selectivities are given by:

$$\mathrm{S_{CO}(\%)} = \frac{\text{moles of CO produced}}{\text{moles of CH}_4\text{converted} + \text{moles of CO}_2\text{converted}} \times 100 \qquad \text{Eqn 9.13}$$

$$\mathrm{S_{C_mH_n}(\%)} = \frac{\text{m} \times \text{moles of C}_\text{m}\text{H}_\text{n}\text{ produced}}{\text{moles of CH}_4\text{converted} + \text{moles of CO}_2\text{converted}} \times 100 \qquad \text{Eqn 9.14}$$

These are based on the assumption that the carbon in CO and C_mH_n can only originate from either the methane or carbon dioxide or both.

Product yield Y_i is defined as the amount of the desired product $i,$ divided by the maximum possible amount of the product that could be yielded from the reactants. For example, the hydrogen yield $Y_{H_2}$from conversion of a fuel will be defined as:

$$\mathrm{Y_{H_2}(\%)} = \frac{\text{moles of H}_2\text{ produced}}{\text{number of H}_2\text{ moles in fuel}} \times 100 \qquad \text{Eqn 9.15}$$

For hydrogen produced in dry reforming of methane with carbon dioxide, the hydrogen yield $Y_{H_2}$is given by:

$$\mathrm{Y_{H_2}(\%)} = \frac{\text{moles of H}_2\text{ produced}}{2 \times \text{moles of CH}_4\text{ input}} \times 100 \qquad \text{Eqn 9.16}$$

The CO yield Y_{CO} is given by:

$$\mathrm{Y_{CO}(\%)} = \frac{\text{moles of CO produced}}{\text{moles of CH}_4\text{input} + \text{moles of CO}_2\text{input}} \times 100 \qquad \text{Eqn 9.17}$$

9.5 Calculation of Volumes Reactants and Products

$$\text{Vol of conv CH}_4 = \frac{\text{CH}_4\text{ peak area without plasma} - \text{CH}_4\text{peak area with plasma}}{\text{CH}_4\text{peak area without plasma}} \times \text{CH}_4\text{feed flowrate} \quad \text{Eqn 9.18}$$

$$\text{Vol of conv CO}_2 = \frac{\text{CO}_2\text{ peak area without plasma} - \text{CO}_2\text{peak area with plasma}}{\text{CH}_4\text{peak area without plasma}} \times \text{CO}_2\text{feed flowrate} \quad \text{Eqn 9.19}$$

$$\text{CO produced (mL)} = \text{CO}_\text{a}\% \times \text{V}_{\text{a\_Total}} \quad \text{Eqn 9.20}$$

$$\text{H}_2\text{ produce (ml)} = \text{H}_{2\text{\_a}}\% \times \text{V}_{\text{a\_Total}} \quad \text{Eqn 9.21}$$

9.6 Product ratio and Carbon balance parameters

Hydrogen: Carbon Monoxide ratio can be defined as:

$$\frac{\text{H}_2}{\text{CO}} = \frac{\text{moles of H}_2\text{ produced}}{\text{moles of CO produced}} \quad \text{Eqn 9.22}$$

Carbon balance can be defined as:

$$\text{B}_\text{C}(\%) = \left(1 - \frac{\text{CH}_{4_{\text{out}}} + \text{CO}_{2_{\text{out}}} + \text{CO}_{\text{out}}}{\text{CH}_{4_{\text{in}}} + \text{CO}_{2_{\text{in}}}}\right) \times 100 \quad \text{Eqn 9.23}$$

Chapter 10 : **PLASMA BASED REFORMING EXPERIMENTAL RESULTS AND DISCUSSIONS**

10.1 Introduction

Plasma based methane reforming is one of the most promising processes to convert the vast global stranded natural gas and biogas resources which are currently not exploitable owing to limitations of conventional transportation methods to centres of demand and the unsuitability of conventional technologies for reforming into value added products. In recent years, there has been growing interest in the use of non-thermal plasma technology in converting methane, the biggest component of natural gas, with carbon dioxide, into value added products. Both greenhouse gases, if successful, this technology will not only be put to economic use instead of being released into the atmosphere, but also help tackling climate change threats due to global warming.

The objective of this part of the study was to evaluate the influence of various parameters such as applied plasma power (voltage), feed gas flowrates, mixing ratio of co-reactants (CH_4 and CO_2), packed dielectric pellet material, pellet size and presence of catalyst in the discharge zone on methane conversion and product distribution. The following sections present the results obtained in these experimental investigations.

10.2 Decomposition of pure methane in plasma

The experimental set up shown *Figure 9-3* was used to investigate the decomposition of pure methane in the reactor packed with 5mm Diameter $BaTiO_3$ balls. Methane of 99.99% purity was fed into the reactor at a constant flow rate of 25mL/min and a varying applied plasma power. The products of the reaction were analysed using the in-line Variant 450 GC and the gases detected and measured by the TCD detector were H_2 and unreacted methane. Meanwhile, the FID detector detected the presence of C_{2+} hydrocarbons. *Table 10-1, Figure 10-1*and *Figure 10-2* reflect the TCD results obtained.

From these results, it can be seen that CH_4 conversion increases with discharge power. This indicates that there is significant positive correlation between applied plasma power (or voltage) and methane conversion. A possible explanation for this might be that at higher input plasma power, the mean electron energy in the plasma discharge is higher and there are more electrons with adequate energy to excite CH_4 molecules into reactive species, hence the higher conversion. However, the selectivity of hydrogen declines with increasing applied plasma power, from 38% at 20W applied plasma power down to 34% at 102W. This implies that while conversion of CH_4 increased with increasing applied plasma power, more and more of other products than hydrogen were formed. These findings, while preliminary, suggest that these other products are higher hydrocarbons and this has important implications for non-thermal plasma as a method of producing CO-free hydrogen as well as coupling of methane into higher hydrocarbons in one stage.

Table 10-1 Conversion of pure methane at 25mL/min flowrate and varying applied plasma power

Power (W)	CH_4 conversion.	H_2%	H_2 vol (mL/min)	Vol of conv CH_4 (mL/min)	H_2 Selectivity	H_2 Yield
0	0%	0	0	0	0%	0%
20	6%	4%	1.2	1.6	38%	2%
40	14%	9%	2.7	3.5	39%	5%
60	21%	12%	4.0	5.3	37%	8%
80	27%	15%	4.9	6.8	36%	10%
102	34%	18%	5.9	8.5	34%	12%

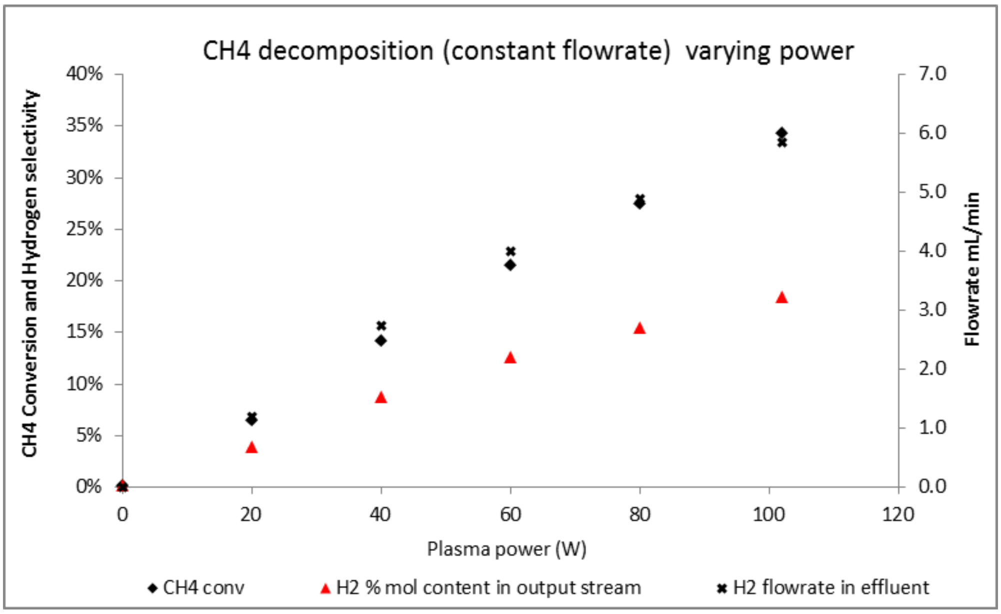

Figure 10-1 CH_4 conversion, H_2 selectivity, H_2 content and H_2 flowrate

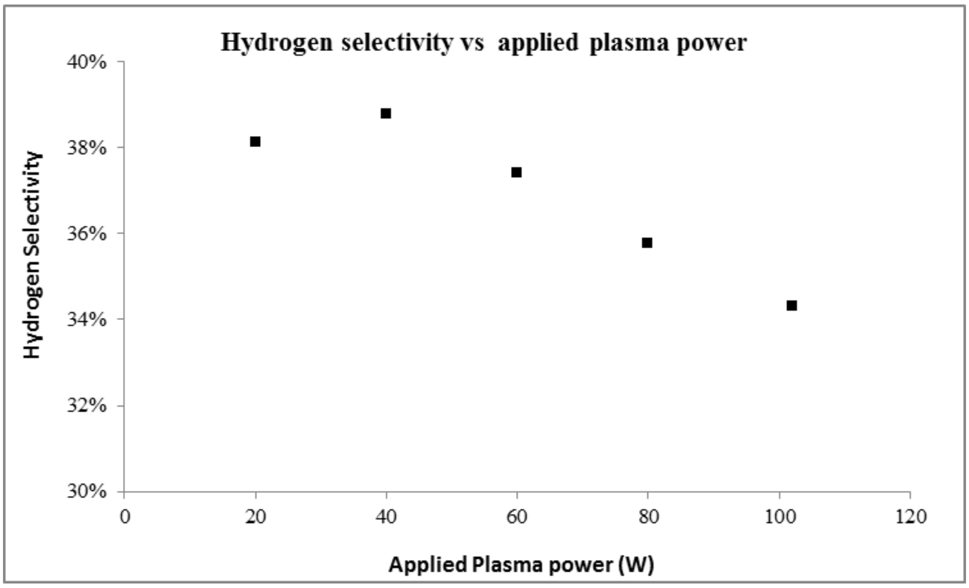

Figure 10-2 H_2 selectivity versus applied plasma power

10.3 Dry reforming of equi-molar CH_4/CO_2 feed (total flowrate of 25ml/min) with varying applied plasma power

In order to understand the effect of CH_4 and CO_2 as co-reactants on the conversion of methane in plasma, an equi-molar mixture of CH_4 and CO_2 of total flow rate 25mL/min in the reactor packed with spherical 5mm diameter $BaTiO_3$ pellets was fed through the reactor under varying applied plasma power (24W to 102W) as was done with pure CH_4. The results obtained are presented in *Table 10-2* and *Figure 10-3* and *Figure 10-4.* It can be observed from *Figure 10-3* that the conversion of both CH_4 and CO_2 increase with increase applied plasma power as was the case with pure CH_4. The conversion of methane in an equi-molar mixture of CH_4 and CO_2 was found to be always higher than that of CO_2 for all values of applied plasma power in this mixture of co-reactants. The conversion of CH_4 rose from 16% at 24W plasma applied power to 54% at 102W while that of CO_2 increased from 12% to 32% for the same applied power. This can be attributed to the lower CH_3-H bond energy (4.55eV) in CH_4 compared to O-CO bond energy (5.52eV) in CO_2.

The H_2 and CO yield *(Figure 10-4)*, show the same trend of increasing with applied plasma power, 7% at 24W to 21% at102 W for hydrogen, and 6% at 24W to 22% at 102 W for CO.

Table 10-2 Dry reforming of equi-molar CH_4/CO_2 feed with varying applied plasma power

Plasma Power (W)	CH_4 conv	CO_2 conv	H_2 content in effluent	CO content in effluent	Vol H_2 mL/min	S-H_2	S-CO	Y-H_2	Y-CO	H_2/CO
0	0%	0%	0%	0%	0	0%	0%	0%	0%	-
24	16%	12%	5%	5%	1.7	41%	46%	7%	6%	1.0
40	26%	17%	8%	8%	2.7	42%	51%	11%	11%	1.0
60	36%	22%	11%	11%	3.6	40%	50%	15%	14%	1.0
80	44%	26%	13%	13%	4.4	39%	50%	17%	18%	1.0
102	54%	32%	15%	16%	5.6	39%	52%	21%	22%	0.9

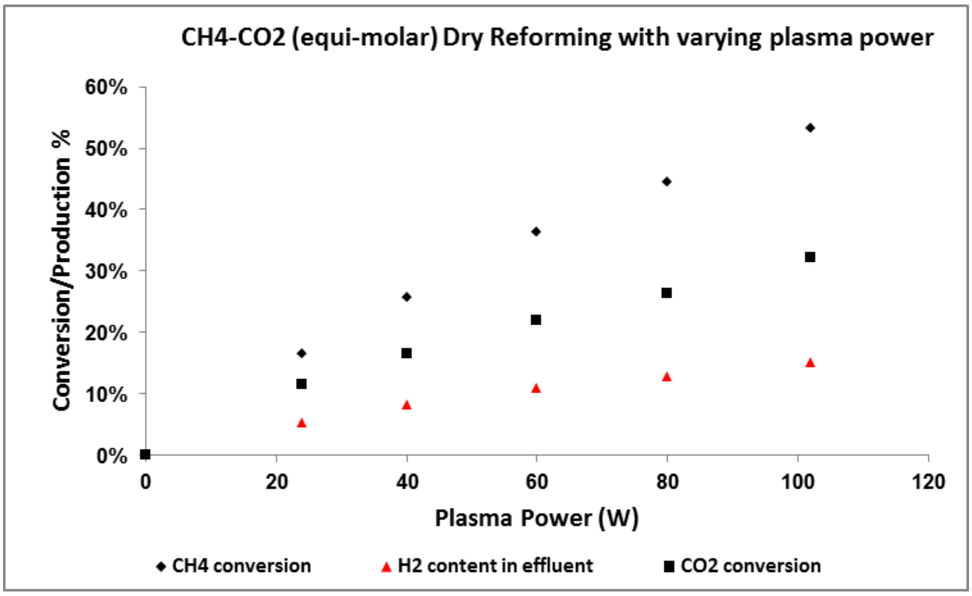

Figure 10-3 Effect of applied Plasma power on reactants conversion CH_4/CO_2 (equi-molar): flowrate of 25mL/min

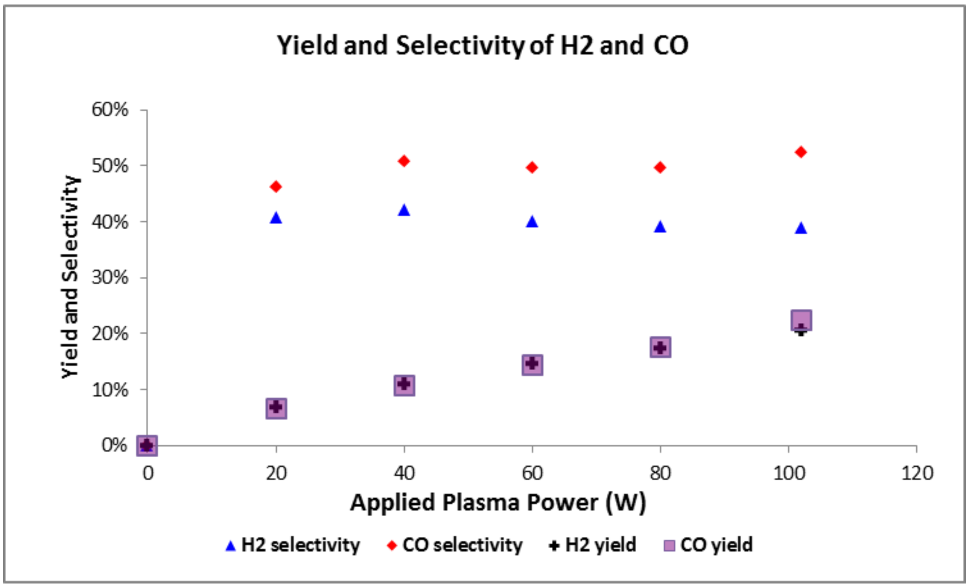

Figure 10-4 H_2 and CO selectivities and yields

In order to explain these results, some basic reactions involving CH_4 and CO_2 in plasma can be considered. The initial step when CH_4 and CO_2 are introduced in plasma is the dissociation of CH_4 to methyl (CH_3) and hydrogen (H) radicals and CO_2 to CO and atomic O radicals from collisions with high energy electrons as in Eqn 10.1 and Eqn 10.2.

$$\mathrm{CH_4 + e \rightarrow\ CH_3 + H + e} \qquad \text{Eqn 10.1}$$

$$\mathrm{CO_2 + e \rightarrow\ CO + O + e} \qquad \text{Eqn 10.2}$$

Prior studies (Liu et al., 1999) suggest that CH_4 can further be converted by hydrogen abstraction with O and H radicals according to Eqn 10.3 and Eqn 10.4.

$$\mathrm{CH_4 + O \rightarrow CH_3 + OH} \qquad \text{Eqn 10.3}$$

$$\mathrm{CH_4 + H \rightarrow CH_3 + H_2} \qquad \text{Eqn 10.4}$$

The OH radical formed as per Eqn 10.3 has a strong H-atom affinity enabling it to abstract an H-atom from methane according to Eqn 10.5:

$$\mathrm{CH_4 + OH \rightarrow CH_3 + H_2O} \qquad \text{Eqn 10.5}$$

According to the above, CH_4/CO_2 mixtures in plasma therefore produce active species such as O, H and OH, all of which can possibly react with methane thus enhancing CH_4 conversion while the same radicals may not have as much effect on CO_2. This, in addition to the lower C-H bond energy than C-O bond energy, explains the steeper conversion profile of CH_4 than that of CO_2. Conversion of CO_2 relies solely on collisions with energetic electrons while CH_4 conversion relies on both collisions with electrons as well as reaction by highly reactive radicals.

It is apparent from the H_2 and CO selectivities results that there were small variations in H_2 selectivity from 41% at 24W applied power to 39% at 102W while that of CO was equally a small positive variation from 46% at 24W to 52% at 102W. It seems possible that the increase in CO selectivity might be due to formation of CO from two sources, CO_2 decomposition and formation of CO from converted CH_4. Table 10-3 compares the calculated absolute volume of converted CO_2 with the absolute volume of CO formed per minute from experimental data using Eqn 9.1- Eqn 9.8. It also has to be remembered that in DBD plasma, the range of electron energies is 1-10eV(Eliasson and Kogelschatz, 1991) , and that the disproportionation of CO to C by electron collision is not very likely owing to the high CO dissociation energy of 11.16eV. It therefore means the majority of the converted CO_2 becomes CO. If the CO formed was only from the conversion of CO_2 it would be expected that the amount of CO formed equates to the amount of CO_2 converted.

Table 10-3 Comparison of CO formed and CO_2 converted

Applied Power (W)	Vol CH_4 conv (mL/min)	Vol CO_2 conv (mL/min)	Vol CO formed (mL/min)	CO formed - CO_2 conv (mL/min)	% of C from CH_4 to CO	% of C from CH_4 to other products
0	0.0	0.0	0.0	0.0	-	-
24	2.1	1.4	1.6	0.2	9%	91%
40	3.2	2.1	2.7	0.6	19%	81%
60	4.6	2.7	3.6	0.9	19%	81%
80	5.6	3.3	4.4	1.1	20%	80%
102	6.6	4.0	5.6	1.6	23%	77%

But as the results of this experiment show, more CO was formed than CO_2 converted as in Table 10-3. The observed difference could be from the formation of additional CO from the converted CH_4. This could be from the oxidation of C (from CH_4) by O from dissociation of CO_2. On the other hand, the reduction of H_2 selectivity could be due to some of the O formed from CO_2 decomposition reacting with H_2 or H atoms to form H_2O (Aziznia et al., 2012). The overall effect of this is the tendency for CO selectivity to increase whereas that of H_2 tends to decrease. The increase in CO selectivity from 46% at 24W to 52% at 102W reflects an increase in CH_4 derived CO with increasing applied power while the H_2 selectivity decline might be due to some H_2 being oxidized to form water.

Figure 10-5 shows the distribution of C from converted CH_4 between CO and HCs and oxygenates.

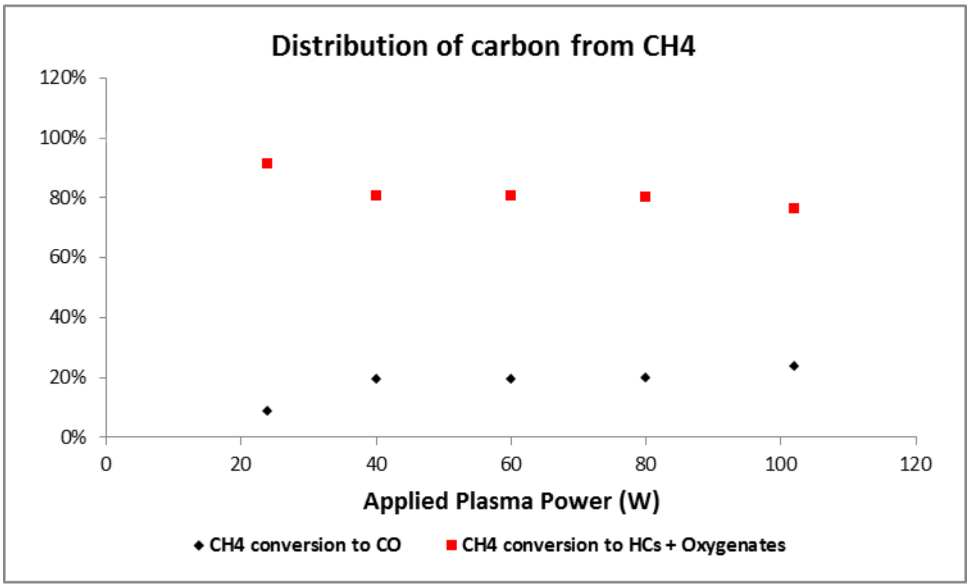

Figure 10-5 Distribution of Carbon in converted CH_4

It is also important to note that while the main gaseous products of the plasma reactions detected were H_2 and CO, significant quantities of hydrocarbons such as C_2, C_3, and C_4 with decreasing concentration with increasing carbon number were also formed and detected by the GC. At higher powers traces of C_5-C_{10} were detected. Table 10-4 shows the relative quantities of the different HCs detected by the GC FID detector. The results show an increasing trend in the HCs concentrations with applied plasma power. It can be seen that there is a much higher conversion to ethene than ethane.

Table 10-4 Relative concentrations of HC detected by FID

Plasma Power (W)	Relative C2H6 conc %	Relative C2H4 conc %	Relative C3 conc %	Relative C4 conc %	Relative C5 conc %
0	0%	0%	0%	0%	0%
24	0%	1.84%	0.36%	0.41%	0.01%
40	0%	4.04%	0%	0.60%	0.03%
60	2.18%	21.06%	0.74%	0.68%	0.07%
80	2.24%	19.77%	0.79%	0.73%	0.09%
102	2.35%	15.71%	0.93%	0.80%	0.012%

10.4 Evaluation of the effect of CO_2 on CH_4 conversion

An evaluation of the effect of CO_2 inclusion on CH_4 conversion can be evaluated from the results in above *Sections 10.2* and *Section 10.3* . Relevant data is as in Table 10-5. Please note that for $CH_{4/}CO_2$ the data for plasma power of 20W was at 24W.

*Table 10-5 Comparison of CH_4 conversion with and without CO_2 co-feed under same flow and applied plasma power conditions (*applied plasma power of 24W)*

Applied Power (W)	CH_4 conversion in equi-molar CH_4/CO_2	CH_4 conversion in pure CH_4	Amount of H_2 produced (mL/min) in CH_4/CO_2 mixture	Amount of H_2 produced (mL/min) in pure CH_4	H_2 yield for CH_4/CO_2 reaction	H_2 yield for pure CH_4 plasma reaction
0	0%	0%	0	0	0%	0%
20	16%*	6%	1.7*	1.2	7%*	2%
40	26%	14%	2.7	2.7	11%	5%
60	36%	21%	3.6	4.0	15%	8%
80	44%	27%	4.4	4.9	17%	10%
102	53%	34%	5.6	5.9	21%	12%

From Table 10-5, it can be seen that CH_4 conversion and H_2 yield with CH_4/CO_2 equi-molar feed mixture were much higher than that of pure CH_4. This result corroborates the findings of a great deal of previous work in the same field where it has been concluded that the presence of CO_2 enhances CH_4 conversion. A look at the absolute production rate of hydrogen shows that about as much hydrogen is produced per minute with 12.5mL/min CH_4 feed flowrate with equal amount of CO_2 as with 25mL/min pure CH_4 feed under same applied power conditions using the reactor packed with the same dielectric pellets. In addition, CO is obtained as a co-product and, depending on the final use; this could be valuable, such as in F-T synthesis. However, for CO-free hydrogen such as necessary for PEM fuel cells, pure methane reforming may be beneficial. The implication of this finding is that to obtain CO-free hydrogen from methane; the penalty is lower conversion and yields using pure methane. On the other hand, carbon dioxide is known to be a common contaminant in some unconventional natural gas streams where it can reach or even overpass 50% (Bellussi et al., 2011); and in biogas. This technology can be used to convert such resources to syngas without the need for sweetening the gas first. The syngas is an important precursor in the manufacture of many valuable products.

10.5 Effect of CH_4/CO_2 feed ratio on conversions and product distribution

Having established the enhancement effect the presence of CO_2 has on conversion of methane using non-thermal plasma; experiments were also conducted to investigate the effect CH_4/CO_2 ratio on conversions and distribution of products using the same experimental set up shown in *Figure 9-3*. Keeping the N_2 and the total feed (CO_2+CH_4) flow rate constant at 50mL/min, the effect of CH_4/CO_2 feed ratio was investigated by varying the molar CH_4/CO_2 ratio using the mass flow meters. For each set of conditions, the reagents mixture of CH_4 and CO_2 (each from a separate cylinder), were controlled by mass flow controllers and fed into the reactor at room temperature. Under each set of mixture conditions, a period of 30 min was allowed for stabilization before quantitative analysis of discharge by-products using an in-line GC. The results of these investigations are summarised in Table 10-6 and *Figure 10-6 - Figure 10-8*. The results show that with an increasing ratio of CO_2/CH_4 in the reactants feed mixture; the conversion of CO_2 slowly rose from 12% for a 5/95 ratio to 21% for a 75/25 ratio. Thereafter, somewhere between a ratio of 75/25 and 85/15, CO_2 conversion slowly dropped to 12% for a CO_2/CH_4 ratio of 97.5/2.5, and shot up 19% for pure CO_2. For CH_4, conversion rose steeply with increasing content of CO2 from 15% for pure methane to 79% for a CO_2/CH_4 ratio of 97.5/2.5.

This might be explained by the fact that the presence of CO_2 in higher proportions plays a role in the conversion of methane. The most probable reason is the oxidising species (O) from the dissociation of CO_2 might play a role in converting methane via oxidative dehydrogenation reactions with methane as follows:

$$\mathrm{CH_4 + O \rightarrow CH_3 + OH} \quad \text{Eqn 10.6}$$

$$\mathrm{CH_4 + OH \rightarrow CH_3 + H_2O} \quad \text{Eqn 10.7}$$

Table 10-6 Effect of CO_2 content in CH_4/CO_2 mixture on conversions

CH4 In	CO2 In	CH4 conv	CO2 conv	S-H2	S-CO	H2/CO Ratio	H_2 content	O_2 content
50.0	0.00	15%	0%	33%	0%	-	10%	0%
47.5	2.50	18%	12%	34%	5%	13.67	12%	0%
45.0	5.00	24%	16%	32%	9%	6.69	13%	0%
42.5	7.50	25%	18%	33%	14%	4.35	14%	0%
37.0	12.50	25%	16%	33%	22%	2.50	12%	0%
25.0	25.00	30%	16%	34%	43%	1.04	10%	0%
12.5	37.50	44%	21%	42%	67%	0.52	8%	0%
7.50	42.50	48%	18%	47%	79%	0.39	7%	0%
5.00	45.00	41%	16%	53%	93%	0.25	4%	0%
2.50	47.50	72%	12%	19%	99%	0.09	1%	0%
1.25	48.75	79%	12%	12%	94%	0.04	0%	2%
0.00	50.00	0%	19%	0%	76%	-	0%	5%

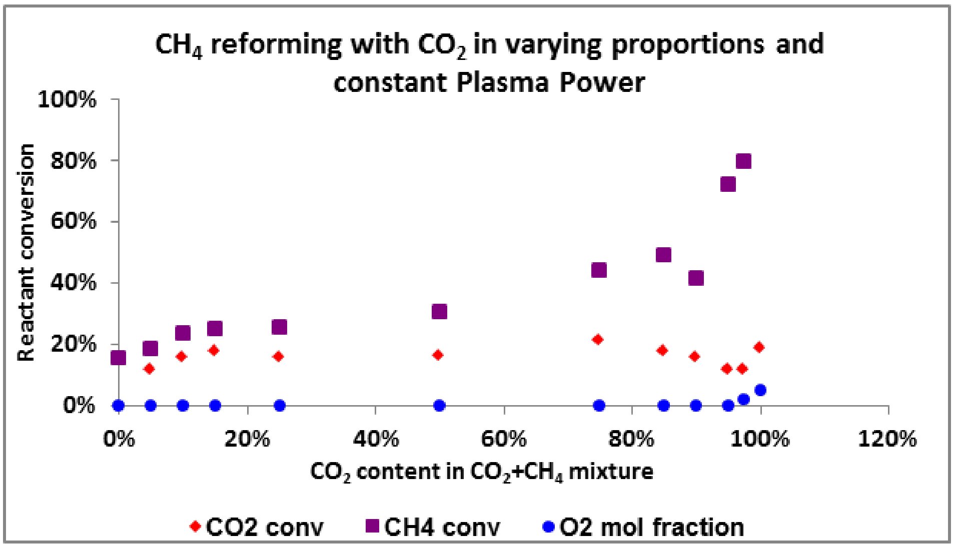

Figure 10-6 Conversion of CH_4, CO_2 and O_2 content in effluent

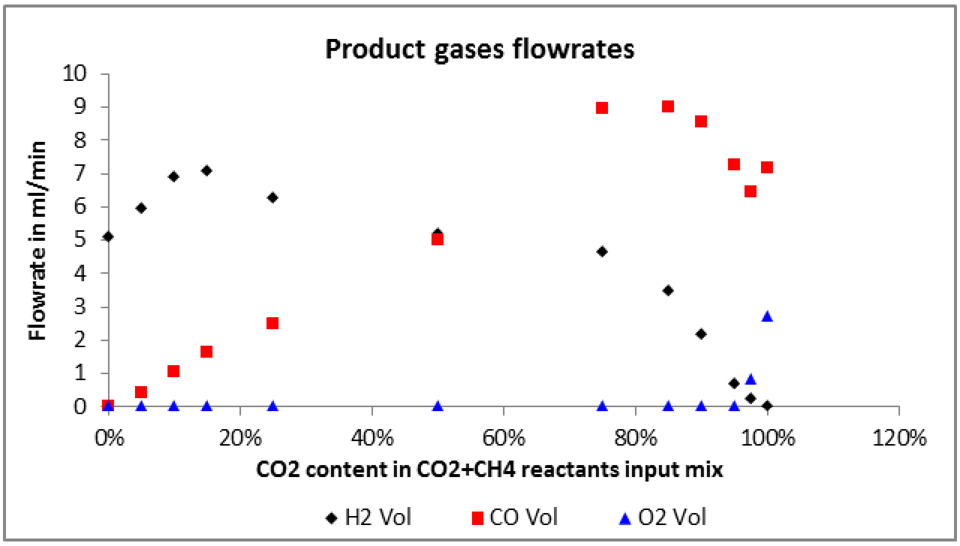

Figure 10-7 Calculated flowrates of component effluent gases.

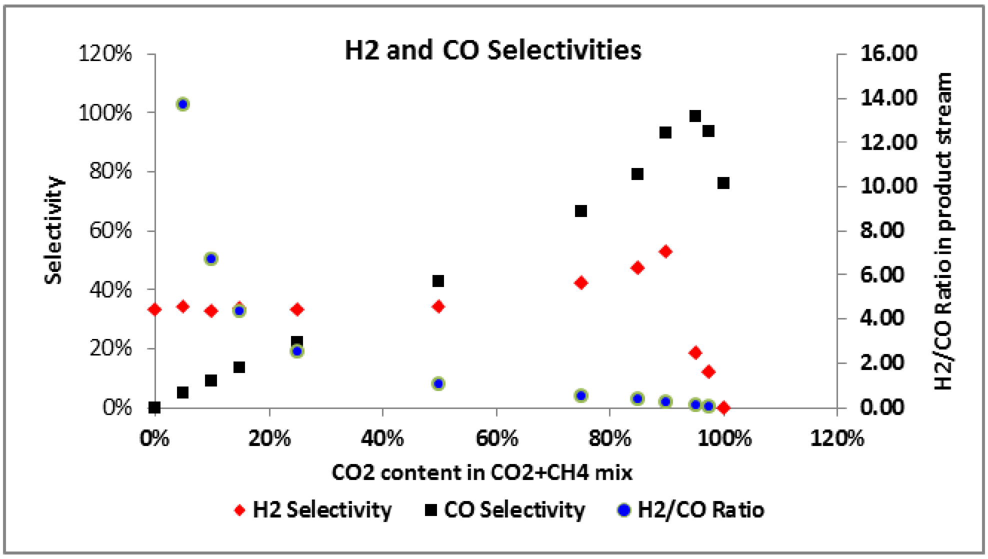

Figure 10-8 H_2 and CO selectivities and H_2/CO ratio

At a 1:1 ratio for CH_4:CO_2 the conversion of CH_4 was about twice that of CO_2. This can be explained by the higher dissociation energy of CO_2 than that of CH_4 as well as the participation of other CH_4/CO_2 plasma species in methane conversion as discussed in previous sections. In other words, under the conditions the experiments were conducted, methane could be converted by both electron collision and reaction with other radicals while CO_2 depended solely on collisions with high energy electrons.

CO content in the effluent rose from 1% at CO_2/CH_4 ratio of 5/95 to 17% at ratio 85/15 and declined to 13% at ratio 97.5/2.5 before rising to 14% for pure CO_2.

H2 content in the effluent stood at 10% for pure methane feed at 50ml/min and increased slowly to 14% for a CO_2/CH_4 ratio of 15/85 and began to decline to 1% at ratio 95/5 and zero for higher CO_2 content.

Oxygen content in effluent was nil for all compositions investigated between CO_2/CH_4 ratios 0/100 to 97.5/2.5. This result shows that all the oxygen generated by interaction of CO_2 with plasma for these compositions must have been consumed. This range of reactant compositions also showed rising CH_4 conversion. It can therefore be concluded that the oxygen produced from CO_2 conversion might have participated in conversion of methane and the coincidental decline in H_2 might indicate consumption of H_2 in the process. This might be due to hydrogen produced from CH_4 being oxidized to H_2O due to increasing presence of O radicals from CO_2 conversion. This by no means implies all the oxygen produced reacted with hydrogen to form water. Some of it might have reacted with other species in the plasma volume to form other products such as oxygenates. Separate experiments with cold trap to liquefy any other reaction products were conducted and the results will be shown in later sections.

One of the most striking observation to emerge from the data presented in *Table 10-6* is that pure (100%) methane conversion at 50ml/min feed flowrate was 15% compared to conversion of pure (100%) carbon dioxide, of 19% under same feed flowrate and applied plasma power of 86W. This finding was unexpected since CH_4 has lower dissociation energy (4.5eV) than that of CO_2 (5.52eV) and, as proposed by (Liu et al., 1999), the possible participation by atomic hydrogen in converting CH_4 by H-abstraction. It is difficult to explain this result but it might be related to catalytic effect of barium titanate packed balls on CO_2. A possible explanation is the significant adsorption property of CO_2 on $BaTiO_3$ substrate. (Cabrera et al., 1994) proposed that due to its ferroelectric properties, $BaTiO_3$ exhibits significant adsorption of CO_2, mediated by dipole-dipole interaction between the ferroelectric $BaTiO_3$ and CO_2. In studies attributed to Tamaru and co-workers by (Cabrera et al., 1995), CO_2 molecule is adsorbed with the carbon atom near the surface and the oxygens standing up away from the surface. The bend between the C-O bonds induces a dipole moment between the C and O atoms. Such adsorption would prolong the retention time of the adsorbed CO_2 in the plasma volume and increases the collision probability between the CO_2 molecules and energetic electrons resulting in enhancement of CO_2 conversion.

The results in the *Figure 10-8* also show that the H_2/CO ratio of 2/1, suitable in FT synthesis is obtained at reactant feed ratio of CO_2/CH_4 ratio of about 27/73 and a 1/1 ratio at about CH_4/CO_2 ratio of 1/1. The latter is consistent with the stoichiometric reaction:

$$\mathrm{CH_4 + CO_2 \rightarrow 2CO + 2H_2} \qquad \text{Eqn 10.8}$$

The results show that the H_2/CO ratio depends strongly on the CH_4/CO_2 feed ratio and that for the production of a syngas mixture of a required ratio, this can be controlled by adjusting the CH_4/CO_2 in the feed.

This is an important finding with regard to conversion of biogas into useful materials. Biogas is a renewable energy source that can be produced relatively easily from biomass. Sources of biogas feedstock include waste material from agricultural harvests and forestry. It is produced by anaerobic digestion of biomass material such as leaves, grass, wood, weeds, organic fraction of municipal solid waste (MSW) and is normally released into the atmosphere (Vergara-Fernández et al., 2008, Nallathambi Gunaseelan, 1997). This is of a major concern because the two major components of biogas, CH_4 and CO_2 are greenhouse gases. Biogas contains mainly methane (40-70%) and carbon dioxide (30-60%) (Goujard et al., 2009). With such proportions of CH_4/CO_2, such resources can be converted into syngas of H_2/CO ratio of around 2 and suitable for F-T synthesis of methanol. This technology could be useful in harnessing this resource into very useful products instead of releasing it into the atmosphere to exacerbate the threat of global warming. It has the potential for simultaneous utilization and reduction of these two abundant and undesirable greenhouse gases (Tu and Whitehead, 2012).

10.6 Effect of feed flowrate

The effect of total feed flow rate on conversion reaction at fixed CH_4/CO_2 ratio of 1/1 with the reactor packed with $BaTiO_3$ was also examined. This was done by adjusting the CO_2 and CH_4 flow rates by means of mass flow meters for each experiment while the applied plasma power and reference nitrogen flow rate were maintained constant at 86W and 6mL/min respectively. The results are summarised in *Table 10-7* and *Figure 10-9-Figure 10-12*.

Table 10-7 Effect of flowrate on conversion of equi-molar CH_4/CO_2 mixture

Flowrate *mL/min*	CH_4conv	CO_2conv	S_H_2	S_CO	Y_H_2	Y_CO	H_2/CO	F_H_2 *mL/min*	F_CO *mL/min*
15	62%	38%	42%	52%	26%	26%	1.0	3.9	3.9
25	49%	28%	38%	50%	19%	19%	1.0	4.7	4.8
50	30%	16%	38%	48%	12%	11%	1.0	5.8	5.6
75	23%	13%	39%	45%	9%	8%	1.1	6.7	6.0
100	16%	9%	37%	42%	6%	5%	1.1	6.0	5.3

where S_i, Y_j and F_k are respectively selectivity (S) of species i, yield (Y) of species j and effluent flowrate (F) of species k.

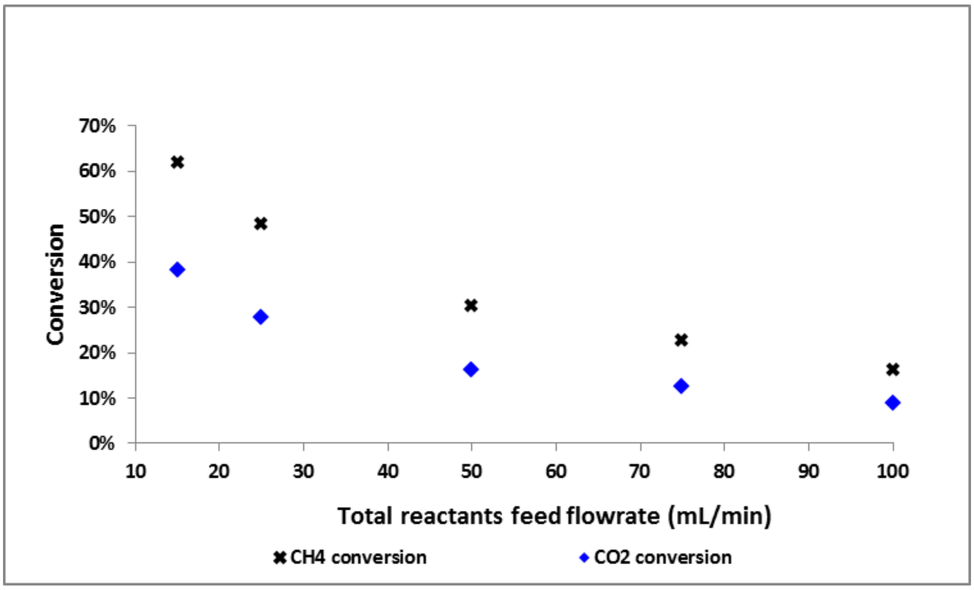

Figure 10-9 Effect of flowrate on reactants conversions

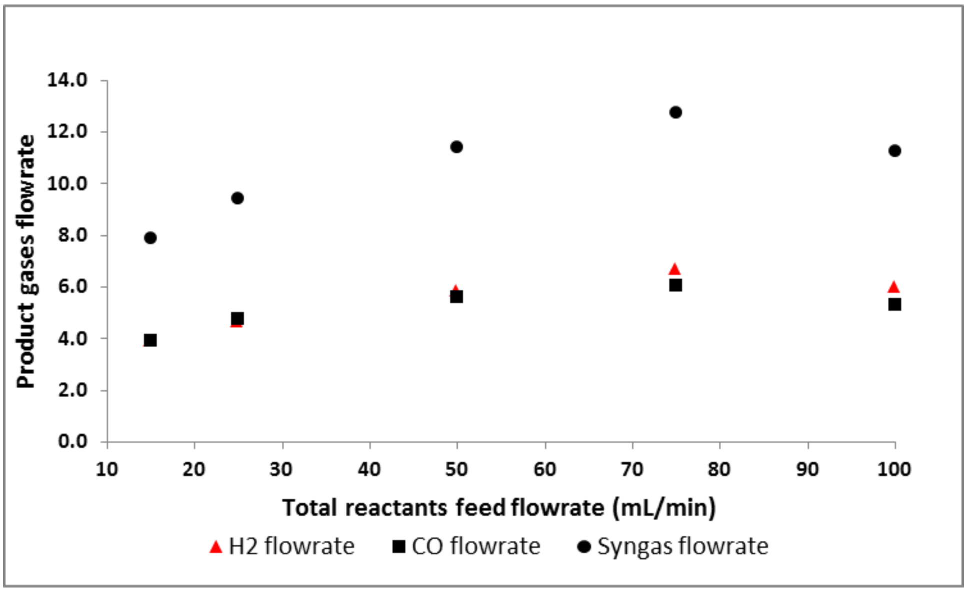

Figure 10-10 Syngas constituents' flowrates in effluent gases

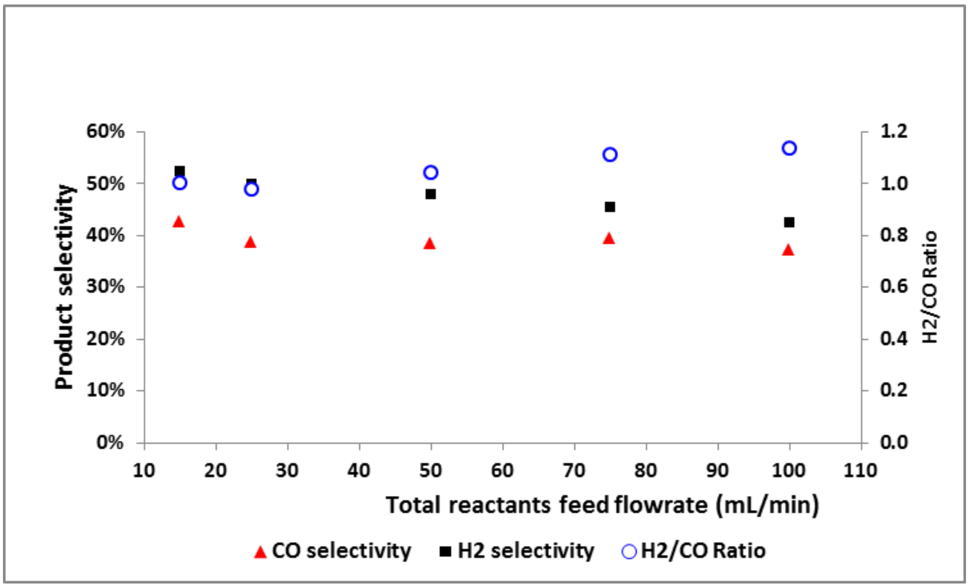

Figure 10-11 H_2, CO selectivities and H_2/CO ratio

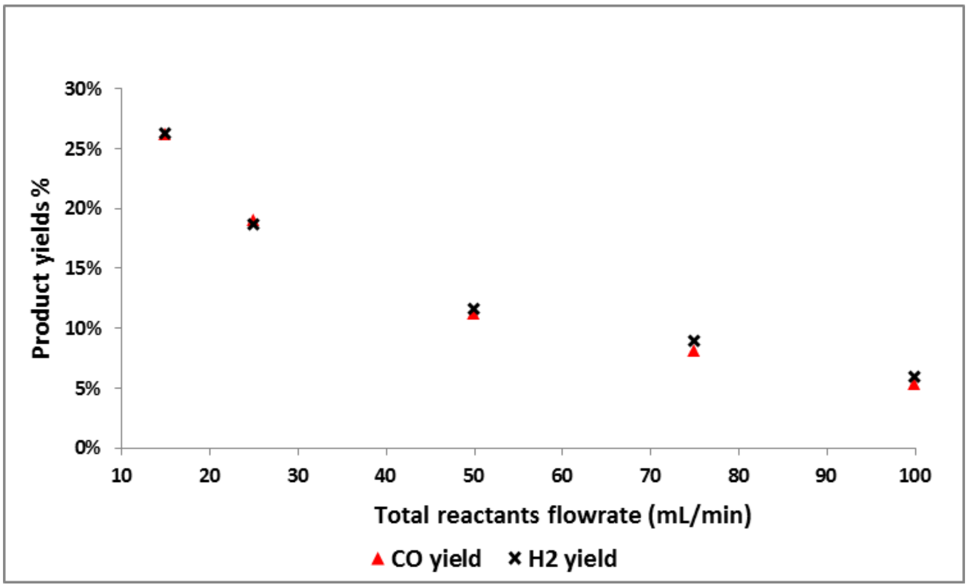

Figure 10-12 H_2 and CO yields

The results show that both methane and carbon dioxide conversions decrease with increasing total flowrate. The conversions of CH_4 and CO_2 were reduced from 64% and 38% for CH_4 and CO_2 at 15mL/min total flowrate to 16% and 9% at 100mL/min respectively. *Figure 10-10* show a graph plotting the volumetric flowrates of H_2 and CO in the products stream against total input flowrate. It shows that the absolute amount of H_2 and CO produced increased with increase in feed flow rate and peaked at a total feed flowrate of co-reactants of about 75ml/min and started to decline above that total flow rate.

The selectivities of both H_2 and CO only decreased slightly with increasing flowrate (*Figure 10-11*). The selectivity of hydrogen fell from 42% at input feed of 15mL/min to 37% at input feed of 100mL/min. The selectivity of CO fell from 52% at 15ml/min feed flowrate to 42% at a feed flowrate of 100mL/min. Goujard et al (Goujard et al., 2009), reported that the selectivity of CO is not significantly changed with varying feed flowrate. The effect of flowrate on H_2/CO ratio hardly changed at all, remaining at about 1 throughout.

From *Figure 10-12*, H_2 yield decreased from 26% to 6% and that of CO decreased from 26% to 5% from total feed flow rate of 15ml/min to 100ml/min. The conversion and yield results can be explained in terms of residence time of reactants in the plasma zone. Residence time is inversely proportional to flowrate or flow velocity. Low flowrates and high flowrates respectively translate to high and low residence time of gas in plasma zone. With a longer residence time (low flowrate), there is a higher chance for reactant molecules (CH_4 or CO_2) being converted than with shorter residence time (high flowrate). Alternatively, this result can be explained by the fact that with increasing flow rate, the gas velocities through the plasma zone is much higher thus the probability of molecules exiting the plasma discharge space unconverted is higher. In addition the increased residence time at low flowrates may also enable new products to remain longer in the discharge volume and further converted as well to secondary products. For instance if ethane is a primary product, due to the increased dwell time owing to low flowrates, ethane molecules may be further converted by collision with energetic electrons to form new radicals resulting in other products such as C_2H_4.

This result shows that conversions of reactants (both CH_4 and CO_2) and H_2 and CO yields have a strong relation to residence time in the plasma zone and it can be concluded that in order to achieve higher conversions of feed gases to H_2 and CO, the residence time of the feed gases stream in the plasma zone must be as long as possible. However results as depicted in *Figure 10-10* show that while low total feed rates are beneficial in terms of conversion efficiency, the absolute amount H_2 and CO (syngas) produced increases with flow rate before peaking somewhere between 75 and 90 mL/min and declining. The implication of this result is that if an upstream efficient separation process to recover and recycle unreacted CH_4, CO_2 and secondary higher hydrocarbons (HCs) formed can be developed, a feed flow rate can be selected that give the most optimum absolute conversion and syngas production. A conceptual schematic of this is depicted in *Figure 10-13*.

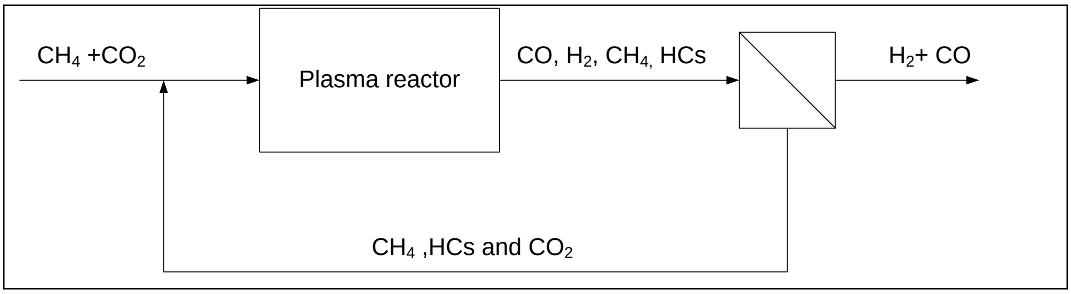

Figure 10-13 Schematic of plasma reactor with separation of syngas and recovery of unreacted CH_4 *and* CO_2.

Gas chromatography of effluent from the reactor revealed that products up to C_5 were present in considerable amounts. *Figure 10-14* depict the relative proportions of HC (C_2-C_4) detected by the GC at the various applied plasma power. The results show ethene as the major product of the gaseous HCs.

Trace amounts of heavier HCs (C_{5+} such as pentane, pentene, hexene, heptene and heptane) were detected by the FID column calibrated for HCs. Trace amounts of ethanol and methanol were also detected by the FID column configured and calibrated to detect alcohols. Experiments were subsequently conducted with cold trap using ice cold water bath for alcohols and water, and dry ice for HCs with very low boiling points.

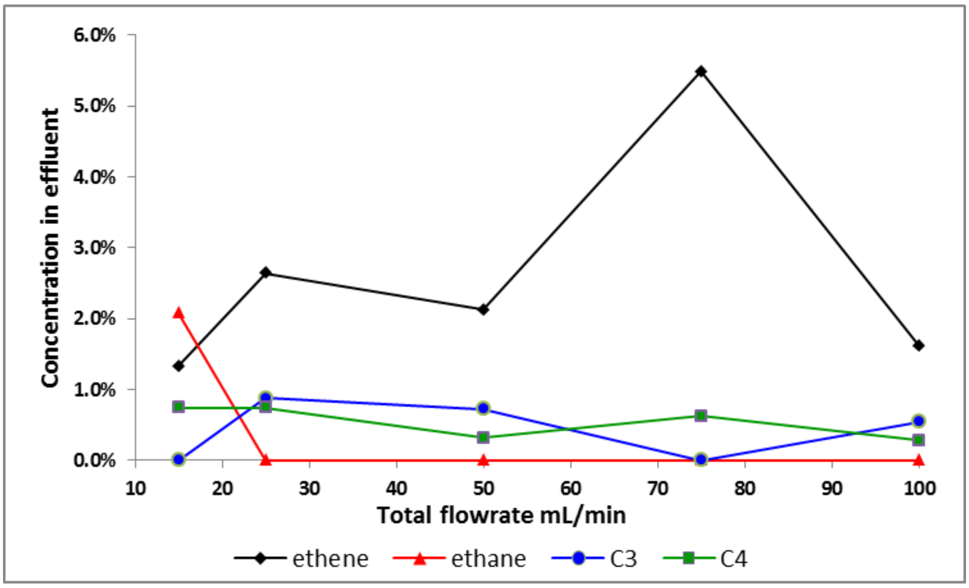

Figure 10-14 Relative proportions of gaseous HCs in effluent

10.7 Effect of flowrate on pure methane conversion using plasma

The effect of flowrate on pure methane conversion was also examined in a similar way by varying the feed flow rate of methane while maintaining the applied plasma power of 80W and reference gas (N_2 to monitor volume change), constant. The results are summarised in *Table 10-8* and *Figure 10-15-Figure 10-17*.

Table 10-8 Effect of residence time on pure methane reforming using plasma

CH4 feed Flowrate mL/min	CH4 Conversion	H2 content	Vol_CH4 Conv	F_H2	S_H2	Y_H2
6.25	51%	18%	3.2	1.3	21%	11%
12.5	37%	17%	4.6	3.2	35%	13%
20.0	29%	16%	5.7	4.1	36%	10%
25.0	27%	15%	6.8	4.9	36%	10%
50.0	15%	10%	7.6	5.7	37%	3%

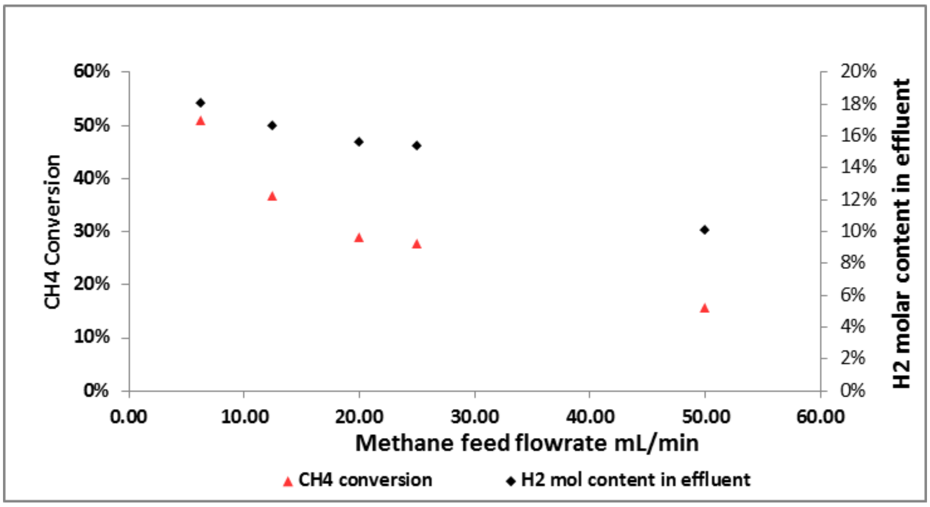

Figure 10-15 Effect of flowrate on conversion of pure methane using plasma

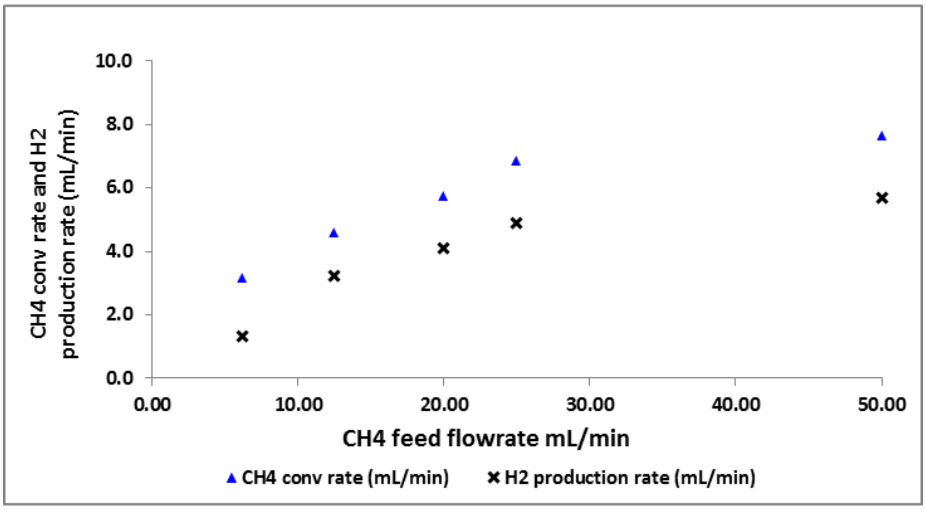

Figure 10-16 Volume per unit time of CH_4 converted and H_2 produced

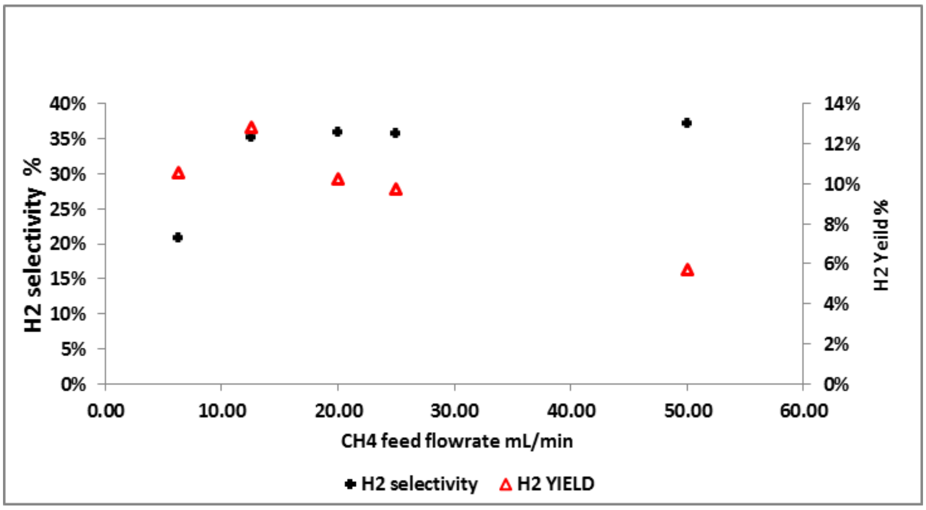

Figure 10-17 H_2 selectivity and yield

Methane conversion significantly increased with decreasing input feed flowrate (increasing residence time) as can be observed from *Table 10-8* and *Figure 10-15*. Longer residence time of methane inside the plasma zone create more chances for methane molecules to be involved in collision with energetic electrons and activated. *Figure 10-16* show that although methane conversion decreases with increasing flowrate, the absolute volumetric amount of converted methane and absolute amount of hydrogen produced increase considerably with increasing feed flowrate at low feed flowrates between 6.25 - 25.00 mL/min. Although the graph shows that this might have plateaued at 50mL/min, this result need to be interpreted with caution because there were no other data points between 25 and 50mL/min.

At higher feed flow rate, these absolute amounts seem to plateau. *Figure 10-17* shows that selectivity of H_2 at methane feed flow rate of 6.25 mL/min is low (21%) but increases to 35% at a feed flow rate 12.50mL/min and hardly change up to feed flow rate of 50mL/min. On the other hand, H_2 yield increases from 11% at feed flow rate of 6.25 mL/min to 13% at 12.50mL/min but fall to 10% at feed flow rate of 20 and 25mL/min. At feed flowrate of 50 ml/min, H_2 yield fall to 6%.

These results show that while low flow rates promote higher methane conversion, higher flow rates are more beneficial in terms of absolute quantity of methane converted and absolute quantity of hydrogen produced. However there is insufficient data to comment on the behaviour at higher feed flowrates. However, the implication of this result is that if an efficient upstream separation process to recover and recycle unreacted methane and secondary higher hydrocarbons (HCs) formed can be developed, a feed flow rate can be selected that give the most optimum absolute conversion and hydrogen production. A conceptual schematic of this is depicted in *Figure 10-18*.

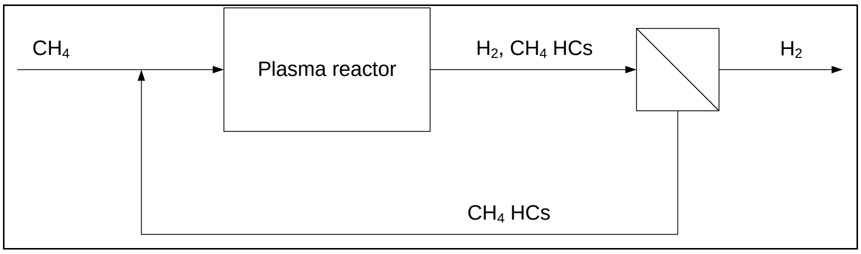

Figure 10-18 Schematic of plasma reactor with an upstream separation unit

10.8 Interpretation of results in terms of Input Energy Density (IED)

The conversion performances of the DBD reactor discussed in previous sections can also be interpreted in terms of Input Energy Density.

Input Energy Density can be defined by Eqn 10.9.

$$\text{Input Energy Densiy} = \frac{\text{Input Plasma Power (W)}}{\text{Total feed flowrate mL/min}} \qquad \text{Eqn 10.9}$$

Input Energy Density in the plasma reactions can be varied in two ways:

1. Vary input power at constant feed flow rate
2. Vary feed flow rate at constant input plasma power

10.8.1 Pure Methane conversion

Table 10-9 and *Figure 10-19* show dependence of pure CH_4 conversion on Input Energy Density (IED) on the basis of varying feed flow rate and constant applied plasma power while *Table 10-10* and *Figure 10-20* show dependence of pure CH_4 conversion on IED on the basis of varying applied plasma power and constant feed flow rate. Although the data ranges are different, clearly the results show the same trend, that is, conversion of pure methane increases with increasing IED for both. However, this result cannot be extrapolated to product distribution. A separate set of experiments would need to be carried out to establish the reaction product distribution including secondary products.

Table 10-9 Pure CH_4 conversion-constant applied power and varying flow rate

Flowrate (mL/min	Plasma power (W)	CH4 conversion	IED (Wmin/mL.	IED (kJ/L)
6.25	80	51%	12.80	768
12.50	80	37%	6.40	384
20.00	80	29%	4.00	240
25.00	80	27%	3.20	192
50.00	80	15%	1.60	96

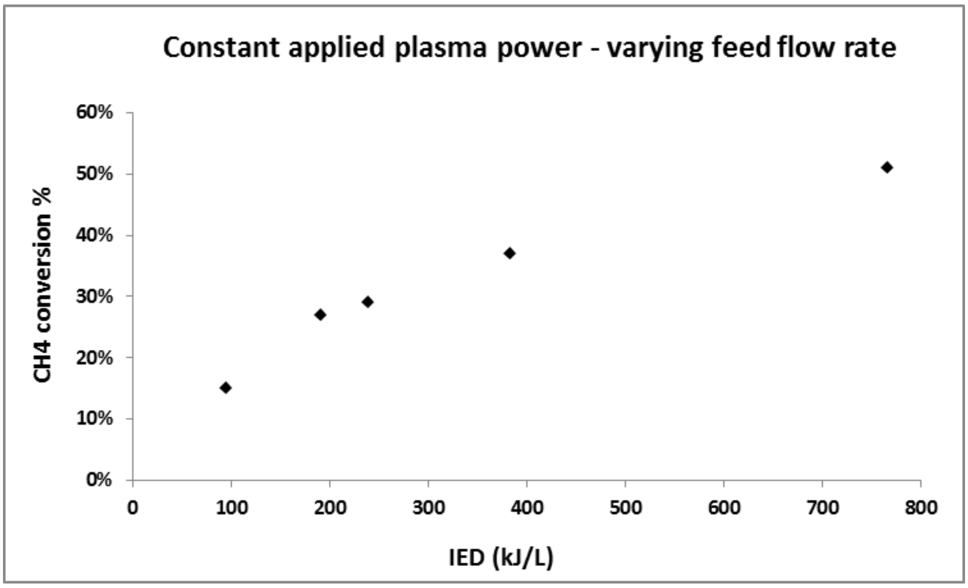

Figure 10-19 Pure CH_4 conversion-constant applied power and varying flow rate

Table 10-10 Pure CH_4 conversion – constant feed flow rate and varying applied power

Flowrate (mL/min)	Plasma power (W)	CH4 conversion (%)	IED (Wmin/mL	IED (kJ/L)
25	20	6%	0.8	48
25	40	14%	1.6	96
25	60	21%	2.4	144
25	80	27%	3.2	192
25	102	34%	4.08	245

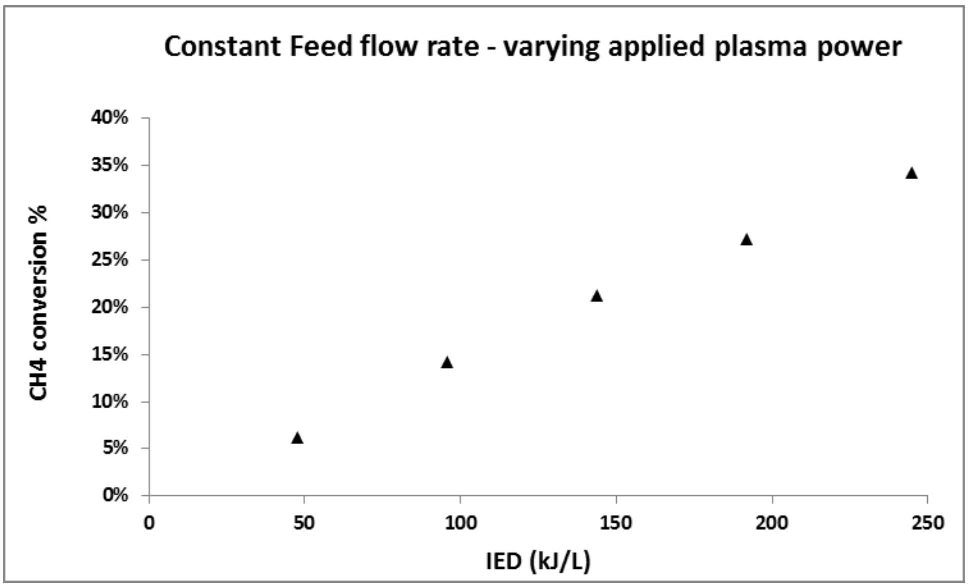

Figure 10-20 Pure CH_4 conversion – constant feed flow rate and varying applied power

10.8.2 *CH_4/CO_2 equi-molar mixture*

Table 10-11 and *Figure 10-21* show the effect on conversion of equi-molar CH_4/CO_2 of Input Energy Density on the basis of a constant feed flowrate of a 25mL/min and varying applied plasma power. *Table 10-12* and *Figure 10-22* show the effect on conversion of CH_4 and CO_2 of Input Energy Density on an equi-molar CH_4/CO_2 mixture on the basis of varying total feed flow rate and a constant applied plasma power of 86W. Despite the differences in the scale of the experimental data, the results show a general trend of increasing conversions of the two co-reactants with increasing IED. In both cases, the CH_4 conversion was always higher than that of CO_2. The results show that there are two ways to adjust IED to change conversion, flow rate or applied power.

Table 10-11 Equi-molar CH_4/CO_2 Mixture- Constant total feed flow rate and varying applied plasma power

Flowrate	Plasma	CH4 conv	CO2 conv	IED (Wmin/mL)	IED (kJ/L)
25	24	16%	12%	0.96	57.6
25	40	26%	17%	1.6	96
25	60	36%	22%	2.4	144
25	80	44%	26%	3.2	192
25	102	53%	32%	4.08	244.8

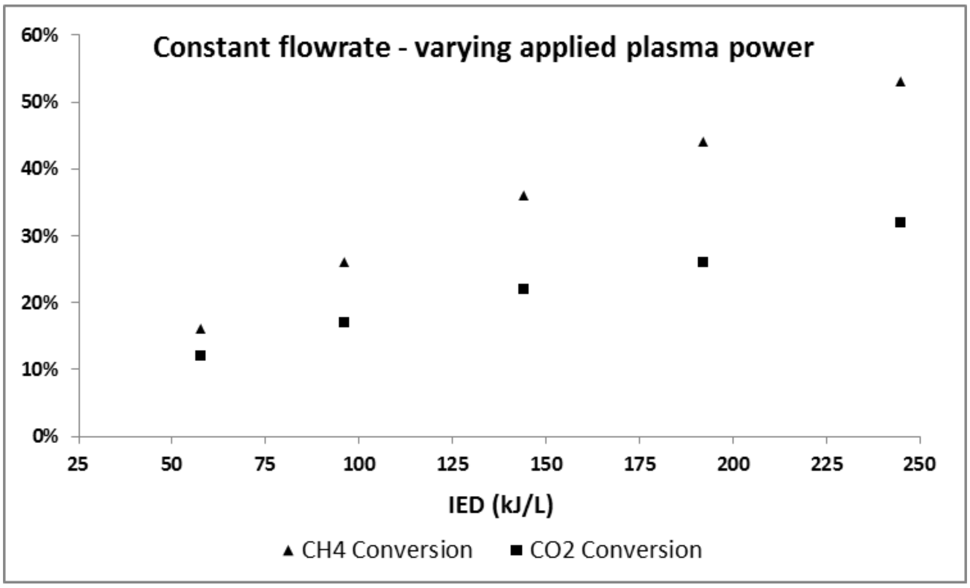

Figure 10-21 Equi-molar CH_4/CO_2- Mixture- Constant total feed flow rate and varying applied plasma power

Table 10-12 Equi-molar CH_4/CO_2 - Mixture- Constant applied plasma power and varying total flow rate

Flowrate	Plasma	CH4 conv	CO2 conv	IED (Wmin/mL)	IED (kJ/L)
15	86	64%	38%	5.7	344
25	86	48%	28%	3.4	206
50	86	30%	16%	1.7	103
75	86	23%	13%	1.1	69
100	86	16%	9%	0.9	52

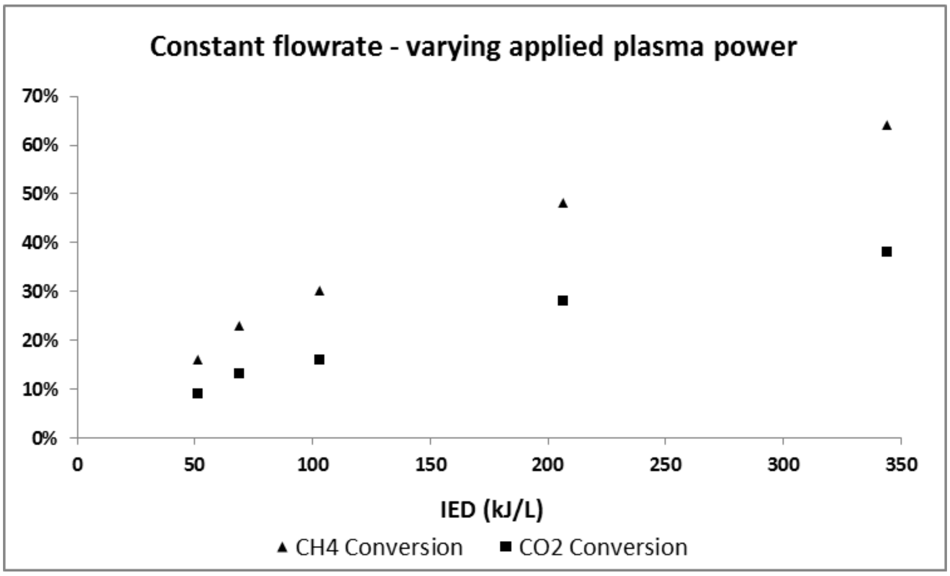

Figure 10-22 Equi-molar CH_4/CO_2 Mixture - Constant applied plasma power and varying total flow rate.

10.9 High Hydrocarbons formed in methane reforming

The gaseous products detected in above experiments consisted mainly of H_2 for pure CH_4 reforming; and CO and H_2 for CH_4 reforming in CO_2. However, in addition to these, considerable amounts of C_2-C_4 HCs and trace amounts of C_5-C_{10} were detected by the FID detector of the Varian 450 GC used for both pure CH_4 and CH_4 reforming in CO_2. Further, in CH_4/CO_2 reforming, traces of some oxygenates such as methanol and ethanol were detected in the effluent. This led to further experimental investigations to determine the distribution of these HCs and oxygenates. Cold traps were used to liquefy the HCs and oxygenates compounds generated. Two cold traps made of glass thimbles were used to liquefy some plasma reaction products as shown in *Figure 9-3*. The two cold traps were connected in series with the first one closer to the plasma reactor chilled with ice cold water bath while the second was chilled with dry ice at -79^oC. The first was to trap any water and higher boiling point products of plasma reactions. The second was to trap products of much lower boiling point. It was important to position the cold traps in this order as arranging them in reverse order would cause blockage of the pipes by frozen water and/or oxygenates at -79^oC. During these cold trap experiments which were conducted continuously over extended period of days, data was collected during daylight hours. The liquid products captured in both traps were later on analysed using a Variant 450 GC. *Figure 10-23* shows a typical chromatogram of cold trap products.

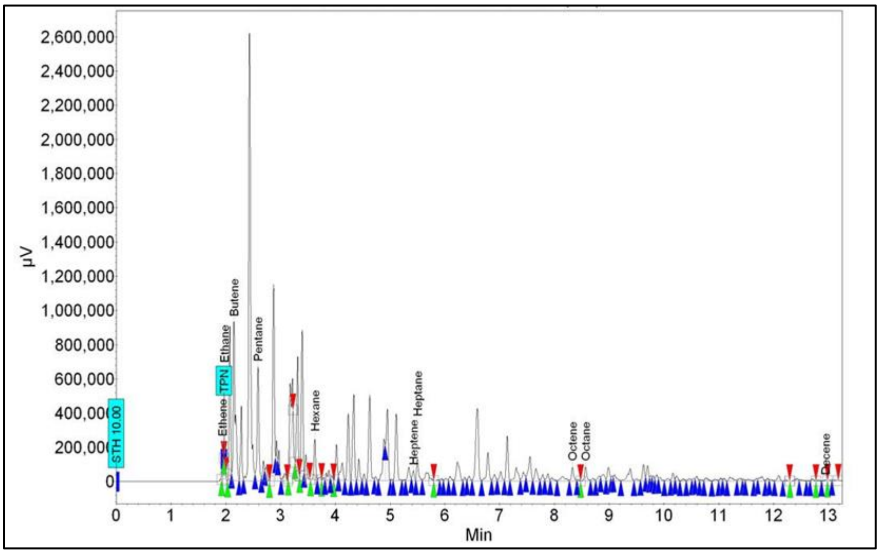

Figure 10-23 CO_2-CH_4 dry ice cold trap liquid products

These products were in liquid phase at -79^oC. In this chromatogram, the only few peaks identified are those for which the GC was calibrated. As *Figure 10-23* shows, there are many more unlabelled peaks for other products for which the GC was not calibrated. The multitude of such peaks demonstrates the complex nature of plasma reactions of pure CH_4 and CH_4/CO_2 mixture, but important is the fact that the products are most probably in C_5- C_{10} hydrocarbons (as several small unidentified peaks appear beyond the pentane peak). The unidentified peaks after the pentane peak might represent some constituents found in gasoline. More sophisticated equipment not available in the lab is necessary to identify these components and quantitating them. *Figure 10-24* shows a typical chromatogram for the ice cold water trap products collected only when a CH_4/CO_2 mixture was fed into the plasma reactor. These products were in liquid phase at about 0^oC. Unlike with CH_4/CO_2 reforming where oxygenates and possibly water were captured in the ice cold water trap, in the case of pure methane, no liquid products were collected in this trap. This was expected as theoretically, plasma reaction of pure methane cannot be expected to produce oxygen-containing products. In the absence of oxygen as a co-feed, or CO_2 as a soft oxidant to supply O radicals, there was no oxidation to water or formation of oxygenates. For CH_4/CO_2 mixture, some of the compounds in the ice cold water trap detected by the GC included methanol, ethanol butanol, acetone and butyric acid. There were several other peaks not identified by the GC used. A typical chromatogram of a specimen tested off-line on an Agilent 5890 GC calibrated to detect and identify several oxygenates is shown in *Figure 10-24*. It shows oxygenates such as methanol, ethanol, acetone, butanol, butyric acid and other unidentified compounds were produced in plasma reactions of CH_4/CO_2.

The composition of the effluent gases and cold trap products provide some insight into the elementary reactions that occur in plasma treatment of CH_4 or CH_4/CO_2 mixture. The high concentration of H_2 confirms dehydrogenation of methane while the presence of unsaturated hydrocarbons such as ethene, pentene, heptene and hexene give a strong indication of possible polymerization since such species are known to undergo easy polymerization via the double bonds. Ethene, for example, can be regarded as a derivative monomer and likely precursor to polymer formation and the presence of C_{3+} hydrocarbons detected in the product stream demonstrate occurrence of chain growth from unsaturated C_{2+}. This result is important as it shows that plasma based dry reforming of methane with carbon dioxide can produce a number of different chemical compounds, including the all-important syngas (H_2 and CO) in one run. The syngas can be used as a source of H_2 or used in further steps such as F-T synthesis into other important products. The other chemical compounds can have important value in the market, e.g. the liquid hydrocarbons and oxygenates as fuel components or precursors. Plasma activated dry reforming can therefore permit possibilities of poly-generation strategies in exploiting the huge resources in natural gas and biogas.

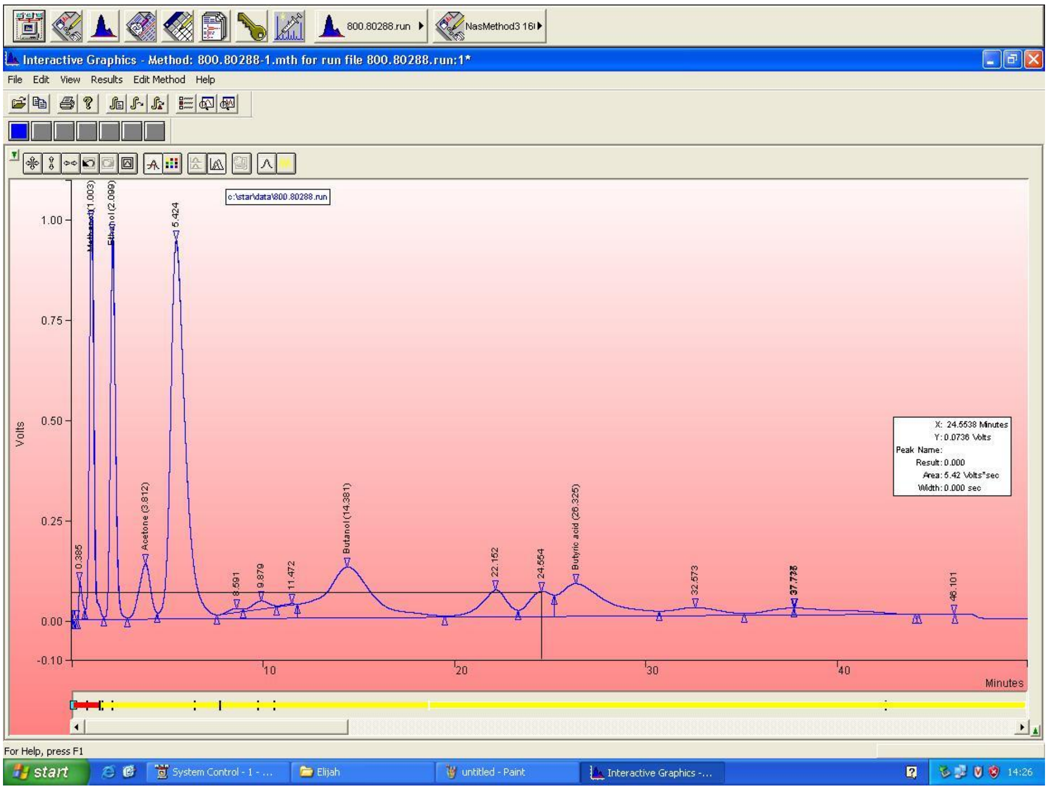

X: 24.5538 Minutes
Y: 0.0736 Volts
Peak Name:
Result: 0.000
Area: 5.42 Volts*sec
Width: 0.000 sec

Figure 10-24 Typical cold water trap products chromatogram

10.10 Stability of plasma reactions over extended continuous operation

From the data collected during the 72 hours continuous operation experiments, the long term stability of the reactor in conversion reactions could be evaluated. The results are as depicted in *Figure 10-25* and *Figure 10-26*. They show that in equi-molar plasma activated reforming of CH_4/CO_2, conversions of both CH_4 and CO_2 and yields of CO and H_2 remain roughly unchanged over continuously running for 72 hours of continuous operation. However, the packed barium titanate balls were increasingly coated with a polymer film which apparently did not noticeably affect the conversion performance of the reactor.

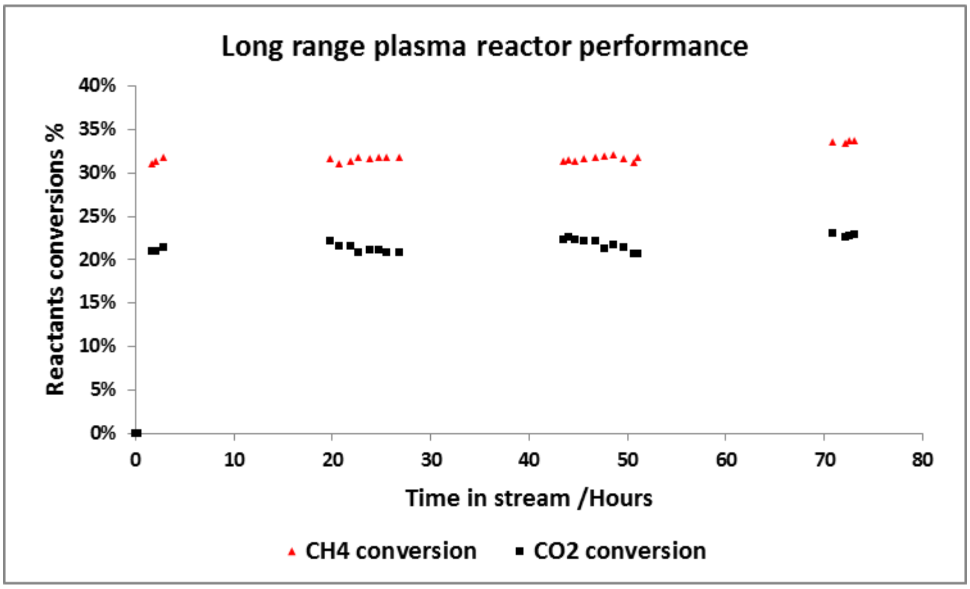

Figure 10-25 Long range conversions

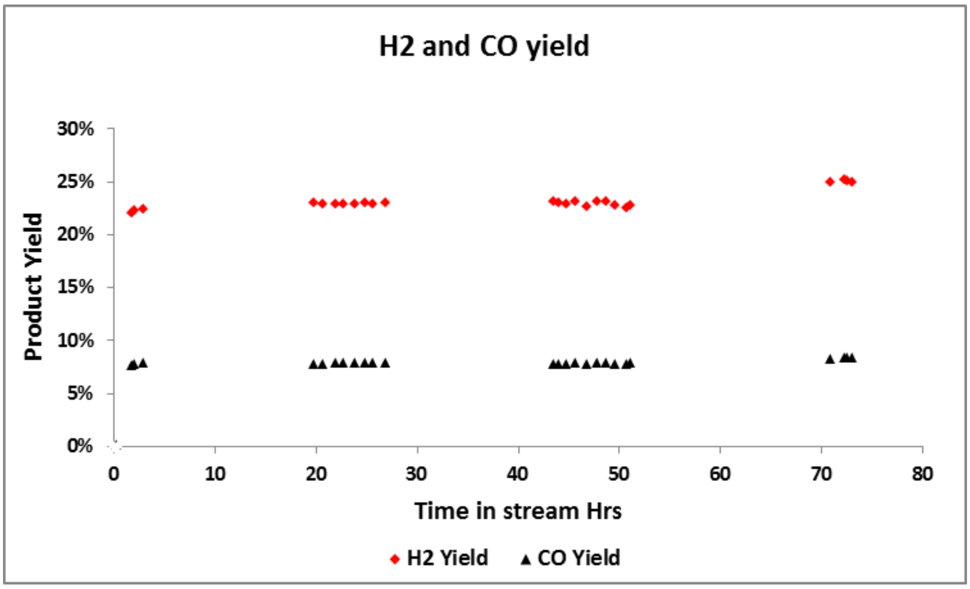

Figure 10-26 Long range product yield performance

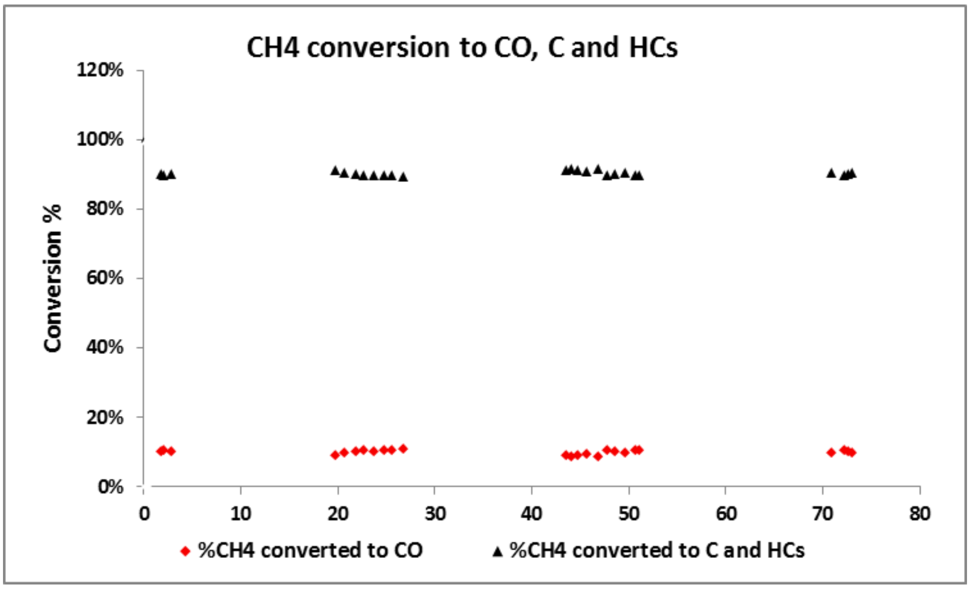

Figure 10-27 CH_4 derived carbon distribution between CO and other products e.g. HCs

Figure 10-27 shows that only about 11% of the carbon from the converted methane goes towards production of CO while the rest goes towards synthesis of HCs and oxygenates. A visual inspection showed no visible signs of coke formation. About 89% of the CO produced comes from the decomposition of CO_2.The other 11% of the CO is derived from the converted CH_4. It can be conceivably be hypothesised that the reaction route for conversion of CH_4 to CO is the reaction of coke from complete methane decomposition with O radicals from CO_2 decomposition to form CO, i.e.

$$\mathrm{CH_4 + e \rightarrow CH_3 + H + e\ (4.45eV)}$$ Eqn 10.10

$$\mathrm{CH_3 + e \rightarrow CH_2 + H + e\ (4.90eV)}$$ Eqn 10.11

$$\mathrm{CH_2 + e \rightarrow CH + H + e\ (4.47eV)}$$ Eqn 10.12

$$\mathrm{CH + e \rightarrow C + H + e\ (3.51eV)}$$ Eqn 10.13

$$\mathrm{CO_2 + e \rightarrow CO + O + e\ (5.5eV)}$$ Eqn 10.14

$$C + O \rightarrow CO \qquad \text{Eqn 10.15}$$

The basis of this explanation is that experimental results show that the converted CO_2 was less than the CO produced, an indication that some of the CO was derived from CH_4. The possible pathway for this CH_4 derived CO is Eqn 10.10 to Eqn 10.15. This reasoning is strengthened by the observation that in decomposition of pure methane in plasma, traces of carbon black formed on the surfaces of the balls. However for CH_4-CO_2 mixture, little or no traces of carbon black were visible indicating the C that might have been formed from methane decomposition was oxidised. This combination of findings provides some support for the conceptual premise that CH_4 derived CO is formed by Eqn 10.15. (De Bie et al., 2011) have reported that Eqn 10.10 is responsible for 79% of the total electron impact dissociation of CH_4 while Eqn 10.11and Eqn 10.12 are responsible for 15% and 5% respectively. The remainder can be assumed to account for by Eqn 10.13 from which the CH_4-derived CO could have been formed.

Another observation from this experiment was that the plasma reactions remained stable for the continuous run of 72 hours despite the coating of the plasma reactor walls and catalyst with a golden brown polymer. *Figure 10-28* shows the golden brown film coating the inside walls of the quartz reactor. The same polymer film was deposited on the dielectric balls but, from the insignificant changes in conversion of the reactants, it appears this did not affect plasma conversion of the two reactants. (Liu et al., 2001) observed similar film formation which was further examined using Infrared Analysis to show a complex chemical highly branched structures with variable alkyl groups and many oxygen containing groups that included ketones. Unfortunately in the current work, such analytical facilities were not available. The result shows CH_4/CO_2 mixture in plasma are good sources of plasma polymerised films under the conditions the experiments were carried out.

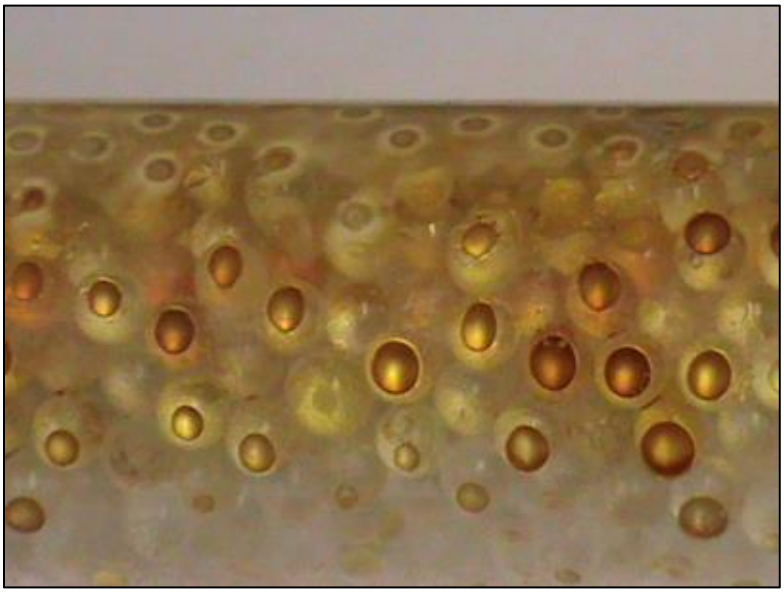

Figure 10-28 Picture of reactor walls coated with golden brown film

10.10.1 Plasma polymerisation

Collision between CH_4 molecules and an energetic electrons produce CH_3 radicals (Eqn 10.16) which may combine to form ethane according to Eqn 10.17.

$$\mathrm{CH_4 + e \rightarrow CH_3 + H + e} \qquad \text{Eqn 10.16}$$

The methyl radicals are very reactive species and can readily interact with each other to form ethane.

$$\mathrm{CH_3 + CH_3 \rightarrow C_2H_6} \qquad \text{Eqn 10.17}$$

Ethane may be converted by electron collision to form free ethyl radicals that can react with other ethyl radicals, methyl radicals or other free radicals to form long chain hydrocarbons in a chain propagation process. Progressively higher molecular weight products may therefore be formed. Free radical branching can also occur and result in plasma induced polymerisation to produce organic material that was deposited on the internal walls of the plasma reactor and packed balls surfaces. In addition, methyl radicals also combine with activated C_2 molecules to form C_3 hydrocarbons, or with activated C_3 molecules to form C_4 hydrocarbons, and so on (Kraus et al., 2002).

10.11 Combining non-thermal plasma and catalysis

Conventional dry reforming of methane with carbon dioxide using catalyst has two major problems. The reactions require extreme conditions of high temperatures and pressure (typically up to 1000°C and 4 bar) (Kraus et al., 2002), and therefore high energy consumption (Hessel et al., 2013). The reaction is represented by Eqn 10.18.

$$\mathrm{CH_4 + CO_2 \leftrightarrow 2CO + 2H_2\ \Delta H = 247kJmol^{-1}} \qquad \text{Eqn 10.18}$$

In addition the catalysts used are susceptible to deactivation before not long by coke deposition on the catalyst surface. Coke formed on the catalyst surface blocks the catalyst active sites, preventing reactant molecules from contacting and interacting with these sites. This results in the need to reactivate the catalyst increasing the costs in terms of lost production time as well as financial costs arising from the reactivation process itself.

The models widely accepted to explain heterogeneous catalytic reactions are the Langmuir-Hinshelwood (LH) mechanism and the Eley-Rideal (ER) mechanism. In the LH mechanism, gas molecules are adsorbed on the catalyst surface and reactions take place between the adsorbed species. In the ER mechanism, gas molecules of one or more reactants are adsorbed on the catalyst surface and react with other molecules (species) still in the gas phase. In thermocatalytic methane reforming reaction of methane and carbon dioxide for instance, the steps in the reaction are (1) the adsorption and dissociation of CH_4 and CO_2 on the active sites of the metal catalyst, (2) adsorption of carbon, and hydrogen and oxygen species on catalyst active sites, (3) surface reactions to form product species, desorption of products from catalyst surface.

Several precious metals are known to have high catalytic activity as well as high resistance to coke deposition. However, the high costs of many of these, and their limited availability has rendered them unsuitable in industrial application. Nickel also has high catalytic activity and is much cheaper. However, it suffers from poor resistance to carbon deposition which deactivates the catalytic activity as well as susceptibility to sintering at the typical reforming reactions temperatures. Hybrid catalytic non-thermal plasma has the potential to improve reforming conversion at low temperatures. Synergetic effect between plasma and catalyst could decrease the reaction temperature and pressure requirements while maintaining required selectivities. Studies on the possible synergy between non-thermal plasma and catalysis needs to be undertaken before the association of non-thermal plasma and catalysis is more clearly understood.

10.11.1 Possible role of catalyst in hybrid plasma catalytic reactions

In non-thermal plasma chemistry, high kinetic energy electrons (~10^4-10^5 K) collide with heavier neutral particles (gas molecules) at much lower temperatures resulting in formation of highly reactive radicals, ions, meta-stables and vibrationally excited species. Unlike in conventional catalytic reactions in which reactants are thermally activated with the catalyst taking part in the bond breaking, in hybrid non-thermal plasma catalytic reactions, activation of reactants is via the electron collision. The energy provided by high temperature to activate the gaseous reactants in the conventional thermal systems is now delivered by energetic electrons in non-thermal plasma. The question of whether or not the presence of a catalyst in the plasma zone can have an effect on the conversion and selectivities of products is what needs to be experimentally tested. There are two scenarios, which may not be mutually exclusive, that can be speculated:

1. That the presence of the catalyst has an effect on the plasma properties which then has an effect on the conversion and /or selectivities, or;

2. That the plasma has an effect on the catalyst which may result in changes in its activity.

According to (Heintze and Pietruszka, 2004), a catalyst placed in the plasma zone can influence the plasma properties, especially metallic catalysts, due to their conductive surfaces. This might be in the form of altering the electron energy distribution which might influence reactants conversions. On the other hand, the plasma can influence the catalyst properties by causing heating the catalyst thereby inducing desorption of surface species. They proposed that synergy between catalysis and plasma is achieved if plasma-catalyst interactions lead to improved reagent conversion or higher selectivity of the desired products compared to purely plasma or catalytic process. (Tu et al., 2011) have proposed that the synergistic effect of combined plasma and catalysis of hydrocarbons depends on the balance between discharge behaviour induced by presence of the catalyst and the catalytic activity induced on the catalyst by the presence of the discharge. From their studies on dry reforming of methane in reduced Ni/Al_2O_3 using non-thermal plasma, they concluded that there is significant enhancement of local electric field and increased charge deposition on the catalyst.

In non-thermal plasma, the high kinetic energy electrons are non-selective (Chen et al., 2010) as to which molecules in the plasma field to collide with. Hence when a mixture of gases is subjected to plasma, the energetic electrons cannot discriminate as to which gas molecules to excite. The extent of excitation of a particular reactant depends on the properties of the reactant in terms of excitation energy thresholds and perhaps its mole concentration in the mixture. In a CH_4/CO_2 gas mixture, CH_4 is dissociated into methyl radicals which can undergo further dehydrogenation in reactions represented by Eqn 10.19. The radicals formed in these steps may recombine leading to the formation of secondary chemical products. For instance CH_3 may recombine to form C_2H_6 (ethane). These secondary products, if they remain in the plasma zone for long enough, can further undergo conversion by electron collision to form more varieties of radicals.

$$CH_x + e \rightarrow CH_{x-1} + xH \;\; ; x = 1,2,3,4 \qquad \text{Eqn 10.19}$$

Turning to CO_2, collision with energetic electrons dissociates CO_2 to CO and O, as represented by Eqn 10.20.

$$\mathrm{CO_2 + e \rightarrow CO + O} \qquad \text{Eqn 10.20}$$

In principle the CO can be further decomposed to C and O in the reaction:

$$\mathrm{CO} + \mathrm{e} \rightarrow \mathrm{C} + \mathrm{O} \qquad \text{Eqn 10.21}$$

However reaction Eqn 10.21 requires much more energy (about 11.16eV). In typical dielectric barrier discharge plasma, electron energies are generally in the range 1-10eV. From this standpoint, there is insignificant disproportionation of CO to C.

From the foregoing, with so many possible highly reactive species especially from methane, it is clearly difficult to predict the results of plasma chemical reaction processes because of the variety of highly reactive species that may be formed by electron collisions. The wide spectrum of chemically reactive species formed can potentially react with each other to form an equally wide spectrum of secondary products. Consequently, it is a challenge to achieve simultaneous high conversion and satisfactory selectivity of desired reaction products.

10.11.2 Experimental investigation of the effect of catalyst in non-thermal plasma dry reforming of CH_4 with CO_2

The effect of inclusion of catalyst in discharge volume in non-thermal plasma activated dry reforming of CH_4 with CO_2 was investigated. In the experiment, the set-up shown in the schematic in *Figure 9-3* was used. Under the same input electrical power, the reactor plasma zone was packed with (A) Barium Titanate balls (5mm Dia), (B) Barium Titanate balls (5mm Dia) in which Ni:Si of 1:4 (molar ratio); is evenly dispersed, (C) Ni:Si of 1:4 (molar ratio) alone, (D) NiFeSi (118) catalyst alone, and (E) Johnson Matthey Catalyst- 33% Ni/Al_2O_3 catalyst.

The Ni:Si 1:4 catalyst with a weight ratio NiO/SiO_2 =0.31 being ((1x74.7)/(4x60) and a NiO loading of 24% by weight, being ($NiO/(NiO+(4xSiO_2)$) was reduced in 50ml of hydrogen flow at 550°C for 24 hours.

The NiFeSi 118 catalyst of molar ratio of Ni:Fe:Si =1:1:8 was reduced in 50ml/min hydrogen flow at 550°C for 24 hours.

The results of hybrid plasma catalytic conversion of equi-molar CH_4/CO_2 mixture with these materials are as in Table 10-13, Table 10-14 and *Figure 10-29*.

Comparing the CH_4:CO_2 conversions using packed $BaTiO_3$ balls alone versus packed $BaTiO_3$ with NiSi(14) particles dispersed in the bed, there is a clear drop in conversions of both CH_4 and CO_2 from 27.3% to 18.8% for CH_4 and 16.2% to 10.6% for CO_2. Selectivity of H_2 and CO were 54.7% and 48.7% respectively for $BaTiO_3$ balls alone while for $BaTiO_3$/NiSi(14) the selectivities were 54.0% and 54.7% for H_2 and CO respectively.

Table 10-13 Conversion of CH_4 and CO_2 in non-thermal plasma with and without catalysts

Catalyst Reactant	BaTiO3 balls	BaTiO3/Ni:Si1:4	NiSi(14)	NiFeSi (118)	JM catalyst
CH4 conversion (%)	27.3	18.8	18.7	26.4	10.0
CO2 conversion (%)	16.2	10.6	10.1	13.3	5.0

Table 10-14 Products selectivities with and without catalysts

Catalyst	Product selectivity (mol %)			H_2/CO ratio	CH_4 converted to:	
	H_2 (%)	CO (%)	HC* (%)		CO (%)	HC*(%)
$BaTiO_3$ balls	54.7	48.7	51.3	1.41	18.2	81.8
$BaTiO_3$/NiSi(14)	54.0	54.3	45.7	1.24	32.0	68.0
NiSi(14)	51.7	53.8	46.2	1.25	28.9	71.1
NiFeSi (118)	56.4	52.5	47.5	1.43	28.6	71.4
JM catalyst	42.0	20.0	-	2.75	-	-

HC = Higher Hydrocarbons and oxygenates (and possibly Carbon)

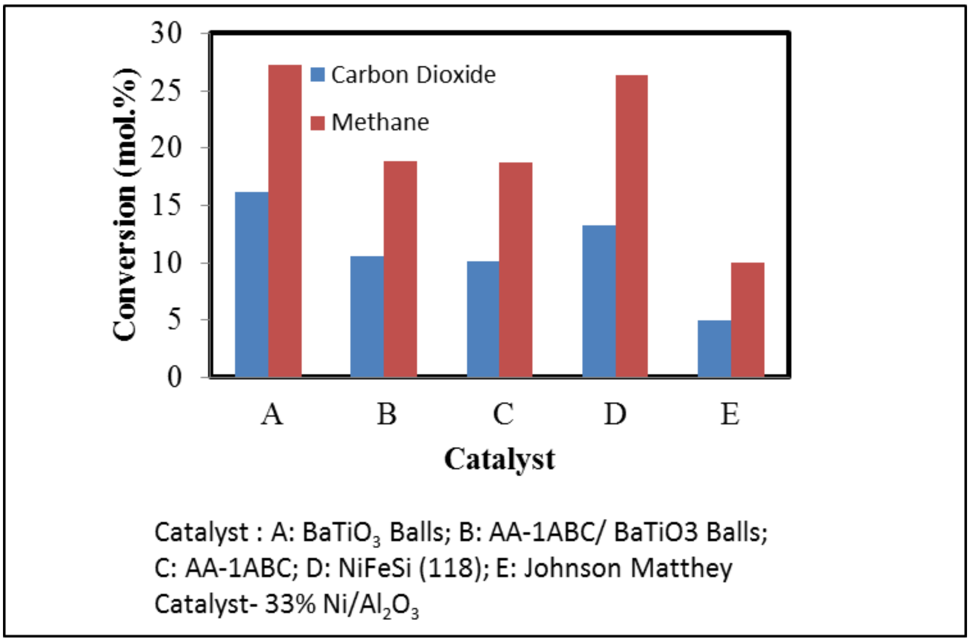

Figure 10-29 Graphical representation of reactant conversions with different catalysts

The fall in conversions of the two reactants might be due to the influence of the presence of metal particles on discharge characteristics such as the effective electric field intensity and the mean electron energy. Interestingly, the selectivity of H2 remained almost unchanged while there was a significant rise in CO selectivity from 48.7% with $BaTiO_3$ alone to 54.7% for $BaTiO_3$/NiSi(14). This is also reflected in the H_2/CO ratio which changed from 1.41 for $BaTiO_3$ alone to 1.24 for $BaTiO_3$/NiSi(14). This apparently is as a result of an increase in the proportion of CH_4 converted to CO from 18.2% to 32.0% respectively meaning the catalyst might have promoted more conversion of CH_4 to CO. From this result it can be concluded that while the NiSi(14) catalyst reduced conversion of reactants, it increased the selectivity in the converted CH_4 to CO.

Similar experiments under same conditions of applied electrical power and feed gas composition and flowrate were conducted with the reactor packed with NiSi(14) only and NiFeSi(118) only. For NiSi(14) catalyst, CH_4 and CO_2 conversions were 18.7% and 10.1% respectively while those for NiFeSi(118) were 26.4% and 13.3%. The H_2 and CO selectivities were 51.7% and 53.8% respectively for NiSi(14) while those for NiFeSi(118) were respectively 56.4% and 52.5%. The proportion of converted CH_4 to CO for both catalysts were roughly the same, 28.9% for NiSi(14) and 28.6% for

NiFeSi(118). Clearly, between these two catalysts, NiFeSi(118) has higher conversion efficiency than NiSi(14) and has higher selectivity towards H2 than CO while NiSi(14) has higher CO selectivity. The presence of the catalyst therefore appears to have induced a modification of the selectivities of CO and H_2.

10.11.3 Comparisons with reports in literature

A comparison of these catalyst used in the current work has been made with results reported in literature under same reactants composition, feed flow and roughly same applied plasma power, but with a Johnson Matthey Catalyst- 33% Ni/Al_2O_3 catalyst and different reactor configurations. The results obtained for conversions were 10% and 5% for CH_4 and CO_2 respectively while the H_2/CO ratio of 2.75 indicating a much higher selectivity of H_2 than CO (Tu et al., 2011). It is difficult to make any judgements on these comparisons because of the reactors were different in several ways such as characteristics of power source unit and size of discharge gap.

Some synergistic effects between non-thermal plasma and catalysts have been claimed in many studies. For instance (Pietruszka and Heintze, 2004) have claimed that non-thermal plasma chemically activate reactants and accelerate the process of reactant adsorption on catalyst and product desorption. (Kraus et al., 2001) also claimed that discharge activated methane was easier to adsorb on the catalyst surface.

10.11.4 Discussions on effect of catalyst on plasma reactions

In hybrid plasma catalytic systems, the reactions can be categorised into several stages (Sentek et al., 2010):

The first stage is reagent activation by electron collisions:

$$\mathrm{CH_4 + e \rightarrow CH_3 + H + e} \qquad \text{Eqn 10.22}$$

$$\mathrm{CH_3 + e \rightarrow CH_2 + H + e} \qquad \text{Eqn 10.23}$$

$$\mathrm{CH_2 + e \rightarrow CH + H + e} \qquad \text{Eqn 10.24}$$

$$\mathrm{CH} + \mathrm{e} \rightarrow \mathrm{C} + \mathrm{H} + \mathrm{e}$$ Eqn 10.25

$$\mathrm{CO_2} + \mathrm{e} \rightarrow \mathrm{CO} + \mathrm{O} + \mathrm{e}$$ Eqn 10.26

The energised electrons may also generate short-life active vibrationally excited molecules from the reagents.

The second stage is the homogeneous gas phase reaction of short-life active species. With these, if the time elapsing between their generation and their contact with catalyst surface is relatively long, their reactions are terminated in the gas phase before reaching the catalyst surface and the catalyst has no influence on them.

The third stage is where the active species generated in the discharge have long enough lives to reach reactor walls or walls of the packed balls/pellets and catalyst surfaces in the discharge volume. On the catalyst surfaces in the discharge volume, a chain of processes may ensue which may include adsorption of species on catalyst surfaces, reaction between adsorbed species and desorption of reaction products. In this case, a catalyst may influence reaction products.

(Zhang et al., 2010) have proposed a possible reaction mechanism showing the role of the catalyst. According to them, the reaction begins with the dissociation of CH_4 and CO_2 by electron collision in the discharge with CH_3 + H radicals being formed from CH_4 dissociation, and CO + O from CO_2 dissociation. In the gas phase some CH_3 can combine to form C_2H_6 and H can form H_2. Meanwhile some of the radicals can also more easily adsorb on the catalyst surface according to the following mechanisms:

$$CH_x + * \rightarrow\ (CH_x)_{ad}\ (x = 0, 1, 2,3)$$ Eqn 10.27

$$H + * \rightarrow\ H_{ad}$$ Eqn 10.28

$O + * \rightarrow O_{ad}$ Eqn 10.29

$(CH_x)_{ad} + O_{ad} \rightarrow CO_{ad} + xH_{ad}$ Eqn 10.30

$CO_{ad} \rightarrow CO + *$ Eqn 10.31

$2H_{ad} \rightarrow H_2 + *$ Eqn 10.32

where $*$ marks an empty adsorption site on the catalyst surface. The intermediate O_{ad} is derived from the dissociation of CO_2 into CO and O. The reaction mechanism suggests that the adsorbed carbon species $CH_x(x = 0, 1, 2, 3)$ from CH_4 dissociation react to form CO and H_2. The effect of combining non-thermal plasma and catalysis according to this model is that plasma discharge's role is providing highly active species while the catalyst surfaces provide sites on which these radicals can be adsorbed and participate in reactions with other species to produce products.

Eqn 10.30 appear to corroborate experimental observation showing higher proportion of CH_4 converted to CO with NiSi(14) catalyst.

In the present work, it has been observed that although there are some changes in reaction performances with catalyst compared to without catalyst, the changes are not big. There may be a number of possible reasons for this. For instance, the presence of solid catalyst particles in the discharge volume may change the plasma properties in significant ways in terms of electric field strength and current density. The presence of conductive metallic particles might modify the effective dielectric constant of the packed pellets in the plasma, according Section 8.4.1 On the other hand, the catalytic function of the catalyst particles may also be significantly altered by the plasma field by way of changes in the catalyst work function (Vandenbroucke et al., 2011). In addition, the envisaged improvement in performance with catalyst may not be forthcoming without high enough temperature (in cold plasma) required for catalytic activity. (Juan-Juan et al., 2009), have suggested that nickel catalyst activation in thermal dry reforming of methane occurs at temperatures above 773K

(500^oC). In non-equilibrium plasma based dry reforming used in current work, the reactor temperature under operating conditions was around 120^oC, well below the 500^oC (773K). The low non-equilibrium plasma temperature might imply the catalyst is not heated to its activation temperature, hence its low effectiveness. A suggested area of further investigation is use of warm plasma operating at above 500^oC. This would require a new reactor design with materials that can withstand such temperatures.

10.11.5 Effect of type and size of dielectric material packed in plasma zone

Other non-thermal plasma operating conditions investigated in order to investigate optimal conditions for improved conversion efficiency were the effect of type and size of dielectric material packed in the reactor.

10.11.5.1 Effect of different materials

Experiments were conducted with CH_4/CO_2 mixture with the reactor packed with the following materials:

1. No solid materials.
2. Borosilicate glass balls
3. Soda lime glass balls.
4. Barium Titanate ($BaTiO_3$) balls.

With (1) and (2), plasma could not be ignited with the equipment used, even with application of the maximum voltage the power source unit could supply, while in cases (3) and (4), plasma ignited at lower applied voltages with the onset ignition voltage for case (4) being lower than that for case (3). This was probably because the breakdown voltages in cases (1) and (2) were probably higher than the power source unit used could provide while that for cases (3) and (4) were within. This preliminary finding shows some dependence of plasma discharge on the material packed in the discharge zone.

The ease with which plasma could be ignited with the reactor packed with $BaTiO_3$

may be due to the higher dielectric constant of barium titanate ($2000 < \varepsilon < 10000$) (Vandenbroucke et al., 2011) than that of the other materials used. It has been reported that ferroelectric materials in plasma induces a shift in accelerated electron distribution, a phenomenon attributed to an increased electric field by a factor of as much as 10-250 (Holzer et al., 2005). Barium Titanate does not only have a high dielectric constant, but it is also a ferroelectric material. An important physical property of ferroelectric materials is that below their Curie temperature, they can be spontaneously polarised even in the absence of an electric field (Fridman et al., 2005), (Brzozowski and Castro, 2000). The Curie temperature is the transition temperature above which the spontaneous polarisation of the ferroelectric material vanishes. When an AC voltage is applied to Barium Titanate in its ferroelectric phase, polarisation is enhanced and strong local electrical fields on the surface up to 10^6V/cm are formed and stimulate discharge from the surface. Hence if the discharge zone in a DBD reactor is packed with barium titanate pellets/balls, plasma can be readily ignited in void spaces between the pellets at lower applied voltage. The ferroelectric induced increase in electric field enable breakdown to occur and ignite plasma (Fridman et al., 2005). According to (Fournaud et al., 2009) $BaTiO_3$ can be polarised because electrons can move on spherical pellets and can accumulate charges on the surface of the balls and enhance the electric field responsible for the creation of discharge streamers, especially close to contact points with neighbouring balls or reactor walls.

(Li et al., 2006) have also suggested that the presence in the plasma area, of materials with high dielectric properties such as $XTiO_3$ allows electrical charges to accumulate on the particles' surfaces especially close to the contact points between the pellets. (Li et al., 2004) experimentally investigated the effect of materials of different permittivity and applied voltage frequency in the conversion of CO_2. The dielectric materials were SiO_2, Al_2O_3, $Ca_{0.7}Sr_{0.3}TiO_3$ with 0.5 wt % $Li_2Si_2O_5$; with relative permittivity values ($\epsilon_r = 4.6, 10.4$ and 207) respectively and observed that CO_2 conversion for each tested frequency 2, 4, 6, 8 and 10MHz were in the order $Ca_{0.7}Sr_{0.3}TiO_3 \gg Al_2O_3 > SiO_2$, in sympathy with increasing permittivity values.

Caution need to be exercised in interpreting this as it might suggest that the conversion efficiency of DBD plasma might be expected to increase with increasing permittivity of packed material ad infinitum. This however is not the case (Li et al., 2006), as it has been observed from previous work that high dielectric constant materials (ceramics) have low dielectric strength and tend to fracture under the tension of high voltage conditions. In addition, as observed by (Chen et al., 2008) who investigated the removal of C_6F_6 it is found that although using high dielectric constant material is favourable, raising the dielectric constant of packed material cannot unlimitedly improve conversion. (Jae-Duk and Sang-Taek, 1997) and (Ogata et al., 1999), in ozone generation studies, have proposed that there is an optimum dielectric constant and that when it is >660, ozone almost vanishes. While this may not be the case with all plasma applications, it is an important indicator. (Holzer et al., 2005), (Futamura et al., 2002) have also experimentally shown that ozone generation deteriorates with too high dielectric constant.

10.11.5.2 The effect of dielectric material pellet size on plasma reactions

Another parameter that might influence non-thermal plasma performance in fuel conversion is the size of packed dielectric pellets in the discharge zone. Sodalime glass balls of size 3mm, 4mm and 5mm diameter were chosen to study the effect of ball sizes on conversions of 1:1 mixture of CH_4:CO_2. A further experiment was conducted with the plasma reactor packed by an evenly distributed mixture of 3mm and 5mm diameter in the ration 1:1 by volume. Comparison of effect on CH_4/CO_2 conversion of $BaTiO_3$ and SLG of same size under the same feed gas composition and flowrate, and under same applied plasma power was done under this set of experimental work. The results are summarised in Table 10-15 and *Figure 10-30.*

Table 10-15 Effect of pellet size on conversion

Reactant	4mm SLG	3-5mm SLG	5mm SLG	4mm BTO
CO_2 conversion	7%	8%	15%	16%
CH_4 conversion	13%	16%	27%	30%

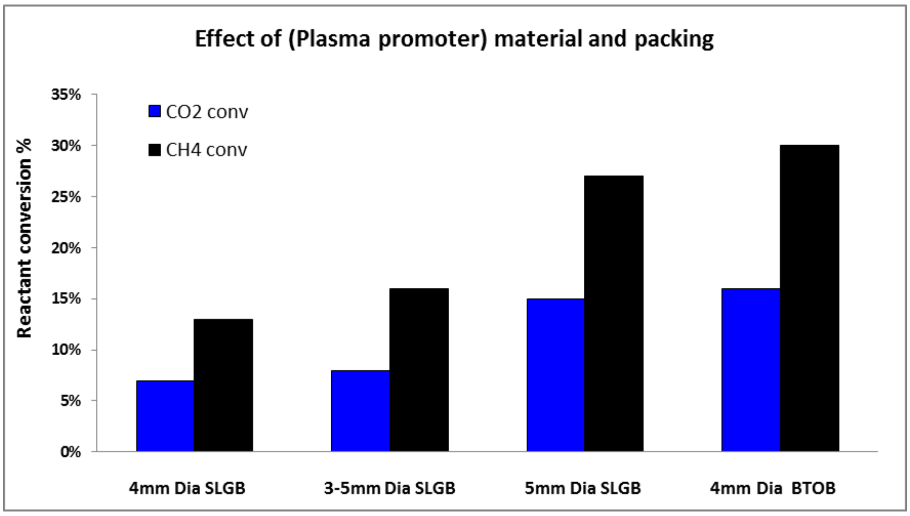

Figure 10-30 Effect of SLG pellet size on conversion

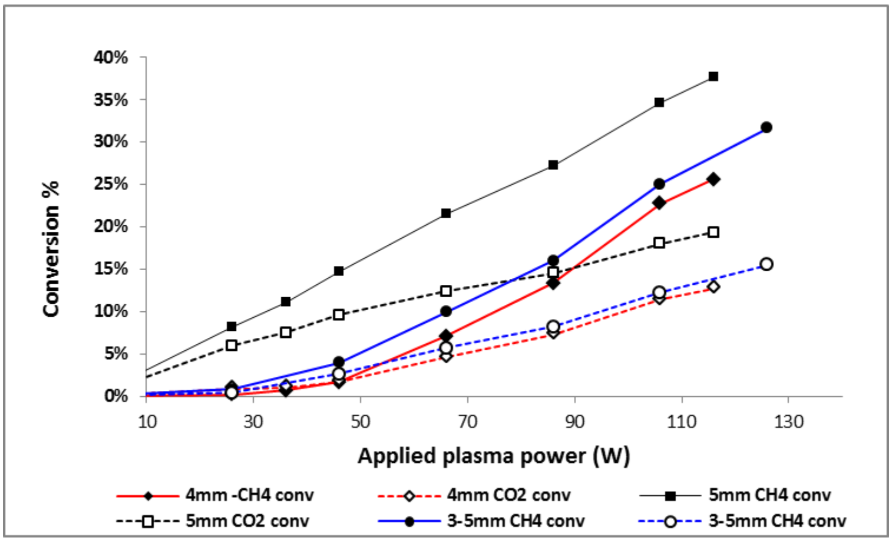

Figure 10-31 Effect of pellet size on equi-molar, 50ml/min flowrate, varying power; on conversions

As can be observed from *Figure 10-31*, the results show that of the three sizes, the conversions were in the order 5mm diameter balls > 3-5mm diameter mixed balls > 4mm diameter balls. For 3mm diameter balls, the plasma did not ignite at all; hence here were no conversion results. Comparing conversion performances of 4mm diameter and 5mm diameter SLG packed balls under same flow and applied power conditions, it is clear conversion increased with size of packed balls. This observation corroborates findings by (A Ohsawa et al., 2000) and (Chen et al., 2008) in ozone generation using dielectric barrier discharge. Ohsawa et al observed that the current pulses amplitudes in the discharge increased with the size of beads, although with reduced frequency. They concluded that as the beads size increase, the number of micro-discharges in the discharge volume decreased but the amount of charge transferred per individual discharge increased. Conversely, since the micro-discharges mainly take place near contact points between beads and between beads and reactor walls, there are more contact points (and therefore micro-discharges) with smaller beads than with bigger beads. With increased number of micro-discharges, the amount of charge transferred (micro-discharge intensity) per micro-discharge is reduced. It is expected that higher the micro-discharge intensity give rise to higher mean electron energy of the discharge. The higher the mean electron energy of the discharge implies more electrons with enough energy to fragment reactant molecules. This might explain the higher conversions with 5mm balls than with 4mm balls. Regarding conversion performance using mechanically mixed equal volumes of 3mm and 5mm diameter SLG balls in plasma volume, it can be seen that the conversion performance is slightly superior to conversion with 4mm diameter balls, but inferior to when 5mm diameter balls are packed. This appears to accord with (A Ohsawa et al., 2000) reasoning.

The result may also be explained in terms of overall packing density or void volume. The void volume consisting of gaps between the packed balls increases with size of balls used. Put differently, the void volume reduces with decreasing size of balls. However, the smaller void volume results in a higher flow velocity of the gas within the packed volume. The higher flow velocity results in reduced residence time of reactants in the plasma and consequently lower conversions as has already been discussed elsewhere in this thesis. Conversely, the higher void volume with bigger ball sizes packed results in lower gas velocity and higher residence time of reactants in the plasma zone and therefore higher conversions.

The packed balls in the plasma zone enhance the electric fields at the contact points between the balls/beads and between the balls and reactor walls. Higher electric fields give rise to higher electronic energies. The effect of soda lime glass balls and BaTiO3 balls of the same sizes have shown higher conversions with BaTiO3 than with Sodalime glass balls. Two mechanisms might explain this result.

What this result indicates is possibly the competing effects of electric field enhancement at contact points and gas flow rate through the packed reactor. Electric field strength increases significantly near the contact points between neighbouring balls and between balls and reactor walls because of the short distances near these contact points. A reactor packed with smaller balls has many more ball to ball contact points than a reactor packed with bigger balls. There are more balls of smaller diameter in the reactor than balls of larger diameter in the same volume and therefore there are more ball to ball contact points with smaller diameter balls than with larger diameter. Based on this reasoning, smaller balls produce a stronger electric field. In this respect one would expect higher conversions with smaller balls/beads than with bigger. However contrary to these expectations, experimental results in the conversion of CO_2 and CH_4 gas mixture have shown higher conversion rates with bigger balls Figure 10-31. There are therefore must be other explanations for this behaviour.

This might be explained by the effect on packing density with different ball sizes. Smaller diameter balls lead to more packing with overall smaller inter-ball void spaces than with bigger balls. This implies that for the same reactant gases feed flowrate and same pressure, the space velocity of gas molecules is higher in the reactor packed zone with smaller diameter balls packed in the reactor than with larger diameter balls. An analogy can be drawn from water velocity through pipes of different diameters while under similar feed conditions. It would be expected that water flows faster through the smaller diameter pipe than through the wider pipe.

Results reported elsewhere in this work show that conversions are inversely proportional to flowrate. The space velocity of gas molecules through such packed reactor is related to gas molecules residence time in the plasma zone. The effect of packing the reactor with smaller beads has the same effect as increasing flowrate and hence lower conversions.

From the above two points of view, bigger beads promote lower flowrate and hence higher conversions while smaller beads promote higher conversions from electric field enhancement at contact points and area of contact points of view. The size of packed beads has therefore at least two competing effects and for a given size of balls of a particular material, the performance depends on the balance of these two effects. There might be an optimum size of balls for the most optimum conversion. More research on this area needs to be undertaken before an association between pellet size and conversion performance is more clearly understood.

10.12 Conclusions

The principal goals of this part of the Thesis were to investigate the effect of various parameters on conversion of CH_4 or CH_4/CO_2 to hydrogen or syngas and other products using non-thermal DBD plasma. The key parameters investigated were:

- Applied plasma power.
- Feed gas flow rate (residence time in plasma zone).
- The effect of the presence of CO_2 and its relative proportion in the CH_4/CO_2 feed mixture on the conversion of CH_4.
- The effect of the presence of conventional and other catalysts in the plasma zone, on the conversion and selectivities of products.
- The effect of type and size of dielectric material on conversion of reagents.

The results from these investigations have shown that:

- Conversions of reagents increase with increasing applied plasma power. However, for pure methane, at higher plasma power, soot was also formed. For CH_4/CO_2, even at higher applied plasma powers much less soot formation was noticed showing the presence of CO_2 inhibited soot formation to some extent.
- The conversion of reagents at constant applied plasma power increased with decreasing feed flowrates or alternatively, increasing residence time of reagents in the plasma zone.
- Conversion of CH_4 is enhanced by the presence of CO_2 in the feed and generally, the higher the CO_2 content, the higher the conversion of CH_4. However, the H_2/CO ratio decreases with increasing CO_2 proportion. A

significant research finding in this investigation is that for equi-molar concentration of CH_4 and CO_2, a H_2/CO ratio of approximately 1 is obtained, and for CH_4/CO_2 feed ratio of about 70/30, the H_2/CO ratio of about 2 is obtained. The latter is a typical ratio of these reactants in biogas, a renewable resource, and the H_2/CO ratio is ideal for F-T synthesis processes for production of liquid fuels from syngas.

- Investigations on the effect of particular catalysts used did not show much change in conversion of reagents although in some reports in literature show significant improvements in both conversion and selectivities.

- The effect of type and size of dielectric pellets in the plasma zone investigated using Barium titanate and Sodalime glass spheres have shown that for the same size of pellets and other plasma conditions, barium titanate spheres with higher dielectric constant, produce higher conversions. A mathematical explanation of this has been shown from capacitance theory of a concentric plasma reactor.

While this study has not studied the effects of all possible parameters, it has shown that a number of parameters can be used for optimising CH_4 or CH_4/CO_2 conversion and product selectivities and yields.

A number of other research accomplishments include the following:

- That apart from hydrogen or syngas, other potentially commercially useful products are formed in DBD plasma activated reforming of CH_4 or CH_4/CO_2 feed. These include unsaturated hydrocarbons (ethene, propene, butene etc) and more importantly, higher hydrocarbons (C_{5+}) were captured using cold trap.

- A continuous run of the experiment for 3 days did not show any significant decline in conversion despite formation of polymer films that deposited on the reactor walls and dielectric spheres. This shows good stability of plasma conversion even with such polymer films coating the spheres.

- Upwards CO component of the syngas produced from CH_4/CO_2 reforming is mainly from CO_2 conversion, and the remainder from CH_4. This finding illustrates that the technology can recycle CO_2, a waste product of many conventional systems and a greenhouse gas too, to a fuel with a significant heating value.

Although it has been rigorously demonstrated in this work that the concept of non-thermal DBD plasma is promising for fuel conversion, a number of issues still need to be addressed for commercial application, amongst which is energy efficiency, which, as reported in literature, is rather low; and separation of unreacted gas and recycling to reduce waste.

Chapter 11 : GENERAL CONCLUSIONS, SIGNIFICANCE AND RECOMMENDATIONS FOR FUTURE WORK

11.1 Introduction

Intensified reactors for conversion of natural gas are an interesting and promising approach to overcome the limitations of conventional methods. The present study was to evaluate two intensified reactor systems which have the potential to be used for natural gas conversion to hydrogen, syngas and other valuable products such as liquid fuels. Two forms of intensified reactor systems have been developed.

11.2 Catalytic Membrane Reactor

The first one is a multi-functional reactor based on the integration of oxygen separation from air and a combustion reaction in the same unit. The scope of this part of the study was the design and construction of membrane reactor, fabrication of planar dense ceramic oxygen selective membranes, sealing membrane and test membrane reactor under inert and reactive conditions.

The results of this study, though carried out at the lower operating temperature range of the oxygen selective perovskite membranes, have shown that integrating the separation function and a combustion reaction enhances the oxygen separation function than in oxygen separation in inert conditions and sequentially using the produced oxygen in a separate reactor. Oxygen permeation flux of around 0.4mL/cm^2/min was obtained under reactive conditions compared to 0.02mL/cm^2/min under inert conditions at borderline operating temperature conditions of 650^{o}C. Results also show that under reactive conditions, oxygen increased due to fast removal of permeate oxygen by a combustion reaction thus reducing the permeate side surface exchange resistance while the temperature rise from exothermic reaction too reduced the bulk diffusion resistance. The subsequent temperature rise of airside membrane surface via heat conduction also reduced the airside surface exchange resistance. Projected to temperatures of 800-1000^{o}C, permeation with combustion reaction can result in even higher permeation due to enhancements of surface exchange reactions and bulk diffusion at high temperatures. Further improvements can be obtained by application of suitable catalysts to further enhance surface reactions at the air side and reaction products selectivity on the permeate side to produce syngas from hydrocarbon feeds. Development of such catalysts is recommended for further work.

The study has also shown the potential of glass as a high temperature sealant in ceramic oxygen membrane reactor applications. The procedure for hermetically joining the dense ceramic membrane to stainless steel with glass is a major contribution of the present work to the development of intensified membrane reactor for fuel conversion. Ordinary sodalime glass was used in this study but glass of suitable composition to improve its adherence to the membrane and metallic parts can be synthesized and are recommended for further work.

Post operation characterization of spent membrane using SEM, EDS and XRD has shown some microstructural changes on the permeate surface of the membrane arising from the reaction with CO_2 formed in the combustion of the reactive gas used in permeation experiments. The enrichment of Sr and detection of C on the permeate side has pointed to formation of $SrCO_3$ as the cause of the observed microstructural changes on post operation examination. A comparison of XRD characterization of the fresh and spent membrane crushed to powder did not show significant changes implying only a minute layer of $SrCO_3$ on the permeate surface of the spent membrane. This shows that the microstructural changes mainly affected the membrane surface and did not affect the bulk membrane.

Oxygen permeable membrane reactors have the potential of fundamentally changing chemical processes fuel conversion because the in-situ chemical reaction and separation can synergistically increase both separation and reaction performances. In other words, the chemical reaction process can be intensified by higher conversion and better product(s) selectivity.

11.3 Non-Thermal Plasma Reactor

Application of non-thermal plasma for conversion of natural gas and /or mixed with carbon dioxide is another promising approach for generating hydrogen or syngas, higher hydrocarbons and oxygenates at room temperature, well outside equilibrium conditions. Its main attractions is the potential to reduce capital and operational costs via use of inexpensive low specification materials such as plastic or glass for construction of reactor, and the ability to operate outside thermodynamic equilibrium limitations.

An important aspect of this work is that up to the present moment, the use of CO_2 has not yet led to much industrial process. Efficient methods for use of CO_2 as a chemical building block in synthesizing fuels have not yet been developed. Thermocatalytic dry reforming of methane still faces several challenges such as deactivation of catalyst due to coke formation. Development of a method of recycling CO_2 formed from fossil fuels combustion is of paramount importance especially when used in reforming methane since both of them are greenhouse gases causing planetary global warming. Use of non-thermal plasma in dry reforming of methane (natural gas) is really promising as it has been observed experimentally that the presence of CO_2 in CH_4 enhances conversion of methane and the products of the plasma reactions include syngas, oxygenates, water and HCs. The results have shown that the majority of CO, an important component of syngas is derived from CO_2, and this is an important contribution of this work to the development of non-thermal plasma reactors for conversion of methane with carbon dioxide or biogas, which is often regarded as of poor quality for state of the art applications. Where the syngas is used in the F-T synthesis of liquid fuels, this implies that the process manages to recycle CO_2 back to fuels, and this is a double achievement because this will not only put CO_2 to economic use, but also help tackling climate change threats due to global warming.

The possibility of decomposing methane at low temperatures using non-thermal plasma has important implications for development of methods of producing CO-free hydrogen for such applications as PEM fuel cells, oil refineries and ammonia production. Other implications emerging from this study are the possibility of direct production of Higher Hydrocarbons ($\mathrm{C_4 - C_{10}}$) and oxygenates from methane or methane with carbon dioxide. The research has contributed to the existing knowledge by showing that significant quantities of $\mathrm{C_4 - C_{10}}$, possibly some constituents of gasoline, are formed. It has been established experimentally in this work that the conversion of methane is enhanced (up to 64%) in the presence of carbon dioxide compared to methane on its own (up to 32%), under similar applied voltage and flow conditions. The $\mathrm{H_2{:}CO}$ ratio of the syngas produced depends on the molar $\mathrm{CH_4/}$

CO_2 co-feed ratio. It has also been established in the present work that conversions increase with applied voltage (power), and decrease with reactant(s) feed flowrate (decreasing resident time).

Biogas is a renewable source mainly composed of methane, carbon dioxide and traces of other gases such as ammonia, hydrogen, nitrogen, hydrogen sulphide and water vapour. This mixture is a result of anaerobic digestion processes of residual biomass sources such as animal waste, sewage treatment plants, industrial wastewater and landfills (Alves et al., 2013). In oil-associated gas, which is gas accompanying petroleum extraction, carbon dioxide is one of most common contaminants whose content can reach and even overpass 50 vol% (Bellussi et al., 2011) and is considered to be of poor calorific value. Non-thermal plasma could be an attractive technology for valorisation of such unconventional streams which would otherwise be released into the atmosphere.

The study has highlighted a number of areas on which further research would be beneficial in bringing this technology closer to commercial application. One suggested area of further investigation is use of warm plasma operating at above 500^oC. This would require a new reactor design with materials that can withstand such temperatures. Such higher temperatures may facilitate catalyst activation and might significantly influence product selectivities.

One of the more significant findings from this study is that while numerous previous studies have focussed on syngas or hydrogen as the main target products of plasma activated dry reforming of methane with carbon dioxide, they have failed to recognise that there is a wealth of other potentially valuable products. In this study, it has been established that up to 90% of the carbon from converted methane is converted into higher hydrocarbons and oxygenates. HCs as large as C_8 have been captured using cold traps. These are potentially HCs that can be upgraded to components making up gasoline. This method could as yet be found to be one step process to convert natural gas to liquid fuels. This result shows the possibility of using non-thermal plasma for coupling of methane to higher hydrocarbons.

References

A Ohsawa, A., Morrow, R. & Murphy, A. B. 2000. An investigation of a dc dielectric barrier discharge using a disc of glass beads. *Journal of Physics D: Applied Physics,* 33**,** 1487–1492.

Akay, G. 2004. Upping the ante in the process stakes. *The Chemical Engineer***,** 37-39.

Akay, G. 2006. Renewable resources come together. *The Chemical Engineer,* 784**,** 27-30.

Alamaro, M. 1994. Rethinking technological economy of scale. *Technology and Society Magazine, IEEE,* 13**,** 20-21.

Alves, H. J., Bley Junior, C., Niklevicz, R. R., Frigo, E. P., Frigo, M. S. & Coimbra-Araújo, C. H. 2013. Overview of hydrogen production technologies from biogas and the applications in fuel cells. *International Journal of Hydrogen Energy,* 38**,** 5215-5225.

Andersson, K. & Johnsson, F. 2006. Process evaluation of an 865 MWe lignite fired O2/CO2 power plant. *Energy Conversion and Management,* 47**,** 3487-3498.

Araki, S., Hoshi, Y., Hamakawa, S., Hikazudani, S. & Muzikami, F. 2008. Synthesis and characterization of mixed ionic-electronic conducting $Ca_{0.8}Sr_{0.2}Ti_{0.7}Fe_{0.3}O_{3-a}$ thin film. *Solid State Ionics,* 178**,** 1740-1745.

Arent, D. J., Wise, A. & Gelman, R. 2011. The status and prospects of renewable energy for combating global warming. *Energy Economics,* 33**,** 584-593.

Armor, J. N. 1998. Applications of catalytic inorganic membrane reactors to refinery products. *Journal of Membrane Science,* 147**,** 217-233.

Arnold, M., Wang, H. & Feldhoff, A. 2007. Influence of CO2 on the oxygen permeation performance and the microstructure of perovskite-type (Ba0.5Sr0.5)(Co0.8Fe0.2)O3−δ membranes. *Journal of Membrane Science,* 293**,** 44-52.

Axinte, E. 2011. Glass as engineering materials: A review. *Materials and Design,* 32**,** 1717-1732.

Aziznia, A., Bozorgzadeh, H. R., Seyed-Matin, N., Baghalha, M. & Mohamadalizadeh, A. 2012. Comparison of dry reforming of methane in low temperature hybrid plasma-catalytic corona with thermal catalytic reactor over Ni/γ-Al2O3. *Journal of Natural Gas Chemistry,* 21**,** 466-475.

Balachandran, U., Dusek, J. T., Maiya, P. S., Ma, B., Mieville, R. L., Kleefisch, M. S. & Udovich, C. A. 1997. Ceramic membrane reactor for converting methane to syngas. *Catalysis Today,* 36**,** 265-272.

Balachandran, U., Dusek, J. T., Mieville, R. L., Poeppel, R. B., Kleefisch, M. S., Pei, S., Kobylinski, T. P., Udovich, C. A. & Bose, A. C. 1995. Dense ceramic membranes for partial oxidation of methane to syngas. *Applied Catalysis A: General,* 133**,** 19-29.

Balat, M. 2008. Potential importance of hydrogen as a future solution to environmental and transportation problems. *International Journal of Hydrogen Energy,* 33**,** 4013-4029.

Bárdos, L. & Baránková, H. 2010. Cold atmospheric plasma: Sources, processes, and applications. *Thin Solid Films,* 518**,** 6705-6713.

Baumann, S., Meulenberg, W. A. & Buchkremer, H. P. 2013. Manufacturing strategies for asymmetric ceramic membranes for efficient separation of oxygen from air. *Journal of the European Ceramic Society,* 33**,** 1251-1261.

Bayani, N. 2001. *Oxygen Transport Properties of Highly-Doped Perovskite-Type Ferrite Oxides Under High and Low Oxygen Chemical Potentials.* Masters of Applied Science, University of Toronto.

Bellussi, G., Broccia, P., Carati, A., Millini, R., Pollesel, P., Rizzo, C. & Tagliabue, M. 2011. Silica–aluminas for carbon dioxide bulk removal from sour natural gas. *Microporous and Mesoporous Materials,* 146**,** 134-140.

Belova, I. V., Brown, M. J. & Murch, G. E. 2004. Analysis of kinetic demixing of (A,B)O oxides in an electric field and an oxygen potential gradient. *Solid State Ionics,* 167**,** 175-182.

Besecker, C. J., Mazanec, T. J., Xu, S. J. & Rytter, E. 2006. *Membrane Systems Containing an Oxygen Transport Membrane and Catalyst* United States patent application 10/154,704.

Bhat, S. A. & Sadhukhan, J. 2009. Process intensification aspects for steam methane reforming: An overview. *AIChE Journal,* 55**,** 408-422.

Birmingham, J. G. & Moore, R. R. 1990. *Reactive bed plasma air purification*. USA patent application 401,199.

Bobzin, K., Schlaefer, T., Zhao, L., Kopp, N. & Schlegel, A. 2010. Brazing of ceramic-to-ceramic and ceramic-to-metal joints in air. *Frontiers of Mechanical Engineering in China,* 5**,** 125-129.

Bouwmeester, H. J. M. 2003. Dense ceramic membranes for methane conversion. *Catalysis Today,* 82**,** 141-150.

Bouwmeester, H. J. M., Kruidhof, H. & Burggraaf, A. J. 1994. Importance of the surface exchange kinetics as rate limiting step in oxygen permeation through mixed-conducting oxides. *Solid State Ionics,* 72.

Bredesen, R. & Sogge, J. 1996. A Technical and Economic Assessment of Membrane Reactors for Hydrogen and Syngas Production. *The United Nations*

Economic Commissionfor Europe Seminar onEcological Applicationsof Innovative Membrane Technology in Chemical Industry, Chem/Sem. 21/R.12. Cetraro, Calabria, Italy.

Brzozowski, E. & Castro, M. S. 2000. Conduction mechanism of barium titanate ceramics. *Ceramics International,* 26**,** 265-269.

Burggraaf, A. J. & Cot, L. (eds.) 1996. *Fundamentals of Inorganic Membrane Science and Technology*: Elsevier.

Cabrera, A. L., Vargas, F. & Albers, J. J. 1995. Adsorption of carbon dioxide by ferroelectric lithium niobate. *Surface Science,* 336**,** 280-286.

Cabrera, A. L., Vargas, F. & Zarate, R. A. 1994. Adsorption of carbon dioxide by barium titanate: Evidence of adsorption process mediated by a dipole-dipole interaction. *Journal of Physics and Chemistry of Solids,* 55**,** 1303-1307.

Calata, J. N., Lu, G. Q. & Chuang, T. J. 2001. Constrained sintering of glass, glass-ceramic and ceramic coatings of metal substrates. *Surface and Interface Analysis,* 31**,** 67-681.

Cales, B. & Baumard, J. F. 1982. Oxygen semipermeability and electronic conductivity in calcia-stabilized zirconia. *Journal of Membrane Science,* 17**,** 3243-3248.

Cales, B. & Baumard, J. F. 1984. Mixed conduction and defect structure of ZrO_2 - CeO_2 - Y_2O_3 solid solutions. *Journal of The Electrochemical Society,* 131**,** 2407-2413.

Carman, R. J. & Mildren, R. P. 2000. Electron energy distribution functions for modelling the plasma kinetics in dielectric barrier discharges. *J. Phys. D: Appl. Phys.,* 33**,** L99.

Caron, N., Bianchi, L. & Méthout, S. 2008. Development of a Functional Sealing Layer for SOFC Applications. *Journal of Thermal Spray Technology,* 17**,** 598-602.

Centi, G. & Perathoner, S. 2009. Opportunities and prospects in the chemical recycling of carbon dioxide to fuels. *Catalysis Today,* 148**,** 191-205.

Chandran Govindaraju, V. G. R. & Tang, C. F. 2013. The dynamic links between CO2 emissions, economic growth and coal consumption in China and India. *Applied Energy,* 104**,** 310-318.

Charpentier, J.-C. 2007. In the frame of globalization and sustainability, process intensification, a path to the future of chemical and process engineering (molecules into money). *Chemical Engineering Journal,* 134**,** 84-92.

Chaubey, R., Sahu, S., James, O. O. & Maity, S. 2013. A review on development of industrial processes and emerging techniques for production of hydrogen from renewable and sustainable sources. *Renewable and Sustainable Energy*

Reviews, 23**,** 443-462.

Chen, C., Bouwmeester, H. J. M., Kruidhof, H., ten Elshof, J. E. & Burggraaf, A. J. 1996. Fabrication of $La_{1-x}Sr_xCoO_{3-d}$ thin layers on porous supports by a polymeric sol-gel process. *Journal Materials Chemistry,* 6**,** 815-819.

Chen, C. H., Kruidhof, H., Bouwmeester, H. J. M. & Burggraaf, A. J. 1997. Ionic conductivity of perovskite $LaCoO_3$ measured by oxygen permeation technique. *Journal of Applied Electrochemistry,* 27**,** 71-75.

Chen, H. L., Lee, H. M. & Chen, S. H. 2008. Review of Packed-Bed Plasma Reactor for Ozone Generation and Air Pollution Control. *Industrial & Engineering Chemistry Research,* 47**,** 2122-2130.

Chen, L., Zhang, X., Huang, L. & Lei, L. 2010. Application of in-plasma catalysis and post-plasma catalysis for methane partial oxidation to methanol over a Fe2O3-CuO/γ-Al2O3 catalyst. *Journal of Natural Gas Chemistry,* 19**,** 628-637.

Chen, Z., Shao, Z., Ran, R., Zhou, W., P., Z. & Liu, S. 2007. A dense oxygen separation membrane with a layered morphologic structure. . *Journal of Membrane Science,* 300**,** 182-190.

Chou, Y.-S., Thomsen, E. C., Williams, R. T., Choi, J.-P., Canfield, N. L., Bonnett, J. F., Stevenson, J. W., Shyam, A. & Lara-Curzio, E. 2011. Complaint alkali silicate sealing glass for solid oxide fuel cell applications: Thermal cycle stability and chemical stability. *Journal of Power Sources,* 196**,** 2079-2716.

Conway, S. J., Greig, J. A. & Thomas, G. M. 1992. Comparison of lanthanum oxide and strontium-modified lanthanum oxide catalysts for the oxidative coupling of methane. *Applied Catalysis A: General,* 86**,** 199-212.

Cook, R. L. & Sammells, A. F. 1991. On the systematic selection of perovskite solid electrolytes for intermediate temperature fuel cells. *Solid State Ionics,* 45**,** 311-321.

Coronas, J., Menendez, M. & Santamaria, J. 1994. Development of ceramic membrane reactors with a non-uniform permeation pattern. Application to methane oxidative coupling. *Chemical Engineering Science,* 49**,** 4749-4757.

Czuprat, O., Arnold, M., Schirrmeister, S., Schiestel, T. & Caro, J. 2010. Influence of CO2 on the oxygen permeation performance of perovskite-type BaCoxFeyZrzO3−δ hollow fiber membranes. *Journal of Membrane Science,* 364**,** 132-137.

Dalmon, J.-A., Cruz-López, A., Farrusseng, D., Guilhaume, N., Iojoiu, E., Jalibert, J.-C., Miachon, S., Mirodatos, C., Pantazidis, A., Rebeilleau-Dassonneville, M., Schuurman, Y. & van Veen, A. C. 2007. Oxidation in catalytic membrane reactors. *Applied Catalysis A: General,* 325**,** 198-204.

Dantas, S. C., Resende, K. A., Rossi, R. L., Assis, A. J. & Hori, C. E. 2012. Hydrogen production from oxidative reforming of methane on supported nickel catalysts: An experimental and modeling study. *Chemical Engineering Journal,* 197**,** 407-413.

Dautzenberg, F. M. & Mukherjee, M. 2001. Process intensification using multifunctional reactors. *Chemical Engineering Science,* 56**,** 251-267.

Davoudi, M., Rahimpour, M. R., Jokar, S. M., Nikbakht, F. & Abbasfard, H. 2013. The major sources of gas flaring and air contamination in the natural gas processing plants: A case study. *Journal of Natural Gas Science and Engineering,* 13**,** 7-19.

De Bie, C., Verheyde, B., Martens, T., van Dijk, J., Paulussen, S. & Bogaerts, A. 2011. Fluid Modeling of the Conversion of Methane into Higher Hydrocarbons in an Atmospheric Pressure Dielectric Barrier Discharge. *Plasma Processes and Polymers,* 8**,** 1033-1058.

Donald, I. W. 1993. Preparation, properties and chemistry of glass- and glass-ceramic-to-metal seals and coatings. *Journal of Materials Science,* 28**,** 2841-2886.

Donald, I. W., Metcalfe, B. L. & Gerrard, L. A. 2008. Interfacial Reactions in Glass-Ceramic- to- Metal Seals. *Journal of American Ceramic Society,* 91**,** 715-720.

Dong, L., Wei, S. a., Tan, S. & Zhang, H. 2008. GTL or LNG: which is the best way to monetize “stranded” natural gas? *Petroleum Science,* 5**,** 388-394.

Drioli, E., Stankiewicz, A. I. & Macedonio, F. 2011. Membrane engineering in process intensification—An overview. *Journal of Membrane Science,* 380**,** 1-8.

Eicher, K., Solow, G., Otschik, P. & Schaffrath, W. 1999. BAS (BaO.Al_2O_3.SiO_2)-glasses for High Temperature Applications. *Journal of the European Ceramic Society,* 19**,** 1101-1104.

Eliasson, B. & Kogelschatz, U. 1991. Nonequilibrium volume plasma chemical processing. *Plasma Science, IEEE Transactions on,* 19**,** 1063-1077.

Elvidge, C. D., Ziskin, D., Baugh, K. E., Tuttle, B., Ghosh, T., Pack, D. W., Erwin, E. H. & Zhizhin, M. 2009. A fifteen Year Record of Global Natural Gas Flaring Derived from Satellite Data. *Energies,* 2**,** 595-622.

Emig, G. & Liauw, M. A. 2002. New Reaction Engineering Concepts for Selective Oxidation Reactions. *Topics in Catalysis,* 21**,** 11-24.

Erkoç, E., Yapici, S., Keskinler, B., Çakici, A. & Akay, G. 2002. Effect of pulsed flow on the performance of carbon felt electrode. *Chemical Engineering Journal,* 85**,** 153-160.

Fournaud, B., Rossignol, S., Tatibouët, J.-M. & Thollon, S. 2009. Spherical pellets of BaTiO3 and Ba0.67Sr0.33TiO3 perovskite-type compounds made by a sol–gel oil drop process for non-thermal plasma applications. *Journal of Materials Processing Technology,* 209**,** 2515-2521.

Freiser, R. G. 1975. A Review of Solder Glasses. *Electrocomponent Science and Technology,* 2**,** 163-199.

Fridman, A. 2008. Plasma Chemistry. Cambridge: Cambridge University Press.

Fridman, A., Chirokov, A. & Gutsol, A. 2005. Non-thermal atmospheric pressure discharges. *Journal of Physics D: Applied Physics,* 38**,** R1-R24.

Futamura, S., Zhang, A., Einaga, H. & Kabashima, H. 2002. Involvement of catalyst materials in nonthermal plasma chemical processing of hazardous air pollutants. *Catalysis Today,* 72**,** 259-265.

Gallucci, F., Fernandez, E., Corengia, P. & van Sint Annaland, M. 2013. Recent advances on membranes and membrane reactors for hydrogen production. *Chemical Engineering Science,* 92**,** 40-66.

Garagounis, I., Kyriakou, V., Anagnostou, C., Bourganis, V., Papachristou, I. & Stoukides, M. 2010. Solid Electrolytes: Applications in Heterogeneous Catalysis and Chemical Cogeneration. *Industrial & Engineering Chemistry Research,* 50**,** 431-472.

Gellings, P. J. & Bouwmeester, H. J. M. (eds.) 1996. *The CRC Handbook of SOLID STATE Electrochemistry,* Boca Raton: CRC Press Inc.

Ghosh, S., Sharma, A. D., Kundu, P. & Basu, R. N. 2008. Glass-Ceramic Sealants for planar IT-SOFC: A Bilayered Approach for Joining Electrolyte and Metallic Interconnect. *Journal of The Electrochemical Society,* 155**,** B473-B478.

Goujard, V., Tatibouët, J.-M. & Batiot-Dupeyrat, C. 2009. Use of a non-thermal plasma for the production of synthesis gas from biogas. *Applied Catalysis A: General,* 353**,** 228-235.

Gozálvez-Zafrilla, J. M., Santafé-Moros, A., Escolástico, S. & Serra, J. M. 2011. Fluid dynamic modeling of oxygen permeation through mixed ionic–electronic conducting membranes. *Journal of Membrane Science,* 378**,** 290-300.

Gross, S. M., Koppitz, T., Remmel, J., Bouche, J.-B. & Reisgen, U. 2006. Joining properties of a composite glass-ceramic sealant. *Fuel Cells Bulletin***,** 12-15.

Gür, T. M., Belzner, A. & Huggins, R. A. 1992. A new class of oxygen selective chemically driven nonporous ceramic membranes. Part I. A-site doped perovskites. *Journal of Membrane Science,* 75**,** 151-162.

Hashim, S. M., Mohamed, A. R. & Bhatia, S. 2010. Current status of ceramic-based membranes for oxygen separation from air. *Advances in Colloidal and Interface Science,* 160**,** 88-100.

Hashim, S. S., Mohamed, A. R. & Bhatia, S. 2011. Oxygen separation from air using ceramic-based membrane technology for sustainable fuel production and power generation. *Renewable and Sustainable Energy Reviews,* 15**,** 1284-1293.

He, Y., Zhu, X., Li, Q. & Yang, W. 2009. Perovskite Oxide absorbents for Oxygen Separation. *American Institute of Chemical Engineers Journal (AIChE),* 55**,** 3125-3133.

Heintze, M. & Pietruszka, B. 2004. Plasma catalytic conversion of methane into syngas: the combined effect of discharge activation and catalysis. *Catalysis Today,* 89**,** 21-25.

Herzog, H. & Golomb, D. 2004. Carbon capture and storage from fossil fuel use. *Encyclopedia of Energy.*

Hessel, V., Anastasopoulou, A., Wang, Q., Kolb, G. & Lang, J. 2013. Energy, catalyst and reactor considerations for (near)-industrial plasma processing and learning for nitrogen-fixation reactions. *Catalysis Today,* 211**,** 9-28.

Holzer, F., Kopinke, F. D. & Roland, U. 2005. Influence of Ferroelectric Materials and Catalysts on the Performance of Non-Thermal Plasma (NTP) for the Removal of Air Pollutants. *Plasma Chemistry and Plasma Processing,* 25**,** 595-611.

Hong, F. & Holland, D. 1989a. Bonding glass ceramics to high temperature alloys. *Surface and Coatings Technology,* 39–40, Part 1**,** 19-27.

Hong, F. & Holland, D. 1989b. Studies of interface reactions between glass ceramic coatings and metals. *Journal of Non-Crystalline Solids,* 112**,** 357-363.

Hong, J., Kirchen, P. & Ghoniem, A. F. 2012. Numerical simulation of ion transport membrane reactors: Oxygen permeation and transport and fuel conversion. *Journal of Membrane Science,* 407–408**,** 71-85.

Hotza, D. & Diniz da Costa, J. C. 2008. Fuel cells development and hydrogen production from renewable resources in Brazil. *International Journal of Hydrogen Energy,* 33**,** 4915-4935.

Hull, A. W. & Burger, E. E. 1934. Glass- to - Metal Seals. *Physics,* 5.

IEA *CO2 Emissions from Fuel Combustion 2009,* OECD Publishing.

Iulianelli, A., Manzolini, G., De Falco, M., Campanari, S., Longo, T., Liguori, S. & Basile, A. 2010. H2 production by low pressure methane steam reforming in a Pd–Ag membrane reactor over a Ni-based catalyst: Experimental and modeling. *International Journal of Hydrogen Energy,* 35**,** 11514-11524.

Jae-Duk, M. & Sang-Taek, G. Year. Discharge and ozone generation characteristics of a ferroelectric-ball/mica-sheet barrier. *In:* Industry Applications Conference, 1997. Thirty-Second IAS Annual Meeting, IAS '97., Conference Record of the 1997 IEEE, 5-9 Oct 1997 1997. 1829-1836 vol.3.

Jin, W. Q., Li, S. G., Huang, P., Xu, N. P. & Shi, J. 2001. Preparation of of an asymmetric perovskite-type membrane and its oxygen permeability. *Journal of Membrane Science,* 185**,** 237-243.

Juan-Juan, J., Román-Martínez, M. C. & Illán-Gómez, M. J. 2009. Nickel catalyst activation in the carbon dioxide reforming of methane: Effect of pretreatments. *Applied Catalysis A: General,* 355**,** 27-32.

Julbe, A., Farrusseng, D. & Guizard, C. 2005. Limitations and potentials of oxygen transport dense and porous ceramic membranes for oxidation reactions. *Catalysis Today,* 104**,** 102-113.

Julbe, A. & Guizard, C. 2001. Role of membranes and membrane reactors in the hydrogen supply of fuel cells. *Annales de Chimie Science des Matériaux,* 26**,** 79-92.

Jung, J.-I. & Edwards, D. D. 2012. Kinetic demixing/decomposition of Ba0.5Sr0.5CoxFe1−xO3−δ (x = 0.2 and 0.8). *Journal of the European Ceramic Society,* 32**,** 3733-3743.

Kado, S., Urasaki, K., Sekine, Y., Fujimoto, K., Nozaki, T. & Okazaki, K. 2003. Reaction mechanism of methane activation using non-equilibrium pulsed discharge at room temperature. *Fuel,* 82**,** 2291-2297.

Kakaras, E., Doukelis, A., Giannakopoulos, D. & Koumanakos, A. 2007a. Economic implications of oxyfuel application in a lignite-fired power plant. *Fuel,* 86**,** 2151-2158.

Kakaras, E., Koumanakos, A., Doukelis, A., Giannakopoulos, D. & Vorrias, I. 2007b. Oxyfuel boiler design in a lignite-fired power plant. *Fuel,* 86**,** 2144-2150.

Kamal, W. A. 1997. Improving energy efficiency—The cost-effective way to mitigate global warming. *Energy Conversion and Management,* 38**,** 39-59.

Kats, G. H. 1990. Slowing global warming and sustaining development: The promise of energy efficiency. *Energy Policy,* 18**,** 25-33.

Kawahara, A., Takahashi, Y., Hirano, Y., Hirano, M. & Ishihara, T. 2011. Importance of pore structure control in porous substrate for high oxygen penetration in La0.6Sr0.4Ti0.3Fe0.7O3 thin film for CH4 partial oxidation. *Solid State Ionics,* 190**,** 53-59.

Kharton, V. V., Kovalevsky, A. V., Yaremchenko, A. A., Figueiredo, F. M., Naumovich, E. N., Shaulo, A. L. & Marques, F. M. B. 2002. Surface modification of La0.3Sr0.7CoO3−δ ceramic membranes. *Journal of Membrane Science,* 195**,** 277-287.

Kirchen, P., Apo, D. J., Hunt, A. & Ghoniem, A. F. 2013. A novel ion transport membrane reactor for fundamental investigations of oxygen permeation and oxy-combustion under reactive flow conditions. *Proceedings of the Combustion Institute,* 34**,** 3463-3470.

Kogelschatz, U. 2003. Dielectric-Barrier Discharges: Their History, Discharge Physics, and Industrial Applications. *Plasma Chemistry and Plasma*

Processing, 23**,** 1-46.

Kogelschatz, U., Eliasson, B. & Egli, W. 1997. Dielectric-Barrier Discharges. Principle and Applications. *J. Phys. IV France,* 07**,** C4-47-C4-66.

Koros, W. J., Ma, Y. H. & Shimidzu, T. 1996. Terminology for membranes and membrane processes (IUPAC Recommendations 1996). *Journal of Membrane Science,* 120**,** 149-159.

Kothiyal, G. P., Goswami, M. & Shrkhande, V. K. 2008. Some developments on ceramic-to-metal and glass-ceramics-to-metal seals and related studies. *Journal of Physics: Conference Series,* 114**,** 1-9.

Kovalevsky, A. V., Kharton, V. V., Maxim, F., Shaula, A. L. & Frade, J. R. 2006. Processing and characterization of $La_{0.5}Sr_{0.5}FeO_3$ suppoerted $Sr_{1-x}Fe(Al)O_3$-$SrAl_2O_4$ composite membranes. *Journal of Membrane Science,* 278**,** 162-172.

Kozhevnikov, V. L., Leonidov, I. A., Patrakeev, M. V., Markov, A. A. & Blinovskov, Y. N. 2009. Evaluation of $La_{0.5}Sr_{0.5}Fe_{3-d}$ membrane reactors for partial oxidation of methane. *Journal of Solid State Electrochemistry,* 13**,** 391-395.

Kraus, M., Egli, W., Haffner, K., Eliasson, B., Kogelschatz, U. & Wokaun, A. 2002. Investigation of mechanistic aspects of the catalytic CO2 reforming of methane in a dielectric-barrier discharge using optical emission spectroscopy and kinetic modeling. *Physical Chemistry Chemical Physics,* 4**,** 668-675.

Kraus, M., Eliasson, B., Kogelschatz, U. & Wokaun, A. 2001. CO2 reforming of methane by the combination of dielectric-barrier discharges and catalysis. *Physical Chemistry Chemical Physics,* 3**,** 294-300.

Kruidhof, H., Bouwmeester, H. J. M., van Doorn, R. H. E. & Burggraaf, A. J. 1993. Influence of order-disorder transitions on the oxygen permeability through selected nonstoichiometric perovskite-type oxides. *Solid State Ionics,* 63-65**,** 816-822.

Kueper, T. W., Visco, S. J. & de Jonghe, L. C. 1992. Application of the stabilized zirconia thin film prepared by spray pyrolysis method to SOFC. *Solid State Ionics,* 52.

Kuhn, B., Wetzel, F. J., Malzbender, J., Steinbrech, R. W. & Singheiser, L. 2009. Mechanical performance of reactive-air-brazed (RAB) ceramic/metal joints for solid oxide fuel cells at ambient temperature. *Journal of Power Sources,* 193**,** 199-202.

Kusaba, H., Shibata, Y., Sasaki, K. & Teraoka, Y. 2006. Surface effect on oxygen permeation through dense membrane of mixed-conductive LSCF perovskite-type oxide. *Solid State Ionics,* 177**,** 2249-2253.

Larsen, P. H. & James, P. F. 1998. Chemical Stability in MgO-CaO-Cr_2O_3-Al_2O_3-B_2O_3 - Phosphate glasses in Solid Oxide Fuel Cell Environment. *Journal of*

Material Science, 33**,** 2499-2507.

Lee, S., Lee, K. S., Woo, S., K. , Won Kim, J. W., Ishihara, T. & Kim, D. K. 2003. Oxygen-permeating property of LaSrBFeO3 (B=Co, Ga) perovskite membrane surface-modified by $LaSrCoO_3$. *Solid State Ionics,* 158**,** 287-296.

Lee, S., Woo, S. K., Lee, S. K. & Kim, D. K. 2006. Mechanical properties and structural stability of perovskite-type oxygen permeable dense membrane. *Desalination,* 193**,** 236-243.

Lein, H. L., Wiik, K. & Grande, T. 2006. Kinetic demixing and decomposition of oxygen permeable membranes. *Solid State Ionics,* 177**,** 1587-1590.

Leo, A., Liu, S. & Diniz da Costa, J. C. 2009. Development of mixed conducting membranes for clean coal delivery. *International Journal of Greenhouse Gas Control,* 3**,** 357-367.

Li, R., Tang, Q., Yin, S. & Sato, T. 2006. Plasma catalysis for CO2 decomposition by using different dielectric materials. *Fuel Processing Technology,* 87**,** 617-622.

Li, R., Tang, Q., Yin, S., Yamaguchi, Y. & Sato, T. 2004. Decomposition of Carbon Dioxide by the Dielectric Barrier Discharge (DBD) Plasma Using $Ca_{0.7}Sr_{0.3}TiO_3$ Barrier. *Chemistry Letters,* 33**,** 412-413.

Li, S., Jin, W., Huang, P., Xu, N., Shi, J. & Lin, Y. S. 2000. Tubular lanthanum cobaltite perovskite type membrane for oxygen permeation. *Journal of Membrane Science,* 166**,** 51-61.

Li, S., Qi, H., Xu, N. & Shi, J. 1999. Tubular Dense Perovskite Type Membranes, Preparation, Sealing, and Oxygen Permeation Properties. *Industrial and Engineering Chemistry Research,* 38**,** 5028-5033.

Lin, Y.-S., Wang, W. & Han, J. 1994. Oxygen permeation through thin mixed-conducting solid oxide membranes. *AIChE Journal,* 40**,** 786-798.

Liu, C.-j., Mallinson, R. & Lobban, L. 1999. Comparative investigations on plasma catalytic methane conversion to higher hydrocarbons over zeolites. *Applied Catalysis A: General,* 178**,** 17-27.

Liu, C.-J., Xue, B., Eliasson, B., He, F., Li, Y. & Xu, G.-H. 2001. Methane Conversion to Higher Hydrocarbons in the Presence of Carbon Dioxide Using Dielectric-Barrier Discharge Plasmas. *Plasma Chemistry and Plasma Processing,* 21**,** 301-310.

Liu, C., Cui, N., Brown, N. M. D. & Meenan, B. J. 2004. Effects of DBD plasma operating parameters on the polymer surface modification. *Surface and Coatings Technology,* 185**,** 311-320.

Liu, T., Gepert, V. & Veser, G. 2005. Process Intensification Through Heat-Integrated Reactors for High-Temperature Millisecond Contact-Time Catalysis.

Chemical Engineering Research and Design, 83, 611-618.

Liu, W. N., Sun, X., Koeppel, B. J. & Khaleel, M. 2010. Experimental Study of the Aging andSself-Healing of the Gass/Ceramic Sealant used in SOFCs. . *International Journal of Applied Ceramic Technology,* 7, 22-29.

Liu, Y., Tan, X. & Li, K. 2006. Mixed Conducting Ceramics for Catalytic Membrane Processing. *Catalysis Reviews,* 48, 145-195.

Lu, G. Q., Diniz da Costa, J. C., Duke, M., Giessler, S., Socolow, R., Williams, R. H. & Kreutz, T. 2007. Inorganic membranes for hydrogen production and purification: A critical review and perspective. *Journal of Colloid and Interface Science,* 314, 589-603.

Lu, H., Tong, J., Cong, Y. & Yang, W. 2005. Partial oxidation of methane in Ba0.5Sr0.5Co0.8Fe0.2O3−δ membrane reactor at high pressures. *Catalysis Today,* 104, 154-159.

Lü, J. & Li, Z. 2010. Conversion of natural gas to C2 hydrocarbons via cold plasma technology. *Journal of Natural Gas Chemistry,* 19, 375-379.

Lu, K. & Mahapatra, M. K. 2008. Network structure and thermal stability of high temperature seal glass. *Journal of Applied Physics,* 104.

Luis, P., Van Gerven, T. & Van der Bruggen, B. 2012. Recent developments in membrane-based technologies for CO2 capture. *Progress in Energy and Combustion Science,* 38, 419-448.

Luo, H., Jiang, H., Efimov, K., Caro, J. & Wang, H. 2011. Influence of the preparation methods on the microstructure and oxygen permeability of a CO2-stable dual phase membrane. *AIChE Journal,* 57, 2738-2745.

Lupis, C. P. 1999. Greenhouse gases and the metallurgical process industry. *Metallurgical and Materials Transactions B,* 30, 841-856.

Mahapatra, M. K. & Lu, K. 2010a. Glass- based seals for solid oxide and electrolyzer cells - A review. *Materials Science and Engineering R,* 67, 65-85.

Mahapatra, M. K. & Lu, K. 2010b. Seal glass for solid oxide fuel cells. *Journal of Power Sources,* 195, 7129-7139.

Malik, M. A. & Jiang, X. Z. 1999. The CO2 Reforming of Natural Gas in a Pulsed Corona Discharge Reactor. *Plasma Chemistry and Plasma Processing,* 19, 505-512.

Mallada, R., Menéndez, M. & Santamaría, J. 2000. Use of membrane reactors for the oxidation of butane to maleic anhydride under high butane concentrations. *Catalysis Today,* 56, 191-197.

Manning, P. S., Sirman, J. D. & Kilner, J. A. 1996. Oxygen self-diffusion and surface exchange studies of oxide electrolytes having flourite structure. *Solid*

State Ionics, 93**,** 125-132.

Manoj Kumar Reddy, P., Rama Raju, B., Karuppiah, J., Linga Reddy, E. & Subrahmanyam, C. 2013. Degradation and mineralization of methylene blue by dielectric barrier discharge non-thermal plasma reactor. *Chemical Engineering Journal,* 217**,** 41-47.

Martin, M. 2003. Materials in thermodynamic potential gradients. *Journal of Chemical Thermodynamics,* 35**,** 1291-1308.

Mazanec, T. J., Cable, T. L. & Frye Jr, J. G. 1992. Electrocatalytic cells for chemical reaction. *Solid State Ionics,* 53–56, Part 1**,** 111-118.

McGlade, C., Speirs, J. & Sorrell, S. 2013. Methods of estimating shale gas resources – Comparison, evaluation and implications. *Energy*.

Meinhardt, K. D., Kim, D.-S., Chou, Y.-S. & Weil, K. S. 2008. Synthesis and properties of barium aluminosilicate solide oxide fuel cell glass-ceramic sealant. *Journal of Power Sources,* 182**,** 188-196.

Meng, G. Y., Song, H. Z., Wang, H. B., Xia, C. R. & Peng, D. K. 2002. Progress in ion-transport inorganic membranes by novel CVD techniques. *Thin Solid Films,* 409**,** 105-111.

Miachon, S. & Dalmon, J.-A. 2004. Catalysis in Membrane Reactors: What About the Catalyst? *Topics in Catalysis,* 29**,** 59-65.

Middleton, H., Diethelm, S., Ihringer, R., Larrain, D., Sfeir, J. & van Herle, J. 2004. Co-casting and co-sintering of porous MgO support plates with thin dense perovskite layers of $LaSrFeCoO_3$ *Journal of the European Ceramic Society,* 24**,** 1083-1086.

Mingdong, B., Xiyao, B., Zhitao, Z. & Mindi, B. 2000. Synthesis of Ammonia in a Strong Electric Field Discharge at Ambient Pressure. *Plasma Chemistry and Plasma Processing,* 20**,** 511-520.

Minoru, I. & Atsuchi, M. 1997. Growth rate of yttria-stabilzed zirconia thin films formed by electrochemical vapour-deposition using NiO as an oxygen source: II Effect of porosity of NiO substrate. *Solid State Ionics,* 104**,** 30-310.

Moreau, M., Orange, N. & Feuilloley, M. G. J. 2008. Non-thermal plasma technologies: New tools for bio-decontamination. *Biotechnology Advances,* 26**,** 610-617.

Moulijn, J. A., Stankiewicz, A., Grievink, J. & Górak, A. 2008. Process intensification and process systems engineering: A friendly symbiosis. *Computers & Chemical Engineering,* 32**,** 3-11.

Mueller-Langer, F., Tzimas, E., Kaltschmitt, M. & Peteves, S. 2007. Techno-economic assessment of hydrogen production processes for the hydrogen economy for the short and medium term. *International Journal of Hydrogen*

Energy, 32**,** 3797-3810.

Nallathambi Gunaseelan, V. 1997. Anaerobic digestion of biomass for methane production: A review. *Biomass and Bioenergy,* 13**,** 83-114.

Nozaki, T. & Okazaki, K. 2013. Non-thermal plasma catalysis of methane: Principles, energy efficiency, and applications. *Catalysis Today,* 211**,** 29-38.

Ogata, A., Shintani, N., Mizuno, K., Kushiyama, S. & Yamamoto, T. 1999. Decomposition of benzene using a nonthermal plasma reactor packed with ferroelectric pellets. *Industry Applications, IEEE Transactions on*, 35**,** 753-759.

Oyama, S. T. & Stagg-Williams, S. M. (eds.) 2011. *Inorganic Polymeric and Composite Membrane Structure, Function and Other Correlations: Chapter 11: A Review of Mixed Ionic and Electronic Conducting Ceramic Membranes as Oxygen Sources for High Temperature Reactors*: Elsevier, Amsterdam, The Netherlands.

Pantu, P., Kim, K. & Gavalas, G. R. 2000. Methane partial oxidation on Pt/CeO2–ZrO2 in the absence of gaseous oxygen. *Applied Catalysis A: General,* 193**,** 203-214.

Park, C. Y., Lee, T. H., Dorris, S. E., Lu, Y. & Balachandran, U. 2011. Oxygen permeation and coal-gas-assisted hydrogen production using oxygen transport membranes. *International Journal of Hydrogen Energy,* 36**,** 9345-9354.

Pask, J. A. 1977. *Fundamentals of wetting and bonding between ceramics and metals*.

Pehnt, M. & Henkel, J. 2009. Life cycle assessment of carbon dioxide capture and storage from lignite power plants. *International Journal of Greenhouse Gas Control,* 3**,** 49-66.

Pekdemir, T., Keskinler, B., Yildiz, E. & Akay, G. 2003. Process intensification in wastewater treatment: ferrous iron removal by a sustainable membrane bioreactor system. *Journal of Chemical Technology & Biotechnology,* 78**,** 773-780.

Pena, M. A. & Fierro, J. L. G. 2001. Chemical Structures and Performance of Perovskite Oxides. *Chemistry Reviews,* 101**,** 1981-2017.

Pietruszka, B. & Heintze, M. 2004. Methane conversion at low temperature: the combined application of catalysis and non-equilibrium plasma. *Catalysis Today,* 90**,** 151-158.

Preis, S., Klauson, D. & Gregor, A. 2013. Potential of electric discharge plasma methods in abatement of volatile organic compounds originating from the food industry. *Journal of Environmental Management,* 114**,** 125-138.

Qi, X., Akin, F. T. & Lin, Y. S. 2001. Ceramic-glass composite high temperature seals for dense ionic-conducting ceramic membranes. *Journal of Membrane*

Science, 193**,** 185-193.

Qiu, L., Lee, T. H., LIU, L.-M., Yang, Y. L. & Jacobson, A. j. 1995. Oxygen permeation studies of $SrCo_{0.8}Fe_{0.2}O_{3-d}$. *Solid State Ionics,* 76**,** 321-329.

Quoc An, H. T., Pham Huu, T., Le Van, T., Cormier, J. M. & Khacef, A. 2011. Application of atmospheric non thermal plasma-catalysis hybrid system for air pollution control: Toluene removal. *Catalysis Today,* 176**,** 474-477.

Radacsi, N., van der Heijden, A. E. D. M., Stankiewicz, A. I. & ter Horst, J. H. Nanoparticle generation by intensified solution crystallization using cold plasma. *Chemical Engineering and Processing: Process Intensification*.

Raduly-Scheuermann, K., Vroon, Z. & Bouwmeester, H. J. M. Public Summary Report of ENCAP deliverable D5.5.1.1: Documented selection with overview stability and durability of perovskite materials. Available from Internet: www.encapco2.org.

Ramshaw, C. 1999. Process Intensification and Green Chemistry. *Green Chemistry,* 1**,** G15-G17.

Reay, D. 2005. Re-Engineering the Chemical Processing Plant: Process Intensification, Andrzej Stankiewicz, Jacob A. Moulijn (Eds.). Marcel Dekker, Inc (2003), 529, ISBN: 0 8247 4302 4. *Chemical Engineering Research and Design,* 83**,** 105-106.

Reddy, P. V. L., Kim, K.-H. & Song, H. 2013. Emerging green chemical technologies for the conversion of CH4 to value added products. *Renewable and Sustainable Energy Reviews,* 24**,** 578-585.

Rehman, F., Lozano-Parada, J. H. & Zimmerman, W. B. 2012. A kinetic model for H2 production by plasmolysis of water vapours at atmospheric pressure in a dielectric barrier discharge microchannel reactor. *International Journal of Hydrogen Energy,* 37**,** 17678-17690.

Reis, S. T. & Brow, R. K. 2006. Designing Sealing Glasses for Solid Oxide Fuel Cells. *Journal of Materials Engineering and Performance,* 15**,** 410-413.

Richerson, D. W. (ed.) 1992. *Modern Ceramic Engineering; Properties, Processing and use in Design.*: Marcel Dekker Inc.

Riess, I. 2008. Solid State Electrochemistry. *Israel Journal of Chemistry,* 48**,** 143-158.

Rueangjitt, N., Akarawitoo, C., Sreethawong, T. & Chavadej, S. 2007. Reforming of CO2-Containing Natural Gas Using an AC Gliding Arc System: Effect of Gas Components in Natural Gas. *Plasma Chemistry and Plasma Processing,* 27**,** 559-576.

Rui, Z., Li, Y. & Lin, Y. S. 2009. Analysis of oxygen permeation through dense ceramic membranes with reactions of finite rate. *Chemical Engineering*

Science, 64**,** 172-179.

Sammells, A. F. & Mundschau, M. V. (eds.) 2006. *Nonporous Inorganic Membranes: for Chemical Processing.*: Wiley-VCH Verlag GmbH & Co. KGaA.

San-José-Alonso, D., Juan-Juan, J., Illán-Gómez, M. J. & Román-Martínez, M. C. 2009. Ni, Co and bimetallic Ni–Co catalysts for the dry reforming of methane. *Applied Catalysis A: General,* 371**,** 54-59.

Schiestel, T., Kilgus, M., Peter, S., Caspary, K. J., Wang, H. & Caro, J. 2005. Hollow fibre perovskite membranes for oxygen separation. *Journal of Membrane Science,* 258**,** 1-4.

Sentek, J., Krawczyk, K., Młotek, M., Kalczewska, M., Kroker, T., Kolb, T., Schenk, A., Gericke, K.-H. & Schmidt-Szałowski, K. 2010. Plasma-catalytic methane conversion with carbon dioxide in dielectric barrier discharges. *Applied Catalysis B: Environmental,* 94**,** 19-26.

Setogchi, A., Sawano, M., Eguchi, K. & Arai, H. 1990. Electrical properties of plasma-sprayed yttria-stabilized zirconia films. *Solid State Ionics,* 40/41.

Shao, Z., Yang, W., Cong, Y., Dong, H., Tong, J. & Xiong, G. X. 2000. Investigation of the permeation behaviour and stability of BSCF 5582 Oxygen Membrane. *Journal of Membrane Science,* 172**,** 177-188.

Simpson, A. P. & Lutz, A. E. 2007. Exergy analysis of hydrogen production via steam methane reforming. *International Journal of Hydrogen Energy,* 32**,** 4811-4820.

Singh, M., Shpargel, T. P. & Asthana, R. 2008. Brazing of Yttria-Stabilized Zirconia to stainless steel using Cu, Ag, and Ti- based brazes. *Journal of Material Science,* 43**,** 23-32.

Singh, R. N. 2007. Sealing Technology for Solid Oxide Fuel Cells (SOFC). *International Journal of Applied Ceramic Technology,* 4**,** 134-144.

Sirkar, K. K., Shanbhag, P. V. & Kovvali, A. S. 1999. Membrane in a Reactor: A Functional Perspective. *Industrial & Engineering Chemistry Research,* 38**,** 3715-3737.

Sirman, J. D. & Chen, J. C. 2003. *Ceramic Membrane Structure and Oxygen Separation Method*. 09/727,472.

Smith, A. R. & Klosek, J. 2001. A review of air separation technologies and their integration with energy conversion processes. *Fuel Processing Technology,* 70**,** 115-134.

Song, H. K., Choi, J.-W., Yue, S. H., Lee, H. & Na, B.-K. 2004. Synthesis gas production via dielectric barrier discharge over Ni/γ-Al2O3 catalyst. *Catalysis Today,* 89**,** 27-33.

Stadler, H., Beggel, F., Habermehl, M., Persigehl, B., Kneer, R., Modigell, M. & Jeschke, P. 2011. Oxyfuel coal combustion by efficient integration of oxygen transport membranes. *International Journal of Greenhouse Gas Control,* 5**,** 7-15.

Stankiewicz, A. & Moulijn, J. A. 2003. RE-Engineering the Chemical Processing Plant : Process Intensification. Hoboken: Marcel Dekker Inc.

Stankiewicz, A. I. & Moulijn, J. A. 2000. Process Intensification: Transforming Chemical Engineering *Chemical Engineering Progress***,** 22.

Stephens, W. T., Mazanec, T. J. & Anderson, H. U. 2000. Influence of gas flow rate on oxygen flux measurements for dense oxygen conducting ceramic membranes. *Solid State Ionics,* 129**,** 271-284.

Stoukides, M. 2000. Solid-Electrolyte Membrane Reactors: Current Experience and Future Outlook. *Catalysis Reviews,* 42**,** 1-70.

Suganuma, K., Miyamoto, Y. & Koizumi, M. 1988. Joining of Ceramics and Metals. *Annual Review of Material Science,* 18**,** 47-73.

Sunarso, J., Baumann, S., Serra, J. M., Meulenberg, W. A., Liu, S., Lin, Y. S. & Diniz da Costa, J. C. 2008. Mixed ionic–electronic conducting (MIEC) ceramic-based membranes for oxygen separation. *Journal of Membrane Science,* 320**,** 13-41.

Tai, l.-W., Nasrallah, M. M., Anderson, H. U., Sparlin, D. M. & Sehlin, S. R. 1995. Structure and Electrical properties of $La_{1-x}Sr_xCo_{1-y}Fe_yO_{3-d}$ Part 2: The System $La_{1-x}Sr_xCo_{0.2}Fe_{0.8}O_{3-d}$. *Solid State Ionics,* 76**,** 273-283.

Tan, L., Gua, X., Yanga, L., Jin, W., Zhang, L. & Xu, N. 2003. Influence of powder synthesis methods on microstructure and oxygen permeation performance of Ba0.5Sr0.5Co0.8Fe0.2O3−δ perovskite-type membranes. *Journal of Membrane Science,* 212**,** 157–165.

Tan, X., Liu, N., Meng, B., Sunarso, J., Zhang, K. & Liu, S. 2012a. Oxygen permeation behavior of La0.6Sr0.4Co0.8Fe0.2O3 hollow fibre membranes with highly concentrated CO2 exposure. *Journal of Membrane Science,* 389**,** 216-222.

Tan, X., Pang, Z., Gu, Z. & Liu, S. 2007. Catalytic perovskite hollow fibre membrane reactors for methane oxidative coupling. *Journal of Membrane Science,* 302**,** 109-114.

Tan, X., Shi, L., Hao, G., Meng, B. & Liu, S. 2012b. La0.7Sr0.3FeO3−α perovskite hollow fiber membranes for oxygen permeation and methane conversion. *Separation and Purification Technology,* 96**,** 89-97.

ten Elshof, J. E., Bouwmeester, H. J. M. & Verweij, H. 1995a. Oxidative coupling of methane in a mixed-conducting perovskite membrane reactor. *Applied Catalysis A: General,* 130**,** 195-212.

ten Elshof, J. E., Bouwmeester, H. J. M. & Verweij, H. 1996. Oxygen transport through La1 − xSrxFeO3 − δ membranes II. Permeation in air/CO, CO2 gradients. *Solid State Ionics,* 89**,** 81-92.

ten Elshof, J. E., van Hassel, B. A. & Bouwmeester, H. J. M. 1995b. Activation of methane using solid oxide membranes. *Catalysis Today,* 25**,** 397-402.

Teraoka, Y., Nobunaga, T. & Yamazoe, N. 1988. Effect of Cation Substitution on the Oxygen Semipermeability of Perovskite-Type Oxides. *Chemistry Letters***,** 503-506.

Teraoka, Y., Zhang, H.-M., Furukawa, S. & Yamazoe, N. 1985. Oxygen permeation through perovskite-type oxides. *Chemistry Letters***,** 1743-1746.

Thursfield, A. & Metcalfe, I. S. 2004. The use of dense mixed ionic and electronic conducting membranes for chemical production. *Journal of Materials Chemistry,* 14**,** 2475-2485.

Tomsia, A. P. & Pask, J. A. 1986. Chemical reactions and adherence at glass/metal interfaces: an analysis. *Dental Materials,* 2**,** 10-16.

Tonkovich, A. L., Jarosch, K., Fitzgerald, S., Yang, B., Kilanowski, D., McDaniel, J. & Dritz, T. 2011. Microchannel Gas-to-Liquid for Monetizing Associated and Stranded Gas Resources. *Oxford Catalyst Group.* Velocys Inc, 7950 Corporate Blvd, Plain City, Ohio 43064, USA.

Tonziello, J. & Vellini, M. 2011. Oxygen production technologies for IGCC power plants with CO_2 capture. *Energy Procedia,* 4**,** 637-644.

Treheux, D., Lourdin, P., Mbongo, B. & Juve, D. 1994. Metal-ceramic solid state bonding: Mechanisms and mechanics. *Scripta Metallurgica et Materialia,* 31**,** 1055-1060.

Tsai, C.-H. & Hsieh, T.-H. 2004. New Approach for Methane Conversion Using an rf Discharge Reactor. 1. Influences of Operating Conditions on Syngas Production. *Industrial & Engineering Chemistry Research,* 43**,** 4043-4047.

Tsai, C.-Y., Dixon, A. G., Ma, Y. H., Moser, W. R. & Pascucci, M. R. 1998. Dense Perovskite, $La_{1-x}A_xFe_{1-y}Co_yO_{3-d}$ (A = Ba, Sr, Ca), Membrane Synthesis, Applications, and Characterization. *Journal of American Ceramic Society,* 81**,** 1437-1444.

Tsai, C.-Y., Dixon, A. G., Moser, W. R. & Ma, Y. H. 1997. Dense Perovskite Membrane Reactors for Partial Oxidation of Methane to Syngas. *Ceramic Processing,* 43**,** 2741-2750.

Tu, X., Gallon, H. J., Twigg, M. V., Gorry, P. A. & Whitehead, J. C. 2011. Dry reforming of methane over Ni/A_2O_3 catalyst in coaxial dielectric barrier discharge. *Journal of Physics D: Applied Physics,* 44 (274007).

Tu, X. & Whitehead, J. C. 2012. Plasma-catalytic dry reforming of methane in an atmospheric dielectric barrier discharge: Understanding the synergistic effect at low temperature. *Applied Catalysis B: Environmental,* 125**,** 439-448.

Twentyman, M. E. 1975. High-temperature metallizing. *Journal of Materials Science,* 10**,** 765-776.

van der Haar, L. M. 2001. *Mixed conducting perovskite membranes for oxygen separation.*

van der Haar, L. M. & Verweij, H. 2000. Homogeneous porous perovskite supports for thin dense oxygen separation membranes. *Journal of Membrane Science,* 180**,** 147-155.

Van Durme, J., Dewulf, J., Leys, C. & Van Langenhove, H. 2008. Combining non-thermal plasma with heterogeneous catalysis in waste gas treatment: A review. *Applied Catalysis B: Environmental,* 78**,** 324-333.

van Hassel, B. A., ten Elshof, J. E. & Bouwmeester, H. J. M. 1994. Oxygen permeation flux through $La_{1-y}Sr_yFeO_3$ limited by carbon monoxide oxidation rate. *Applied Catalysis. A:,* General 119**,** 279-291.

Vandenbroucke, A. M., Morent, R., De Geyter, N. & Leys, C. 2011. Non-thermal plasmas for non-catalytic and catalytic VOC abatement. *Journal of Hazardous Materials,* 195**,** 30-54.

Velterop, F. M. 1992. *Method of Connecting Ceramic Materials to another Material*. Netherlands patent application 733,092.

Vergara-Fernández, A., Vargas, G., Alarcón, N. & Velasco, A. 2008. Evaluation of marine algae as a source of biogas in a two-stage anaerobic reactor system. *Biomass and Bioenergy,* 32**,** 338-344.

Wagner, C. 1975. Equations for Transport in Solid Oxides and Sulfides of Transition Metals. *Progress in Solid-State Chemistry,* 10**,** 3-16.

Wagner, T., Kirchheim, R. & Rühle, M. 1995. Chemical reactions at metal/ceramic interfaces during diffusion bonding. *Acta Metallurgica et Materialia,* 43**,** 1053-1063.

Wang, B., Zydorczak, B., Poulidi, D., Metcalfe, I. S. & Li, K. 2011. A further investigation of the kinetic demixing/decomposition of La0.6Sr0.4Co0.2Fe0.8O3−δ oxygen separation membranes. *Journal of Membrane Science,* 369**,** 526-535.

Wang, B., Zydorczak, B., Wu, Z. T. & Li, K. 2009. Stabilities of $La_{0.6}Sr_{0.4}Co_{0.2}Fe_{0.8}O_{3-d}$ oxygen separation membranes- Effects of kinetic demixing/decomposition and impurity segregation. *Journal of Membrane Science,* 344**,** 101-106.

Wang, H., Cong, Y. & Yang, W. 2002. Oxygen permeation study in a tubular Ba0.5Sr0.5Co0.8Fe0.2O3-δ oxygen permeable membrane. *Journal of*

Membrane Science, 210**,** 259-271.

Wei, W.-C. J. 2008. Sealing Glass-Ceramics for Solid Oxide Fuel Cell. *Recent Patents on Materials Science* 1**,** 217-222.

Weil, K. S. 2006. The State of the Art in Sealing Technology for Solid Oxide Fuel Cells. *Journal of Membrane* 37-44.

Weil, K. S., Coyle, C. A., Hardy, J. S., Kim, J. Y. & Xia, G.-G. 2004. Alternative planar SOFC sealing concepts. *Fuel Cells Bulletin,* 2004**,** 11-16.

Weil, K. S., Kim, J. Y. & Hardy, J. S. 2005. Reactive Air Brazing: A Novel Method of Sealing SOFCs and Other Solid-State Electrochemical Devices. *Electrochemical and Solid-State Letters,* 8**,** A133-A136.

Westermann, T. & Melin, T. 2009. Flow-through catalytic membrane reactors—Principles and applications. *Chemical Engineering and Processing: Process Intensification,* 48**,** 17-28.

Wiik, K., Aasland, S., Hansen, H. L., Tangen, I. L. & Odergard, R. 2002. Oxygen permeation in the system $SrFeO_{3-x}$ - $SrCoO_{3-y}$. *Solid State Ionics,* 152-153**,** 675-680.

Will, J., Mitterdorfer, A., Kleinlogel, C., Perednis, D. & Gauckler, L. J. 2000. Fabrication of thin electrolytes for second generation solid oxide fuel cells. *Solid State Ionics,* 131**,** 79-96.

Wood, D. A., Nwaoha, C. & Towler, B. F. 2012. Gas-to-liquids (GTL): A review of an industry offering several routes for monetizing natural gas. *Journal of Natural Gas Science and Engineering,* 9**,** 196-208.

Xia, C. & Liu, M. 2001. A Simple and Cost-Effective Approach to Fabrication of Dense Ceramic Membranes on Porous Substrates. *Journal of American Ceramic Society,* 84**,** 1903-1905.

Yan, A., Liu, B., Dong, Y., Tian, Z., Wang, D. & Cheng, M. 2008. A temperature programmed desorption investigation on the interaction of Ba0.5Sr0.5Co0.8Fe0.2O3−δ perovskite oxides with CO2 in the absence and presence of H2O and O2. *Applied Catalysis B: Environmental,* 80**,** 24-31.

Yang, W., Wang, H., Zhu, X. & Lin, L. 2005. Development and Application of Oxygen Permeable Membrane in Selective Oxidation of Light Alkanes. *Topics in Catalysis,* 35**,** 155-167.

Yang, Y. 2003. Direct Non-oxidative Methane Conversion by Non-thermal Plasma: Modeling Study. *Plasma Chemistry and Plasma Processing,* 23**,** 327-346.

Yantovsky, E., Gorski, J. & Shokotov, M. 2009. Zero Emissions Power Cycles. 1 ed. Boca Raton: CRC Press.

Yehia, A. 2012. Assessment of ozone generation in dry air fed silent discharge reactors. *Physics of Plasmas,* 19**,** 023503-9.

Yext, W. F., Shook, B. J., Katzenberger, W. S. & Michalek, R. c. 1983. Improved Glass-to Metal Sealing Through Furnace Atmosphere Composition Control. *IEEE Transactions on Components, Hybrids, and Manufacturing Technology,* 6**,** 455.

Yildiz, E., Keskinler, B., Pekdemir, T., Akay, G. & Nuhogˇlu, A. 2005. High strength wastewater treatment in a jet loop membrane bioreactor: kinetics and performance evaluation. *Chemical Engineering Science,* 60**,** 1103-1116.

Yin, Q. & Lin, Y. S. 2007. Beneficial effect of order–disorder phase transition on oxygen sorption properties of perovskite-type oxides. *Solid State Ionics,* 178**,** 83-89.

Zaman, J. & Chakma, A. 1994. Inorganic membrane reactors. *Journal of Membrane Science,* 92**,** 1-28.

Zeng, A., Lin, Y. S. & Swartz, S. L. 1998. Perovskite-type ceramic membrane: synthesis, oxygen permeation and membrane reactor performance for oxidative coupling of methane. *Journal of Membrane Science,* 150**,** 87-98.

Zeng, P., Ran, R., Chen, Z., Gu, H., Shao, Z., da Costa, J. C. D. & Liu, S. 2007. Significant effects of sintering temperature on the performance of La0.6Sr0.4Co0.2Fe0.8O3−δ oxygen selective membranes. *Journal of Membrane Science,* 302**,** 171-179.

Zhang, A.-J., Zhu, A.-M., Guo, J., Xu, Y. & Shi, C. 2010. Conversion of greenhouse gases into syngas via combined effects of discharge activation and catalysis. *Chemical Engineering Journal,* 156**,** 601-606.

Zhang, J.-Q., Zhang, J.-S., Yang, Y.-J. & Liu, Q. 2002. Oxidative Coupling and Reforming of Methane with Carbon Dioxide Using a Pulsed Microwave Plasma under Atmospheric Pressure. *Energy & Fuels,* 17**,** 54-59.

Zhang, K., Sunarso, J., Shao, Z., Zhou, W., Sun, C., Wang, S. & Liu, S. 2011. Research progress and materials selection guidelines on mixed conducting perovskite-type ceramic membranes for oxygen production. *RSC Advances,* 1**,** 1661-1676.

Zhang, K., Yang, Y. L., Ponnusamy, D., Jabson, A. J. & Salama, K. 1999. Effect of microstructure on oxygen permeation in $SrCo_{0.8}Fe_{0.2}O_{3-d}$. *Journal of Materials Science,* 34**,** 1367-1372.

Zhang, W., Smit, J., van Sint Annaland, M. & Kuipers, J. A. M. 2007. Feasibility study of a novel membrane reactor for syngas production: Part 1: Experimental study of O2 permeation through perovskite membranes under reducing and non-reducing atmospheres. *Journal of Membrane Science,* 291**,** 19-32.

Zhao, J., Zhang, K., Gao, D., Shao, Z. & Liu, S. 2010. Optimization of BaxSr1−xCo0.9Nb0.1O3−δ perovskite as oxygen semi-permeable membranes by compositional tailoring. *Separation and Purification Technology,* 71**,** 152-159.

Zhu, Q., Peng, L. & Zhang, T. (eds.) 2007. *Stable glass seals for intermediate temperature (IT) SOFC applications.,* San Diego: Springer.

Zhu, X., Li, M., Liu, H., Zhang, T., Cong, Y. & Yang, W. 2012. Design and experimental investigation of oxide ceramic dual-phase membranes. *Journal of Membrane Science,* 394–395**,** 120-130.